Publicly Accessible Penn Dissertations

2021

Search For Trilepton Resonances From R-Parity Violating Chargino Decays In The B-l Mssm

George Ian Dyckes
University of Pennsylvania

Search For Trilepton Resonances From R-Parity Violating Chargino Decays In The B−l Mssm

Abstract

This dissertation presents a search for the electroweak pair-production of charginos and the associated production of charginos and neutralinos in the B−L Minimal Supersymmetric Standard Model with spontaneous R-parity violation. The chargino and neutralino each decay via R-parity violating couplings to a charged lepton or neutrino and a W, Z, or Higgs boson. This analysis searches for resonances in the trilepton invariant mass spectrum, targeting events with charginos decaying to three electrons or muons via a leptonically decaying Z boson. The dataset includes 139 1/fb of 13 TeV proton-proton collisions produced at the Large Hadron Collider and collected by the ATLAS detector. With no significant excess observed, limits are set on chargino and neutralino masses between 100 GeV and 1100 GeV, depending on the assumed branching fractions to leptons (electron, muon, or tau) and bosons (W, Z, or Higgs).

Degree Type
Dissertation

Degree Name
Doctor of Philosophy (PhD)

Graduate Group
Physics & Astronomy

First Advisor
Evelyn Thomson

Keywords
ATLAS, CERN, Chargino, LHC, Supersymmetry, TRT

Subject Categories
Elementary Particles and Fields and String Theory | Physics

SEARCH FOR TRILEPTON RESONANCES FROM R-PARITY VIOLATING CHARGINO DECAYS IN THE $B − L$ MSSM

George Ian Dyckes

A DISSERTATION

in

Physics and Astronomy

Presented to the Faculties of The University of Pennsylvania
in Partial Fulfillment of the Requirements for the Degree of Doctor of Philosophy

2021

_____

Evelyn Thomson, Associate Professor, Physics and Astronomy
Supervisor of Dissertation

_____

Joshua Klein, Edmund J. and Louise W. Kahn Professor, Physics and Astronomy
Graduate Group Chairperson

<u>Dissertation Committee</u>
James Aguirre, Associate Professor, Physics and Astronomy
I. Joseph Kroll, Professor, Physics and Astronomy
Burt Ovrut, Professor, Physics and Astronomy
Hugh H. Williams, Mary Amanda Wood Professor of Physics and Astronomy
Evelyn Thomson, Associate Professor, Physics and Astronomy

SEARCH FOR TRILEPTON RESONANCES FROM R-PARITY
VIOLATING CHARGINO DECAYS IN THE $B - L$ MSSM

Acknowledgements

First, I would like to thank Brig Williams, Joe Kroll, Elliot Lipeles, and Evelyn Thomson for their support over the years. The friendly and collaborative atmosphere you have created in the ATLAS group is deeply appreciated, and I feel incredibly lucky to have experienced it. Thank you for all the insights, advice, and opportunities you have given me. I am especially grateful to my advisor, Evelyn Thomson, for her mentorship over the last six years. Thank you for encouraging me to pursue my physics interests, and for helping me stand out in such a large collaboration.

Contributing to the operation of the TRT was a highlight of my graduate school career. Over the years, I had the opportunity to work with many wonderful people from all over the world. While I cannot list everyone here, I would like to specifically acknowledge my colleagues on the TRT DAQ team: Shion, Keisuke, Khilesh, Elodie, Chris, Bijan, Sarah, Paul, Mike, Mitch, Daniil, Vincent, and Joe. Working with you all to record high-quality data was deeply rewarding. Thank you.

I was fortunate to work on a new search for supersymmetry with a small group of analyzers. Thank you Leigh Schaefer, Lucas Flores, Jeff Dandoy, and Evelyn Thomson for the incredible time and effort you put into the analysis. It was special working with you, and I am extremely proud of our results. I would also like to thank Burt Ovrut, Austin Purves, and Sebastian Dumitru for the many discussions and your deep investigation of the wino LSPs in your $B - L$ model.

Thank you to all my CERN and Geneva friends for all the great times we've had over the years. There are way too many people to name, but I would like to especially thank Lucas Flores, Jeff Shahinian, Sophia Bennett, and Greg Mederer. The skiing and backpacking trips, music festivals, lakeside barbecues, movies in the park, and boating excursions were awesome. I look forward to creating more memories with you in the future.

My time in Philadelphia was full of new experiences and friendships. Thank you to all my friends in the Penn physics department, especially the students of the ATLAS group. Again, there are too

many people to list, but I would like to specifically mention Lucas Flores, Sebastian Hurtado, and Khilesh Mistry. I would also like to thank Brandon Kamrava, Christian Adkisson, and all my friends from Temple Med. We had some great times on Catharine Street.

Thank you Frank Wuerthwein and Avi Yagil for hiring me out of undergrad and providing my first research experience in high energy physics. Thank you Vince Welke, Giuseppe Cerati, and all the members of the *Surf and Turf* group. Also, I would like to thank Bob Cousins, whose class inspired me to pursue a graduate degree in experimental particle physics.

Emily, I've relied on you and your family heavily throughout my PhD, and I could not have accomplished this without your love and support. Thank you.

Finally, I would like to thank my family for all their love and encouragement. Dad, thank you for fostering my interest in math and science. Maddie, thank you for your emotional support and for keeping the family connected. I love you both. Mom, thank you for always being my biggest fan. I love and miss you.

ABSTRACT

SEARCH FOR TRILEPTON RESONANCES FROM R-PARITY
VIOLATING CHARGINO DECAYS IN THE $B - L$ MSSM

George Ian Dyckes

E. Thomson

This dissertation presents a search for the electroweak pair-production of charginos and the associated production of charginos and neutralinos in the $B - L$ Minimal Supersymmetric Standard Model with spontaneous R-parity violation. The chargino and neutralino each decay via R-parity violating couplings to a charged lepton or neutrino and a W, Z, or Higgs boson. This analysis searches for resonances in the trilepton invariant mass spectrum, targeting events with charginos decaying to three electrons or muons via a leptonically decaying Z boson. The dataset includes 139 fb^{-1} of $\sqrt{s} = 13$ TeV proton-proton collisions produced at the Large Hadron Collider and collected by the ATLAS detector. With no significant excess observed, limits are set on chargino and neutralino masses between 100 GeV and 1100 GeV, depending on the assumed branching fractions to leptons (electron, muon, or τ-lepton) and bosons (W, Z, or Higgs).

Contents

List of Tables

List of Figures

Preface

In 2014, during my final year of undergrad at UCLA, I enrolled in a particle physics course taught by Professor Bob Cousins. After enjoying his class immensely, I considered pursuing a graduate degree in experimental particle physics. As graduation approached, I began emailing ATLAS and CMS professors all over California, hoping to gain some research experience. Fortunately, UC San Diego Professors Frank Wuerthwein and Avi Yagil offered me a research position on CMS for the 2014-2015 academic year. During my year in San Diego, I investigated a known mismodeling of the missing transverse energy, an important kinematic variable in many measurements and searches for new physics. I also joined a search for supersymmetric particles produced through the strong interaction, focusing on the same-sign dilepton final state. With the LHC in the middle of Long Shutdown 1, I primarily worked on simulation-based studies of the background from fake and non-prompt leptons. This search was eventually released to the public at the end of 2015 with the first 2.2 fb^{-1} of $\sqrt{s} = 13$ TeV data, becoming one of the earliest supersymmetry results in Run 2.

In the summer of 2015, I moved to Philadelphia to start graduate school with the Penn ATLAS group. Immediately upon my arrival, I joined the team of students, postdocs, engineers, instrumentation specialists, and faculty members contributing to the Data Acquisition (DAQ) system of the Transition Radiation Tracker (TRT). After only a couple weeks in Philadelphia, I was sent out to CERN for the first time. Under the guidance of Penn postdocs Sarah Heim and Chris Meyer, I started learning the ins and outs of operating the TRT. The timing of my trip was perfect, as the Run 2 data-taking campaign was just beginning. The highlight of this trip was my first tour of the detector. I remember my excitement growing as we put on our hard hats and crossed through the iris scanning biometric gates before entering the elevator down to the ATLAS cavern. When we finally opened the door to the main cavern, I was blown away by the size of the detector. Over the next hour, we climbed and crawled through ATLAS, visiting the various locations where the TRT

electronics are housed. I left feeling amazed that such a complicated detector could operate so well.

As I finished my graduate coursework back in Philadelphia, I started the ATLAS authorship qualification process. With the increased number of interaction per LHC bunch crossing, the TRT was in danger of saturating its readout bandwidth. Working primarily with Penn instrumentation physicist Paul Keener and fellow graduate student Leigh Schaefer, I began studying new data compression schemes to reduce the bandwidth usage. After settling on a particular lossy scheme, I studied its compression performance and effect on tracking. Using the knowledge I gained from my qualification task, I continued to study the TRT compression as the pileup increased over the course of Run 2.

In the summer of 2017, I moved to Geneva to take a larger role in the operation of the TRT. For the next few years, I contributed to the operation, calibration, maintenance, and upgrades of the TRT. Over this time period, I routinely served as the on-call TRT DAQ expert, which required 24 hour availability for a week at a time. If any issue arose during the data-taking, we would receive a phone call from the ATLAS control room asking for swift action to minimize data loss. This occasionally required urgent debugging sessions while out for dinner or in the early hours of the morning. While the TRT DAQ work was stressful at times, it felt incredibly rewarding to contribute to the data-collection process.

In the final few months of 2017, I decided to join a new physics analysis searching for supersymmetric particles. This analysis was born from a recurring collaboration between Penn ATLAS members and a group of Penn theorists led by Professor Burt Ovrut. With his graduate students and postdocs over the years, Burt developed a realistic model of supersymmetry with novel detector signatures. Inspired by this model, the Penn ATLAS group performed searches for the supersymmetric partner of the top quark in both Run 1 and Run 2. After completing the second search with the partial Run 2 dataset, Professor Evelyn Thomson (my advisor), postdoc Jeff Dandoy, and graduate student Leigh Schaefer began discussing which other supersymmetric particles to target with the full Run 2 dataset. The collaboration with Burt's group was renewed, this time including his former postdoc Austin Purves and current graduate student Sebastian Dumitru. After some interesting conversations about the model and its various features, the discussion focused on the superpartner of the W boson, the *wino chargino*, for its novel detector signature. Among its many possible decay paths, the wino chargino can decay to three leptons, producing a resonance in the trilepton invariant mass spectrum. As the theorists began investigating the phenomenology of the wino chargino in detail, the experimentalists started designing the search.

While I attended the discussions with the theorists, I did not immediately join the analysis

effort. At the time, I was exploring the many searches being planned by the ATLAS supersymmetry and exotics groups. However, I soon recognized the incredible opportunity this chargino search presented. I could participate in a new analysis with a unique detector signature, while working in a small group of only Penn ATLAS members. As a result, I could play a significant role in the design and execution of the search, making meaningful contributions to many aspects of the analysis.

By the time I decided to join the analysis, the early studies were already underway. I first worked on the basic search strategy with Leigh, developing an algorithm for classifying the many possible final states into three signal regions. Using truth information, I studied how often we correctly reconstructed the charginos from the leptons in the event. I later contributed to the optimization of the signal region definitions, maximizing the signal to background ratio. Perhaps my largest contribution to this analysis was the estimate of the fake and non-prompt lepton background. Towards the end of the analysis, I assisted with the statistical interpretation of the results. Finally, to facilitate reinterpretations of our results by the wider physics community, I reimplemented our statistical analysis in the `pyhf` framework. As a result of this effort, our full likelihoods could be published on HEPData.

Our preliminary results were presented by Evelyn at the APS April meeting in 2020. A few weeks later, I had the opportunity to present our results again at the eighth annual conference on Large Hadron Collider Physics, alongside other recent ATLAS and CMS searches for R-parity violating supersymmetry. At the time of this thesis, the official results are submitted to Physical Review D.

During my time as a graduate student, I've had incredible opportunities and experiences. Living in Geneva and working at CERN was amazing, with so many interesting and intelligent people from all over the world. I worked with an awesome group of physicists, both on the trilepton resonance search and as a member of the TRT DAQ team. I contributed to ATLAS data-taking and to a novel search for supersymmetry. I traveled to Benasque, Copenhagen, and Lecce for summer schools and workshops. For all this, I am deeply indebted to Evelyn, the other Penn ATLAS faculty members, and the many people that shaped my graduate school experience.

Ian Dyckes

February 2021

CHAPTER 1

Introduction

The Standard Model of particle physics (SM) is a theory encapsulating our understanding of three of the four known fundamental forces of nature. Using the framework of quantum field theory, the Standard Model describes the electromagnetic, weak, and strong interactions. The matter particles are spin-1/2 fermions that interact through the exchange of spin-1 gauge bosons. In addition to the force carriers and matter particles, the Standard Model contains the Higgs field, which is responsible for generating the masses of the fermions and gauge bosons. While the theory was established by the 1970s, the last SM particle was not observed until 2012 when the Higgs boson was discovered by the ATLAS and CMS collaborations at the Large Hadron Collider (LHC).

While the Standard Model has been incredibly successful in describing the outcomes of experiments across a wide range of energy scales, some observed phenomena are left unexplained. As a result, the SM is seen as a low-energy approximation of some full theory. This new theory may present itself through modifications to the known interactions, or through the appearance of new interactions and particles. With its high energy and luminosity, the LHC provides an excellent opportunity to discover new physics.

By examining the shortcomings of the Standard Model, some aspects of the superseding theory may be revealed. The most obvious outstanding issue of the SM is the lack of a quantum description of gravity. While the other three forces are described by a quantum field theory, gravity is instead described by the classical theory of general relativity. There is also some uncertainty in the behavior of the three quantized forces at high energies. While the electromagnetic and weak forces are known to unify above the electroweak scale, it is not clear if the strong and electroweak interactions unify at sufficiently high energies as well. Such Grand Unified Theories would reduce the number of free parameters and possibly explain the observed charge quantization, anomaly cancelation, and fermion

family structure of the Standard Model. Turning now to unexplained observations, the Standard Model does not provide a dark matter candidate or a mechanism for generating neutrino masses. Finally, the observed Higgs mass appears to be unnaturally light, as its quantum corrections are quadratically dependent on the highest mass scales of the theory.

These shortcomings of the Standard Model may be resolved by supersymmetry (SUSY), a conjectured symmetry that relates the fermions and bosons of a theory. In minimal supersymmetric models, each SM particle receives a superpartner whose spin differs by a half unit. SUSY therefore predicts a doubling of the particle content, with some of these new superpartners possibly within the reach of the LHC.

However, these minimal supersymmetric extensions also introduce baryon and lepton number violating interactions, which together can cause rapid proton decay. To prohibit such interactions, a discrete symmetry known as *R-parity* is often imposed. While enforcing R-parity conservation restores lepton and baryon number conservation, it also prevents the lightest supersymmetric particle (LSP) from decaying to Standard Model particles. The LSP is therefore an electrically neutral, weakly interacting, and stable dark matter candidate. For these reasons, the majority of SUSY searches at the LHC target stable LSPs from R-parity conserving models. These LSPs would be invisible to the detector, so their presence must be inferred from the missing transverse momentum.

While R-parity conserving SUSY models have a natural dark matter candidate, the imposition of a discrete symmetry to prevent proton decay is *ad hoc*. In the $B - L$ Minimal Supersymmetric Standard Model (MSSM), a more elegant solution is proposed. The gauge group of the Standard Model is extended by a local $U(1)_{B-L}$ symmetry, prohibiting the baryon and lepton number violating interactions introduced by SUSY. This symmetry is then spontaneously broken when the superpartner of a right-handed neutrino acquires a vacuum expectation value. While lepton number and R-parity are also broken in the process, baryon number is still conserved and the proton remains stable. Since R-parity is no longer conserved, the LSPs in this model can carry electric charge and decay directly to Standard Model particles. With its many possible LSP candidates, each with their own unique detector signatures, the $B - L$ MSSM has a rich phenomenology that can be explored through novel searches at the LHC.

Theorists at Penn have studied the $B - L$ MSSM in detail, from its low-energy phenomenology to its origin in heterotic string theory. A fruitful collaboration between these theorists and the Penn ATLAS group has inspired multiple searches at the LHC. First, the superpartner of the top quark was targeted at both $\sqrt{s} = 8$ TeV and $\sqrt{s} = 13$ TeV. Since these superpartners are produced at high rates via the strong force, these searches could be performed with more limited datasets. Now, with

the incredible statistics of the full Run 2 dataset, SUSY searches can target particles produced via the electroweak interaction. One such particle is the *chargino*, $\tilde{\chi}_1^\pm$, which is a likely LSP candidate in the $B - L$ MSSM with a unique detector signature.

This dissertation presents a search for charginos decaying to three charged leptons via $\tilde{\chi}_1^\pm \to Z\ell^\pm \to \ell^\pm \ell^\mp \ell^\pm$. Such a signal would produce a resonance in the trilepton invariant mass spectrum that peaks over a smoothly falling background. In Chapter 2, the theoretical framework of the Standard Model and $B - L$ MSSM is presented, as well as the phenomenology of the chargino LSPs. The LHC and ATLAS detector are then briefly described in Chapter 3. Afterwards, the Transition Radiation Tracker data acquisition system and compression algorithm will be discussed in detail in Chapter 4. This will include an examination of the readout limitations faced during Run 2 and the upgrades performed to overcome them. Finally, the search for trilepton resonances from R-parity violating chargino decays is presented in Chapter 5, with a brief conclusion in Chapter 6.

Theoretical Framework

2.1 The Standard Model

The Standard Model (SM) of particle physics is a renormalizable quantum field theory which encapsulates our understanding of the electromagnetic, weak, and strong interactions [1–19]. As a Yang-Mills gauge theory, the SM is defined by a Lagrangian that respects the gauge group

$$\mathrm{SU}(3)_C \times \mathrm{SU}(2)_L \times \mathrm{U}(1)_Y. \tag{2.1}$$

With the 2012 discovery of the Higgs boson by the ATLAS [20] and CMS [21] collaborations, all particles of Standard Model have been observed.

In this section, the field content and interactions of the Standard Model are first presented. Afterwards, the details of electroweak symmetry breaking and the gauge anomaly cancellations are analyzed. Finally, the shortcomings of the Standard Model are discussed to illustrate the need for new physics.

2.1.1 Field Content and Lagrangian

The field content of the Standard Model is summarized in Figure 2.1, both before and after electroweak symmetry breaking. Associated with each generator of the gauge symmetries is a vector gauge field, the quanta of which are the gauge bosons. This results in eight gluon fields for the $\mathrm{SU}(3)_C$ symmetry of quantum chromodynamics (QCD); the W_1, W_2, and W_3 fields for the $\mathrm{SU}(2)_L$ symmetry of weak isospin; and the B field for the $\mathrm{U}(1)_Y$ symmetry of weak hypercharge. After electroweak symmetry breaking, the W_1 and W_2 bosons will mix to form the $W^{\pm}$ bosons, and the W_3 and B bosons will mix to form the Z^0 boson and the photon, A^0.
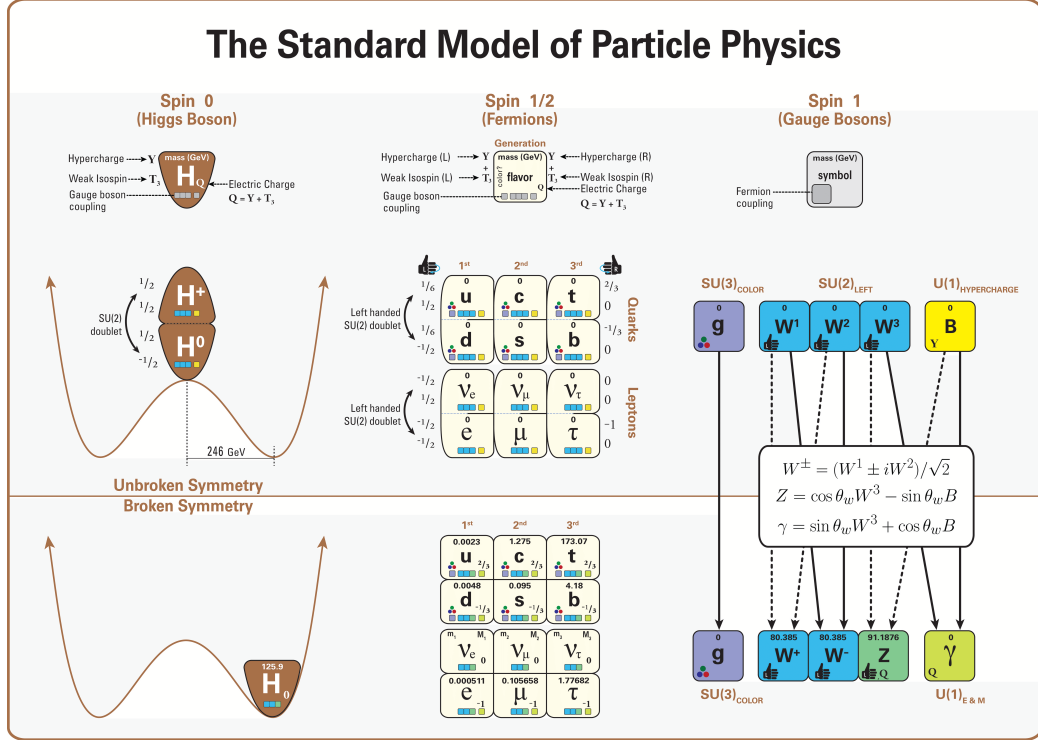
Figure 2.1: The field content of the Standard Model before and after electroweak symmetry breaking, including the masses and quantum numbers [22]. Note the convention for the hypercharge normalization differs by a factor of $1/2$ from that used in this thesis.

In addition to the gauge fields, the Standard Model contains fermionic matter fields. These matter fields are organized in three generations, with the corresponding particle in each generation having identical quantum numbers under the gauge symmetries. The fermions can be divided into quarks and leptons. While the quarks are charged under all three gauge groups, the leptons are only charged under weak isospin and hypercharge. As a result, the leptons do not couple to gluons. The leptons include the electron, muon, tau, and their associated neutrinos, while the quarks include the up, down, strange, charm, bottom, and top flavors. The SM is a chiral theory, as the left-handed and right-handed fermions are in different representations of the $SU(2)_L$ symmetry; the left-handed fermions are organized in isospin doublets, while the right-handed fermions are singlets. The two chiralities of fermions also have different hypercharges. Unlike the other fermions, which have both left-handed and right-handed components, right-handed neutrinos are absent in the Standard Model.[1]

---

[1]The observation of neutrino oscillations [23–25] suggest that neutrinos are massive. This may be explained by the existence of right-handed neutrinos.

Finally, the SM includes a complex scalar isospin doublet known as the Higgs field, which interacts with the fermions and gauge bosons. Additionally, the Higgs field interacts with itself according to a potential, the minimum of which defines the vacuum expectation value (VEV) of the field. As a scalar, the Higgs field is the only field that can have a nonzero VEV without violating Lorentz invariance. The shape of the Higgs potential and the location of its minimum play a major role in the spontaneous breaking of the electroweak symmetry from $SU(2)_L \times U(1)_Y \to U(1)_{QED}$ and the generation of fermion and gauge boson masses.

Spin-1 Gauge Fields				
Symbol	Associated Charge	Group	Coupling	Representation
B	Weak Hypercharge	$U(1)_Y$	g'	$(\mathbf{1}, \mathbf{1}, 0)$
W_1, W_2, W_3	Weak Isospin	$SU(2)_L$	g	$(\mathbf{1}, \mathbf{3}, 0)$
G_a	Color	$SU(3)_C$	g_s	$(\mathbf{8}, \mathbf{1}, 0)$
Spin-1/2 Matter Fields				
Symbol	Name	Baryon Number	Lepton Number	Representation
$L_i = \begin{pmatrix} \nu \\ e \end{pmatrix}_{L_i}$	Left-handed leptons	0	1	$(\mathbf{1}, \mathbf{2}, -1)$
e_{R_i}	Right-handed charged leptons	0	1	$(\mathbf{1}, \mathbf{1}, -2)$
$Q_i = \begin{pmatrix} u \\ d \end{pmatrix}_{L_i}$	Left-handed quarks	1/3	0	$(\mathbf{3}, \mathbf{2}, 1/3)$
u_{R_i}	Right-handed up-type quarks	1/3	0	$(\mathbf{3}, \mathbf{1}, 4/3)$
d_{R_i}	Right-handed down-type quarks	1/3	0	$(\mathbf{3}, \mathbf{1}, -2/3)$
Spin-0 Scalar Field				
Symbol	Name	Representation		
$\phi = \frac{1}{\sqrt{2}} \begin{pmatrix} \phi^+ \\ \phi^0 \end{pmatrix}$	Higgs Field	$(\mathbf{1}, \mathbf{2}, 1)$		

Table 2.1: The field content of the Standard Model.

The interactions of the fields is governed by a Lagrangian[2]. The SM Lagrangian is constrained by the internal local gauge symmetries, as well as the global Poincaré symmetry of special relativity. With the field content summarized in Table 2.1, the most general dimension-4 Lagrangian that

---

[2]Technically, the object discussed here is a *Lagrangian density*. The Lagrangian is obtained by integrating the Lagrangian density over space.

respects these symmetries is given by

$$\mathcal{L}_{\text{SM}} = \mathcal{L}_{\text{gauge}} + \mathcal{L}_{\text{fermion}} + \mathcal{L}_{\text{Yukawa}} + \mathcal{L}_{\text{Higgs}}$$

$$\mathcal{L}_{\text{gauge}} = -\frac{1}{2}\text{tr}G_{\mu\nu}G^{\mu\nu} - \frac{1}{2}\text{tr}W_{\mu\nu}W^{\mu\nu} - \frac{1}{4}B_{\mu\nu}B^{\mu\nu}$$

$$\mathcal{L}_{\text{fermion}} = \bar{L}\slashed{D}L + \bar{e}_R\slashed{D}e_R + \bar{Q}\slashed{D}Q + \bar{u}_R\slashed{D}u_R + \bar{d}_R\slashed{D}d_R + h.c. \tag{2.2}$$

$$\mathcal{L}_{\text{Yukawa}} = y^e_{ij}\bar{L}_i\phi e_{R_j} + y^u_{ij}\bar{Q}_i\bar{\phi}u_{R_j} + y^d_{ij}\bar{Q}_i\phi d_{R_j} + h.c.$$

$$\mathcal{L}_{\text{Higgs}} = |D_\mu\phi|^2 - V(\phi), \quad V(\phi) = \lambda|\phi|^4 + \mu^2|\phi|^2.$$

Both the gauge and family indices are largely suppressed. Also, the Feynman slash ($\slashed{D} = \gamma^\mu D_\mu$) and the Dirac adjoint ($\bar{\psi} = \psi^\dagger\gamma^0$) notations are used, where γ^μ are the Dirac matrices. Notice the Yukawa term involving the up-type quarks uses the conjugate of the Higgs field, $\bar{\phi} = i\sigma_2\phi^*$, which also behaves like an isospin doublet but with the opposite hypercharge. This will be important in an upcoming discussion.

In the SM, the gauge covariant derivative, D_μ is given by

$$D_\mu = \partial_\mu - i\frac{g'}{2}YB_\mu - i\frac{g}{2}\sigma_i W^i_\mu - i\frac{g_s}{2}\lambda_a G^a_\mu, \tag{2.3}$$

where Y is the hypercharge, and σ_i and λ_a are the Pauli and Gell-Mann matrices that generate $\text{SU}(2)_L$ and $\text{SU}(3)_C$, respectively. Since the right-handed fermions are isospin singlets, they do not couple to the W bosons. Also, since the lepton and Higgs fields are color singlets, they do not couple to the gluons.

The field strength tensors in $\mathcal{L}_{\text{gauge}}$ are defined for each gauge field X^a_μ as

$$X^a_{\mu\nu} = \partial_\mu X^a_\nu - \partial_\nu X^a_\mu + gf^{abc}X^b_\mu X^c_\nu, \tag{2.4}$$

where f^{abc} are the structure constants of the gauge group. These structure constants are defined such that

$$[t_a, t_b] = if^{abc}t_c, \tag{2.5}$$

where $\boldsymbol{t}$ are the generators of the group. Since the $\text{U}(1)_Y$ symmetry is Abelian, the generators commute and the structure constants are zero. As a result, $\mathcal{L}_{\text{gauge}}$ produces no terms cubic or quartic in B_μ, so the B bosons do not self-couple. In contrast, the $\text{SU}(2)_L$ and $\text{SU}(3)_C$ symmetries are non-Abelian, so their associated bosons can self-couple.

In addition to the gauge symmetries in Equation 2.1 and the Poincaré symmetry of special relativity, the Standard Model has a set of continuous U(1) global symmetries. These symmetries are considered *accidental*, as all dimension-4 terms that would violate them are coincidentally prohibited

by the gauge symmetries. First, the Lagrangian is invariant under a global rotation of all the quark fields: $\psi_q \to e^{i\alpha/3}\psi_q$. According to Noether's theorem, there must be a conserved charge associated with this symmetry. If the quarks and antiquarks are assigned a baryon number of $+1/3$ and $-1/3$, respectively, the total baryon number will be conserved in any process.[3] The Lagrangian is similarly invariant under independent phase rotations of the electron, muon, and tau flavor fields, resulting in the conservation of electron, muon, and tau number.

The conservation of the individual lepton family numbers results from the omission of right-handed neutrinos from the Standard Model. When right-handed neutrinos are added to the SM and given Dirac masses via the Higgs mechanism, the neutrino mass eigenstates become linear combinations of the flavor eigenstates. Analogous to the Cabibbo–Kobayashi–Maskawa matrix of the quark sector, the neutrino mass and flavor eigenstates are related via the Pontecorvo–Maki–Nakagawa–Sakata matrix. While lepton family number is now violated through neutrino oscillations, the total total lepton number is still conserved. However, if the neutrinos are given Majorana masses, the neutrinos and antineutrinos are no longer distinguishable, and lepton number is broken as well.

2.1.2 Spontaneous Electroweak Symmetry Breaking

Notice fermion and gauge boson mass terms are not contained in $\mathcal{L}_{\text{SM}}$. Under an infinitesimal gauge transformation by $\boldsymbol{\alpha}(x)$, the gauge fields transform like $X_\mu^a \to X_\mu^a + \frac{1}{g}\partial_\mu\alpha^a + f^{abc}X_\mu^b\alpha^c$. Consequently, mass terms of the form $m^2 X_\mu^a X^{a\mu}$ are clearly not gauge invariant. For the fermions, a mass term would be of the form $m\bar{\psi}\psi = m(\bar{\psi}_L\psi_R + \bar{\psi}_R\psi_L)$, which is not gauge invariant due to the left-handed and right-handed fields belonging to different isospin representations with different hypercharges. As a result, it appears $\mathcal{L}_{\text{SM}}$ can only describe a theory of massless fermions and gauge bosons. However, through the Higgs mechanism, fermion and gauge boson masses can be generated.

The Higgs potential $V(\phi)$ contains quadratic and quartic terms with real constants μ^2 and λ. The λ parameter is assumed to be positive, otherwise the vacuum will not be stable. When the dimensionful μ^2 parameter is positive, the Higgs potential is concave-up everywhere and the potential is minimized by $\phi = 0$. However, if the μ^2 parameter is driven to negative values, the Higgs potential takes on a "Mexican hat" shape with a minimum displaced from $\phi = 0$, as shown in Figure 2.2. Consequently, the Higgs field obtains a nonzero vacuum expectation value, and any perturbative calculations should involve expansions around the new minimum.

---

[3]While baryon and lepton number are conserved perturbatively, both can be violated non-perturbatively through sphaleron processes. However, $B - L$ remains conserved.
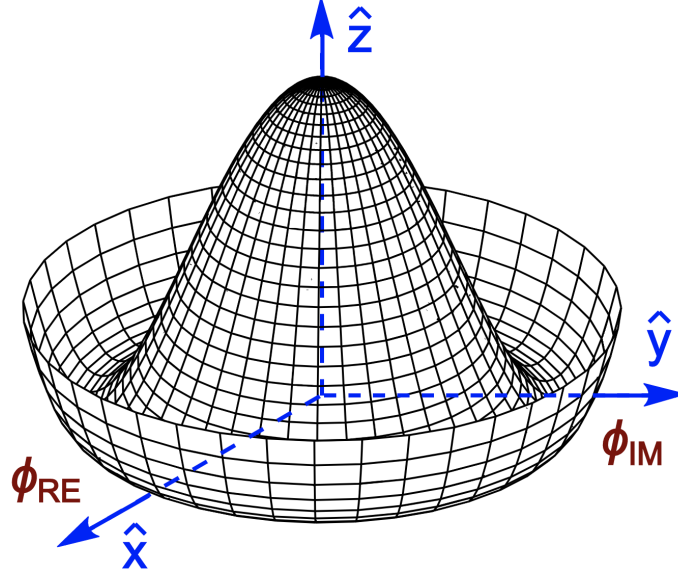
Figure 2.2: The Higgs potential after electroweak symmetry breaking, which resembles a "Mexican hat" [26]. The x and y axis are the magnitudes of the real and imaginary parts of the Higgs field, respectively. When μ^2 becomes negative, the Higgs field acquires a nonzero vacuum expectation value.

Defining the Higgs field as

$$\phi = \frac{1}{\sqrt{2}} \begin{pmatrix} \phi_1 + i\phi_2 \\ \phi_3 + i\phi_4 \end{pmatrix}, \tag{2.6}$$

one finds $V(\phi)$ with $\mu^2 < 0$ is minimized if $\phi_1^2 + \phi_2^2 + \phi_3^2 + \phi_4^2 = |\text{Re}(\phi)|^2 + |\text{Im}(\phi)|^2 = -\mu^2/\lambda$. Therefore, the vacuum manifold is given by a 3-sphere. Without loss of generality, the vacuum defined by $\phi_1 = \phi_2 = \phi_4 = 0$, $\phi_3^2 = -\mu^2/\lambda \equiv v^2$ can be chosen, spontaneously breaking the $\text{SU}(2)_L \times \text{U}(1)_Y$ symmetry. However, there is a residual symmetry which can be found be examining which combination of the $\text{SU}(2)_L$ and $\text{U}(1)_Y$ gauge transformation preserves the vacuum $\phi_0 = \frac{1}{\sqrt{2}}(0, v)$. Equivalently, one can find which linear combination of generators annihilates the vacuum. One finds

$$(\sigma_3 + \frac{1}{2}Y)\phi_0 = \left[\frac{1}{2} \begin{pmatrix} 1 & 0 \\ 0 & -1 \end{pmatrix} + \frac{1}{2}(1) \begin{pmatrix} 1 & 0 \\ 0 & 1 \end{pmatrix} \right] \begin{pmatrix} 0 \\ v \end{pmatrix} = \begin{pmatrix} 1 & 0 \\ 0 & 0 \end{pmatrix} \begin{pmatrix} 0 \\ v \end{pmatrix} = 0, \tag{2.7}$$

so a rotation about the third isospin axis can be undone by a half-rotation in hypercharge space. This combination of generators defines a residual $\text{U}(1)$ symmetry with a conserved charge $Q = T_3 + \frac{1}{2}Y$, which can be identified as $\text{U}(1)_{\text{QED}}$ and the electric charge, respectively.

According to Goldstone's theorem, a massless scalar boson is expected to appear for each broken generator. Between $SU(2)_L$ and $U(1)_Y$, there are four generators. Since one linear combination of the generators preserves the vacuum and defines the residual $U(1)_{QED}$ symmetry, three Goldstone bosons are expected.

To expand around the displaced vacuum ϕ_0, the Higgs field can then be redefined as

$$\phi(x) = \frac{1}{\sqrt{2}} e^{i\boldsymbol{\sigma\theta}(x)/v} \begin{pmatrix} 0 \\ v + h(x) \end{pmatrix} \cong \frac{1}{\sqrt{2}} \begin{pmatrix} \theta_2 + i\theta_1 \\ v + h - i\theta_3 \end{pmatrix}, \tag{2.8}$$

where $\theta_{1,2,3}$ can be identified with the three massless Goldstone bosons, and h is the massive Higgs boson with $m_h^2 = -2\mu^2$. The Goldstone bosons can be gauged away by performing an $SU(2)_L$ transformation, resulting in

$$\phi(x) = \frac{1}{\sqrt{2}} \begin{pmatrix} 0 \\ v + h(x) \end{pmatrix} \qquad \text{(unitary gauge)}. \tag{2.9}$$

Substituting Equation 2.9 into the kinetic term in $\mathcal{L}_{\text{Higgs}}$, one finds that the W_1 and W_2 bosons acquire a mass $m_W = vg/2$ and mix to form the familiar $W^\pm$ bosons. Additionally, the W_3 and B bosons mix, with one linear combination forming the massive Z boson with $m_Z = v\sqrt{g^2 + g'^2}/2$, and the other forming the massless photon of the residual $U(1)_{QED}$ symmetry. The real scalar degrees of freedom associated with the three Goldstone bosons become the longitudinal polarizations of the now massive $W^\pm$ and Z bosons. By inserting Equation 2.9 into $\mathcal{L}_{\text{Yukawa}}$ and $V(\phi)$, the fermion and Higgs boson masses can also be found.

2.1.3 Chiral Anomalies

In quantum field theories, a classical symmetry of the action can be violated when the theory is quantized. Such violations are known as *anomalies*, and their presence can ruin the renormalizability of the theory. In gauge theories, chiral anomalies [27, 28] may occur when the left-handed and right-handed fermions are in different representations of the gauge symmetries. These chiral anomalies are caused by diagrams connecting the axial current to two gauge currents via a fermion triangle, like in the one-loop corrections to the triple gauge vertices. The remainder of this section is dedicated to discussing the cancellation of these chiral anomalies in the Standard Model, closely following Chapter 22.2 of [18].

In the Standard Model, it is easiest to evaluate these possibly anomalous diagrams in the $SU(2)_L \times U(1)_Y$ basis with massless fermions. This way, the left-handed and right-handed fermions
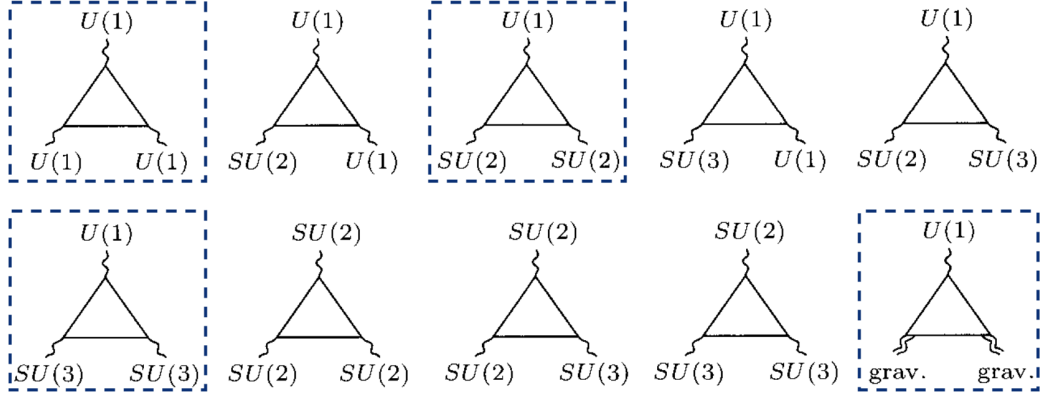
Figure 2.3: Possible chiral anomalies of the Standard Model [18]. Those boxed in blue require nontrivial cancellations.

have distinct quantum numbers. In principle, chiral anomalies can result from any diagram with at least one $SU(2)_L$ or $U(1)_Y$ boson. In contrast, diagrams where all three gauge bosons have left-right symmetric couplings do not contribute to chiral anomalies (e.g. three $SU(3)_C$ bosons). Various possibly anomalous diagrams are shown in Figure 2.3.

These triangle diagrams are proportional to

$$\mathrm{tr}[\gamma^5 t^a \{t^b, t^c\}], \tag{2.10}$$

where γ^5 is the fifth Dirac matrix and t^a, t^b, and t^c are the generators associated with the gauge bosons at the vertices. The trace is performed over all fermions that can circulate in the loop. The anticommutator is the result of summing over the two diagrams with the fermions traversing the loop in opposite directions. The presence of the γ^5 matrix is expected since these diagrams involve the chiral current, and it provides a relative factor of (-1) between the contributions from the left-handed and right-handed fermions. Consequently, diagrams containing only gauge bosons with equal couplings to both chiralities will have equal and opposite contributions from the left-handed and right-handed fermions. Such diagrams with therefore cancel automatically, as claimed earlier.

The diagram with three $SU(2)_L$ bosons serendipitously cancels due to a special property of the anticommutators of the Pauli matrices. Additionally, diagrams containing only one $SU(2)_L$ or $SU(3)_C$ boson are proportional to the trace of the associated generator. Since the generators of $SU(2)_L$ and $SU(3)_C$ are traceless, these diagrams also cancel. This leaves only the four boxed diagrams in Figure 2.3, which must be canceled nontrivially through relations between the quantum numbers of the various fermions.

For example, the diagram with two $\text{SU}(2)_L$ bosons and one $\text{U}(1)_Y$ boson is proportional to

$$\text{tr}[\sigma^a \sigma^b Y] = \frac{1}{2} \delta^{ab} \sum_L Y_L, \tag{2.11}$$

where the sum runs over the hypercharges of all left-handed fermions. Each generation of left-handed leptons contributes a factor of (-1) to the sum, while each generation of left-handed quarks contributes a factor of $3(1/3) = +1$. Therefore, this anomaly cancels. Despite this diagram containing only electroweak gauge bosons, its cancellation is surprisingly dependent on the three color charges of QCD. The anomaly cancellation also relies on the generation structure of the fermions. Together, these two observations may suggest that the quarks and leptons should be unified in a single multiplet of some larger gauge symmetry.

The other boxed diagrams in Figure 2.3 have similar miraculous cancellations, so the Standard Model remains renormalizable. It appears the fermions have just the right quantum numbers to cancel all chiral anomalies.

2.1.4   Shortcoming of the Standard Model

The Standard Model has been incredibly successful in describing the outcomes of experiments across a wide range of energy scales. In Figure 2.4, the production cross sections of various SM processes as measured by ATLAS are compared with the theoretical predictions, showing excellent agreement.

Despite this success, the Standard Model has some shortcomings, the most obvious of which is the lack of a quantum description of gravity. A non-exhaustive list of outstanding issues includes the cosmological constant problem [30], the hierarchy problem [31], the nature of dark matter [32,33], the strong CP problem [34], the miraculous chiral anomaly cancellation and the generational structure of fermions [18,27,28], the number of fermion generations [35], charge quantization and the number of free parameters [36], neutrino masses and oscillations [23–25], the vacuum instability [37], and the observed baryon asymmetry [38]. For these various shortcomings, the SM is seen as a low-energy approximation of a more complete theory.

The hierarchy problem in particular is worth discussing here. While the masses of the fermions and vector bosons are protected by chiral and gauge symmetries, the Higgs mass is destabilized by quantum corrections. The squared mass is quadratically sensitive to the mass of any new particle that couples directly or indirectly to the Higgs; that is, the correction from a new particle of mass m_X is $\Delta m_h^2 \sim m_X^2$. As a result, any new massive particle should pull the Higgs mass away from the electroweak scale unless the radiative corrections are carefully canceled by counter terms. If the

Figure 2.4: Comparison of the theoretical and measured total production cross sections for various Standard Model processes at $\sqrt{s} = 7$, 8, and 13 TeV [29].

Standard Model is correct up to the Planck scale, the corrections are on the order of $(10^{18} \text{ GeV})^2$. For the Higgs mass to remain near 10^2 GeV, the counter terms must be finely tuned over $2(18 - 2) = 32$ orders of magnitude. While this is not an issue of renormalization, the need for such a delicate cancellation is unnatural, suggesting new physics may be present at a scale not too far above the Higgs mass.

2.2   Supersymmetry

Supersymmetry (SUSY) is a spacetime symmetry that relates the fermions and bosons of a theory, providing solutions to some of the outstanding issues of the Standard Model [39–44]. The fields are organized in *supermultiplets* which contain both fermionic and bosonic states, with those falling in the same supermultiplet being known as *superpartners*. The SM fermions are contained in chiral supermultiplets with new scalar superpartners, and the SM bosons are placed in vector supermul-

tiplets with new spin-1/2 fermionic superpartners.[4] To distinguish the new superpartners from the SM particles, the following nomenclature is introduced: the superpartners of the SM fermions have an "s" prepended to their name (e.g. *squarks* and *sleptons*), while the superpartners of the SM Higgs and gauge bosons are appended with "ino" (e.g. *Higgsinos* and *gauginos*).

While the motivations for supersymmetry are diverse, just a few are mentioned here. First, supersymmetry modifies the renormalization group running of the SM gauge couplings, allowing their unification at high energies. As a result, SUSY may be a property of Grand Unified Theories (GUTs), which specify a larger gauge symmetry that breaks to the SM gauge group. Such theories reduce the number of free parameters and may explain the observed charge quantization and generational structure of fermions. Additionally, SUSY provides a mechanism for electroweak symmetry breaking through radiative corrections. Running the parameters of the scalar potential to the electroweak scale modifies its shape and induces a Higgs VEV, breaking the $\mathrm{SU}(2)_L \times \mathrm{U}(1)_Y$ symmetry. When supersymmetry is promoted to a local symmetry, it becomes theory of supergravity with the *gravitino* serving as the mediating gauge fermion. Also, supersymmetry is a property of M-theory [45], which is the best current Theory of Everything (TOE). Depending on whether or not R-parity[5] is conserved, SUSY may provide an excellent dark matter candidate or small neutrino masses. Finally, supersymmetry alleviates the hierarchy problem, as discussed in the following section.

2.2.1 Alleviating the Hierarchy Problem and Softly Broken SUSY

In supersymmetry, the chiral symmetry protecting the fermion masses is extended to the Higgs. Since the Standard Model particles and their superpartners are arranged in supermutiplets, they have the same quantum numbers under the gauge and accidental symmetries. Additionally, since the mass squared operator (P^2) commutes with the supersymmetry operators that transform the bosons and fermions of a supermultiplet into each other, the SM particles and their superpartners should have the same mass. As a result, the SM particles and their superpartners will have identical contributions to the Higgs mass correction, but with opposite signs due to their differing spin statistics. Therefore, the quadratic sensitivity of the Higgs to higher mass scales is canceled to all orders, and the Higgs mass naturally remains near the electroweak scale.

However, no superpartners of the SM particles have been observed at the same mass, so supersymmetry must be broken. To avoid reintroducing the quadratic sensitivity to high scales,

---

[4]The fermions of the Standard Model cannot be placed in vector supermultiplets, as the left-handed and right-handed fermions transform differently under the gauge group.

[5]R-parity will be discussed in Section 2.2.3

supersymmetry must be broken spontaneously and softly. In softly broken SUSY, the Lagrangian can be written as

$$\mathcal{L} = \mathcal{L}_{\text{SUSY}} + \mathcal{L}_{\text{soft}}. \tag{2.12}$$

While $\mathcal{L}_{\text{SUSY}}$ preserves supersymmetry and removes the quadratic sensitivity of the Higg mass, $\mathcal{L}_{\text{soft}}$ contains terms that violate SUSY and introduce new corrections. However, $\mathcal{L}_{\text{soft}}$ only contains mass terms and couplings with positive mass dimension. If m_{soft} is the largest mass scale in $\mathcal{L}_{\text{soft}}$, sending $m_{\text{soft}} \to 0$ should restore supersymmetry and cancel all corrections to the Higgs mass. Therefore, any correction due to the soft terms must be proportional to m_{soft}, so $\Delta m_h^2 \sim m_{\text{soft}}^2$.[6] As long as m_{soft} is not too large, the Higgs mass naturally stays at the electroweak scale. Naturalness therefore suggests that at least the lightest supersymmetric particles could be within the reach of the LHC.

2.2.2 The MSSM

The Minimal Supersymmetric Standard Model (MSSM) is the simplest supersymmetric extension of the Standard Model, in both field content and allowed interactions [46–51]. The MSSM field content is summarized in Table 2.2. Each Standard Model particle is organized in a supermultiplet with a new superpartner. The SM fermions and Higgs fields are placed in chiral supermultiplets, while the gauge bosons are placed in vector supermultiplets.

Chiral Supermultiplets	Spin-0	Spin-1/2	$\text{SU}(3)_C$, $\text{SU}(2)_L$, $\text{U}(1)_Y$
Q	$(\tilde{u}_L, \tilde{d}_L)$	(u_L, d_L)	$(\mathbf{3}, \mathbf{2}, 1/3)$
$\bar{u}$	$\tilde{u}_R^*$	$u_R^\dagger$	$(\bar{\mathbf{3}}, \mathbf{1}, -4/3)$
$\bar{d}$	$\tilde{d}_R^*$	$d_R^\dagger$	$(\bar{\mathbf{3}}, \mathbf{1}, 2/3)$
L	$(\tilde{\nu}_L, \tilde{e}_L)$	(ν_L, e_L)	$(\mathbf{1}, \mathbf{2}, -1)$
$\bar{e}$	$\tilde{e}_R^*$	$e_R^\dagger$	$(\mathbf{1}, \mathbf{1}, 2)$
H_u	(H_u^+, H_u^0)	$(\tilde{H}_u^+, \tilde{H}_u^0)$	$(\mathbf{1}, \mathbf{2}, 1)$
H_d	(H_d^0, H_d^-)	$(\tilde{H}_d^0, \tilde{H}_d^-)$	$(\mathbf{1}, \mathbf{2}, -1)$
Vector Supermultiplets	Spin-1/2	Spin-1	$\text{SU}(3)_C$, $\text{SU}(2)_L$, $\text{U}(1)_Y$
G	$\tilde{g}$	g	$(\mathbf{8}, \mathbf{1}, 0)$
W	$\tilde{W}^\pm, \tilde{W}^0$	$W^\pm, W^0$	$(\mathbf{1}, \mathbf{3}, 0)$
B	$\tilde{B}^0$	B^0	$(\mathbf{1}, \mathbf{1}, 0)$

Table 2.2: Chiral and vector supermultiplets of the MSSM, following the notation from [48].

---

[6]This is analogous to how chiral and gauge symmetries protect the fermion and gauge boson masses.

While the extension of the chiral symmetry to the Higgs boson protects its mass from any quadratic sensitivity to new scales, it also introduces fermionic Higgsinos that contribute to the chiral anomalies described in Section 2.1.3. In order to cancel these anomalies, a second Higgs doublet and its superpartners must be added with the opposite hypercharge.

These two Higgs supermultiplets, H_u and H_d, are also needed to give mass to both the up-type and down-type quarks. Recall in the Standard Model, both the up-type and down-type quarks acquire mass through a single Higgs doublet ϕ and its conjugate $\bar{\phi} = i\sigma_2\phi^*$.[7] However, in the MSSM, these Yukawa terms are part of the *superpotential*, which has to be a holomorphic function of the chiral superfields to be invariant under supersymmetry. As a result, the complex conjugate of the Higgs cannot be used, and a second doublet is needed for both the up-type and down-type quarks to acquire mass.

Notice that no Standard Model particle can be identified as the superpartner of another. While the down-type Higgs H_d and left-handed lepton L chiral supermultiplets have the same quantum numbers under the gauge symmetries, a Higgs boson cannot be identified as a sneutrino. The two supermultiplets carry different lepton number, which is conserved in the MSSM, and both are needed to cancel chiral anomalies.

Recall that the Standard Model provides no mechanism for driving the Higgs mass parameter μ^2 negative, triggering electroweak symmetry breaking. In the MSSM, the scalar potential is complicated by the two Higgs doublets and the various soft breaking terms. However, primarily through radiative corrections from the top Yukawa coupling, the soft breaking mass parameter of the up-type Higgs, $m^2_{H_u}$, runs to negative values. As a result, H_u and H_d acquire VEVs, labeled v_u and v_d, and the electroweak symmetry is broken. To reproduce the Standard Model electroweak phenomenology, the VEV of the SM Higgs field must be related to the VEVs of the MSSM via $v^2 = v_u^2 + v_d^2 = 2m_Z^2/(g^2 + g'^2)$. The ratio of VEVs is quantified by $\tan\beta \equiv v_u/v_d$, which is a free parameter of the MSSM.

Between the two complex scalar Higgs doublets, there are eight real degrees of freedom. Three of these become the Goldstone bosons of electroweak symmetry breaking, or in the unitary gauge, the longitudinal polarization states of the $W^\pm$ and Z bosons. The remaining five degrees of freedom are associated with a light and heavy CP-even Higgs boson (one of which is identified with the 125 GeV SM-like Higgs boson), a CP-odd pseudoscalar Higgs boson, and two charged Higgs bosons. The

---

[7]This can be seen by inserting the Higgs vacuum $\phi_0 = \frac{1}{\sqrt{2}}(0, v)$ into the up-type Yukawa term $y^u_{ij}\bar{Q}_i\bar{\phi}u_{R_j}$ to determine their masses. The conjugate field $\bar{\phi}$ is required to move the VEV to the upper component of the doublet, producing the mass term $\frac{v}{\sqrt{2}}y^u_{ij}\bar{u}_{L_i}u_{R_j}$.

superpartners of the various Higgs bosons include two neutral ($\tilde{H}_u^0$, $\tilde{H}_d^0$) and two charged ($\tilde{H}_u^+$, $\tilde{H}_d^-$) Higgsinos.

The superpartners of the Standard Model gauge bosons include the bino ($\tilde{B}^0$), charged and neutral winos ($\tilde{W}^\pm$, $\tilde{W}^0$), and the gluinos ($\tilde{G}$). After electroweak symmetry breaking, the bino, neutral wino, and two neutral Higginos mix to form mass eigenstates known as *neutralinos* ($\tilde{\chi}_1^0$, $\tilde{\chi}_2^0$, $\tilde{\chi}_3^0$, $\tilde{\chi}_4^0$). The *charginos* ($\tilde{\chi}_1^\pm$, $\tilde{\chi}_2^\pm$) are then the mass eigenstates of the charged winos and charged Higgsinos.

2.2.3   *R*-parity

The most general Lagragian with the MSSM gauge symmetries and field content does not respect the accidental symmetries of the Standard Model. The superpotential, which specifies the non-gauge interactions of the chiral superfields, is given by

$$W = \bar{u}y_u Q H_u - \bar{d}y_d Q H_d - \bar{e}y_e L H_d + \mu H_u H_d$$
$$+ \epsilon L H_u + \lambda L L \bar{e} + \lambda' L Q \bar{d} + \lambda'' \bar{u}\bar{d}\bar{d}, \tag{2.13}$$

where the gauge and generation indices are suppressed. The first line contains the three Yukawa interaction terms, as well as the Higgsino mass term. However, the first three terms of the second line violate lepton number, while the last term violates baryon number. If these terms are not suppressed or prohibited by an additional symmetry, the proton will decay at rates above the current stringent limits [52]. For example, a proton can decay to a neutral pion and a positron through the λ' and λ'' couplings, as shown in Figure 2.5.
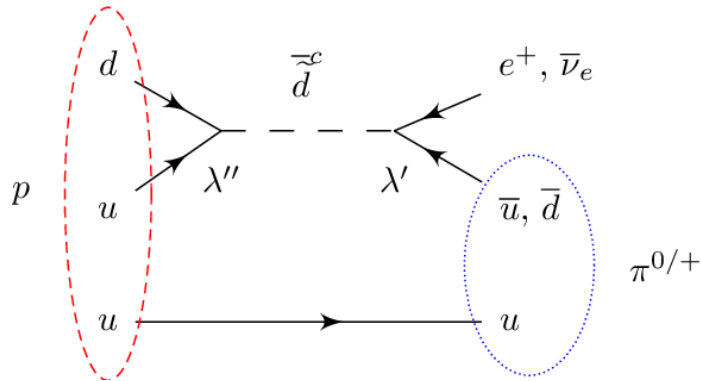
Figure 2.5: Feynman diagram of proton decay via *R*-parity violating couplings [53]. Notice proton decay requires both baryon and lepton number violating vertices.

Consequently, a new discrete $\mathbb{Z}_2$ symmetry is imposed in the MSSM [54]. A multiplicative quantum number know as *R-parity* is defined as

$$R_p = (-1)^{3(B-L)+2s}. \tag{2.14}$$

Notice that all SM particles have $R_p = +1$, while their superpartners have $R_p = -1$. By imposing R-parity conservation, all of the lepton and baryon number violating terms in the superpotential are prohibited. An additional consequence of R-parity conservation is that the lightest supersymmetric particle (LSP) is stable. Astrophysical observations strongly suggest that if the stable LSP exists, it is electrically neutral. Therefore, the LSP is likely a weakly interacting massive particle (WIMP) and a good dark matter candidate.

However, this *ad hoc* imposition of R-parity conservation may be too heavy-handed. Notice that to prevent proton decay, only lepton number or baryon number must be conserved. Generally, the limits on the R-parity violating couplings are less stringent when only one or a few are nonzero. Additionally, discrete symmetries like R-parity are violated by quantum gravitational effects [55]. Therefore, R-parity should be a discrete remnant of some spontaneously broken local gauge symmetry. However, this gauge symmetry and the field used to break it are not specified in the MSSM. Also, this gauge symmetry has to be anomaly-free, which places constraints on the field content [56, 57].

2.3 The $B - L$ MSSM

The $B - L$ MSSM is arguably the most minimal supersymmetric extension of the Standard Model that specifies the origin of the discrete symmetry used to prevent proton decay [58–65]. In this model, the gauge group is extended by a local $\mathrm{U}(1)_{B-L}$ symmetry and is given by

$$G = \mathrm{SU}(3)_C \times \mathrm{SU}(2)_L \times \mathrm{U}(1)_Y \times \mathrm{U}(1)_{B-L}, \tag{2.15}$$

although it is equivalent and useful in calculations to replace the $\mathrm{U}(1)_Y$ symmetry with $\mathrm{U}(1)_{3R}$ to eliminate kinetic mixing in the field strengths of the two $\mathrm{U}(1)$ symmetries [66].[8] Associated with this new $\mathrm{U}(1)_{B-L}$ symmetry is a gauge boson, B', and its superpartner, $\tilde{B}'$.[9] In order to cancel chiral anomalies, the sum of $B - L$ over each generation of left-handed and right-handed fermions must be zero. Therefore, three generations of right-handed neutrinos and their superpartners must be

---

[8]The $\mathrm{U}(1)_{3R}$ symmetry is generated by $T_{3R} = Y - \frac{1}{2}(B - L)$, which is also the diagonal generator of $\mathrm{SU}(2)_R$.
[9]Or when using the $\mathrm{U}(1)_{3R}$ symmetry, the W_R boson and its superpartner, $\tilde{W}_R$.

added to the field content of the MSSM. These new chiral supermultiplets $\bar{\nu}_i$ have a representation of $(\mathbf{1}, \mathbf{1}, 0, 1)$ under the gauge group in Equation 2.15. With the addition of the $\bar{\nu}_i$ fields, the supersymmetric Lagrangian gains another Yukawa term in the superpotential and new soft SUSY breaking terms.

From its definition in Equation 2.14, it can be seen that R-parity is a discrete subgroup of $\mathrm{U}(1)_{B-L}$. Consequently, the R-parity violating terms in the superpotential are forbidden while the $\mathrm{U}(1)_{B-L}$ symmetry is intact. However, this symmetry must be broken since no massless B' boson has been observed. Generically, a $\mathrm{U}(1)_{B-L}$ symmetry in some supersymmetric model can be spontaneously broken by a scalar field acquiring a VEV. Whether or not R-parity survives this symmetry breaking depends on the quantum numbers of the scalar field; if the scalar carries even $3(B - L)$, R-parity will be conserved. Since there are no such fields in the traditional or $B - L$ MSSM, either the field content must be augmented to achieve R-parity conservation, or R-parity must be broken.

In the $B - L$ MSSM, the $\mathrm{U}(1)_{B-L}$ local gauge symmetry is broken by one of the right-handed sneutrinos acquiring a vacuum expectation value. Without loss of generality, this is assumed to be the third generation sneutrino, $\tilde{\nu}_{R_3}^* \equiv \tilde{\nu}_3^c$.[10] Since the sneutrinos carry L and an odd $3(B - L)$ quantum number, both lepton number and R-parity conservation are broken. However, baryon number is still conserved, and the proton is sufficiently stable. The Goldstone boson associated with the $\mathrm{U}(1)_{B-L}$ symmetry breaking is "eaten" by the B' boson, resulting in a massive Z' boson.

As alluded to earlier, the $B - L$ MSSM with R-parity violation is not a unique solution to rapid proton decay in supersymmetric models. For example, a model with a spontaneously broken $\mathrm{U}(1)_{B-L}$ gauge symmetry can exhibit R-parity conservation [67]. However, such a model still requires three generations of right-handed neutrino superfields, plus a new scalar field carrying an even $3(B - L)$ quantum number. Alternatively, a discrete symmetry other than R-parity can be used to prevent some of the problematic terms in the superpotential [57]. For example, baryon triality [68] is a discrete $\mathbb{Z}_3$ symmetry that prevents the baryon number violating $\lambda'' \bar{u} \bar{d} \bar{d}$ term. This discrete symmetry can be a remnant of an anomaly-free $\mathrm{U}(1)$ gauge symmetry. While such a model does not require the addition of right-handed neutrino superfields, it does require a chiral superfield known as a *flavon* to break the $\mathrm{U}(1)$ symmetry.

---

[10] Note the small change in notation. The left-handed sneutrinos are now labeled $\tilde{\nu}_i$.

Symmetry Breaking Details

In the $B - L$ MSSM, the third generation right-handed sneutrino acquires a VEV, $\langle \tilde{\nu}_3^c \rangle = v_R/\sqrt{2}$, breaking the $\mathrm{U(1)}_{3R} \times \mathrm{U(1)}_{B-L} \to \mathrm{U(1)}_Y$. The $\mathrm{SU(3)}_C \times \mathrm{SU(2)}_L \times \mathrm{U(1)}_Y$ symmetries remains intact, since the right-handed sneutrinos are uncharged under the Standard Model gauge group. The $\mathrm{SU(2)}_L \times \mathrm{U(1)}_Y$ symmetry is then spontaneously broken when the up-type and down-type Higgs fields acquiring VEVs, $\langle H_u^0 \rangle = v_u/\sqrt{2}$ and $\langle H_d^0 \rangle = v_d/\sqrt{2}$. The Yukawa terms of the superpotential then induce a mixing of the three left-handed (s)neutrinos and the third generation right-handed (s)neutrinos. As a result, the three left-handed sneutrinos also acquire VEVs, $\langle \tilde{\nu}_i \rangle = v_{Li}/\sqrt{2}$.

Recall that electroweak symmetry breaking generates bilinear terms that mix the left-handed and right-handed fermions. In a similar fashion, the $B - L$ symmetry breaking generates bilinear terms that mix the leptons with the gauginos and Higgsinos. These new bilinear terms are generated when the sneutrino fields in the various Yukawa terms are replaced by their VEVs. The terms from the superpotential mix the leptons with the Higgsinos, while the terms from the super-covariant derivatives mix the leptons with the gauginos. As a result of these R-parity and lepton number violating terms, the chargino and neutralino mass eigenstates of the $B - L$ MSSM are a bit more complicated. The neutralinos are linear combinations of the bino $\tilde{B}^0$,[11] neutral wino $\tilde{W}^0$, neutral Higgsinos $\tilde{H}_u^0$ and $\tilde{H}_d^0$, the blino $\tilde{B}'$, the three left-handed neutrinos v_i, and the third generation right-handed neutrino v_3^c. The charginos are linear combinations of the charged winos $\tilde{W}^\pm$, charged Higgsinos $\tilde{H}^\pm$, and both the left-handed and right-handed charged leptons e_i and e_i^c.

With the addition of the right-handed fields, Dirac neutrino masses can be generated via electroweak symmetry breaking. Through the $B - L$ symmetry breaking, Majorana neutrino masses are generated as well. Since the third generation right-handed sneutrino acquires a VEV at the $B - L$ breaking scale, its corresponding neutrino is heavy. Through their $Y_{\nu i3}$ couplings with this heavy neutrino, the three left-handed neutrinos are driven to low masses via the seesaw mechanism. The first and second generation right-handed neutrinos, which couple to the left-handed neutrinos through $Y_{\nu_{i1}}$ and $Y_{\nu_{i2}}$, remain light as well. Therefore, the $B - L$ MSSM provides a natural explanation for the small active neutrino masses predicted by the neutrino oscillation observations. All neutrinos are mostly Majorana, with the Dirac masses controlling the active-sterile (left-right) mixing. The three active neutrinos and the first two sterile neutrinos remain light, while the third sterile neutrino becomes heavy.

---

[11]Or the $\tilde{W}_R^0$ in the $\mathrm{U(1)}_{3R}$ basis.

Additional Motivation

Interestingly, the $B-L$ MSSM is well-motivated from a *top-down* perspective, with the gauge group resulting from the breaking of an SO(10) Grand Unified Theory in the context of $E_8 \times E_8$ heterotic M-theory [69–74]. In this model, the SO(10) GUT is broken by two Wilson lines, χ_{3R} and χ_{B-L}, as shown in [66]. If the mass scale of χ_{B-L} is higher, the SO(10) symmetry will first break to a *left-right* model with a gauge group of $\mathrm{SU}(3)_C \times \mathrm{SU}(2)_L \times \mathrm{SU}(2)_R \times \mathrm{U}(1)_{B-L}$. If the mass scale of χ_{3R} is higher, the SO(10) symmetry will instead break to a *Pati-Salam*-like model with a gauge group of $\mathrm{SU}(4)_C \times \mathrm{SU}(2)_L \times \mathrm{U}(1)_{3R}$. In either case, the second Wilson line breaks the gauge group to that of the $B-L$ MSSM: $\mathrm{SU}(3)_C \times \mathrm{SU}(2)_L \times \mathrm{U}(1)_{3R} \times \mathrm{U}(1)_{B-L}$. The $\mathrm{U}(1)_{3R} \times \mathrm{U}(1)_{B-L}$ symmetry is then spontaneously broken to $\mathrm{U}(1)_Y$ by a radiatively-induced vacuum expectation value for the third generation right-handed sneutrino.

2.3.1 Parameter Space Scan

In order to understand the phenomenological viability of the $B-L$ MSSM, a parameter space scan is performed in [75]. The various model parameters, including the soft SUSY breaking masses, are randomly scattered at high energies in the context of the SU(10) GUT described above. These parameters are then renormalization group evolved down to the electroweak scale.

A set of low energy requirements are applied sequentially to each point in the scan. First, the $B-L$ symmetry must be spontaneously broken at a sufficiently high scale such that the resulting massive Z' boson is above 4.1 TeV, the existing ATLAS limit [76]. Second, the electroweak symmetry must be spontaneously broken, resulting in the correct $W^\pm$ and Z boson masses. Third, all sparticles must be above the measured bounds. Finally, the SM-like Higgs must have a mass within three standard deviations of the value measured by ATLAS [77].

The results of this scan are summarized in the left plot of Figure 2.6. Each point of the scan can be identified by two separate linear combinations of soft SUSY breaking parameters, $S_{BL'}$ and S_{3R}, which dominate the renormalization group equations. The points in green successfully break the $B-L$ symmetry and have a sufficiently massive Z' boson. The points that additionally break the electroweak symmetry with the correct $W^\pm$ and Z boson masses are shown in purple. Of these points, those that evade the lower bounds on sparticle masses are shown in cyan. Finally, the points that reproduce the phenomenology of the Standard Model, including the correct Higgs mass, are shown in black. The mass spectra of each of these valid black points was analyzed, resulting in the histogram on the right in Figure 2.6, which shows the frequency of each sparticle as the LSP.
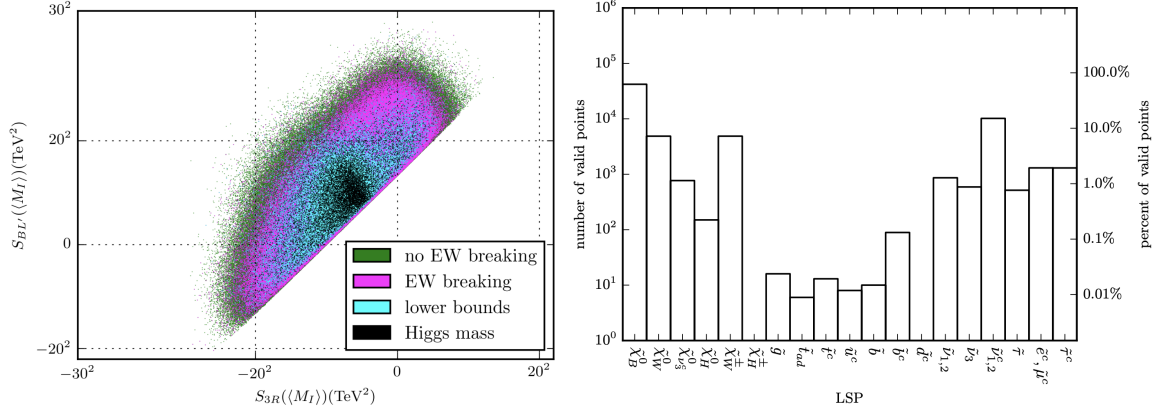
Figure 2.6: The results of the $B-L$ parameter space scan in [75]. On the left are all points where the $U(1)_{B-L}$ symmetry is spontaneously broken and the Z' boson is sufficiently massive. The points in black satisfy all low-energy phenomenological requirements. These are shown in the $S_{BL'}$-S_{3R} space at the intermediate mass scale, M_I, where the *left-right* model is broken to the $B-L$ MSSM. On the right is a histogram showing the frequency of each sparticle as the LSP for these black points.

Designing an LHC Search

Searches targeting the various possible LSPs of the $B-L$ MSSM can be performed at the LHC. Since R-parity is violated in this model, the LSPs can carry charge and decay to Standard Model particles. As a result, these signatures may not be covered by traditional searches for R-parity conserving SUSY models, which typically require significant missing transverse energy from stable and neutral LSPs escaping the detector.

As described above, the R-parity violating bilinear terms are generated from the Yukawa couplings when the sneutrinos acquire vacuum expectation values. Almost all of these R-parity violating vertices are proportional to the left-handed sneutrino VEVs, v_{Li}, and the neutrino Yukawa couplings, $Y_{\nu_{ij}}$, which must be small if the active neutrinos are nearly massless. Therefore, the R-parity violating vertices are suppressed and are only relevant for the otherwise forbidden decays of the LSP. As a consequence of this suppression, the LSPs are produced primarily through R-parity conserving processes. Since the colliding partons each have $R_p = +1$ and each LSP has $R_p = -1$, the LSPs must be produced in pairs.

According to the results of the parameter space scan, the predominantly bino neutralino $\tilde{\chi}_B^0$ is the most likely LSP. However, the $\tilde{\chi}_B^0$ is difficult to target at the LHC since it is associated with the Abelian $U(1)_Y$ symmetry and does not self-couple. As a result, it cannot be pair-produced via s-channel diagrams involving Z bosons. Instead, the production of bino LSPs is reliant on other supersymmetric particles, either through the exchange of heavier sparticles or in their cascade

decays. Consequently, the mass spectrum must be more carefully specified, and the final state may be complicated by the other decay products of the heavier sparticles.

The second most common LSP in the scan is the $\tilde{\nu}^c_{1,2}$, which is a linear combination of the first two generations of right-handed sneutrinos. However, the right-handed sneutrinos are uncharged under the Standard Model gauge group and therefore have small production cross sections via the SM bosons.[12] Additionally, the $\tilde{\nu}^c_{1,2}$ LSP primarily decays to two neutrinos, resulting in a detector signature with missing transverse energy, similar to traditional R-parity conserving searches.

After the $\tilde{\chi}^0_B$ and $\tilde{\nu}^c_{1,2}$, the predominantly wino chargino $\tilde{\chi}^\pm_W$ and neutralino $\tilde{\chi}^0_W$ are the next most likely LSP candidates. The winos are a more exciting target for a dedicated search due to their relatively high LHC production cross sections and interesting R-parity violating decays. Shown in Figure 2.7 are the production cross sections of various supersymmetric particles. Among the electroweak gauginos and Higgsinos, the winos are produced at the highest rate, primarily through s-channel $W^\pm$ and Z bosons. Note that this calculation was performed for an R-parity conserving model where the $\tilde{\chi}^0_2$ and $\tilde{\chi}^\pm_1$ are assumed to be mass-degenerate winos, while the $\tilde{\chi}^0_1$ LSP is assumed to be a pure bino. Since the contributions of the bino LSP to the $\tilde{\chi}^\pm_1 \tilde{\chi}^\mp_1$ and $\tilde{\chi}^\pm_1 \tilde{\chi}^0_2$ production cross sections are expected to be negligible, these cross sections also apply to the $B - L$ MSSM with mass-degenerate wino $\tilde{\chi}^\pm_1$ and $\tilde{\chi}^0_1$ LSPs. The wino $\tilde{\chi}^\pm_1 \tilde{\chi}^\mp_1 + \tilde{\chi}^\pm_1 \tilde{\chi}^0_1$ signal cross section ranges from 1.2 pb at 250 GeV to 1.9 fb at 1 TeV.

The phenomenology of the wino LSPs and their decays was studied in detail in [75] and [78]. The results relevant to the trilepton resonance search presented in this thesis will be discussed in the following section.

---

[12]These right-handed sneutrinos can be pair-produced in the decays of the heavy Z' boson associated with the broken $B - L$ symmetry. Therefore a monojet search may have some sensitivity to $Z'(\to \tilde{\nu}^c \tilde{\nu}^c \to \nu\nu\nu\nu) + j$ if the Z' is light enough to be produced at the LHC.
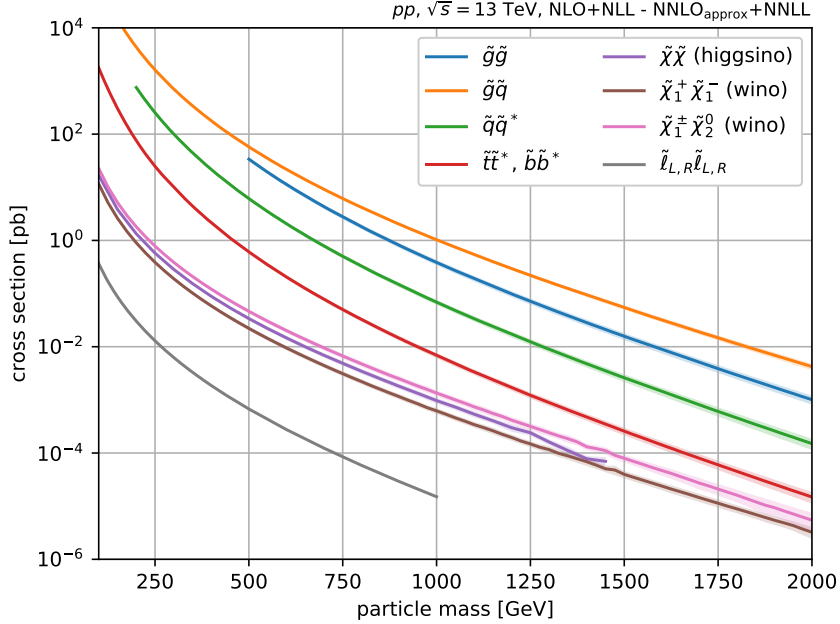
Figure 2.7: LHC production cross sections for various R-parity conserving supersymmetric processes vs. sparticle mass [79]. The wino cross sections are calculated assuming a mass-degenerate wino $\tilde{\chi}_1^\pm$ and $\tilde{\chi}_2^0$ and a light bino $\tilde{\chi}_1^0$, with all other sparticles decoupled [80, 81].

2.3.2 Wino LSP Phenomenology

The phenomenology of the valid points in the $B - L$ parameter space with predominantly wino $\tilde{\chi}_1^\pm$ and $\tilde{\chi}_1^0$ LSPs was studied in [75] and [78]. The first interesting observation was that the $\tilde{\chi}_1^\pm$ and $\tilde{\chi}_1^0$ have high wino purity, so the mass of each is dominated by the same wino mass parameter. Therefore, the LSP and the next-to-lightest supersymmetric particle (NLSP) are nearly mass-degenerate winos, as shown in Figure 2.8. Due to this sub-GeV mass difference, the R-parity conserving decay of the NLSP to the LSP via a W boson is kinematically suppressed. Consequently, both the wino LSP and NLSP will dominantly decay via the R-parity violating couplings to Standard Model particles. Regardless of which is slightly heavier, the wino $\tilde{\chi}_1^\pm$ and $\tilde{\chi}_1^0$ behave as effectively mass-degenerate LSPs.

The $\tilde{\chi}_1^\pm$ and $\tilde{\chi}_1^0$ both decay through their mixings with the leptons, which is induced by the R-parity violating bilinear terms. The $\tilde{\chi}_1^\pm$ can decay via $\tilde{\chi}_1^\pm \to Z^0 \ell_i^\pm$, $W^\pm \nu_i$, or $h^0 \ell_i^\pm$, while the $\tilde{\chi}_1^0$ can decay via $\tilde{\chi}_1^0 \to Z^0 \nu_i$, $W^\pm \ell_i^\mp$, or $h^0 \nu_i$. The branching fractions of the $\tilde{\chi}_1^\pm$ and $\tilde{\chi}_1^0$ to each SM boson are calculated for each valid point in the scan with wino LSPs. The results are
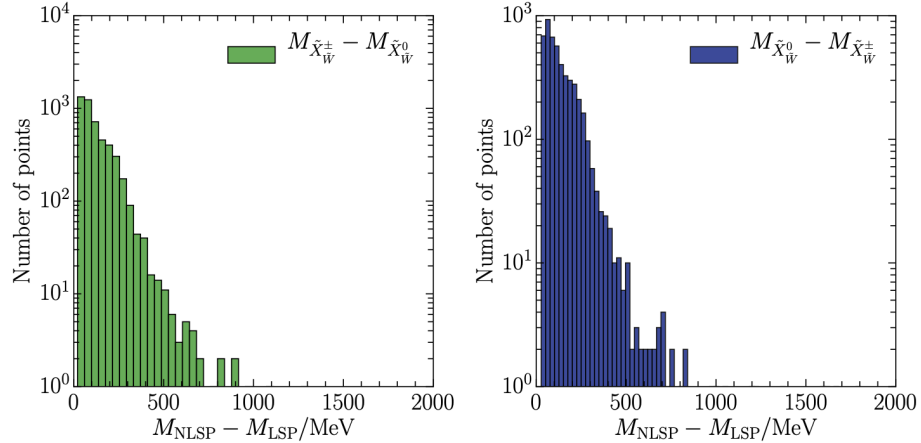
Figure 2.8: The mass splitting (in MeV) between the two winos when the $\tilde{\chi}_1^0$ is the LSP and the $\tilde{\chi}_1^\pm$ is the NLSP (left), and vice versa (right). The wino $\tilde{\chi}_1^\pm$ and $\tilde{\chi}_1^0$ are nearly mass-degenerate [78].

shown in Figures 2.9 and 2.10 for three ranges of $\tilde{\chi}_1^\pm/\tilde{\chi}_1^0$ mass and four ranges of $\tan\beta$. In all cases, the branching fractions to Higgs bosons are the largest, becoming more dominant as $\tan\beta$ is increased. For both the $\tilde{\chi}_1^\pm$ and $\tilde{\chi}_1^0$, the branching fraction to Z bosons decreases from about 15-20% for $1.2 < \tan\beta < 5$ to about 5% for $16 < \tan\beta < 65$. While the branching fractions are mostly independent of the $\tilde{\chi}_1^\pm/\tilde{\chi}_1^0$ mass, there is a slight enhancement of the branching fractions to W and Z bosons at high mass. According to the Goldstone boson equivalence theorem, the $\tilde{\chi}_1^\pm/\tilde{\chi}_1^0$ decays proceeding through the longitudinal polarizations of the W and Z bosons are enhanced with increasing $\tilde{\chi}_1^\pm/\tilde{\chi}_1^0$ mass.

Recall, the R-parity violating bilinear terms that induce the mixing between the gauginos, Higgsinos, and leptons are generated by the sneutrinos acquiring vacuum expectation values. As a result, the neutrino sector is related to the branching fractions of the $\tilde{\chi}_1^\pm$ and $\tilde{\chi}_1^0$ to each lepton flavor. The leptonic branching fractions of each valid point in the scan are shown in Figures 2.11 and 2.12. These branching fractions depend on the nature of the neutrino hierarchy (normal or inverted) and the various parameters of the neutrino sector. However, the measurement of the θ_{23} neutrino mixing angle has a 68% confidence interval with two statistically degenerate best-fit values for each hierarchy [82]. These best-fit values are $\sin^2\theta_{23} = 0.417$ or 0.597 for the normal hierarchy, and $\sin^2\theta_{23} = 0.421$ or 0.529 for the inverted hierarchy. Accordingly, the $\tilde{\chi}_1^\pm/\tilde{\chi}_1^0$ branching fractions to leptons are shown for both hierarchies and for each choice of θ_{23}.

Depending on the nature of the neutrino hierarchy, the valid points from the scan tend to populate different regions of the leptonic branching fraction space. Consequently, if a signal were seen at the
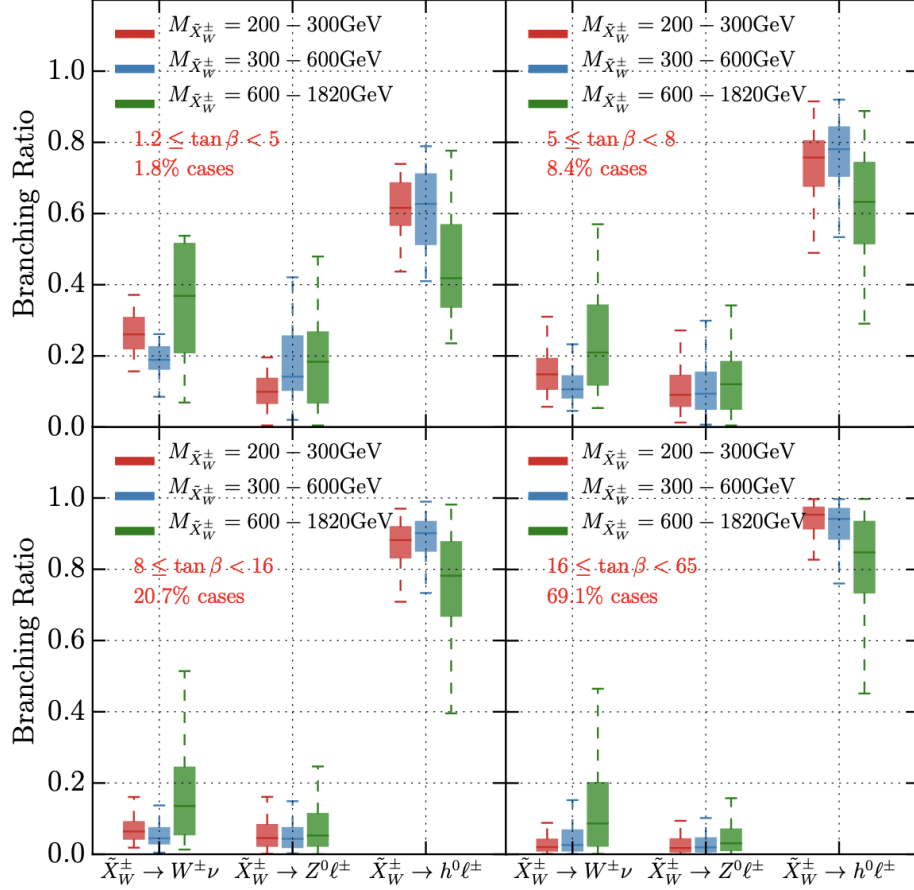
Figure 2.9: The branching fractions of the wino $\tilde{\chi}_1^{\pm}$ to the different Standard Model bosons. The results are shown for three ranges of $\tilde{\chi}_1^{\pm}$ mass and four ranges of $\tan\beta$. The dashed error bars show the maximum and minimum values in the scan, while the colored boxes show the interquartile ranges [78].

LHC, the observed decay rates to each lepton flavor could constrain the neutrino hierarchy. In the normal neutrino mass hierarchy, the lightest mass eigenstate is dominated by the electron neutrino flavor eigenstate. Since the neutrino masses are proportional to the square of the R-parity violating couplings, the decays of the winos to the electron-flavored leptons are suppressed relative to the other flavors, reducing the branching fractions to electrons and electron neutrinos. In the inverted hierarchy, the lightest mass eigenstate is a mix of the muon and tau flavors. Consequently, the scan points avoid high branching fractions to the muon or tau flavors.

Finally, since the R-parity violating decays are suppressed, the decay lengths of the wino $\tilde{\chi}_1^{\pm}$ and $\tilde{\chi}_1^0$ must be investigated. If sufficiently suppressed, the $\tilde{\chi}_1^{\pm}/\tilde{\chi}_1^0$ may travel a measurable distance
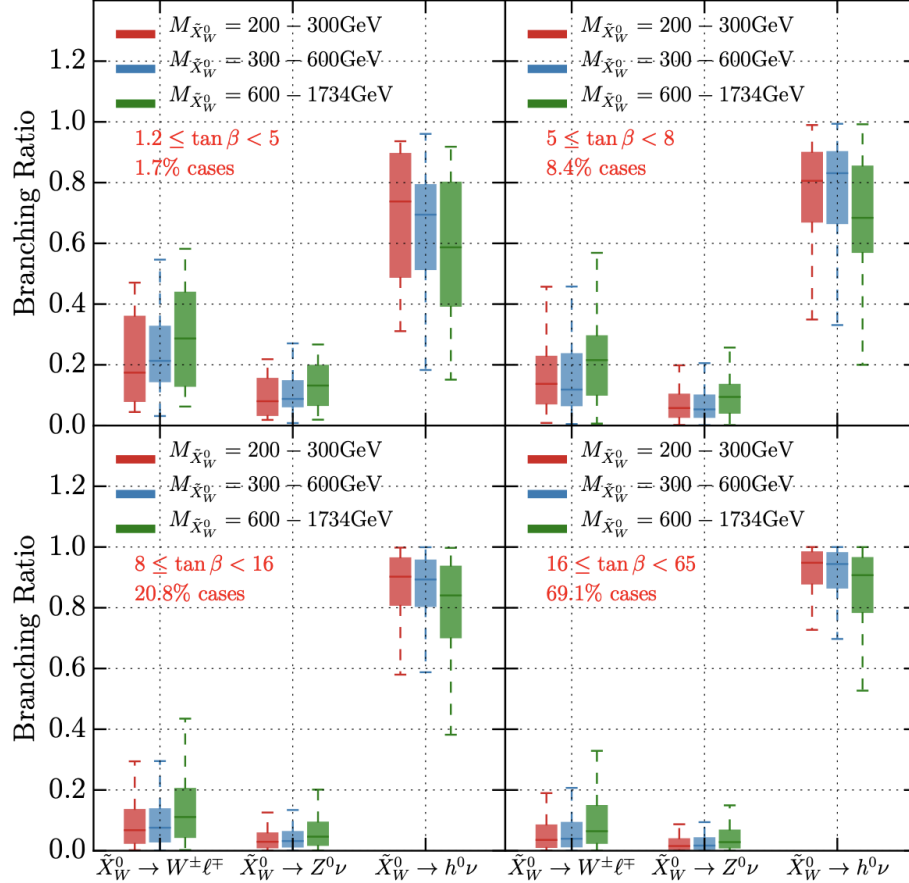
Figure 2.10: The branching fractions of the wino $\tilde{\chi}_1^0$ to the different Standard Model bosons. The results are shown for three ranges of $\tilde{\chi}_1^0$ mass and four ranges of $\tan\beta$. The dashed error bars show the maximum and minimum values in the scan, while the colored boxes show the interquartile ranges [78].

in the ATLAS detector before decaying, resulting in a significantly different detector signature. For each viable point, the decay lengths $L = c\tau$ are calculated under both neutrino hierarchies. The results are shown for $\tilde{\chi}_1^\pm$ and $\tilde{\chi}_1^0$ decays in Figures 2.13 and 2.14, respectively.[13] With such short lifetimes, the $\tilde{\chi}_1^\pm/\tilde{\chi}_1^0$ decays are considered prompt.

To summarize, the mostly wino $\tilde{\chi}_1^\pm$ and $\tilde{\chi}_1^0$ are likely LSP candidates in the $B - L$ MSSM. They would be produced in $\tilde{\chi}_1^\pm\tilde{\chi}_1^\mp$ or $\tilde{\chi}_1^\pm\tilde{\chi}_1^0$ pairs with a sizable cross section, at least compared to the other electroweak supersymmetric particles. The $\tilde{\chi}_1^\pm$ and $\tilde{\chi}_1^0$ would be nearly mass-degenerate, with each decaying promptly via R-parity violating couplings to a lepton and a massive SM boson.

---

[13]Note the actual distance traveled by the $\tilde{\chi}_1^\pm/\tilde{\chi}_1^0$ before decaying is $D = \beta\gamma c\tau$, which is larger than $L = c\tau$ for $\beta > 1/\sqrt{2} \approx 70\%$.
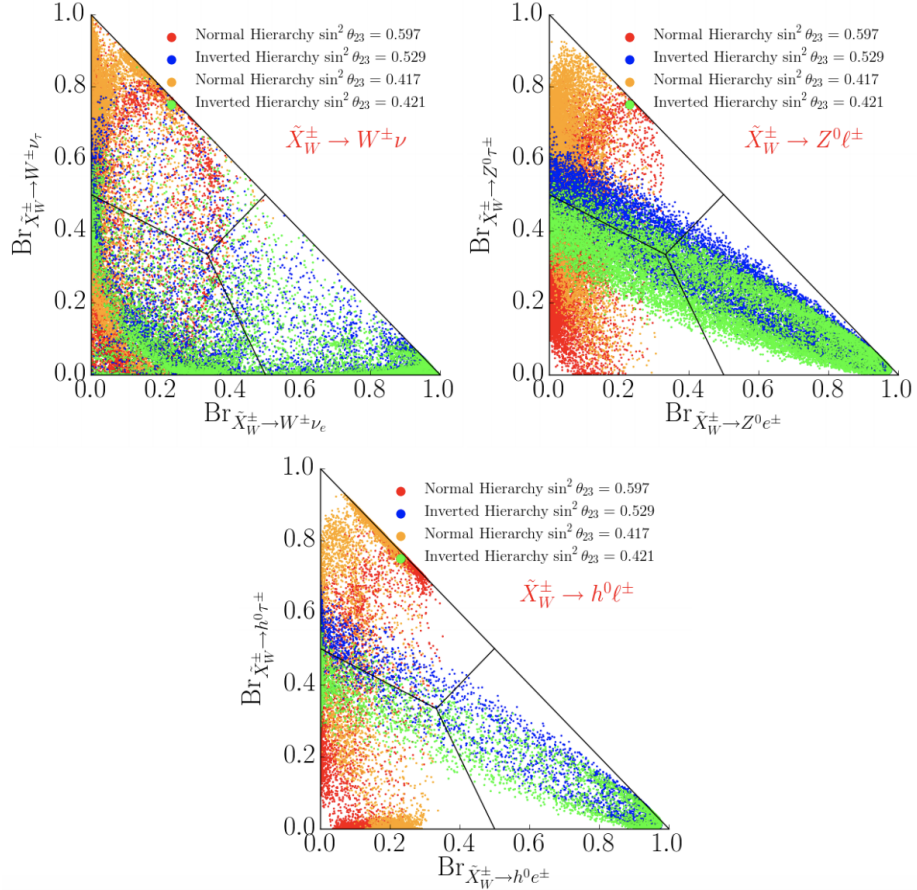
Figure 2.11: The branching fractions of the wino $\tilde{\chi}_1^{\pm}$ to the different lepton flavors. The results are shown separately for both neutrino hierarchies and both choices of θ_{23} [78].

Among the various possible final states, the $\tilde{\chi}_1^{\pm} \to Z\ell \to \ell\ell\ell$ decay is particularly interesting from an experimental perspective. Due to the excellent lepton momentum resolution of the ATLAS detector, the $\tilde{\chi}_1^{\pm}$ four-vector and mass can be reconstructed accurately. While this decay channel is suppressed by the small leptonic branching fractions of the Z boson,[14] the trilepton mass resonance is a striking signature that provides strong discrimination against the background over a wide range of possible wino masses. This $\tilde{\chi}_1^{\pm} \to Z\ell \to \ell\ell\ell$ signature is targeted by the search presented in this thesis.

---

[14]$\mathcal{B}(Z \to \ell\ell) = 3.4\%$ for each lepton flavor.
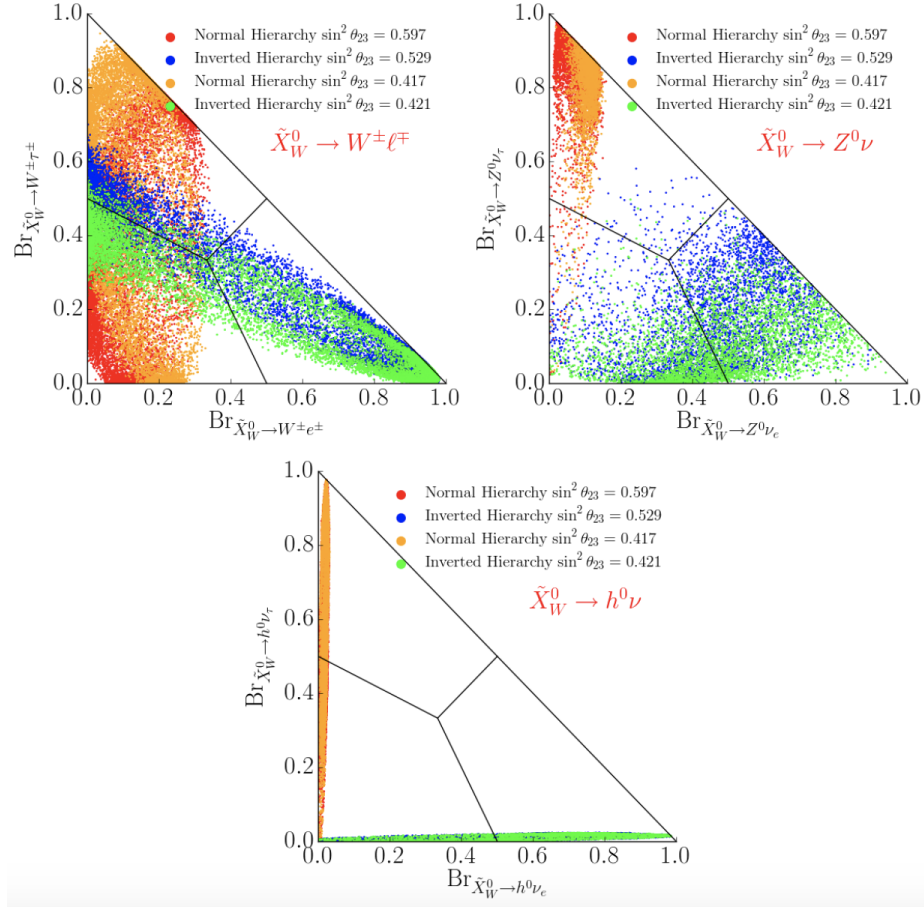
Figure 2.12: The branching fractions of the wino $\tilde{\chi}_1^0$ to the different lepton flavors. The results are shown separately for both neutrino hierarchies and both choices of θ_{23} [78].
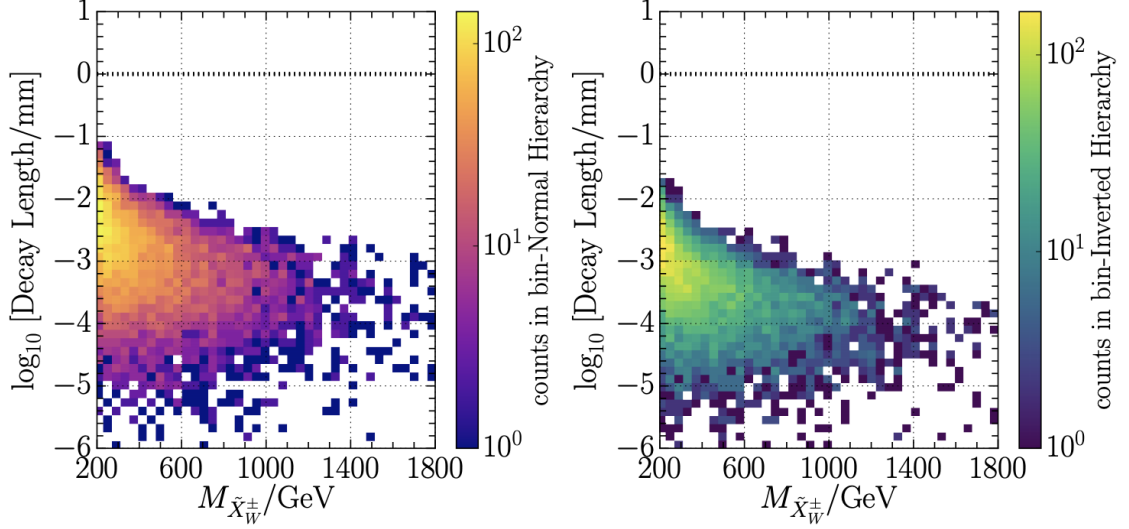
Figure 2.13: The wino $\tilde{\chi}_1^{\pm}$ decay length $L = c\tau$ for the normal (left) and inverted (right) neutrino hierarchies [78].
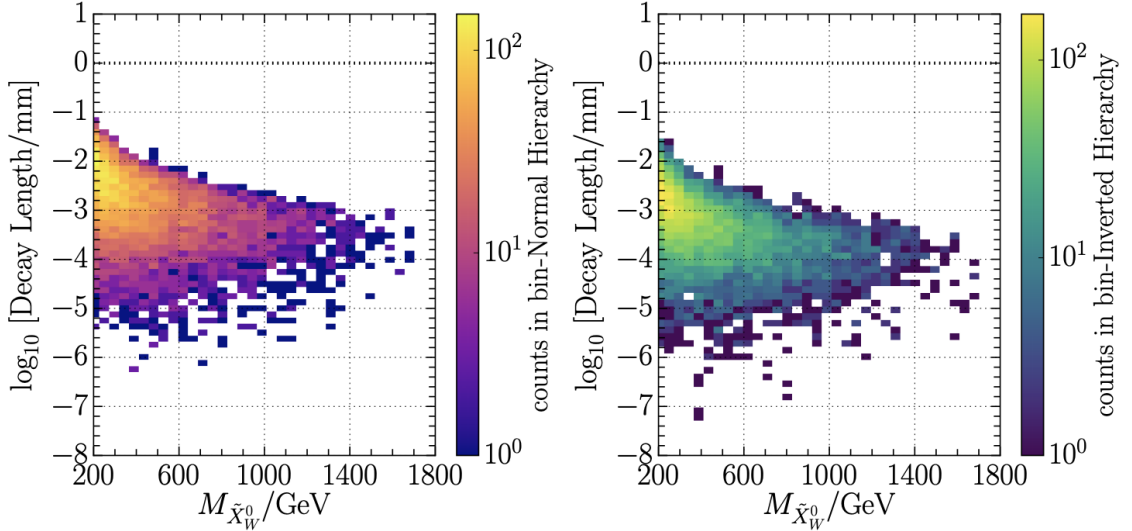
Figure 2.14: The wino $\tilde{\chi}_1^0$ decay length $L = c\tau$ for the normal (left) and inverted (right) neutrino hierarchies [78].

CHAPTER 3

The LHC and the ATLAS Detector

3.1   The Large Hadron Collider

The Large Hadron Collider (LHC) [83] is the world's largest particle accelerator, located outside Geneva on the Swiss-French border. A 27 km circumference synchrotron, the LHC can accelerate protons (and occasionally heavy ions) to nearly the speed of light. This is achieved using radio frequency cavities to accelerate the protons, as well as dipole and quadrupole superconducting electromagnets to steer and focus the beam. The circulating proton beams are collided at four interaction points, around which the ATLAS [84], CMS [85], LHCb [86], and ALICE [87] detectors are constructed.

A schematic of the CERN accelerator complex is shown in Figure 3.1. The protons that are eventually collided by the LHC originate from a bottle of hydrogen gas. After ionizing the gas, the protons are injected into LINAC 2, a linear particle accelerator, where the protons are accelerated to 50 MeV in energy. The protons then move on to the Proton Synchrotron Booster, then the Proton Synchrotron (PS) itself. The protons circulate in the PS until they reach 25 GeV in energy, when they are injected into the Super Proton Synchrotron (SPS). The SPS then accelerates the protons to 450 GeV. Finally, the protons are injected into the LHC, forming two counter-rotating beams. During Run 2, which spanned the years 2015 to 2018, the protons in each beam were accelerated to 6.5 TeV, resulting in a center-of-mass energy of $\sqrt{s} = 13$ TeV.

While the total energy and momentum of the colliding protons are well-measured, the longitudinal momenta of the quarks and gluons constituting the protons are unknown. Instead, their momenta are described by parton distribution functions (PDFs), which give the probability density for observing a particular parton with some fraction of the proton's longitudinal momentum. Since

it is the partons that interact in the collisions, the center-of-mass energy of any interaction is below 13 TeV, and the interaction's initial boost along the beamline is unknown.
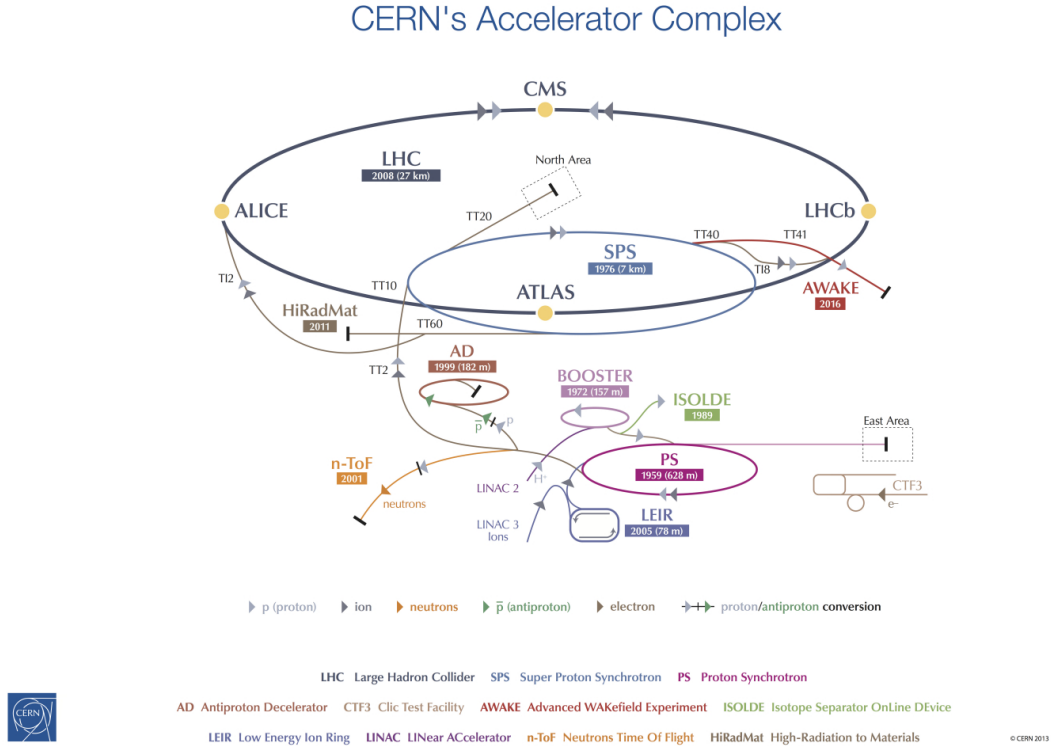
Figure 3.1: The CERN accelerator complex [88].

To be properly accelerated by the RF cavities, the protons must pass through the cavities in phase with the oscillating electric field. This requires the protons to be injected in bunches, and for the RF frequency to be an integer multiple of the beam's revolution frequency. This integer is known as the *harmonic* number. With a revolution frequency of 11.2455 kHz and an RF cavity frequency of 400 MHz, the harmonic number of the LHC is 35640. The harmonic number provides the upper limit on the number of bunches, partitioning the beam into 35640 *buckets*. During Run 2, only one in every ten buckets can be filled, resulting in a minimum bunch spacing of 25 ns. Of the 3564 available buckets, only about 2000-2500 are actually filled with bunches in any LHC run. The number and placement of these bunches was varied over the course of Run 2 to increase the luminosity and combat unexpected beam dumps from a malfunctioning LHC half-cell [89–91].

Luminosity

After the center-of-mass energy, the luminosity is the most important quantity describing the beams. Defined such that

$$\frac{dN}{dt} = \mathcal{L} \cdot \sigma, \tag{3.1}$$

the luminosity ($\mathcal{L}$) relates the production cross section for some process (σ) to the expected rate for observing such events (dN/dt). It can be shown [92] that the luminosity can be expressed as

$$\mathcal{L} = \frac{N_p^2 n_b f_{\text{rev}}}{4\pi \sigma_x^2 \sigma_y^2} F, \tag{3.2}$$

where N_p is the number of protons per bunch ($\sim 10^{11}$), n_b is the number of bunches in the beam (~ 2500), f_{rev} is the beam revolution frequency (~ 11 kHz), σ_x^2 and σ_y^2 are the beam widths in the x and y directions at the interaction point (~ 15 μm), and F is a geometric factor accounting for the crossing angle of the beams (0.3–1). The luminosity is typically measured in units of cm^{-2} s^{-1} or in b s^{-1} (1 barn = 10^{-24} cm^{-2}). The luminosity is the highest at the beginning of a run, decreasing over time due to beam losses. This is tracked by splitting each run into many *luminosity-blocks* (LBs), which are periods during which the instantaneous luminosity, trigger rate, detector configuration, and data quality are all approximately constant. In the second half of Run 2, the LHC regularly reached peak instantaneous luminosities of 2×10^{34} cm^{-2} s^{-1}, double its design luminosity.

By integrating both sides of Equation 3.1 over time, one finds that the total number of expected events for some process is given by $N = \mathcal{L}_{\text{int}} \cdot \sigma$, where $\mathcal{L}_{\text{int}}$ is the integrated luminosity. The integrated luminosity therefore quantifies the total amount of data that has been delivered. Over the course of Run 2, the LHC delivered 153 fb^{-1} of 13 TeV pp data with a 25 ns bunch spacing. The ATLAS detector recorded 145 fb^{-1} of this data, with 139 fb^{-1} deemed suitable for physics analysis [93].

Pileup

As each bunch contains many protons, multiple proton pairs can scatter every bunch crossing. The number of pp inelastic interactions per bunch crossing is known as the *pileup*, labeled μ. The in-time pileup, which only includes the interactions from the same bunch crossing, is determined by the instantaneous luminosity per bunch ($\mathcal{L}_{\text{bunch}}$), the inelastic cross section (σ_{inel}), and the revolution frequency:

$$\mu = \frac{\mathcal{L}_{\text{bunch}} \, \sigma_{\text{inel}}}{f_{\text{rev}}}. \tag{3.3}$$

Additionally, because the readout windows and characteristic relaxation time scales of the ATLAS subsystems are often longer than the 25 ns minimum bunch spacing, there is an out-of-time contribution to the pileup in each event from the neighboring bunch crossings. The pileup averaged over all bunches over the course of a luminosity-block is a useful metric for summarizing the detector conditions, and is denoted as $\langle \mu \rangle$.

The luminosity-weighted pileup distributions for the full Run 2 $\sqrt{s} = 13$ TeV pp collision dataset is shown in Figure 3.2, along with the cumulative luminosity by year. The pileup averaged over all of Run 2 is $\langle \mu \rangle = 33.7$, exceeding the design peak pileup of $\mu \approx 25$. This is mostly driven by the 2017 and 2018 runs, when the luminosity and beam structure had to be modified due to abnormal beam losses in the 16L2 cryogenic half-cell [89–91]. In September 2017, the 8b4e bunch structure was developed to address this issue. Instead of long trains of bunches separated by the minimum 25 ns spacing, short trains of only 8 bunches were used, with each train separated by 4 empty bunch crossings. While this scheme improved the beam stability, it also reduced the number of bunches from 2556 to about 1900. In order to recover the lost luminosity, the number of protons per bunch was increased and the beam waist was reduced. As an unfortunate side effect, the pileup drastically increased, exceeding $\mu = 60$ with the nominal beam separation at the interaction point. Since this pileup was too high for the experiments, the luminosity at the start of the runs was leveled such that the pileup did not exceed $\langle \mu \rangle \approx 60$. This was achieved by adjusting the beam separation at the interaction point, reducing the separation as the beam intensity decreased over the course of the run. Through this leveling, a pileup of $\langle \mu \rangle \approx 60$ was maintained for the first few hours of each run, resulting in a bimodal pileup distribution in 2017. In 2018, the LHC returned to a bunch structure with long trains and 2556 bunches, maintaining the peak pileup of $\langle \mu \rangle \approx 60$ without leveling and reaching peak instantaneous luminosities of about 2×10^{34} cm^{-2} s^{-1}. The peak pileup in each 13 TeV pp run is shown in Figure 3.3, separated by year.
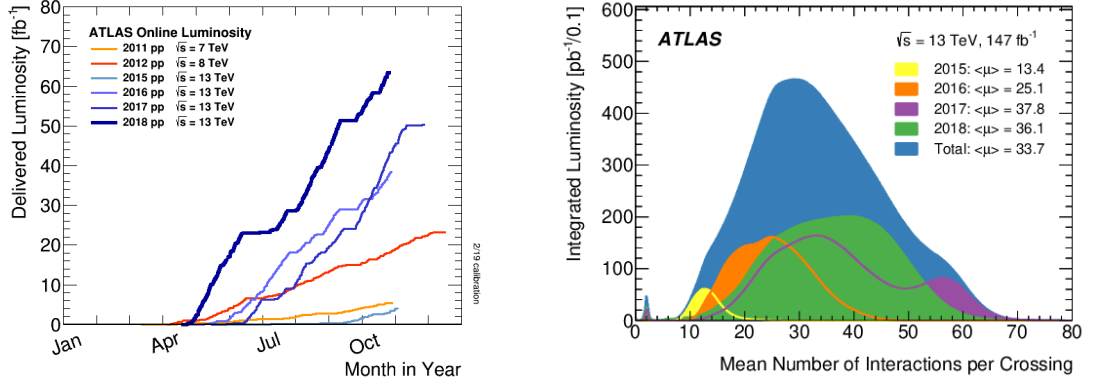
Figure 3.2: The Run 1 and Run 2 cumulative luminosity, split by year (left) [94], and the luminosity-weighted pileup distributions for the full Run 2 $\sqrt{s} = 13$ TeV pp collision dataset (right) [93]. All data recorded by the ATLAS detector is shown in the pileup profile, including special physics, commissioning, and calibration runs. The average pileup is also shown by year.
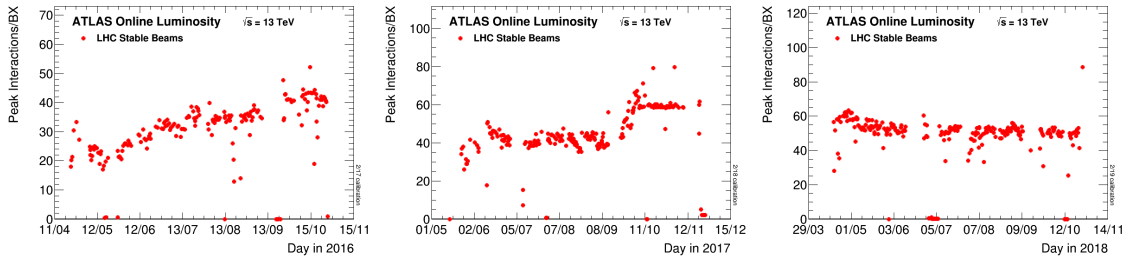
Figure 3.3: The peak pileup for each 13 TeV pp run in 2016 (left), 2017 (center), and 2018 (right), the main production years of Run 2 [94]. Notice the change in y-axis scale across plots. The peak pileup was increased to $\mu \approx 60$ in September 2017 with the switch to the 8b4e bunch structure. A few runs in late 2017 used the 8b4e scheme without the luminosity leveling, resulting in peak pileup values as high as $\mu = 79$.

3.2   The ATLAS Detector

ATLAS is a general-purpose particle detector located at one of the interaction points of the LHC. Roughly cylindrical in shape, ATLAS consists of various sub-detectors arranged concentrically around the beamline, providing nearly 4π coverage in solid angle. The ATLAS detector was built to discover the Higgs boson; to provide precision measurements of the electroweak interaction, QCD, and flavor physics; and to search for new physics beyond the Standard Model.

ATLAS uses a right-handed coordinate system with its origin at the nominal interaction point (IP) in the center of the detector and the z-axis along the beam pipe. The x-axis points from the IP to the center of the LHC ring, and the y-axis points upwards. Cylindrical coordinates (r, ϕ)

are used in the transverse plane, ϕ being the azimuthal angle around the z-axis. As the boost of the interactions along the z-axis are unknown, the rapidity and pseudorapidity are used instead of the polar angle (θ). The rapidity y of a particle is defined as $y = (1/2)\ln[(E + p_z)/(E - p_z)]$, where E is energy and p_z is longitudinal momentum. The pseudorapidity is defined simply as $\eta = -\ln\tan(\theta/2)$, and is equal to the rapidity in the limit of massless particles. Differences in y (and in the massless limit, η) are Lorentz invariant. For this reason, angular distances are measured in units of $\Delta R \equiv \sqrt{(\Delta\eta)^2 + (\Delta\phi)^2}$.

A cutaway view of the ATLAS detector is provided in Figure 3.4. The innermost sub-detectors are the trackers, which measure the trajectories of the charged particles. The tracking detectors collectively constitute the Inner Detector (ID). The ID is surrounded by a solenoid magnet, which provides a 2 T magnetic field along the z-axis. This field causes the charged particle tracks to bend, creating helical paths through the trackers. By measuring the sagitta of each track, the radius of curvature and momentum of each charged particle can be determined. Outside the solenoid are the LAr and Tile calorimeters, which measure the energy of electromagnetically and hadronically interacting particles. Particles passing through the calorimeters initiate particle showers, and the deposited energy is collected and measured. For accurate energy measurements, the calorimeters are designed to contain the full showers of most particles. As a result, usually only neutrinos and minimum ionizing muons escape the calorimeters. Finally, the outermost layer of the ATLAS detector is the Muon Spectrometer (MS), which identifies and tracks muons. The MS is immersed in a magnetic field produced by large toroidal magnets, causing the muon tracks to bend, enabling additional momentum measurements. More detailed information is given for each sub-system in the following subsections.

3.2.1 The Inner Detector

The Inner Detector [95–97] reconstructs tracks from charged particles using silicon pixel, silicon microstrip, and straw tube tracking detectors. The Pixel detector [98, 99] is the innermost sub-system, followed by the Semiconductor Tracker (SCT) [100–102] and the Transition Radiation Tracker (TRT) [103–110]. The ID extends to a radius of about 1.1 m and a pseudorapidity of $|\eta| = 2.5$. The tracks reconstructed by the ID are used directly or indirectly in lepton, photon, and jet reconstruction, as well as vertex reconstruction and the missing transverse energy calculation. During the long shutdown before Run 2, the Insertable B-Layer (IBL) [111, 112] was installed just 3.3 cm from the beamline, significantly improving track and vertex reconstruction, as well as the
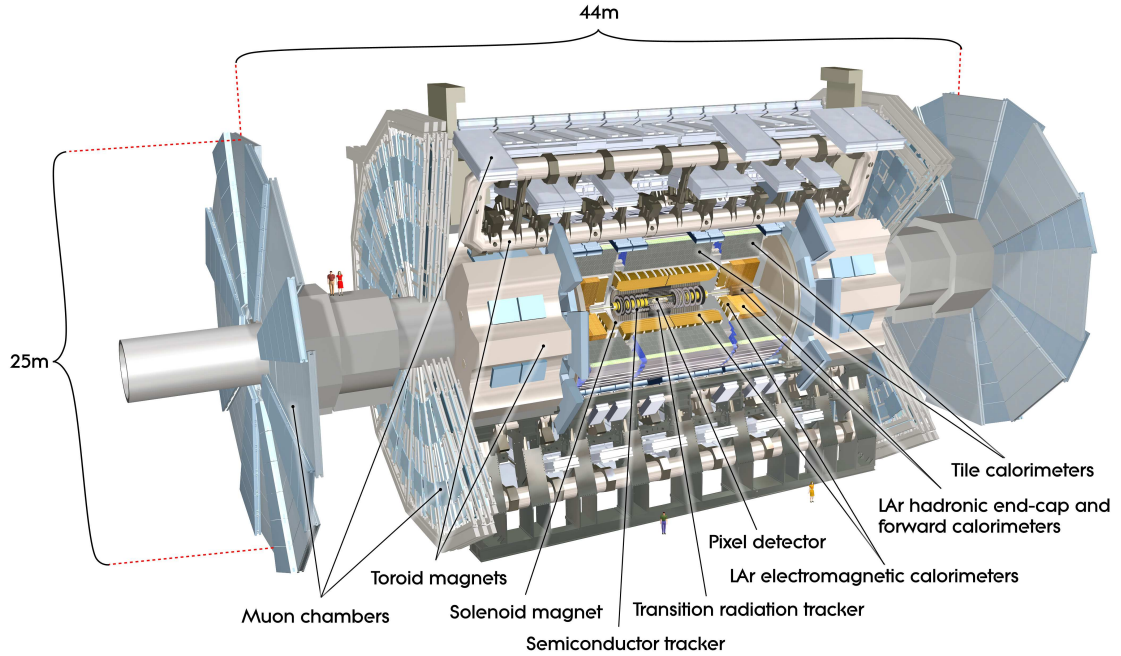
Figure 3.4: Cut-away view of the ATLAS detector [84].

identification of jets initiated by heavy-flavor hadrons. Schematics of the Inner Detector are shown in Figures 3.5 and 3.6.

3.2.1.1   Pixel Detector

Including the IBL, the Pixel detector consists of four cylindrical barrel layers and three disk-shaped endcap layers. The IBL contains about 12 million silicon pixels with a typical size of 50 μm ($r\phi$) $\times$ 250 μm (z), resulting in a hit position resolution of 8×40 μm^2. The following three layers, which constitute the original Pixel detector, contain over 80 million pixels total. These pixels are around 50 μm $\times$ 400 μm in size, with a hit position resolution of 10 μm $\times$ 115 μm. The Pixel detector typically records four hits per track, including the IBL.

3.2.1.2   Semiconductor Tracker

The Semiconductor Tracker contains four cylindrical barrel layers and nine endcap wheels on each side. The SCT uses silicon microstrips with a pitch of 80 μm and lengths of around 10 cm. By elongating the silicon sensor, the SCT can cover a larger volume with a manageable number of
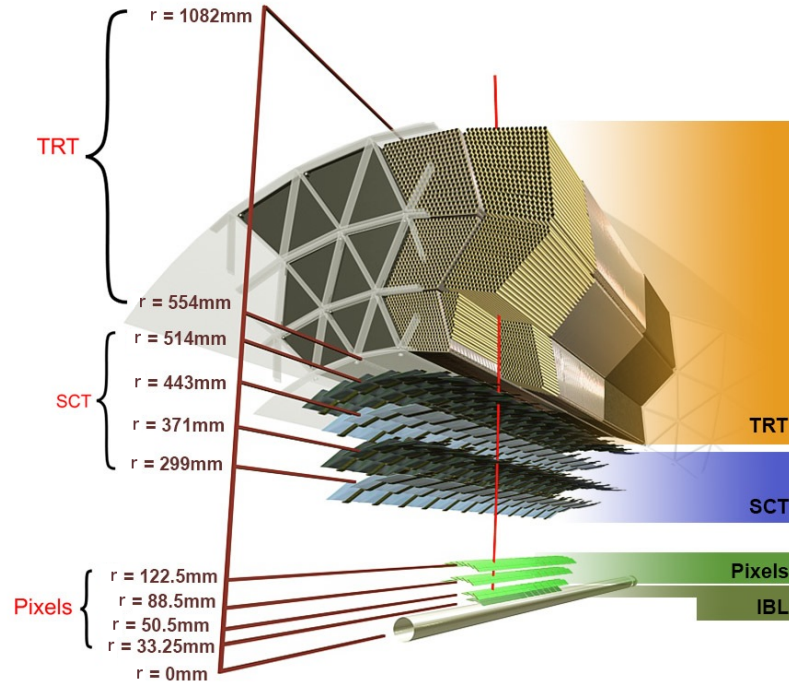
Figure 3.5: The Inner Detector barrel sub-systems [113].

channels (about 6 million) and a reduced material budget. The strips are arranged axially in the barrel and radially in the endcaps, providing excellent resolution in the bending direction. Each SCT module contains microstrip sensors on both sides which are slightly rotated relative to each other, improving the resolution in the z-direction in the barrel and the r-direction in the endcap. The spatial resolution of the barrel strips is 17 μm ($r\phi$) × 580 μm (z). A track will typically transit four SCT layers, crossing eight microstrip sensors and producing four measured space points.

3.2.1.3   Transition Radiation Tracker

The outermost layer of the Inner Detector is the Transition Radiation Tracker. The TRT is a straw tube detector used to track particles and to assist in the identification of electrons. The primary detector element of the TRT is the 4 mm diameter straw. An anode wire running down the center of each straw is kept at ground while the straw wall is held at a −1.5 kV potential. These straws are arranged parallel to the beamline in the barrel ($|\eta| < 1.0$) and radially in the endcaps ($0.7 < |\eta| < 2.0$), with over 350,000 straws in total.

Interleaved between the straws are polypropylene/polyethylene fibers and foils, which are used
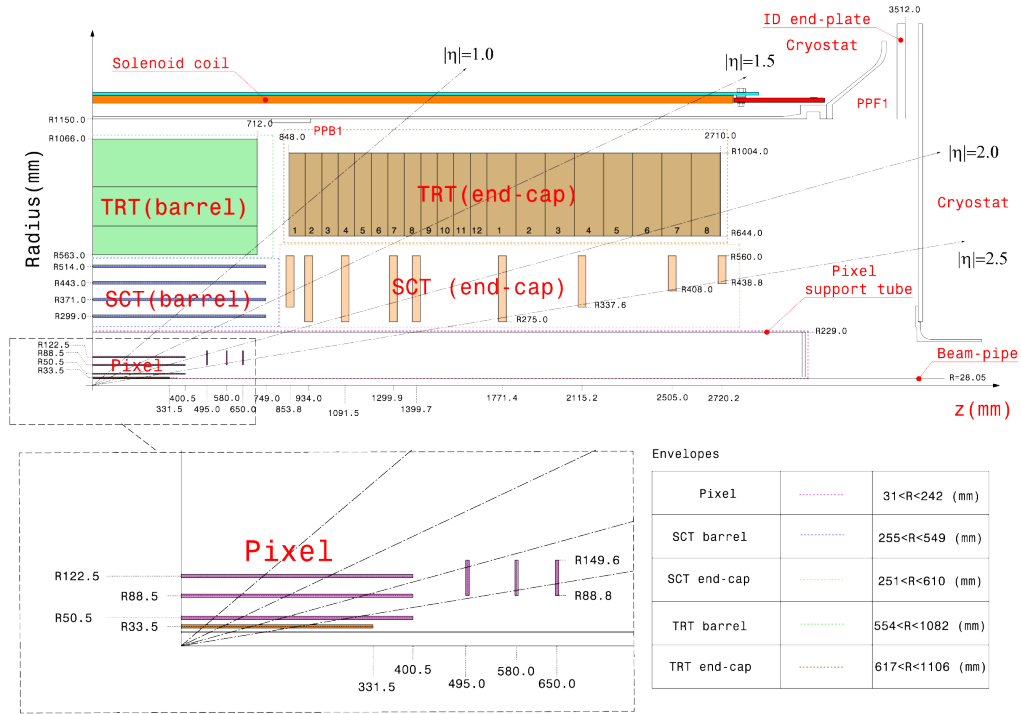
Figure 3.6: Schematic of the Inner Detector [114].

to produce transition radiation. Relativistic charged particles passing through material of varying indices of refraction will produce transition radiation. The total energy radiated is proportional to the Lorentz factor (γ) of the particle and is mostly confined to a forward cone defined by an angle of $1/\gamma$. As the lightest charged particle, an electron will deposit more energy through transition radiation than other charged particles of the same energy.

The TRT straws are filled with a gas mixture containing 70% either xenon or argon, as well as 27% carbon dioxide and 3% oxygen. When a charged particle passes through a TRT straw, it ionizes the gas. Due to the potential differences between the straw wall and the central anode wire, these liberated electrons accelerate towards the wire, creating an avalanche current. By measuring the arrival time of the first ionization electrons, the track's distance of closest approach to the wire can be determined. The X-ray transition radiation photons produced in the material between the straws will liberate additional electrons from the Xe or Ar gas through the photoelectric effect, producing larger currents on the anode wire. By discriminating the analog signal with separate low and high thresholds, the TRT can be used for both tracking and electron identification.

Spanning the region defined by $563 < R < 1066$ mm and $|z| < 2710$ mm, the TRT covers a large volume with a low material budget. While the 4 mm diameter straws are much larger than the silicon sensors of the Pixel and SCT detectors, the TRT can achieve a spatial resolution of about 130 μm. This is due to its precise timing information, large lever arm, and high hit multiplicity. A charged particle will traverse approximately 30 straws as it passes through the TRT, providing many position measurements over a large distance. To provide precise tracking information at high straw occupancies, the TRT requires fast electronics and high data transmission rates. The TRT data acquisition system and the challenges it faced in Run 2 will be discussed in Chapter 4.

3.2.2 The Calorimeters

Beyond the Inner Detector and solenoid are the calorimeters, covering the region with $|\eta| < 4.9$. ATLAS has separate calorimeter systems used to measure the energies of particles interacting electromagnetically and hadronically. These are sampling calorimeters, with alternating layers of absorber and active material. As particles pass through the calorimeters, the absorber layers initiate showers while the active layers collect and measure the deposited energy. For accurate energy measurements and particle identification, the electromagnetic and hadronic showers must be contained in their respective calorimeters, and the punch-through into the Muon Spectrometer must be mitigated. For this reason, both calorimeters must be sufficiently thick. At $\eta = 0$, the EM calorimeter is about 22 radiation lengths thick, while the hadronic calorimeter is about 11 interaction lengths deep. The good containment and large η-coverage are vital in measuring the missing transverse energy. A cut-away view of the calorimeters is shown in Figure 3.7.

3.2.2.1 Electromagnetic Calorimeters

Immediately beyond the solenoid is a high-granularity lead and liquid-argon (LAr) electromagnetic (EM) sampling calorimeter [116] used to measure the energy of electrons and photons. With its accordion geometry, the EM calorimeter has complete ϕ coverage without cracks. The EM calorimeter is divided into barrel ($|\eta| < 1.475$) and endcap ($1.375 < |\eta| < 3.2$) components, with the endcaps further divided into inner ($1.375 < |\eta| < 2.5$) and outer ($2.5 < |\eta| < 3.2$) wheels. Over the region corresponding to the Inner Detector ($\eta < 2.5$), the EM calorimeter is segmented in three layers with fine $\Delta\eta \times \Delta\phi$ granularity, enabling accurate measurements of electrons and photons. The first layer has particularly fine granularity in the η direction, providing good discrimination between prompt photons and the showers from neutral pions decaying to two collimated photons. The outer endcap
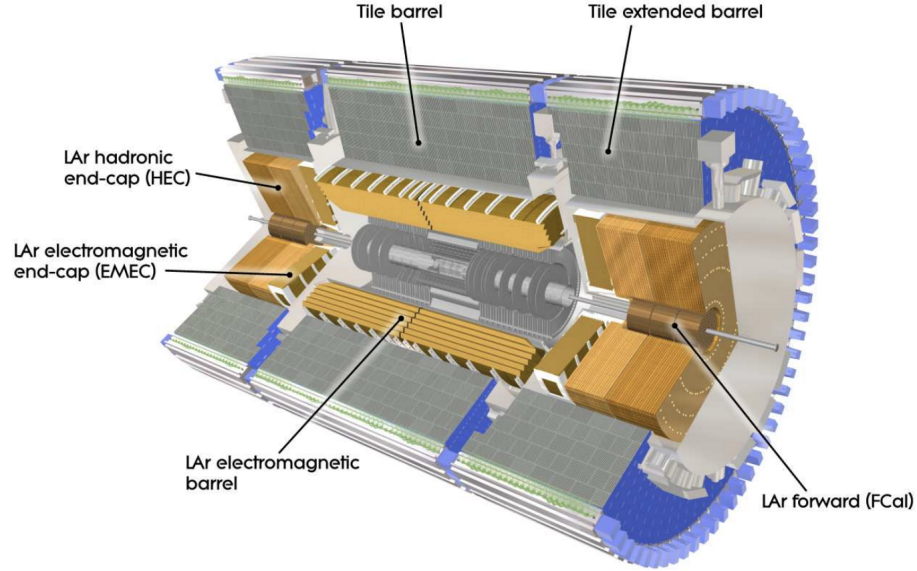
Figure 3.7: Cut-away view of the ATLAS calorimeters [115].

wheels are segmented in just two layers and have a coarser lateral granularity. Finally, the $|\eta| < 1.8$ region has a presampler layer of LAr before the first layer of the calorimeter. This presampler is used to correct for energy lost before the calorimeter. A schematic of the EM calorimeter near $\eta = 0$ is provided in Figure 3.8.

3.2.2.2 Hadronic Calorimeters

Outside the electromagnetic calorimeters are the hadronic calorimeters [118], used to measure the energy of strongly interacting particles. The barrel ($|\eta| < 1.0$) and extended barrel ($0.8 < |\eta| < 1.7$) calorimeters consist of alternating layers of steel and scintillating tiles. These calorimeters are divided into 64 modules azimuthally and three layers radially. Both sides of the scintillating tiles are read out separately using photomultiplier tubes. The hadronic endcap calorimeters ($1.5 < |\eta| < 3.2$) consist of copper plates interleaved with LAr layers. Each endcap is composed of two wheels, which are divided into 32 modules azimuthally and two segments radially. As hadronic showers are typically broader than electromagnetic showers, the active material of the hadronic calorimeters has a coarser granularity of about $\Delta\eta \times \Delta\phi = 0.1 \times 0.1$.

In addition to the EM and hadronic calorimeters described above, the most forward region ($3.1 < |\eta| < 4.9$) is covered by copper/LAr and tungsten/LAr calorimeters optimized for electromagnetic
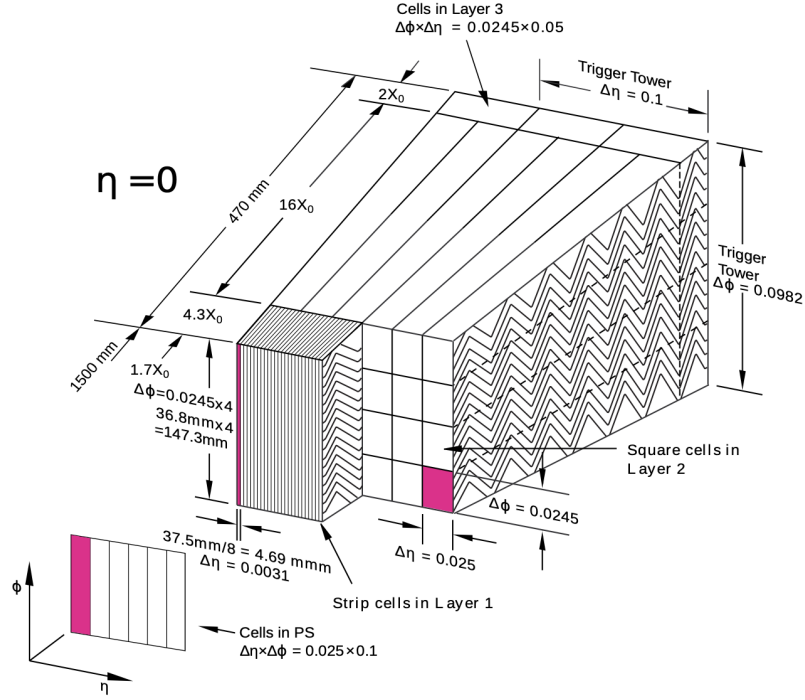
Figure 3.8: Schematic of the electromagnetic calorimeter near $\eta = 0$ [117].

and hadronic measurements, respectively.

3.2.3   The Muon Spectrometer

Muons produced in the collisions typically pass through the Inner Detector and calorimeters without depositing a significant fraction of their energy. Since muons are minimum ionizing and about 200 times heavier than electrons, they lose little energy in the electromagnetic calorimeter through ionization or bremsstrahlung. Also, since muons are colorless, they do not interact significantly with the hadronic calorimeter.

Before escaping the detector, the muons pass through the Muon Spectrometer [119]. The outer-most sub-system of the ATLAS detector, covering the region of $|\eta| < 2.7$, the MS is instrumented with tracking and triggering chambers. The MS is immersed in a magnetic field produced by the barrel ($|\eta| < 1.4$) and endcap ($1.6 < |\eta| < 2.7$) toroids. These air-core magnets produce an toroidal field of about 0.5 T and 1.0 T in the barrel and endcaps, respectively. Muons passing through the MS are therefore deflected in rz-plane, enabling an additional momentum measurement independent from the Inner Detector. In the barrel, the MS is instrumented with three cylindrical layers of Mon-
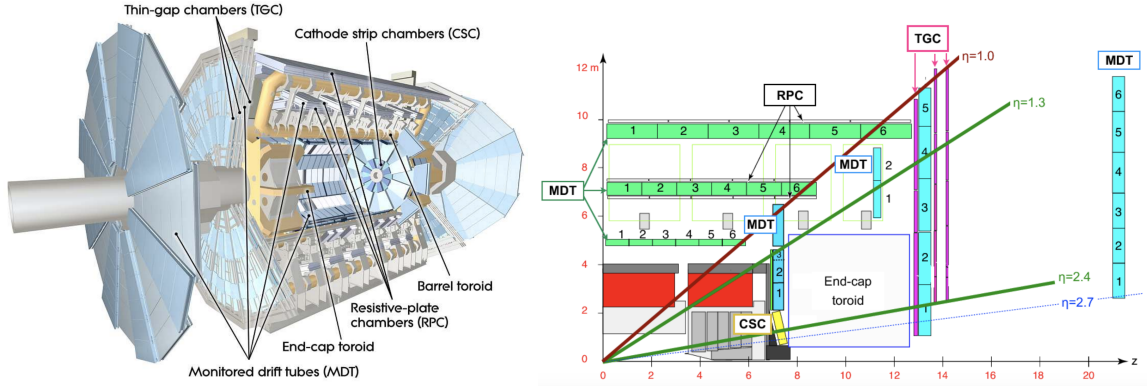
Figure 3.9: The ATLAS muon system [84, 120].

itored Drift tubes (MDTs), which provide precision tracking. In the endcaps, MDTs are arranged
in three planes perpendicular to the beam. Due to high muon and background rates, the innermost
endcap plane uses high granularity Cathode Strip Chambers (CSCs) at the highest pseudorapidities
$(2 < |\eta| < 2.7)$. The MS also contains Resistive Plate Chambers (RPCs) and Thin Gap Chambers
(TGCs) in the barrel and endcaps, respectively, which are used for triggering and for tracking in the
non-bending $(r\phi)$ plane.

3.2.4   Trigger and Data Acquisition System

When digitized, the detector signals from each event produce about 1.5 MB of data. With a collision
rate of 40 MHz, the ATLAS detector produces about 60 TB/s. To reduce the amount of data that
needs to be read out by the detectors and stored offline, ATLAS uses a trigger system to select
events with potentially interesting features.

An overview of the ATLAS Trigger and Data Acquisition (TDAQ) system is provided in Fig-
ure 3.10. ATLAS uses a two-level trigger system [84, 121], with a hardware-based first-level (L1)
trigger and a software-based high-level trigger (HLT). Using coarse granularity information from the
calorimeters and the muon system, the L1 trigger forms a decision in 2.5 μs, reducing the event rate
from the 40 MHz LHC collision frequency to 100 kHz. When a L1 accept signal is received by the
various sub-detectors, the event data from the front end electronics is packaged by ReadOut Drivers
(RODs) and sent off-detector to the ATLAS Readout System (ROS). The L1 trigger also identifies
Regions of Interest (RoIs) that contain interesting features, and passes their η and ϕ coordinates to
the HLT. The HLT then uses the full detector readout to form a trigger decision within hundreds of
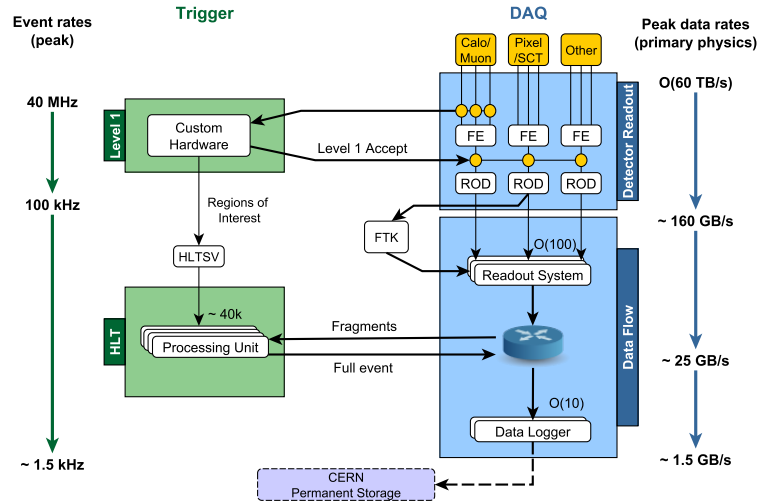
Figure 3.10: ATLAS Trigger and Data Acquisition system in Run 2.

milliseconds, reducing the event rate to about 1.5 kHz. Despite the limited time to form a trigger decision, the quality of the event reconstruction in the RoIs approaches that of the offline algorithms. Events passing the HLT are reconstructed fully offline and stored permanently.

3.3 Particle Identification and Reconstruction

Physics objects, such as leptons and jets, are reconstructed from the digitized signals in the various sub-detectors. The detector signatures of various Standard Model particles are illustrated in Figure 3.11. Electrons and photons are characterized by energy deposits in the electromagnetic calorimeter, with little or no energy deposited in the hadronic calorimeter. As electrons are charged, they leave a track in the Inner Detector. Stable hadrons, such as protons and neutrons, leave little energy in the EM calorimeter, depositing their energy primarily in the hadronic calorimeter instead. Since the muons produced at the LHC are approximately minimum ionizing, colorless, and too heavy to lose energy through bremsstrahlung radiation, they travel through the entire detector without depositing a significant fraction of their energy. However, they leave tracks in both the Inner Detector and Muon Spectrometer. Finally, neutrinos escape direct detection, as they are neutral and weakly interacting.

Due to color confinement, strongly interacting particles produced in the collisions hadronize,

forming sprays of color-neutral bound states known as jets. Generally, it is difficult to distinguish between jets initiated by gluons and light (u, d, s) quarks, although multivariate taggers exist [122, 123]. However, jets initiated by b-quarks (and to a lesser extent, c-quarks) can be distinguished due to the longer lifetimes of their associated hadrons. With lifetimes on the order of a picosecond, B-hadrons travel a few millimeters in the transverse direction before decaying, producing displaced vertices. Finally, top quarks are unique in that they decay via the weak force to bottom quarks before hadronizing.

As discussed earlier, the boost of the parton-parton interaction along the z-axis is unknown. However, the momentum in the transverse plane before and after the collision must sum to zero. The negative vector sum of the momenta of all visible physics objects in an event is the missing transverse momentum, $\boldsymbol{p}_{\mathrm{T}}^{\mathrm{miss}}$, and its magnitude is the missing transverse energy, $E_{\mathrm{T}}^{\mathrm{miss}}$. By measuring the $E_{\mathrm{T}}^{\mathrm{miss}}$, the presence of neutrinos or new invisible particles can be inferred.

When performing physics analysis, additional selection criteria are applied to the various physics objects. These selections are simultaneously optimized for signal efficiency and background rejection. The criteria applied to the leptons, photons, jets, and $E_{\mathrm{T}}^{\mathrm{miss}}$ in the trilepton resonance analysis are described in Chapter 5.
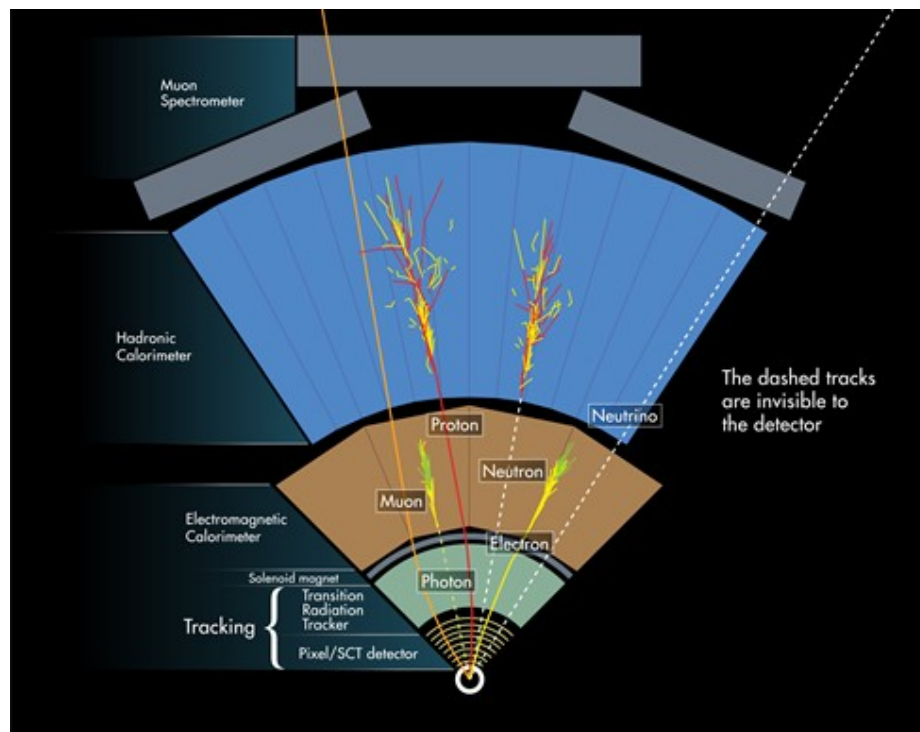
Figure 3.11: Detector signature of various Standard Model particles [124].

CHAPTER 4

TRT Compression

The front end electronics of the Transition Radiation Tracker (TRT) produce about a megabyte of data every bunch crossing by digitizing the straw signals. In order to read this data off the detector at Level-1 trigger rates as high as 100 kHz, it must first be compressed. The TRT employs a Huffman compression algorithm that drastically reduces the size of the data; however, this compression scheme proved insufficient under the harsher conditions of Run 2. As the pileup, detector occupancy, and L1 trigger rate increased, the TRT approached its bandwidth limit. Faced with a possible TRT-induced throttling of the ATLAS L1 trigger rate, two possible upgrades to the readout system were studied: increasing the bandwidth through a hardware replacement, or improving the compression performance by adopting a lossy scheme. The latter purposed upgrade is discussed in detail in this Chapter.

First, an overview of the TRT data acquisition system is provided in Section 4.1. Next, the formation and digitization of the straw signals is detailed in Section 4.1.1, followed by the data path in Section 4.1.2. Afterwards, the nominal Huffman compression algorithm and the method by which its performance is evaluated are presented in Sections 4.2 and 4.2.1. The saturation of the bandwidth is examined in Section 4.2.2, followed by the definition of a new lossy compression scheme in Sections 4.3 and 4.3.1. The performance of this new lossy scheme is examined in Section 4.3.2. Finally, the ultimate Run 2 DAQ system configuration is presented in Section 4.4, with some concluding remarks in Section 4.5.

47

4.1 Data Acquisition Overview

In this section, an overview of the TRT data acquisition (DAQ) system is provided, including the digitization of the straw signals and the flow of the straw data off the detector. A schematic of the TRT DAQ system is shown in Figure 4.1. The paths of the timing, trigger, and control (TTC) information is shown in blue, while the path of the data is shown in red. The ATLAS Central Trigger Processor (CTP) passes the TTC information to the four TRT Local Trigger Processors (LTPs). The LTPs then propagate the information to the 48 TRT-TTC modules, which are located in Versa Module Eurocard (VME) crates in USA15, the underground counting room. The TRT-TTC modules send the TTC information down to their associated TTC patch panels. Located inside the ATLAS toroid, the patch panels fan the TTC signals out to the many front end boards. Additionally, the TRT-TTC modules pass the TTC information to the TRT ReadOut Drivers (RODs), which are the back end data processing boards, residing in the same VME crates as the TRT-TTC modules. When a trigger is received by the front end, data is sent off-detector through ROD patch panels (also in the toroid) to the RODs in USA15. After combining the data from many front end boards into a single data fragment, the RODs send the data to the ATLAS ReadOut System (ROS).
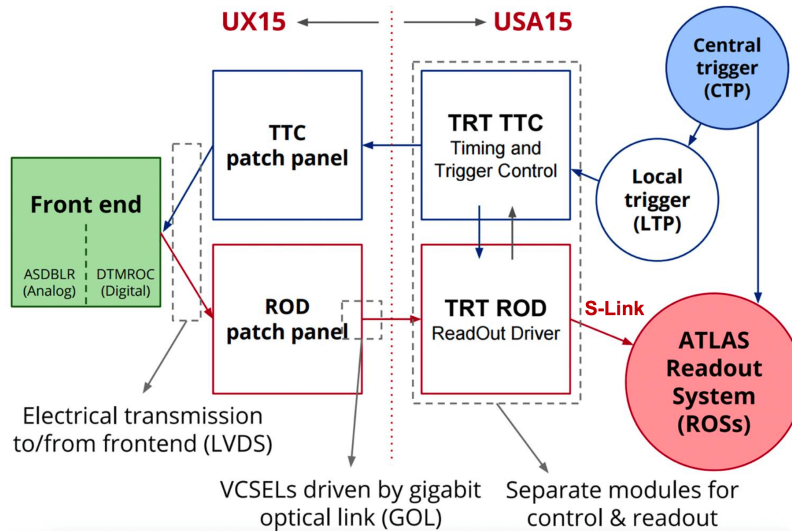
Figure 4.1: Schematic of the TRT data acquisition system.

As shown in Figure 4.2, the TRT is divided into barrel and endcap segments, each of which has an A and C side. The barrel and endcap segments are further divided into 32 ϕ-sectors, and the endcaps are separated into low-z and high-z wheels. For each side of the barrel, one TRT ROD is responsible for the straws covering a single ϕ-sector. In each endcap, two RODs are needed to cover

the low-z and high-z straws of a single ϕ-sector. This results in 192 RODs total.
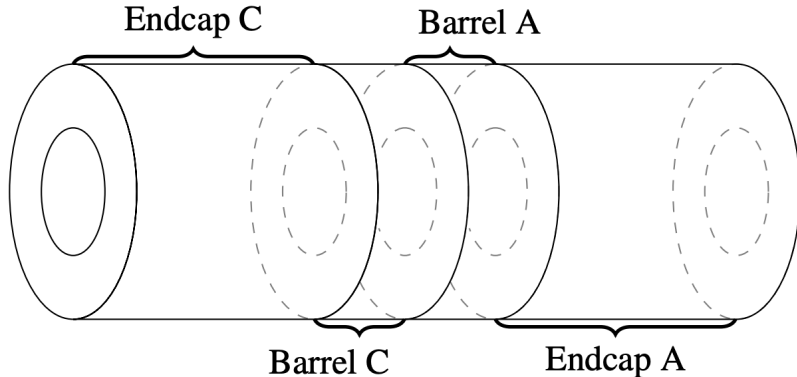
Figure 4.2: The TRT barrel and endcaps sections.

4.1.1 The Straw Word

The formation and digitization of the straw signals are discussed in this section. When a minimum ionizing particle passes through a TRT straw, it deposits about 2 keV in the gas mixture, creating 5-6 primary ionization clusters per millimeter along its track. Due to the potential difference between the straw wall and the central anode wire, these liberated primary electrons drift towards the wire. In the strong electric field near the wire, collisions between the primary electrons and the gas create an avalanche current. By measuring the arrival time of the earliest ionization electrons, the track's distance of closest approach to the wire can be determined. The primary ionization electrons liberated near the straw walls will take about 50 ns to drift to the wire, and will therefore not arrive in the same bunch crossing that produced the charged particle. The primary ionization clusters produced by a charged particle passing through the TRT are shown in Figure 4.3.

As the electrons from the collision have higher Lorentz γ-factors than other charged particles of the same energy, they often deposit significantly more energy through transition radiation. The X-ray transition radiation photons produced in the material between the straws will liberate additional electrons from the Xe or Ar gas through the photoelectric effect, resulting in larger currents on the anode wire. The transition radiation photons produced by these electrons typically have energies in the 5-15 keV range.

The wire signal is then processed by an Application Specific Integrated Circuit (ASIC) known as the ASDBLR [108], which performs the amplification, shaping, baseline restoration, and ultimate discrimination of the analog signal. The TRT makes use of two discriminators: a low threshold
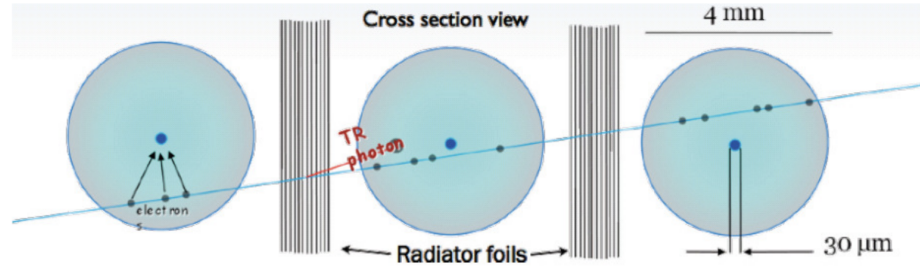
Figure 4.3: The primary ionization clusters and transition radiation produced by a charged particle passing through the TRT. The liberated electrons drift to the anode wires running down the center of the straws. The distance of closest approach to the wire can be determined by the arrival time of the earliest ionization electrons.

(LT) and high threshold (HT). The LT is set at an effective energy of about 300 eV, well below the typical energy deposited by a minimum ionizing particle. This enables the detection of the very first primary ionization electrons to reach the wire, which is important for determining the track's distance of closest approach. The HT is optimized simultaneously for identifying electrons and rejecting charged pions, resulting in an effective energy threshold of about 6 keV. A typical electron will cross about 30 straws, exceeding the HT in about 6 straws. An idealized straw signal pulse is shown in Figure 4.4. In Figure 4.5, the probability of a straw signal satisfying the high threshold as a function of the transiting particle's Lorentz γ-factor is shown, as well as the fraction of hit straws on track exceeding the high threshold.
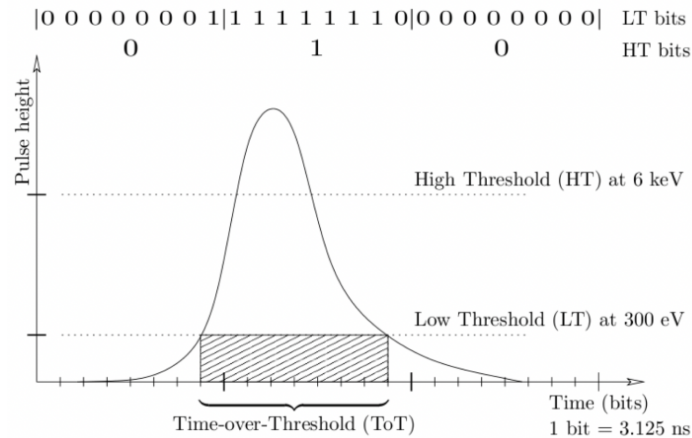
Figure 4.4: Idealized straw signal pulse from an electron and the resulting bit pattern. Due to the large Lorentz factor, the electron deposits enough energy through transition radiation to satisfy the high threshold.

The ternary output of the ASDBLR is sampled and digitized by the Drift Time Measuring Read
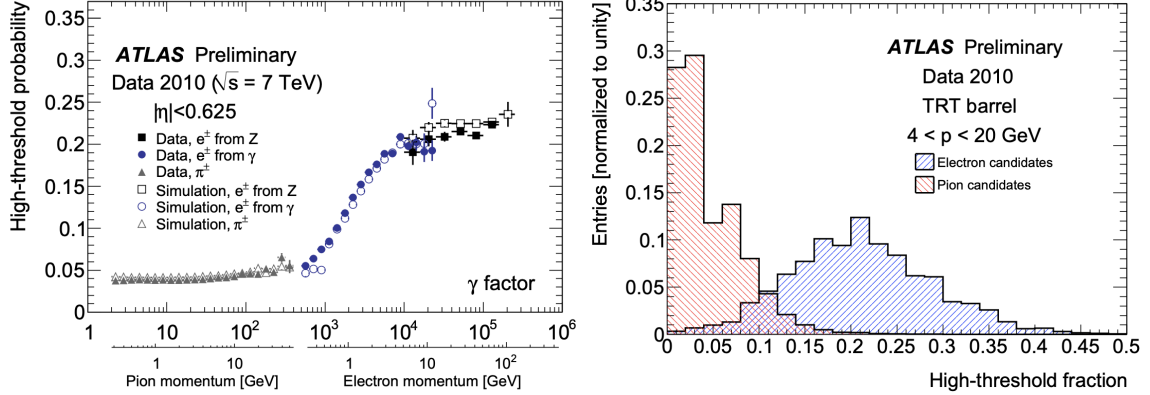
Figure 4.5: The probability of a straw signal satisfying the high threshold as a function of the transiting particle's Lorentz γ-factor (left) and the fraction of hit straws on track exceeding the high threshold (right) in the TRT barrel [125].

Out Chip (DTMROC), which creates bits indicating if the thresholds are exceeded in some time bin. The low tracking threshold is sampled every 3.125 ns, resulting in eight bits per bunch crossing. A ninth bit is created indicating if the high threshold is exceeded at any time during the 25 ns. These nine bits per straw are stored in the L1 Pipeline on the DTRMROC, which is a first-in, first-out (FIFO) buffer. The result of the low and high threshold sampling of the signal pulse is also shown in Figure 4.4.

When a L1 trigger is received by the DTMROCs, the data from the bunch crossing of interest and the two following bunch crossings is packaged and sent off the detector. These 27 bits of data constitute a *straw word* or *bit pattern*, the structure of which is shown in Figure 4.6.[15] These straw words are the fundamental unit of data, and they are extremely important in the upcoming discussion of the TRT compression algorithm.
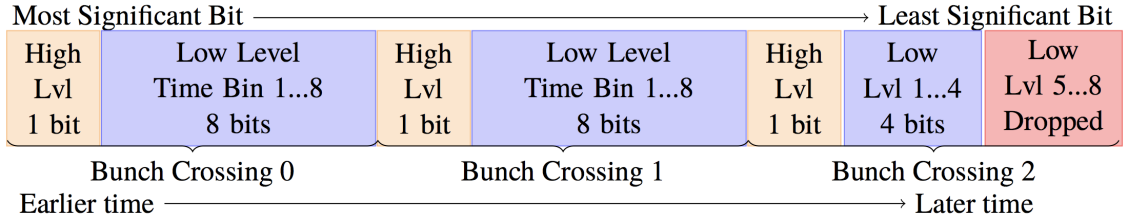
Figure 4.6: Structure of the 23-bit straw word. For Run 2, the last four low threshold bits are dropped.

---

[15]Notice the last four LT bits are no longer read out of the DTMROC buffers in Run 2. This modification will be justified in Section 4.1.2.

4.1.2 Data Flow

Now that the structure of the straw word has been presented, the flow of the data off the detector will be described. First, there are a couple of relevant details regarding the DTMROC that must be introduced here. In addition to the nine bits from each bunch crossing, a four bit bunch crossing identifier (BCID) and a single bit error flag are stored in the L1 Pipeline. In order to sample the LT output eight times every bunch crossing, the DTMROC needs eight buffered clocks separated by 3.125 ns. The error flag indicates the latching of these eight clocks to an internal 25 ns clock with a 50% duty cycle. The error flag is set if the duty cycle of the latch pattern is not within $50 \pm 12.5\%$, updating every bunch crossing.

When a L1 trigger is received, the data from the desired and following two bunch crossings is serialized into a single DTMROC data fragment, the structure of which is summarized in Table 4.1. With eight straws per ASDBLR, and two ASDBLRs per DTMROC, these data fragments contain the bit patterns from 16 straws. A 12-bit header is added to the data fragment which contains, among other information, the L1 identifier (L1ID), BCID, and a common error status. This results in 444 bits of data per DTMROC per triggered readout.

Data	Bits	Note
Preamble	3	101
Send-ID	1	
L1ID	3	
BCID	4	9 bit header
Error	1	
Straw 0	27	
Straw 1	27	
...	...	9 bits per bunch crossing $\times$ 3 bunch crossings.
Straw 15	27	

Table 4.1: The 444-bit DTMROC data fragment.

The data fragments from each DTMROC are then sent over twisted-pair cables to the ROD patch panels via low-voltage differential signaling at 40 Mbit/s. As the DTMROC data fragments are 444 bits in length, this limits the maximum L1 rate at which the TRT can run to 40 Mbps/444 bits $\approx$ 90 kHz. In order to reach the Run 2 target trigger rate of 100 kHz, the last four LT bits of each straw word are no longer included in the DTMROC fragments.

Each endcap (barrel) ROD patch panel receives data from 120 (104) DTMROCs, serializing the

fragments onto four Gigabit Optical Links (GOLs) [126]. Each GOL can multiplex, encode[16], and serialize the data from up to 32 input channels synchronously with the 40 MHz LHC clock, resulting in a 1.28 Gbit/s data stream. This data is then driven over optical cables to the RODs in the counting room (USA15) using 850 nm vertical-cavity surface-emitting lasers (VSCELs).

In the ROD, the data from the four GOL channels is deserialized first into individual DTMROC fragments, then again into individual straw words. To ensure synchronization, the header information of each DTMROC fragment is checked against the L1ID and BCID provided by the TRT-TTC. The ROD then serializes the straw words into a single event fragment, the structure of which is shown in Figure 4.7. The 23-bit straw patterns are first zero-padded out to full 32-bit words. With 16 straws per DTMROC and 120 (104) DTMROCS per endcap (barrel) ROD, the data block is 1920 (1664) words in length. In addition to the data block, a variable-length error block is built. Half of a 32-bit word is written for each DTMROC with incorrect event identifiers or a set error flag in its header, resulting in a maximum error block size of 60 words. Various event metadata are included in a nine word header and three word trailer, including the L1ID, BCID, and a ROD identifier, among other information.

Header	Straw 0 Data	Straw 1 Data	Straw 2-14 Data
9×32 bits	120×32 bits	120×32 bits	$\cdots$

Straw 2-14 Data	Straw 15 Data	Error Block	Trailer
$\cdots$	120×32 bits	Variable Width	3×32 bits
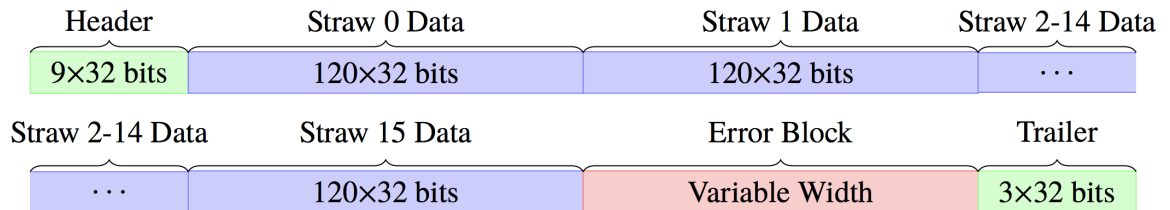
Figure 4.7: Structure of the data fragment for an endcap ROD, which has 120 DTMROCs and 1920 straws. The 23-bit straw words are expanded to 32-bit words by padding with zeros. The barrel ROD data fragments have an identical structure, except there are only 104 DTMROCs and 1664 straws per ROD.

Finally, the ROD fragment is sent to the ATLAS ReadOut System (ROS) via a duplex fiber using the S-LINK specification [127]. The S-LINK is implemented using High-Speed Optical Link for ATLAS (HOLA) interface cards [128]. While designed to transmit 32-bit words at 40 MHz (160 MByte/s or 1.28 Gbit/s), the HOLA cards were overclocked to 50 MHz in Run 2. If this S-LINK bandwidth is exceeded, the ROS will assert a Link Full signal, causing the ROD to assert BUSY to its TRT-TTC. This prevents any new L1 trigger requests until the current data can be read out, causing dead-time for the entire ATLAS detector. With the overclocked 50 MHz S-LINKs, the TRT can only reach the target 100 kHz L1 trigger rate if the event fragments are shorter

---

[16]The straw data is 8b/10b encoded by the GOLs, resulting in an actual data transmission speed of 1.6 Gbit/s.

than (50M words/s)/(100 kHz) = 500 words. This can only be achieved if the ROD fragments are compressed before they are transmitted through the S-LINK.

4.2   Huffman Compression

The TRT RODs use Huffman coding [129] to compress the event fragments before sending them through the S-LINK, allowing the TRT to operate at high L1 trigger rates. The Huffman algorithm takes advantage of the fact that most of the 2^{23} possible straw patterns are used rarely, if at all. Charged particles passing through straws tend to produce trains of set LT bits, with the time over threshold (i.e. the number of consecutively set bits times 3.125 ns) related to the track's distance of closest approach. Straws that are not traversed by any charged particles during the readout window will produce 23 bits of zeros. The Huffman algorithm assigns short code words to the straw bit patterns, such that the most frequent patterns receive the shortest code words. The translation between bit patterns and code words is stored in a compression table, which is loaded in the ROD firmware. Once compressed, the ROD fragment is sent though the S-LINK to the ROS, where it is decompressed using the same table. The name of the compression table used to compress the fragment is stored in the header, so the ROD fragments are self-describing.

Since the memory allocated to the compression table is limited in size, only about 100,000 of the most common patterns can be assigned code words. The remaining patterns are sent through the S-LINK uncompressed, preceded by a 5-bit escape code. As empty straws are by far the most common pattern at most occupancies, they are assigned the shortest possible code word: 0b1. The average code word length of the hit straws is about 11 bits, significantly shorter than the uncompressed 23-bit patterns.

In general, Huffman coding is an invertible process, as there is a one-to-one mapping between symbols (straw patterns in this case) and code words. When data is encoded and decoded, the original data is recovered. Since no information is lost, Huffman coding is considered a lossless compression scheme. For any lossless compression scheme, the average code word length, and therefore the compressed data size, is bounded from below by the Shannon entropy [130]. The entropy, H, is the weighted average of the information content, h_i, of all symbols:

$$H = \sum_i w_i h_i = \sum_i w_i \log_2 \frac{1}{w_i} = -\sum_i w_i \log_2 w_i. \tag{4.1}$$

The weight of a symbol, w_i, is just its frequency normalized by the total number of symbols. Huffman coding is optimal among lossless compression schemes when each symbol is encoded separately, with

1. **"A_DEAD_DAD_CEDED_A_BAD_BABE_A_BEADED_ABACA_BED"**

2.
```
C:  2 ⎫
B:  6 ⎬──→   CB:  8
E:  7 ⎭      0/   \1
_:10        C:  2   B:  6
D:10
A:11
```

5.
```
A:11 ⎫
ECB:15 ⎬──→  AECB:26
_D:20 ⎭      0/   \1
             A:11   ECB:15
                    0/   \1
                   E:  7   CB:  8
                          0/   \1
                         C:  2   B:  6
```

3.
```
E:  7 ⎫
CB:  8 ⎬──→  ECB:15
_:10 ⎬       0/   \1
D:10 ⎭      E:  7   CB:  8
A:11               0/   \1
                  C:  2   B:  6
```

6.
```
_D:20 ⎫
AECB:26 ⎬──→ _DAECB:46
             0/          \1
            _D:20        AECB:26
            0/   \1      0/   \1
           _:10  D:10   A:11   ECB:15
                                0/   \1
                               E:  7   CB:  8
                                      0/   \1
                                     C:  2   B:  6
```

4.
```
_:10 ⎫
D:10 ⎬──→   _D:20
A:11 ⎬      0/   \1
ECB:15      _:10   D:10
```

7.
```
_ :  00
D :  01
A :  10
E :  110
C :  1110
B :  1111
```

8. "10000111010010001100100111011001110010010001111100100111110111110
0010001111111010011100100101111101110100011111001"

Figure 4.8: Huffman coding example from [131]. A Huffman tree is generated from the string of characters in Step 1, as shown in Steps 2-6. The compression table in Step 7 is determined by traversing the tree from the root to each leaf. Finally, the encoded message is shown in Step 8.

the length of the compressed data often approaching the theoretical limit.

A generic example of Huffman coding from [131] is provided in Figure 4.8. Each character in the string being compressed is analogous to a TRT straw pattern in the ROD fragment. The compression table is generated by creating a binary tree of nodes. First, all characters are sorted by their frequencies. Next, the two characters with the lowest frequencies are used to create a new internal parent node, having these two characters as child nodes. The child nodes are then removed from the list, and the parent node is added to the list with a frequency equal to the sum of the frequencies of the two children. This process is continued iteratively until there are is only one node left: the root of the Huffman tree. To create the compression table, the binary tree is traversed from the root down to each leaf.

In Huffman coding, the code words are variable in length, and no code word is a prefix for any other. For this reason, Huffman coding is said to be *prefix-free*. As a result, when parsing the compressed fragment, bits can be read until a code word is recognized; no delimiters are needed between code words. This can be seen for the compression table in Step 7 and the encoded data

stream in Step 8 of Figure 4.8. Also, notice that no character in this example is so common that it receives a single-bit code word. It is actually more advantageous to code the most common character (A) with two bits as 0b10, since encoding it as 0b1 would prevent all other codes from starting with a 1 in the leftmost (most significant) bit.

4.2.1 Compression Performance

As mentioned in the Section 4.2, the empty straws receive the shortest possible code word, 0b1, as they are by far the most common bit pattern at most detector occupancies. Consequently, the size of the compressed ROD fragment is dominated by the number of empty straws. Together with the average code word length for the hit straws, l_{ave}, the compressed ROD fragment size can be estimated (in 32-bit words) using the following equation:

$$\text{compressed fragment size} = N_{\text{straws}} \times [\text{occ} \times l_{\text{ave}} + (1 - \text{occ}) \times 1] \,/\, 32 + \text{error block} + \text{fixed overhead}$$
$$= N_{\text{straws}} \times [\text{occ} \times (l_{\text{ave}} - 1) + 1] \,/\, 32 + \text{ error block} + \text{fixed overhead,}$$

$$(4.2)$$

where N_{straws} is the number of straws associated with the ROD and occ is the occupancy. The fixed overhead includes fragment headers and frame words associated with the S-LINK protocol. The error block ranges from 0 to 60 words in length, depending on the number of DTMROCs with errors. The maximum L1 trigger rate at which the TRT can run before saturating the S-LINK bandwidth is then given by:

$$\text{max L1 rate} = \text{S-LINK rate} \,/\, \text{compressed fragment size.} \qquad (4.3)$$

Note l_{ave} is generally not constant; it varies with the detector conditions and the compression table used to collect the data. Huffman coding creates a compression table that is optimized for the data from which it is generated, since the assignment of code words is based on the frequency of each straw pattern. As a result, if the beam or detector conditions change, the bit pattern frequency distribution will shift and the compression table will become suboptimal.

In practice, the compression table is optimized on data from the earliest luminosity-blocks of LHC runs, when the luminosity, pileup, TRT occupancy, and L1 trigger rate are the highest. Under these conditions, the S-LINK bandwidth usage is closest to the limit. As the pileup and occupancy decrease over the course of the run, the bit pattern frequency distribution changes, and the compression table becomes suboptimal for the hit straws. However, any possible lengthening of l_{ave} is counteracted and dominated by the increasing number of empty straws. As a result, the compressed fragment size decreases over the course of the run, as shown in Figure 4.9. Additionally, the trigger rate decreases

over the run, further alleviating the S-LINK bandwidth usage. If the run conditions change, the new data is first collected with the existing compression table. Offline, the new data is decompressed using the existing table, and a new table is generated from the straw pattern frequency distribution of the new data. This new table is then loaded in the ROD firmware and used in future runs.
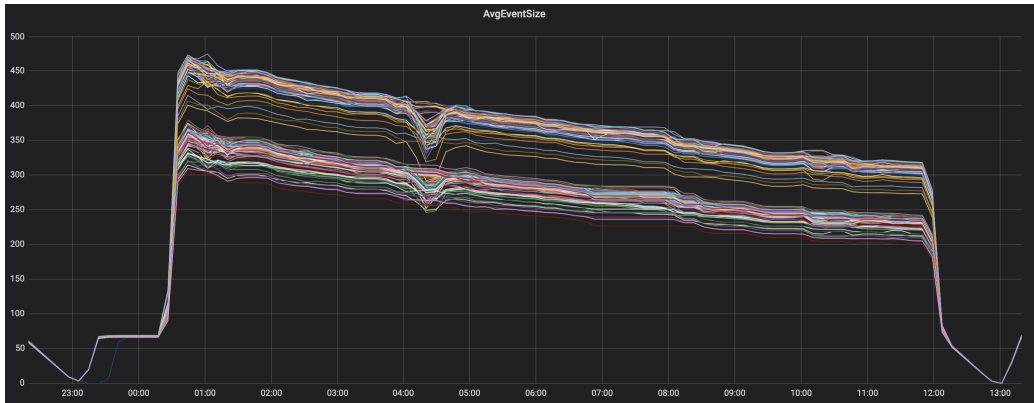
Figure 4.9: The average compressed fragment size for all RODs over the course of a 2016 run, measured in 32-bit words. The event size decreases over the run with the increase in empty straws. Some separation can be seen between the high-z endcap RODs and the low-z endcap and barrel RODs. The straw occupancy increases in the forward direction, and the endcap RODs are responsible for more straws. As a result, the RODs covering the high-z endcap wheels have the largest event fragments.

To measure l_{ave} for some given data and compression table, the data is first decompressed offline with whichever table was used to collect it. The decompressed data is then compressed again using the desired table, allowing the calculation of l_{ave} from the observed code words. Typically, l_{ave} is about 11 bits when using a compression table generated from similar (but orthogonal) data, growing slowly as the pileup increases. This suggests that the bit pattern frequency distribution may shift significantly with the run conditions, but its width changes more slowly. When the frequency distribution flattens, the Huffman algorithm loses predictive power, and l_{ave} lengthens.

4.2.2 Bandwidth Saturation

Early in Run 2, the LHC delivered data with $\langle \mu \rangle \approx 40$ at the start of the runs. In the high-z endcap RODs, where the occupancy is the highest, this resulted in a straw occupancy of about 66%. The compression table in use at the time was generated from $\langle \mu \rangle = 37$ data and was well suited for the run conditions. ATLAS collected this data with a L1 trigger rate of about 85 kHz, resulting in an S-LINK bandwidth usage of about 80% for these RODs.

Assuming a constant l_{ave} and using Equations 4.2 and 4.3, the maximum possible L1 rate at which the TRT can run before saturating the S-LINK can be estimated as a function of the TRT occupancy. This projection is shown in Figure 4.10. The thickness of the purple band reflects the variable length error block; the upper and lower edges correspond to the minimal and maximal lengths, respectively. The green star marks the occupancy and L1 rate at which the high-z endcap RODs collected this $\langle\mu\rangle \approx 40$ data, while the red star marks the maximum possible L1 rate at which the data could have been collected before saturating the S-LINK. From this projection, it is clear that the TRT is already approaching the S-LINK bandwidth limit when running at 100 kHz, and a large error block would result in saturation. This point is reinforced by Figure 4.9, which shows that some ROD fragments are approaching the 500 word limit for reading out data at a 100 kHz with the 50 MHz S-LINK. The projection also suggests that at higher pileup and straw occupancy, the TRT may be unable to reach 100 kHz with even a minimal error block.
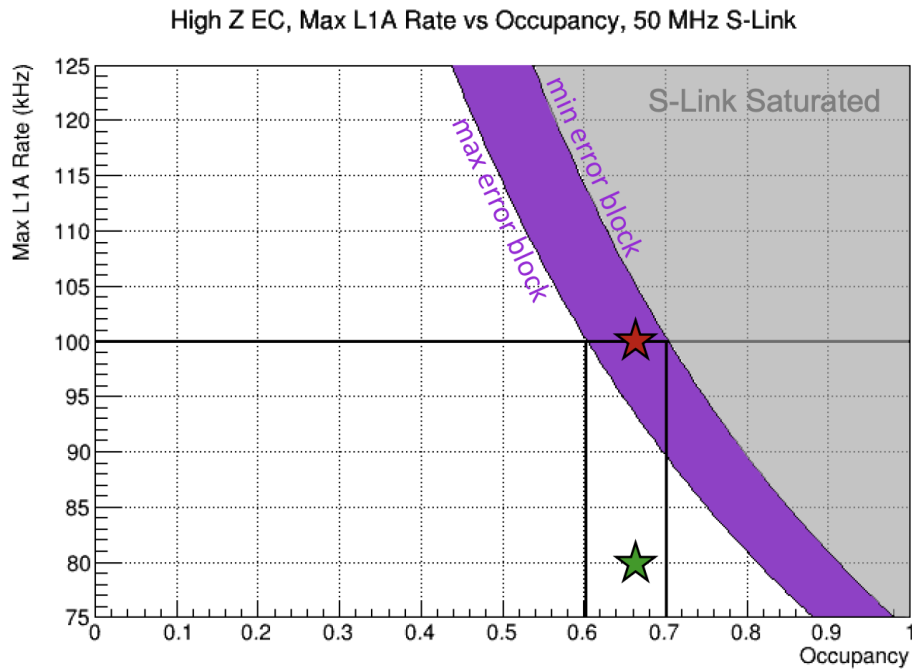
Figure 4.10: Projection of the maximum possible L1 rate at which the TRT can run before saturating the S-LINKs, as a function of the TRT occupancy. This projection is for the 50 MHz overclocked S-LINKs. The width of the purple band reflects the variable width error block; the upper (lower) edges correspond to minimal (maximal) error blocks. The green star marks the occupancy and L1 rate at which the $\langle\mu\rangle \approx 40$ data was collected during a 2016 run, while the red star marks the maximum possible L1 rate at which the data could have been collected before saturating the S-LINK.

This projection was made after several modification to the readout that decreased the S-LINK

usage. As described in Section 4.1.1, the last four LT bits were dropped from the straw patterns in Run 2. Furthermore, the first and last HT bits are masked to zero, and only the middle HT bit is used for particle identification. Both of these modifications reduce the space of possible straw words, which benefits the Huffman compression. Finally, a hardware validity gate was installed in the ROD firmware which requires at least one set LT bit in a window of 13 bits. If no set bits fall within the window, the entire word is masked to zero and encoded as if it were an empty straw, effectively decreasing the occupancy and improving the compression. The hardware validity gate is implemented as a bitwise AND between the 23-bit straw pattern and the hex word 0xDFEE (0b00000001101111111101110).

Faced with a possible TRT induced throttling of the ATLAS L1 trigger rate, the TRT data acquisition and software teams began investigating two possible solutions to the bandwidth saturation, one hardware and one software/firmware:

- Replace the HOLA cards on the RODs to increase the S-LINK rate to 60 MHz.

- Implement a new lossy compression scheme that improves the compression by removing information, such that the tracking is unaffected.

The HOLA card upgrade was completed in the Spring of 2017, just before the pileup was unexpectedly increased to $\langle \mu \rangle = 60$ to maintain the desired luminosity while avoiding beam dumps triggered by the problematic 16L2 cryogenic half-cell [89–91]. Even with the increased bandwidth from the HOLA care upgrade, it was not clear if the TRT would be able to reach 100 kHz at $\langle \mu \rangle = 60$ without observing the data, as the behaviour of the straw pattern frequency distribution at high pileup was unknown. It was possible that the distribution would flatten, increasing l_{ave}. The compressed fragment size would then increase faster than the projections from $\langle \mu \rangle = 40$ data would suggest. For this reason, it was imperative that both possible upgrades were pursued.

4.3 Lossy Compression

For any lossless compression scheme, including Huffman coding, the average code word length is bounded from below by the Shannon entropy of the symbols to be encoded. Once this limit is reached, the data can only be compressed further if some information is removed. For example, instead of an invertible one-to-one mapping between symbols and code words, an N-to-1 mapping can be implemented such that multiple symbols correspond to a single code word. This N-to-1

mapping is not an invertible transformation, as the original data cannot be recovered in its entirety after encoding and decoding. This is known as a lossy scheme.

In the context of the TRT, the implementation of a lossy compression scheme only adds one step to the data readout: the N-to-1 mapping. This can be done in the ROD firmware after the hardware validity gate. All bit patterns that pass the validity gate would be transformed by the non-invertible N-to-1 mapping, then encoded. The compression table used for encoding would be generated using the Huffman algorithm on data that has undergone the N-to-1 mapping. Once encoded, the data would be sent through the S-LINK and decoded in the ROS, just as it is done when using the lossless compression scheme. The primary difference is that the original ROD fragment is not recovered upon decoding; all analysis must be done using the N-to-1 mapped straw words.

4.3.1 Scheme0p Definition

While multiple lossy schemes were studied for their compression performance and their effect on tracking, the conservative *Scheme0p* was chosen for the initial implementation. A track's distance of closest approach to a straw wire is partially determined by a 0 to 1 transition in the LT bits of the straw pattern. This *leading edge* is expected to occur over a range of LT bits in the middle of the straw pattern for particles produced in the collision of interest. Leading edges in the first and last few LT bits are often the result of out-of-time pileup or noise. Scheme0p was designed to exploit this by masking these first and last LT bits if specific conditions are met, while also preserving leading edges from in-time particles.

Labeling the low threshold bits 1-20 (since 21-24 are dropped) and ignoring the high threshold bits, the Scheme0p bit pattern transformation is defined as the following sequence of steps:

1. If the first two bits are 01, replace them with 11.

2. If the first bit is 1 and there is a leading edge in the bit range [3,16], replace all leading 1's with a single 1 in first bit.

3. If the 17th (or 18th or 19th) bit is 0, set all following bits to 0.

A few examples of the Scheme0p bit pattern transformation are shown in Table 4.2. In the first example, Step 1 does not affect the pattern. Despite the leading train of 1's beginning in the first bit, the pattern is unchanged by Step 2 since there is no leading edge in the specified range. Finally, the pattern is unchanged by Step 3, so the Scheme0p transformed pattern is identical to the original pattern. In the second example, Step 1 applies and the first two bits are replaced with 11. This

creates a leading train of 1's starting in the first bit, which is then replaced by a single 1 in the first bit, as per Step 2. Again, step 3 does not apply. In the third example, both Step 2 and Step 3 apply.

Original Pattern	Applicable Steps	Scheme0p
1111 0000 0000 0000 1111	-	1111 0000 0000 0000 1111
0111 0000 1111 0000 0000	1, 2	1000 0000 1111 0000 0000
1111 0000 1100 0011 1011	2, 3	1000 0000 1100 0011 1000

Table 4.2: Example bit patterns, the applicable Scheme0p transformation steps, and the resultant transformed patterns. For the sake of simplicity, the HT bits are ignored here. The most significant bits correspond to the beginning of the readout window, while the least significant bits correspond to the end. A detailed explanation of each example is given in the text.

4.3.2   Scheme0p Performance

With the upgraded HOLA cards, which increased the S-LINK bandwidth to 60 MHz, the TRT successfully collected $\langle \mu \rangle \approx 60$ data in 2017 at an average trigger rate of about 75 kHz. Using this data and S-LINK speed, new projections of the maximum possible L1 rate vs. TRT occupancy could be made for both the lossless Huffman compression scheme and the lossy Scheme0p. These are shown in Figure 4.11.

First, this new $\langle \mu \rangle \approx 60$ data was completely decompressed offline, yielding the straw patterns. In the Scheme0p case, the N-to-1 transformation was then applied to the straw patterns. Compression tables were then generated from both the original and transformed patterns. These two tables were then used to compress orthogonal data from the same luminosity-block, providing optimal compression for both schemes. Finally, the measured l_{ave} values for the two schemes were used to make the projections. While the compression tables were generated using data from all RODs, only fragments from the high-z endcap RODs were compressed in the l_{ave} calculation, as these RODs are closest to the bandwidth limit. The projections suggests that Scheme0p significantly outperforms the default lossless scheme, allowing 100 kHz running at 10% higher straw occupancies. However, the re-optimized lossless scheme with the upgraded HOLA cards is sufficient for 100 kHz running, at least under the 2017 run conditions.

The effects of Scheme0p on tracking were studied in detail [109,110] and were ultimately found to be acceptable. The hit-level and track-level distributions were compared between the two compression schemes using $\langle \mu \rangle = 40$ data (the highest at the time) and $\langle \mu \rangle = 60$ Monte Carlo simulation. To emulate Scheme0p, the data and MC were first decompressed offline, providing access to the straw
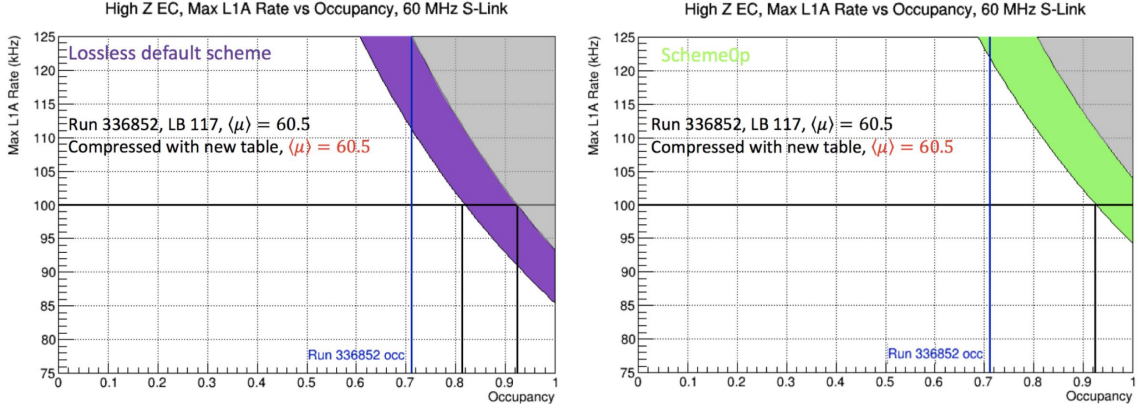
Figure 4.11: The projected maximum achievable L1 rate for a given TRT occupancy for both the lossless Huffman scheme (left) and Scheme0p (right). These projections use new compression tables optimized for $\langle\mu\rangle = 60$ data and the upgraded 60 MHz S-LINKs. The average hit straw code word length, l_{ave}, is measured in data from the same luminosity-block, using high-z endcap RODs only. The average occupancy of these RODS during this luminosity block is indicated by the blue line. With Scheme0p, the targeted 100 kHz L1 rate can be achieved at 10% higher occupancies. With either compression scheme, this $\langle\mu\rangle = 60$ data can be easily collected at 100 kHz without saturating the S-LINKs.

words. The N-to-1 mapping was then applied to the straw words, and the track reconstruction was performed using these transformed patterns. While some differences in the hit-level distributions were observed, the effects on tracking were negligible.

4.4 Final Run 2 Setup

The hardware upgrade of the HOLA cards and re-optimization of the lossless Huffman compression scheme proved sufficient for running at 100 kHz at $\langle\mu\rangle = 60$ without saturating the S-LINKs. Additionally, the more complicated logic of Scheme0p was difficult to implement in the ROD firmware without timing violations. As a result, the lossless Huffman compression scheme was kept for the remainder of Run 2.

To optimize the Huffman compression for high-$\langle\mu\rangle$ running, a new table was generated from the data; however, there was a complication. Above $\langle\mu\rangle = 55$, the empty straw word is no longer the overwhelmingly dominant pattern. Since Huffman coding is prefix-free, no code word can be the prefix of another. For this reason, it becomes more advantageous to encode the empty straw word in two bits as 0b11. Recall, the Huffman encoding example in Section 4.2 is also a case where no symbol is common enough to receive a code word of 0b1.

The code used to make the compression tables does not force the assignment of 0b1 to the empty straw word; it will assign whatever is most advantageous. Although the firmware previously had the empty straw word hard-coded as 0b1, it was updated to use whatever the table assigns. Unfortunately the byte stream converter, which converts the ROD event fragments into raw data objects [132], does assume that the empty straw word is encoded as 0b1. As the byte stream converter is an extremely important piece of software, used both online by the HLT and offline in event reconstruction, any modifications require great care. To avoid this issue, the new compression table was generated from 2017 data with $\langle \mu \rangle = 55$. This new table, Table-140, has the empty straw word encoded as 0b1.

Validating Table-140

This new table was first validated by taking standalone and combined noise runs, and checking the straw hitmaps in TRTViewer [133]. When parsing the compressed ROD fragment, bits are read until a code word is recognized. The particular straw associated with this code word is determined by counting the number of previously read out patterns. If there is a corruption in the compressed fragment, an incorrect code word will be read. Since the code words vary in length, the corrupted code word may be shorter or longer than the uncorrupted code word. As a result, all following code words may be parsed and decompressed incorrectly. For this reason, it is useful to examine the straw hitmaps, looking for the known dead front end boards. If they appear in the expected locations, the compressed fragments are probably being parsed correctly.[17]

The straw hitmaps of barrel side C from two different noise runs are shown in Figure 4.12. The colors represent the occupancy of each straw over some large number of events.[18] The data for the left hitmap was collected using the old compression table, Table-139, while the data for the hitmap on the right was collected using Table-140. Using the new compression table, the known dead boards do appear in the correct locations.

Finally, a cosmic muon run was taken using Table-140 to confirm that tracks could be seen. The TRT has the capability to trigger on cosmic ray muons passing through the detector. In Figure 4.13, an event collected using this trigger and Table-140 is shown. At the time, the LHC was circulating

---

[17]Corruptions of individual fragments is not expected. However, in the past, the compression table loaded in the ROD firmware could be corrupted if the previous table was not cleared. Also, this validation method is used to confirm that the tables loaded in the firmware match the tables used offline and in the HLT to decompress the TRT data.

[18]For this noise test, the low thresholds were lowered to increase the occupancy. In normal data-taking, the low thresholds are tuned such that noise produces 2% occupancy.

but not colliding beams. As a result, this event has many more tracks than a typical cosmic muon event. With no sign of corruption, Table-140 was used to collect physics data in 2018.
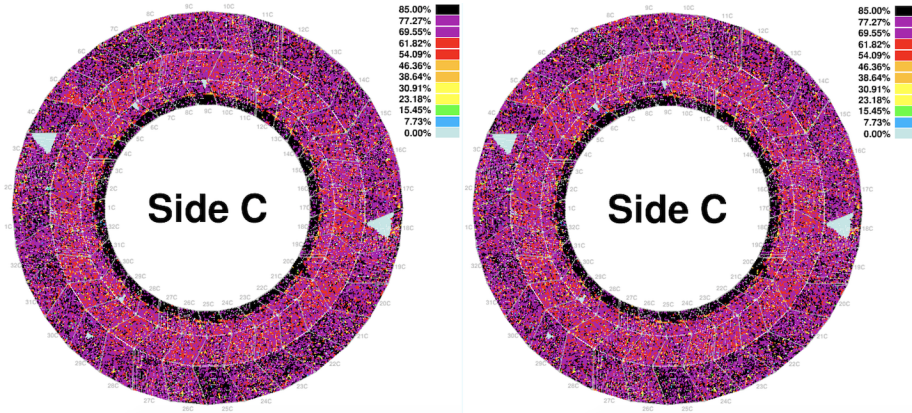
Figure 4.12: Straw hitmaps from high occupancy noise runs using Table-139 (left) and Table-140 (right). The known dead boards appear in the same location, indicating that there is no corruption from the new table.
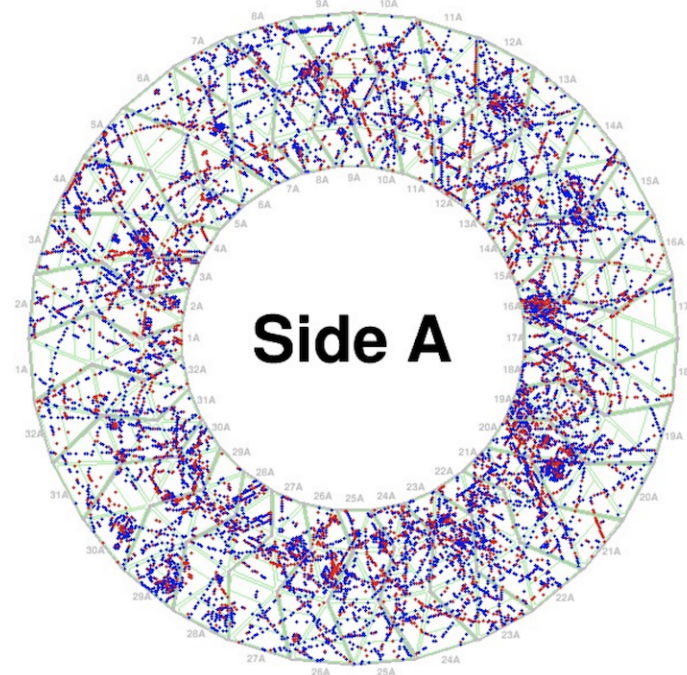
Figure 4.13: Straw hitmap from a run collected during unstable beams using the cosmic muon trigger and Table-140. Tracks can be seen, further validating Table-140.

Performance of Table-140

To evaluate the compression performance of the new table, the conditions of a high-z endcap ROD are examined during a typical 2018 run. Shown in Figure 4.14 are the L1 rate, S-LINK usage, and average event size for ROD 0x341b02 during the beginning of a 2018 run with $\langle \mu \rangle = 57$. This ROD is particularly interesting, as it is the closest to the S-LINK bandwidth limit. The ROD's data was collected with Table-140 at a L1 rate of about 90 kHz. With an average event size of 538 words, an error block of 9 words, and an occupancy of 76%, this ROD's S-LINK usage was about 82%. Scaling the S-LINK usage to 100%, the maximum L1 rate achievable on this ROD is 109 kHz, at least from an S-LINK bandwidth perspective.
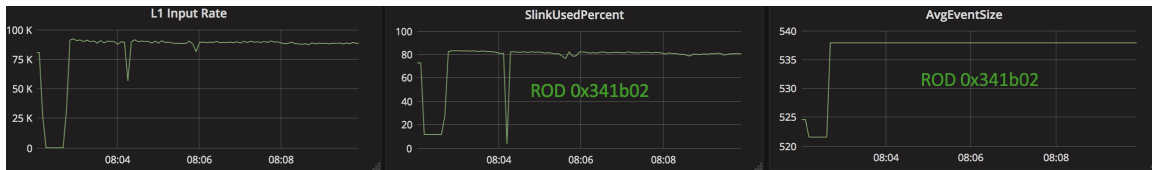
Figure 4.14: L1 trigger rate, S-LINK bandwidth usage, and average compressed fragment size for high-z endcap ROD 0x341b02 during the beginning of Run 350160, which has the 2018 beam structure and peak $\langle \mu \rangle = 57$. This data was collected with Table-140 after the HOLA card upgrade, which increased the S-LINK rate to 60 MHz.

After evaluating the compression performance at $\langle \mu \rangle = 57$ and 76% ROD occupancy, the maximum achievable L1 rate before S-LINK saturation can be projected to higher occupancies. This projection is shown in Figure 4.15 using Table-140 and the upgraded 60 MHz S-LINK. The value of l_{ave} used in this projection was measured by compressing the data from all high-z endcap RODs, using Run 350160 (same as Figure 4.14). The red star marks the L1 rate and occupancy at which ROD 0x341b02 collected the data, while the green star marks the maximum L1 rate at which this ROD could have collected the data before saturating its S-LINK. Based on this projection, the TRT should be able to reach 100 kHz for occupancies up to 86% (76%) for minimal (maximal) length error blocks.

Possible Future Improvements

In terms of future improvements to the compression, a few options were investigated. Recall from Chapter 3 that the LHC bunch structure changed between 2017 and 2018, from the 8b4e scheme to long trains with 48 bunches. As a result, 2018 data of the same $\langle \mu \rangle$ results in slightly higher TRT occupancies due to out-of-time pileup. Training a new table from 2018 data with the new
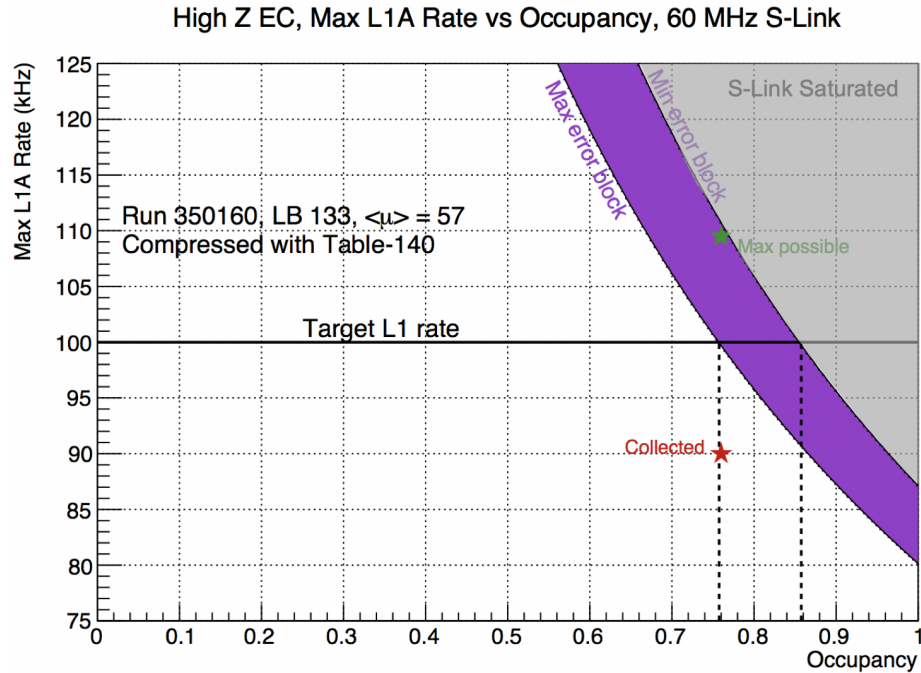
Figure 4.15: Projection of the maximum achievable L1 rate vs. TRT occupancy using Table-140 to compress $\langle\mu\rangle = 57$ data with the 2018 beam structure. This projection is made after the HOLA card upgrade, which increased the S-LINK rate to 60 MHz. The red star marks the L1 rate and occupancy at which ROD 0x341b02 collected data, while the green star marks the maximum L1 rate at which this ROD could have collected the data before saturating its S-LINK. With the new table and the upgraded HOLA cards, the TRT can reach 100 kHz at $\langle\mu\rangle = 60$ without saturating the S-LINK.

beam structure was studied, but no significant improvement was seen. Also, when training on only the collisions from the middle of the bunch trains, which have the most out-of-time pileup and therefore the largest data fragments, there was again no significant improvement. Generating separate compression tables for the barrel and endcap RODs, whose straws have different geometric layouts, occupancies, and gas configurations, also had little effect. Next, the effect of shortening the hardware validity gate was studied. Offline studies found that shortening the gate by a single bit at the end would not significantly affect the tracking performance [109]. However, this only reduces the occupancy by 1.5%, which results in just a 5-10 word reduction in the data fragment size at $\langle\mu\rangle = 60$. The most significant improvement may come from modifying the byte stream converter to allow empty straw words to be encoded with multiple bits. Such a table created from $\langle\mu\rangle = 60$ data would reduce the ROD fragment size by 25-30 words at high pileup.

4.5   Conclusion

In order to reach the target L1 rate of 100 kHz at an average pileup of $\langle\mu\rangle = 60$, multiple upgrades to the TRT readout were investigated and implemented. The largest improvement resulted from the HOLA card replacement, which increased the S-LINK rate from 40 MHz (50 MHz when overclocked) to 60 MHz. A particular N-to-1 lossy compression scheme, labeled Scheme0p, was studied in detail. Scheme0p offered better compression performance with an acceptable effect on tracking; however, it proved difficult to implement in the ROD firmware without timing violations. As a result, the lossless scheme was kept for Run 2, and a new compression table was created from $\langle\mu\rangle = 55$ data. With the new compression table and upgraded HOLA cards, the TRT can reach 100 kHz at $\langle\mu\rangle = 60$ without saturating the S-Link.

Further improvements to the TRT readout can be made during Long Shutdown 2 in preparation for Run 3. The S-LINK bandwidth usage can be reduced by shortening the hardware validity gate or by allowing empty straw patterns to be encoded with multiple bits. Additionally, the N-to-1 mapping firmware can be revisited. Finally, a new table can be generated from early Run 3 data, therefore optimizing the compression for the new beam and detector conditions.

Trilepton Resonance Search

Supersymmetry (SUSY) is a well-motivated extension of the Standard Model that may resolve many of its outstanding issues. However, due to the wide variety of possible supersymmetric models, the LHC experiments must engage in broad search campaigns. Searches for new supersymmetric particles produced through the strong interaction benefit from large cross sections, especially with the increase in the LHC center-of-mass energy to $\sqrt{s} = 13$ TeV. Consequently, analyses targeting natural supersymmetric models with light squarks and gluinos were particularly interesting in Run 1 and the start of Run 2. Unfortunately, no significant deviation from the Standard Model was observed.

With the vast ATLAS Run 2 dataset, searches for new supersymmetric particles produced through the electroweak interaction are now compelling, particularly those targeting the direct production of the superpartners of the gauge and Higgs bosons. In the Minimal Supersymmetric Standard Model (MSSM), these superpartners include the bino ($\tilde{B}$), neutral wino ($\tilde{W}_3$), and the two neutral higgsinos ($\tilde{h}_1^0$, $\tilde{h}_2^0$), which mix to form four mass eigenstates known as neutralinos ($\tilde{\chi}_1^0$, $\tilde{\chi}_2^0$, $\tilde{\chi}_3^0$, $\tilde{\chi}_4^0$). Also included are the charged winos ($\tilde{W}^\pm$) and higgsinos ($\tilde{h}^\pm$), which mix to form the chargino mass eigenstates ($\tilde{\chi}_1^\pm$, $\tilde{\chi}_2^\pm$). The strategies used to search for these particles will vary significantly between analyses targeting R-parity conserving and violating models.

Searching for new particles by reconstructing the invariant mass of their decay products has proved to be a fruitful strategy throughout the history of particle physics. Many of the Standard Model particles were discovered by hunting for resonant signals peaking above a smooth background. Most recently, the Higgs boson was discovered by the ATLAS and CMS collaborations using this method in the diphoton ($H \to \gamma\gamma$) and four lepton ($H \to ZZ^* \to 4\ell$) decay channels [20, 21]. This strategy is still utilized in searches for new heavy bosons and other exotic particles.

However, resonance searches are not performed often in the hunt for supersymmetry, since most analyses target R-parity conserving models. In the traditional MSSM with R-parity conservation, the lightest supersymmetric particle (LSP) is stable and therefore constrained to be neutral by astronomical observations. These weakly-interacting LSPs are invisible to the detector, so their presence must be inferred from the missing transverse momentum. However, once R-parity violation is allowed, the LSP can carry charge and will decay directly to Standard Model particles. Therefore, resonance searches can be used to target SUSY models with R-parity violation.

As discussed in Chapter 2, charginos and neutralinos are likely LSP candidates in the $B - L$ MSSM with spontaneous R-parity violation.[19] Of the various possible mixings, the predominately wino chargino is particularly interesting from an experimental perspective due to its relatively large production cross section and unique detector signatures. The chargino can decay via $\tilde{\chi}_1^{\pm} \to Z\ell \to \ell\ell\ell$, potentially producing a striking trilepton resonance rising above a smoothly falling background.

In this chapter, a search for charginos decaying via an R-parity violating coupling to three light leptons (e/μ) is presented [134]. After providing an overview of the analysis in Section 5.1, the analysis dataset and simulated MC samples are described in Section 5.2. In Section 5.3, the details of the event reconstruction are presented. Afterwards, the search strategy and background estimation methods are detailed in Sections 5.4 and 5.5, respectively. The systematic uncertainties are then discussed in Section 5.6. The statistical model and methods used in this analysis are described in Section 5.7, with the results of the statistical inference presented in Section 5.8. Finally, a brief discussion of the outlook for this analysis and the targeted $B - L$ model is given in Section 5.9.

5.1 Analysis Overview

In the targeted $B-L$ model, the wino $\tilde{\chi}_1^{\pm}$ and $\tilde{\chi}_1^0$ LSPs are dominantly produced in pairs ($\tilde{\chi}_1^{\pm}\tilde{\chi}_1^{\mp}$ and $\tilde{\chi}_1^{\pm}\tilde{\chi}_1^0$) through R-parity conserving processes. As the masses of both the $\tilde{\chi}_1^{\pm}$ and $\tilde{\chi}_1^0$ are dominated by the wino mass M_2, the $\tilde{\chi}_1^{\pm}$ and $\tilde{\chi}_1^0$ are nearly mass degenerate. With no R-parity conserving decay paths available, each $\tilde{\chi}_1^{\pm}/\tilde{\chi}_1^0$ decays promptly via a suppressed R-parity violating coupling to a lepton and a Standard Model boson.[20] The chargino can decay into a Z boson and a charged lepton ($Z\ell$), a Higgs boson and a charged lepton ($H\ell$), or a W boson and a neutrino ($W\nu$), while

---

[19]Recall in the $B - L$ MSSM, there is an additional neutral gaugino from the $U(1)_{B-L}$ gauge symmetry. Furthermore, as both R-parity and lepton number conservation are broken spontaneously, the neutral and charged leptons mix with the gauginos and higgsinos.

[20]In realistic models, one of the two winos will be slightly heavier and can therefore decay via an R-parity conserving vertex to the other, but this decay requires a very off-shell W boson and is kinematically suppressed. Consequently, the R-parity violating decays of the NLSP dominate, despite being suppressed themselves by the lightness of the active neutrino masses.
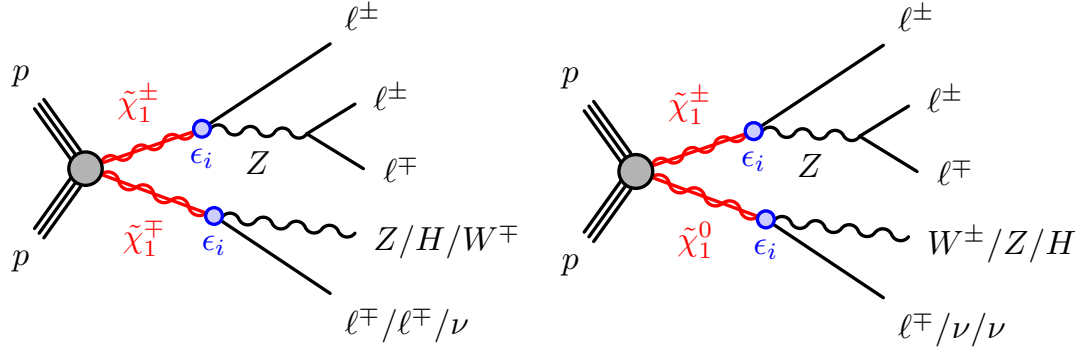
Figure 5.1: Diagrams of (left) $\tilde{\chi}_1^\pm \tilde{\chi}_1^\mp$ and (right) $\tilde{\chi}_1^\pm \tilde{\chi}_1^0$ production with at least one $\tilde{\chi}_1^\pm \to Z\ell \to \ell\ell\ell$ decay. The R-parity violating coupling ϵ_i allows prompt $\tilde{\chi}_1^\pm$ decays into $Z\ell$, $H\ell$, or $W\nu$ and prompt $\tilde{\chi}_1^0$ decays into $W\ell$, $Z\nu$, or $H\nu$.

the neutralino can decay into $W\ell$, $Z\nu$, or $H\nu$, as shown in Figure 5.1. As described in Chapter 2, the branching fractions of the $\tilde{\chi}_1^\pm / \tilde{\chi}_1^0$ to the different boson types and lepton flavors are related to the ratio of the vacuum expectation values of the two Higgs doublets ($\tan\beta$) and the neutrino mass hierarchy, among other model parameters.

Of the many possible final states, those involving a $\tilde{\chi}_1^\pm \to Z\ell \to \ell\ell\ell$ ($\ell = e/\mu$) decay are particularly interesting, as the $\tilde{\chi}_1^\pm$ mass can be accurately reconstructed from the momenta of the three leptons. Due to the excellent momentum resolution of reconstructed electrons and muons, a $\tilde{\chi}_1^\pm$ signal will produce a narrow resonance in the trilepton mass ($m_{Z\ell}$) distribution. With no Standard Model particles decaying resonantly to three leptons, the combinatorial background distribution is smooth.

Three orthogonal signal regions (SRs) are defined to target $\tilde{\chi}_1^\pm \tilde{\chi}_1^\mp / \tilde{\chi}_1^\pm \tilde{\chi}_1^0$ events where at least one chargino decays via $\tilde{\chi}_1^\pm \to Z\ell \to \ell\ell\ell$. To remain as inclusive as possible to signals with various branching fractions to the different boson types and lepton flavors, no constraints are placed on the decay of the second $\tilde{\chi}_1^\pm / \tilde{\chi}_1^0$. Instead, information from the decay of this second $\tilde{\chi}_1^\pm / \tilde{\chi}_1^0$ is used to differentiate the three SRs. The $m_{Z\ell}$ distributions in the three SRs are binned and fit simultaneously in a statistical strategy known as a *shape-fit*. Limits are set on the $\tilde{\chi}_1^\pm \tilde{\chi}_1^\mp + \tilde{\chi}_1^\pm \tilde{\chi}_1^0$ signal by scanning over the $\tilde{\chi}_1^\pm / \tilde{\chi}_1^0$ mass and branching fractions. Additionally, limits on generic BSM processes are set in each SR $m_{Z\ell}$ bin, and the full statistical model is made public to facilitate reinterpretations of the results for other new physics models.

This analysis is the first trilepton resonance search from the LHC using Run 2 data. Previous searches for new particles decaying resonantly to a lepton and SM heavy boson were performed by

both the ATLAS [135, 136] and CMS [137] collaborations. All three searches are interpreted in the context of the type-III seesaw mechanism, which introduces a new heavy lepton isospin triplet (L^+, N^0, L^-) to generate small masses for the SM neutrinos. These heavy leptons have similar gauge interactions and decays as the $\tilde{\chi}_1^{\pm}$ and $\tilde{\chi}_1^0$ in the $B - L$ model. In [135], only the $N^0 L^{\pm} \to W\ell W\nu$ production mode and decay channels were targeted. The Run 1 search presented in [136] is very similar to this $B - L$ chargino analysis; it targets $L^{\pm}L^{\mp} + N^0 L^{\pm}$ production, requiring at least one $L^{\pm} \to Z\ell \to \ell\ell\ell$ decay. The signal and background candidate events in data are determined by performing an (unbinned) maximum likelihood fit to the trilepton mass distributions in various SRs. Limits are set on new heavy leptons in both type-III seesaw and vector-like (non-chiral) lepton models. Finally, the CMS search [136] targets $L^{\pm}L^{\mp} + N^0 L^{\pm}$ production but does not directly target any specific decay process (and is therefore not a trilepton resonance search). Instead, the analysis simultaneously fits 48 independent SRs defined to target the many possible final states. Limits are set on the signal cross-section as a function of the heavy lepton mass, assuming equal branching fractions to the three lepton flavors.

The lowest chargino and neutralino mass considered for this search is 100 GeV. This is informed by the precision measurements of the electroweak sector performed at the Large Electron-Positron Collider (LEP) [35]. As no deviations from the SM were observed, the chargino is assumed to be above the Z mass. Furthermore, direct searches for charginos at LEP resulted in a fairly robust lower limit on the chargino mass of 103.5 GeV [82, 138]. While this limit does assume the chargino is decaying via an R-parity conserving vertex to a W boson and a neutralino LSP, it should apply to charginos in the $B - L$ MSSM with R-parity violation if the branching fraction to $W\nu$ is sizeable. This same logic extends to the limits set by the ATLAS and CMS collaborations, for example in the three lepton final state [139–142].

The major Standard Model backgrounds in this analysis all contain at least one Z boson and at least three prompt leptons. These include WZ, ZZ and $t\bar{t}Z$, which are all estimated using simulated Monte Carlo samples normalized in dedicated control regions. Additionally, Drell-Yan ($Z/\gamma^* + \text{jets}$) and $t\bar{t}$ events can enter the analysis despite only containing two prompt leptons. This occurs when a jet is misidentified as an electron, or when a heavy flavor hadron produces a non-prompt lepton in its decay. This *fake* and non-prompt lepton background is not modeled well in simulation, and is instead estimated with a data-driven method. Finally, minor backgrounds with prompt leptons are estimated directly from the MC simulation. These include triboson, Higgs, tWZ, $t\bar{t}W$, and tZ processes. The full background estimation strategy is detailed in Section 5.5.

5.2   Dataset and Simulated Monte Carlo Samples

Dataset

Over the course of Run 2, the ATLAS detector recorded 145 fb^{-1} of pp collisions at $\sqrt{s} = 13$ TeV. Of this data, 139 fb^{-1} is certified as being good for physics analysis, for a total data quality efficiency of 95.6% [93]. This search utilizes the full dataset, taking advantage of the high statistics to probe the electroweak SUSY sector. More information on this dataset is provided in Chapter 3, including the beam luminosity, bunch structure, and pileup profile.

Simulated Monte Carlo Samples

Monte Carlo simulation is used to model the various SM background processes and the targeted $\tilde{\chi}_1^\pm \tilde{\chi}_1^\mp$ and $\tilde{\chi}_1^\pm \tilde{\chi}_1^0$ signals. The shapes of the primary WZ, ZZ, and $t\bar{t}Z$ background distributions are taken from the simulation, while the normalization is constrained by the observed data in dedicated control regions. For the minor prompt backgrounds, both the shape and normalization are taken directly from the simulation. While the *fake* lepton background from misidentified hadrons and non-prompt leptons is estimated via a data-driven method, MC simulation provides insight into the processes giving rise to these fake leptons and is used to assess a corresponding systematic uncertainty. More details on the background estimation are provided in Section 5.5. Using the signal and background simulation, the analysis regions and object selection criteria are optimized to maximize the sensitivity to the targeted signal. The generators and parameters used in the MC samples are summarized in Table 5.1.

Table 5.1: Details of the MC simulation for each physics process, including the event generator used for matrix element calculation, the generator used for the PS and hadronization, the PS parameter tunes, and the order in α_S of the production cross-section calculations.

Process	Event generator	PS and hadronization	PS tune	Cross section (in QCD)
Diboson, triboson, $(Z + \text{jet})$	Sherpa 2.2	Sherpa 2.2	Default	NLO (NNLO)
$t\bar{t}W$, $t\bar{t}Z$, (Other top)	MadGraph5_aMC@NLO 2	Pythia 8	A14	NLO (LO)
$t\bar{t}$, (tW), $[t\bar{t}H]$	Powheg-Box v2	Pythia 8	A14	NNLO+NNLL (NLO+NNLL) [NLO]
Higgs: ggF, (VBF, VH)	Powheg-Box v2	Pythia 8	AZNLO	NNNLO (NNLO+NNLL)
$\tilde{\chi}_1^\pm \tilde{\chi}_1^\mp$, $\tilde{\chi}_1^\pm \tilde{\chi}_1^0$	MadGraph 2.6	Pythia 8	A14	NLO+NLL

Diboson, triboson, and $Z + \text{jet}$ samples [143, 144] were simulated using the Sherpa 2.2 [145] generator. Triboson and most diboson processes were simulated with Sherpa 2.2.2 while $Z + \text{jet}$ and semileptonically decaying diboson processes were simulated with Sherpa 2.2.1. The matrix element calculations were matched to the parton shower (PS) simulation using Catani–Seymour dipole

factorization [146, 147]. The matching was performed separately for different jet multiplicities and merged into an inclusive sample using an improved CKKW matching procedure [148, 149] extended to next-to-leading-order (NLO) accuracy in QCD using the MEPS@NLO prescription [148–151]. The virtual QCD correction for matrix elements at NLO accuracy was provided by the OpenLoops library [152, 153]. The `NNPDF3.0nnlo` [154] set of parton distribution functions (PDFs) was used together with a dedicated set of tuned PS parameters (tune) developed by the Sherpa authors [147].

The Z+jet (diboson) samples were calculated for up to two (one) additional partons at NLO and up to four (three) additional partons at leading order (LO) in QCD, and the triboson samples were calculated at NLO in QCD for the inclusive processes and at LO in QCD for up to two additional parton emissions. Diboson samples include loop-induced and electroweak production. The diboson and triboson samples do not include Higgs boson contributions. The cross sections calculated by the event generators were used for all samples except for $Z + \text{jet}$, which was normalized to a next-to-next-to-leading-order (NNLO) cross-section prediction [155].

The $t\bar{t}$ [156], $t\bar{t}H$ [157], and tW [158] process samples were simulated at NLO in QCD using the Powheg-Box [159–161] v2 generator and the `NNPDF3.0nlo` PDF set. The matrix element calculations were interfaced with Pythia 8.230 [162] for the PS using the A14 tune [163] and the `NNPDF2.3lo` PDF set [164]. The h_{damp} parameter[21] was set to be 1.5 times larger than the top-quark mass [165]. The $t\bar{t}$ inclusive production cross section was corrected to the theory prediction calculated at NNLO in QCD and included the resummation of next-to-next-to-leading logarithmic (NNLL) soft-gluon terms calculated with Top++2.0 [166]. The tW inclusive production cross section was corrected to the theory prediction at NLO in QCD with NNLL corrections to the soft-gluon terms [167, 168]. Both samples were generated in the five-flavor scheme, setting all quark masses to zero except for the top quark. The diagram-removal strategy [169] was employed in the tW sample to remove the interference with $t\bar{t}$ production [165].

Other top-quark production processes were simulated with the MadGraph5_aMC@NLO v2 [170] generator at either NLO in QCD with the `NNPDF3.0nlo` PDF set or at LO in QCD using the `NNPDF2.3lo` PDF set. They were interfaced with Pythia 8 using the A14 tune and the `NNPDF2.3lo` PDF set. Generator versions MadGraph5_aMC@NLO v2.3 and Pythia 8.212 were used for tZ, tWZ, $t\bar{t}Z$, $t\bar{t}W$, and $t\bar{t}WZ$ processes, while versions MadGraph5_aMC@NLO v2.2 and Pythia 8.186 were used for $t\bar{t}\gamma$, $t\bar{t}WW$, and four-top processes. These top-quark processes were generated at LO in QCD with the exception of $t\bar{t}Z$, $t\bar{t}W$, and tWZ, which were generated at NLO in QCD.

---

[21]The h_{damp} parameter controls the transverse momentum p_{T} of the first additional emission beyond the leading-order Feynman diagram in the PS and therefore regulates the high-p_{T} emission against which the $t\bar{t}$ system recoils.

Higgs boson production via gluon–gluon fusion (ggF) was simulated at NNLO accuracy in QCD using the POWHEG-BOX v2 NNLOPS program [171] and interfaced with PYTHIA 8.212 using the AZNLO tune [172] and PDF4LHC15 NNLO PDF set [173]. The MC prediction was normalized to the next-to-next-to-next-to-leading-order (NNNLO) cross section in QCD plus electroweak corrections at NLO [174, 175].

Higgs boson production via vector-boson fusion (VBF) and Higgs boson production in association with a W or Z boson (VH) were generated using POWHEG-BOX v2 and interfaced with PYTHIA 8.212 using the AZNLO tune and CTEQ6L1 [176] PDF set. The POWHEG predictions are accurate to NLO in QCD and were tuned to match calculations including effects due to finite heavy-quark masses and soft-gluon resummations up to NNLL. The MC predictions were normalized to NNLO QCD cross-section calculations with NLO electroweak corrections [177–180].

The $\tilde{\chi}_1^\pm \tilde{\chi}_1^\mp$ and $\tilde{\chi}_1^\pm \tilde{\chi}_1^0$ signal samples were produced using MADGRAPH5_aMC@NLO v2.6 and the NNPDF2.3lo PDF set with up to two additional partons calculated at LO in QCD and interfaced with PYTHIA 8.230 using the A14 tune and NNPDF2.3lo PDF set. The scale parameter for jet–parton CKKW-L matching was set to a quarter of the $\tilde{\chi}_1^\pm / \tilde{\chi}_1^0$ mass. The samples were generated with $\tilde{\chi}_1^\pm / \tilde{\chi}_1^0$ masses ranging from 100 GeV to 1500 GeV in steps of 50 GeV, with an extra mass point just below the Higgs mass at 120 GeV.

Both the $\tilde{\chi}_1^\pm \tilde{\chi}_1^\mp$ and $\tilde{\chi}_1^\pm \tilde{\chi}_1^0$ signal samples were produced with equal branching fractions to the three lepton flavors. The $\tilde{\chi}_1^\pm \tilde{\chi}_1^\mp$ signal samples were generated with equal branching fractions to the kinematically available bosons (i.e. $W\nu/Z\ell/H\ell$ when above the Higgs mass, but only $W\nu/Z\ell$ when below). In contrast, the $\tilde{\chi}_1^\pm$ is forced to decay to Zl with 100% branching fraction in the $\tilde{\chi}_1^\pm \tilde{\chi}_1^0$ signal samples, while the $\tilde{\chi}_1^0$ decays democratically to the bosons. This restriction saves computational resources, as fewer events need to be generated to reach the requisite statistics for events with $\tilde{\chi}_1^\pm \to Z\ell$ decays.[22] Ultimately, limits are set on the $\tilde{\chi}_1^\pm \tilde{\chi}_1^\mp + \tilde{\chi}_1^\pm \tilde{\chi}_1^0$ signal while scanning over these lepton and boson branching fractions. This is achieved by reweighting individual events up and down according to their truth decays, assuming the $\tilde{\chi}_1^\pm$ and $\tilde{\chi}_1^0$ have fully correlated branching fractions. More information on this reweighting is provided in Section 5.4.

To further improve the event generation efficiency, a filter is applied to both signal samples that requires at least one Z boson that decays leptonically (tau leptons included). An additional filter is applied to the $\tilde{\chi}_1^\pm \tilde{\chi}_1^0$ samples, requiring at least three light leptons (e/μ). Finally, the $\tilde{\chi}_1^\pm \tilde{\chi}_1^0$ samples are filtered such that all leptons satisfy $p_T > 9$ GeV and $|\eta| < 2.8$.

---

[22] As a result of this choice, it is not possible to evaluate the efficiency and acceptance of $\tilde{\chi}_1^\pm \tilde{\chi}_1^0$ events where the $\tilde{\chi}_1^\pm$ decays to $W\nu$ or $H\ell$, or the additional sensitivity these events provide. However, it is assumed to be negligible.

The signal production cross sections were calculated assuming mass-degenerate, pure-wino $\tilde{\chi}_1^\pm$ and $\tilde{\chi}_1^0$,[23] and were calculated at NLO in QCD with next-to-leading-logarithmic (NLL) corrections to the soft-gluon terms [80, 81, 181–183]. The cross sections and their uncertainties were derived from an envelope of cross section predictions using different PDF sets and factorization and renormalization scales [184]. The inclusive cross sections for $\tilde{\chi}_1^\pm \tilde{\chi}_1^\mp$ ($\tilde{\chi}_1^\pm \tilde{\chi}_1^0$) production at a center-of-mass energy of $\sqrt{s} = 13$ TeV range from 11.6 ± 0.5 (22.7 ± 1.0) pb for masses of 100 GeV to 0.040 ± 0.006 (0.080 ± 0.013) fb for masses of 1500 GeV.

The modeling of c- and b-hadron decays in samples generated with Powheg-Box or Mad-Graph5_aMC@NLO was performed with EvtGen 1.2.0 [185]. Events from all generators were propagated through a full simulation of the ATLAS detector [186] using Geant4 [187] to model the interactions of particles with the detector. A parameterized simulation of the ATLAS calorimeter [186] was used for faster detector simulation of signal, tW, and $t\bar{t}H$ processes and was found to be in agreement with the full simulation. The effect of multiple interactions in the same and neighboring bunch crossings (pileup) was modeled by overlaying simulated minimum-bias events onto each hard-scattering event. The minimum-bias events were generated with Pythia 8.210 using the A3 tune [188] and `NNPDF2.3lo` PDF set.

5.3   Event Reconstruction

A set of quality criteria is applied to each event and physics object used in the analysis. Data events collected with single lepton triggers must be included in the Good Runs List [93], which contains all luminosity blocks that are certified for use in physics analysis. Each data and MC event must contain at least one reconstructed vertex associated to two or more tracks with $p_T > 500$ MeV. The reconstructed vertex with the largest Σp_T^2 of associated tracks is designated as the *primary vertex* [189].

The electrons, muons, and jets used in the analysis are first required to pass a set of loose *baseline* selections. These baseline analysis objects are then used as input to the overlap removal algorithm and the E_T^{miss} calculation. While photons are not otherwise used by the analysis, a set of baseline photons is defined and included in the E_T^{miss} calculation. After overlap removal, tighter *signal* selections are applied to the remaining baseline objects. These signal objects are then used for the analysis.

---

[23]Technically, the cross sections correspond to wino-like $\tilde{\chi}_1^\pm \tilde{\chi}_1^\mp$ and $\tilde{\chi}_1^\pm \tilde{\chi}_2^0$ production in the R-parity conserving MSSM. The LSP is assumed to be a light bino-like $\tilde{\chi}_1^0$, and all other supersymmetric particles are decoupled. As the bino-like $\tilde{\chi}_1^0$ is not expected to contribute significantly to the production cross section, this was deemed acceptable.

Trigger

Data events used for this analysis were collected with unprescaled single electron and single muon triggers. Each event must contain a signal lepton that matches the online object that activated the trigger and exceeds an offline p_T threshold. The triggers used in this analysis and their offline p_T thresholds are summarized in Table 5.2. These offline p_T threshold are set just above the online thresholds, which increase with loosening trigger-level identification, isolation, and impact parameter requirements. Typically, trigger-matched signal electrons must have a fully-calibrated p_T at least 1 GeV above the online threshold, while signal muons must have a p_T above 1.05 times the online threshold. However, for consistency, this analysis uses the tighter offline p_T thresholds of the 2016-2018 triggers for 2015 as well. The one exception is the 2015 `HLT_e120_lhloose` electron trigger, which uses a lower threshold of 121 GeV. The single lepton triggers are more than 90% efficient for the signal model with $m_{\tilde{\chi}_1} = 100$ GeV, and more than 99% efficient for signal models with $m_{\tilde{\chi}_1} \geq 300$ GeV.

Table 5.2: The single lepton triggers and their associated offline p_T thresholds, separated by year.[24]

Year	Electron Trigger	Offline Threshold [GeV]	Muon Trigger	Offline Threshold [GeV]
2015	HLT_e24_lhmedium_L1EM20VH	27	HLT_mu20_iloose_L1MU15	27.3
	HLT_e60_lhmedium	61	HLT_mu50	52.5
	HLT_e120_lhloose	121	-	-
2016-2018	HLT_e26_lhtight_nod0_ivarloose	27	HLT_mu26_ivarmedium	27.3
	HLT_e60_lhmedium_nod0	61	HLT_mu50	52.5
	HLT_e140_lhloose_nod0	141	-	-

These trigger requirements are applied to the MC simulation as well, with scale factors applied to the MC to account for differences in the trigger efficiencies between data and MC. These scale factors are provided centrally by the electron/photon and muon combined performance groups.

Electrons

Baseline electrons must satisfy $p_T > 10$ GeV, be within the Inner Detector acceptance ($|\eta| < 2.47$), and pass the `LooseAndBLayerLLH` working point of the likelihood-based electron identification [190]. Electrons falling in the region between the barrel and endcap calorimeters ($1.37 < |\eta| <$

---

[24]The trigger names can be understood as follows. The number following either "e" or "mu" is the online p_T threshold in GeV. The "lhloose", "lhmedium", and "lhtight" labels refer to the trigger-level electron likelihood identification working point. The "iloose", "ivarloose", and "ivarmdedium" labels refer to the trigger-level isolation working point, where "var" indicates a variable-sized isolation cone that shrinks with increasing p_T. The "nod0" text indicates that no requirement is placed on the track's transverse impact parameter (d_0) or its significance ($d_0/\sigma(d_0)$). Finally, the text following "L1" is the Level-1 trigger seed, which is only included in the HLT trigger name when it is seeded by multiple L1 triggers [121].

1.52) are vetoed, as are electrons with clusters compromised by hardware malfunctions (labeled `BADCLUSELECTRON`). Finally, baseline electrons must have a longitudinal impact parameter compatible with the primary vertex with $|z_0 \sin\theta| < 0.5$ mm.

Baseline electrons passing overlap removal are considered for signal electrons. Signal electrons must satisfy the tighter `MediumLLH` identification criteria, and pass a stricter $p_T > 12$ GeV cut. Additionally, signal electrons must pass the `FCTight` isolation criteria, which utilizes information from both the calorimeters and trackers. First, the nonassociated calorimeter transverse energy in a cone of radius $\Delta R = 0.2$ around the electron may not exceed 6% of the electron p_T. Second, the scalar p_T sum of all nonassociated tracks (but still consistent with the primary vertex) in a variable-width cone around the electron must not exceed 6% of the electron p_T. This cone starts with a radius of $\Delta R = 0.2$, decreasing indefinitely with the electron p_T above 50 GeV according to $\Delta R = 10$ GeV$/p_T$. Finally, signal electrons must satisfy a longitudinal impact parameter significance cut of $|d_0/\sigma_{d_0}| < 5$. The baseline and signal electron requirements are summarized in Table 5.3.

Cut	Value/description
Baseline Electrons	
Acceptance	$p_T > 10$ GeV, $|\eta| < 2.47$, crack veto
Impact parameter	$z_0 \sin(\theta) \leq 0.5$ mm
Identification WP	`LooseAndBLayerLLH`
Object quality	`BADCLUSELECTRON` electron veto
Signal Electrons	
Acceptance	$p_T > 12$ GeV
Impact parameter	$|d_0/\sigma_{d_0}| < 5$
Identification WP	`MediumLLH`
Isolation WP	`FCTight`

Table 5.3: Summary of the baseline and signal electron selection criteria. Signal criteria are applied on top of baseline criteria after overlap removal.

Muons

Baseline muons must satisfy $p_T > 10$ GeV, be within the Muon Spectrometer acceptance ($|\eta| < 2.7$), and pass the `Medium` identification criteria [191]. Additionally, baseline muons must have a longitudinal impact parameter compatible with the primary vertex with $|z_0 \sin\theta| < 0.5$ mm.

Baseline muons passing overlap removal are considered for signal muons. Signal muons must satisfy the tighter $p_T > 12$ GeV requirement and pass the `FCTight_FixedRad` isolation criteria, which

again utilizes both the calorimeter and tracker information. First, the nonassociated calorimeter transverse energy in a cone of radius $\Delta R = 0.2$ around the muon may not exceed 15% of the muon p_T. Second, the scalar p_T sum of all nonassociated tracks in a variable-width cone around the muon (and consistent with the primary vertex) must not exceed 4% of the muon p_T. This cone starts with a radius of $\Delta R = 0.3$ for muons with $p_T \leq 33$ GeV, before decreasing like $\Delta R = 10$ GeV$/p_T$ for muons satisfying 33 GeV $< p_T < 50$ GeV. For muons with $p_T \geq 50$ GeV, the cone size remains fixed at $\Delta R = 0.2$ to better reject non-prompt muons from heavy flavor decays.

Additionally, signal muons must pass both a cosmic and bad muon veto. The former requires the longitudinal and transverse impact parameters to be consistent with the primary vertex, while the latter requires the momenta measured by the inner detector and muon spectrometer to be consistent. The impact of these two vetoes is minimal after the baseline selection. Finally, signal muons must satisfy a longitudinal impact parameter significance cut of $|d_0/\sigma_{d_0}| < 3$. The baseline and signal muon requirements are summarized in Table 5.4.

Cut	Value/description
Baseline Muons	
Acceptance	$p_T > 10$ GeV, $|\eta| < 2.7$
Impact parameter	$z_0 \sin(\theta) \leq 0.5$ mm
Identification WP	`Medium`
Signal Muons	
Acceptance	$p_T > 12$ GeV
Impact parameter	$|d_0/\sigma_{d_0}| < 3$
Identification WP	`Medium`
Isolation WP	`FCTight_FixedRad`
Object quality	Cosmic muon veto, bad muon event veto

Table 5.4: Summary of the baseline and signal muon selection criteria. Signal criteria are applied on top of baseline criteria after overlap removal.

Jets

This analysis uses `EMTopo` jets clustered using the anti-k_T algorithm with a radius parameter R of 0.4. Baseline jets must satisfy $p_T > 20$ GeV and may fall within the full calorimeter acceptance ($|\eta| < 4.5$). The track-based jet vertex tagger (JVT) [192] and calorimeter-based forward jet vertex tagger (fJVT) [193] are used to tag jets that likely originate from the primary vertex. Jets with $p_T < 120$ GeV inside the Inner Detector acceptance ($|\eta| < 2.5$) are tagged using the `Medium` JVT

working point. Untagged jets, which are likely to originate from pileup interactions, are not vetoed at the baseline level; however, the tagging information is used in the missing transverse energy calculation. Baseline jets that pass overlap removal become candidates for signal jets.

Signal jets must pass a tighter $|\eta| < 2.8$ cut. To suppress jets from pileup, signal jets with $p_T < 120$ GeV within the Inner Detector acceptance ($|\eta| < 2.5$) must be tagged by the JVT (but not the fJVT). Finally, if any signal jet fails the `LooseBad` object quality criteria, the event is vetoed.

Baseline and signal jets containing b-hadrons (b-jets) are tagged using multiple low-level algorithms as input to a high-level multivariate classifier [194]. The low-level algorithms utilize tracking information, analyzing the impact parameters of individual tracks associated to the jet and building secondary displaced vertices. The results of these low-level algorithms are given as input to the high-level `MV2c10` boosted decision tree algorithm, providing separate discriminants for b-jets, c-jets, and light flavor jets. With this algorithm, jets are tagged using the `Fixed 85%` working point. This corresponds to an average b-tagging efficiency of 85% in $t\bar{t}$ simulation, with rejection factors of 25, 2.7, and 6.1 for jets originating from light quarks and gluons, c-quarks, and τ-leptons, respectively.

Cut	Value/description
Baseline jets	
Acceptance	$p_T > 20$ GeV, $|\eta| < 4.5$
Signal jets	
Acceptance	$|\eta| < 2.8$
JVT	`Medium`, $p_T < 120$ GeV, $|\eta| < 2.5$
Object quality	`LooseBad` event veto
Signal b-tagged jets	
Acceptance	$|\eta| < 2.5$
b-tagging algorithm	`MV2c10`
b-tagging WP	`Fixed 85%`

Table 5.5: Summary of the baseline and signal jet selection criteria. Signal criteria are applied on top of baseline criteria after overlap removal. JVT requirement only applies to central, softer jets.

Photons

While not used in this analysis directly, baseline photons are provided as input to the missing energy calculation in each event. Baseline photons must satisfy $p_T > 25$ GeV, and must be within the acceptance of the Inner Detector and the finely-segmented first layer of the LAr calorimeter ($|\eta| <$

2.37), excluding the calorimeter crack region $(1.37 < |\eta| < 1.52)$. Additionally, baseline photons must satisfy the `Tight` identification criteria [195]. Finally, photons labeled as `BADCLUSPHOTON` due to detector malfunctions are vetoed.

Missing Transverse Energy

The missing transverse momentum, $\boldsymbol{p}_\mathrm{T}^\mathrm{miss}$, is defined as the negative vector sum of all baseline electron, muon, photon and hard-scatter jet momenta, plus an additional soft term [196]. Hard-scatter jets are baseline jets that pass the JVT and fJVT requirements described above. The soft term is calculated from all tracks associated with the primary vertex but none of the baseline objects. By using fully-calibrated baseline objects and the soft term, the pileup dependence is minimized. The missing transverse energy, $E_\mathrm{T}^\mathrm{miss}$, is the magnitude of $\boldsymbol{p}_\mathrm{T}^\mathrm{miss}$.

Overlap Removal

As the electron, muon, and jet reconstruction algorithms are run independently, a single particle can be reconstructed as multiple analysis objects. To resolve these ambiguities, an overlap removal algorithm is performed on all baseline leptons and jets. The algorithm is applied sequentially as follows:

1. Electrons sharing a track with a higher p_T electron are removed.

2. Electrons sharing a track with a non-calorimeter-tagged muon are removed.

3. Jets within $\Delta R(e, \mathrm{jet}) \leq 0.2$ of an electron are removed, unless the jet is b-tagged with $p_\mathrm{T} < 100$ GeV.

4. Electrons within $\Delta R(e, \mathrm{jet}) \leq 0.4$ are removed.

5. Jets within $\Delta R(\mu, \mathrm{jet}) \leq 0.2$ of an muon are removed, unless the jet is b-tagged with $p_\mathrm{T} < 100$ GeV.

6. Muons within $\Delta R(\mu, \mathrm{jet}) \leq 0.4$ are removed.

Notice that if a lepton and jet have $\Delta R(\ell, \mathrm{jet}) \leq 0.2$, the overlap removal decision depends on the b-tag status of the jet. If the jet is b-tagged, the lepton is removed; otherwise, the jet is removed. By preferentially keeping the b-tagged jet over the lepton, the non-prompt leptons from heavy flavor hadron decays are suppressed. However, this preference for b-tagged jets can reduce the efficiency

for prompt leptons from the high mass $\tilde{\chi}_1^{\pm}\tilde{\chi}_1^{\mp}/\tilde{\chi}_1^{\pm}\tilde{\chi}_1^0$ signals, where the decay products of the $\tilde{\chi}_1^{\pm}/\tilde{\chi}_1^0$ can be collimated. Therefore, this favoring of b-tagged jets only applies to jets with $p_{\text{T}} < 100$ GeV.

The ΔR calculation here uses the rapidity, as opposed to η, and is therefore Lorentz invariant even for jets with masses comparable to their momenta. The baseline leptons and jets passing this overlap removal algorithm are considered for the signal objects used by the analysis.

5.4   Search Strategy

In this $B - L$ model, the $\tilde{\chi}_1^{\pm}$ and $\tilde{\chi}_1^0$ are dominantly produced in pairs through R-parity conserving processes. With no R-parity conserving decay paths available, each $\tilde{\chi}_1^{\pm}/\tilde{\chi}_1^0$ decays via a suppressed R-parity violating coupling to a lepton and a Standard Model boson. Of the many possible final states, those involving a $\tilde{\chi}_1^{\pm} \to Z\ell \to \ell\ell\ell$ decay are particularly interesting, as the $\tilde{\chi}_1^{\pm}$ mass can be accurately reconstructed from the momenta of the three leptons. Due to the excellent momentum resolution of reconstructed electrons and muons, a $\tilde{\chi}_1^{\pm}$ signal will produce a narrow resonance in the trilepton mass ($m_{Z\ell}$) distribution. With no Standard Model particles decaying resonantly to three leptons, the combinatorial background distribution is smooth.

Three orthogonal signal regions (SRs) are defined to target $\tilde{\chi}_1^{\pm}\tilde{\chi}_1^{\mp}/\tilde{\chi}_1^{\pm}\tilde{\chi}_1^0$ events where at least one chargino decays via $\tilde{\chi}_1^{\pm} \to Z\ell \to \ell\ell\ell$. To remain as inclusive as possible to signals with various branching fractions to the different boson types and lepton flavors, no constraints are placed on the decay of the second $\tilde{\chi}_1^{\pm}/\tilde{\chi}_1^0$. Instead, information from the decay of this second $\tilde{\chi}_1^{\pm}/\tilde{\chi}_1^0$ is used to differentiate the three SRs. The algorithm used to classify the many possible final states into three SRs is presented in the following discussion. Afterwards, the matching procedure used to select the correct three leptons that reconstruct the $\tilde{\chi}_1^{\pm}$ mass is presented. Finally, the event kinematic and object multiplicity requirements used to mitigate the combinatorial background are described.

Signal Regions

As mentioned previously, this analysis targets $\tilde{\chi}_1^{\pm}\tilde{\chi}_1^{\mp} + \tilde{\chi}_1^{\pm}\tilde{\chi}_1^0$ production, where at least one chargino decays via $\tilde{\chi}_1^{\pm} \to Z\ell \to \ell\ell\ell$. An event classification algorithm was developed to handle the many possible final states, utilizing information from the second $\tilde{\chi}_1^{\pm}/\tilde{\chi}_1^0$ decay to define three complementary signal regions. The first two signal regions, SR3ℓ and SR4ℓ, target partially invisible decays of the second $\tilde{\chi}_1^{\pm}/\tilde{\chi}_1^0$, while SRFR targets final states where the decays of both winos can be fully reconstructed. Should the signal be present, a trilepton mass resonance would appear in each signal region. The algorithm is summarized in Figure 5.2.
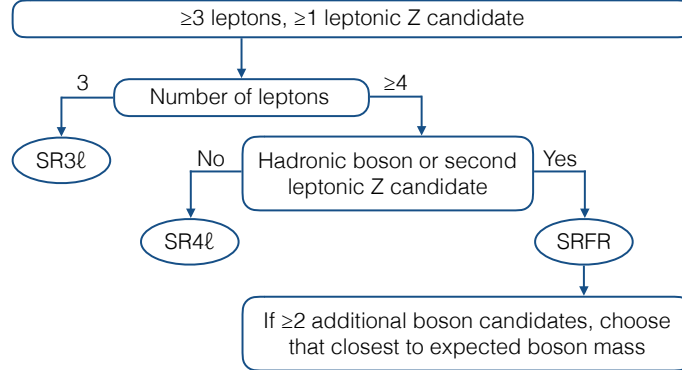
Figure 5.2: Schematic flow chart describing the assignment of an event to a given signal region.

First, to target $\tilde{\chi}_1^\pm \to Z\ell \to \ell\ell\ell$ decays, all events must contain at least three leptons. Two of these leptons must reconstruct a Z boson, forming a same-flavor opposite-sign (SFOS) pair with a dilepton mass within 10 GeV of the Z mass. If there are no additional leptons in the event, it is considered for SR3ℓ. Final states targeted by SR3ℓ include:

- $\tilde{\chi}_1^\pm \tilde{\chi}_1^\mp \to Z\ell \, W\nu \to \ell\ell\ell \, qq\nu$
- $\tilde{\chi}_1^\pm \tilde{\chi}_1^0 \to Z\ell \, H\nu \to \ell\ell\ell \, bb\nu$
- $\tilde{\chi}_1^\pm \tilde{\chi}_1^0 \to Z\ell \, Z\nu \to \ell\ell\ell \, qq\nu$
- $\tilde{\chi}_1^\pm \tilde{\chi}_1^0 \to Z\ell \, Z\nu \to \ell\ell\ell \, \nu\nu\nu$

If an event contains at least four leptons, but a second boson candidate cannot be formed, the event is considered for SR4ℓ. Final states targeted by SR4ℓ include:

- $\tilde{\chi}_1^\pm \tilde{\chi}_1^\mp \to Z\ell \, Z\ell \to \ell\ell\ell \, \nu\nu\ell$
- $\tilde{\chi}_1^\pm \tilde{\chi}_1^\mp \to Z\ell \, W\nu \to \ell\ell\ell \, \ell\nu\nu$
- $\tilde{\chi}_1^\pm \tilde{\chi}_1^0 \to Z\ell \, Z\nu \to \ell\ell\ell \, \ell\ell\nu$
- $\tilde{\chi}_1^\pm \tilde{\chi}_1^0 \to Z\ell \, W\ell \to \ell\ell\ell \, \ell\nu\ell$

Finally, if an event contains at least four leptons and a second boson candidate, the event is considered for SRFR. For this second boson candidate, pairs of jets are considered if their dijet mass satisfy $71.2 < m_{jj} < 111.2$ GeV, consistent with a W or Z boson. This mass requirement is relaxed to $71.2 < m_{jj} < 150$ GeV if at least one of these jets is b-tagged, providing sensitivity to $H \to bb$ decays. To maintain sensitivity to possible $\tilde{\chi}_1^\pm \tilde{\chi}_1^\mp$ events where both charginos decay via $\tilde{\chi}_1^\pm \to Z\ell \to \ell\ell\ell$, additional pairs of SFOS leptons with $81.2 < m_{\ell\ell} < 101.2$ GeV are also considered for the second boson candidate. Such events, however, must contain at least six leptons. Final states targeted by SRFR include:

- $\tilde{\chi}_1^\pm \, \tilde{\chi}_1^\mp \to Z\ell \, Z\ell \to \ell\ell\ell \, \ell\ell\ell$

- $\tilde{\chi}_1^\pm \, \tilde{\chi}_1^\mp \to Z\ell \, H\ell \to \ell\ell\ell \, bb\ell$

- $\tilde{\chi}_1^\pm \, \tilde{\chi}_1^\mp \to Z\ell \, Z\ell \to \ell\ell\ell \, qq\ell$

- $\tilde{\chi}_1^\pm \, \tilde{\chi}_1^0 \to Z\ell \, W\ell \to \ell\ell\ell \, qq\ell$

While not explicitly targeted, final states involving tau leptons and Higgs decays other than $H \to bb$ can enter any of the SRs depending on the decay details. For example, a $\tilde{\chi}_1^\pm \, \tilde{\chi}_1^\mp \to Z\ell \, H\ell \to \ell\ell\ell \, WW^*\ell$ event can enter either SR4ℓ or SRFR depending on the decays of the two W bosons. Even when one (or more) light lepton in the $\tilde{\chi}_1^\pm \to Z\ell \to \ell\ell\ell$ decay is replaced by a tau lepton, the event can still enter the SRs if the tau decays leptonically. However, the trilepton mass in such events will not accurately reconstruct the $\tilde{\chi}_1^\pm$ mass, as some momentum is lost to neutrinos.

Due to an imperfect detector efficiency, acceptance, and resolution, an event targeted by one particular SR may *migrate* into another. For example, if the second wino is a $\tilde{\chi}_1^0$ decaying via $\tilde{\chi}_1^0 \to W\ell \to qq\ell$, the event is targeted by SRFR. However, if an object is lost or the dijet mass is outside the boson mass window, the event may be considered for SR3ℓ or SR4ℓ instead. Additionally, event migration can occur in the opposite direction due to fake or non-prompt leptons, or by random pileup jet pairs satisfying the boson mass window requirements and faking a boson.

Trilepton Mass Reconstruction

In each signal region, the correct three leptons must be chosen to reconstruct the $\tilde{\chi}_1^\pm \to Z\ell \to \ell\ell\ell$ decay. The choice is unambiguous in SR3ℓ, as there are only three leptons in the event. However, in SR4ℓ and SRFR, at least one lepton is expected to originate from the decay of the second $\tilde{\chi}_1^\pm/\tilde{\chi}_1^0$, causing an ambiguity. If an incorrect lepton is chosen, the trilepton mass will not reconstruct the chargino mass, causing the signal resonance to smear, potentially reducing the statistical significance.

In SRFR, this ambiguity can be resolved by fully reconstructing the two decay chains and taking advantage of the mass degeneracy of the $\tilde{\chi}_1^\pm\tilde{\chi}_1^\mp/\tilde{\chi}_1^\pm\tilde{\chi}_1^0$ pair. Each event contains a leptonic Z boson candidate, a second boson candidate, and at least two additional leptons. Of these additional leptons, the two hardest are assumed to be produced directly from the $\tilde{\chi}_1^\pm/\tilde{\chi}_1^0$ decay vertices; henceforth, such leptons will be referred to as *direct* leptons. To reconstruct the $\tilde{\chi}_1^\pm\tilde{\chi}_1^\mp/\tilde{\chi}_1^\pm\tilde{\chi}_1^0$ pair, these two *direct* leptons are matched with the two boson candidates by minimizing the mass asymmetry, defined as:

$$m_{Z\ell}^{\text{asym}} = \frac{|m_{Z\ell} - m_{B\ell}|}{m_{Z\ell} + m_{B\ell}}, \tag{5.1}$$

where $m_{Z\ell}$ is the invariant mass of the $\tilde{\chi}_1^\pm \to Z\ell \to \ell\ell\ell$ decay leg, and $m_{B\ell}$ is the invariant mass of the other $\tilde{\chi}_1^\pm/\tilde{\chi}_1^0$ decay leg. The B subscript represents the second reconstructed W, Z, or H

boson. This algorithm has an efficiency for choosing the correct three leptons to reconstruct the $\tilde{\chi}_1^\pm \to Z\ell \to \ell\ell\ell$ decay ranging from 60% for $m_{\tilde{\chi}_1} = 100$ GeV signals to 80% or more for signals with $m_{\tilde{\chi}_1} \geq 200$ GeV.

In SR4ℓ, the second $\tilde{\chi}_1^\pm/\tilde{\chi}_1^0$ decay cannot be fully reconstructed, and the mass asymmetry therefore cannot be used to choose the correct three leptons. Each event contains at least four leptons, two of which reconstruct a Z boson. Choosing the correct third lepton to pair with the Z is difficult, as the event kinematics changes drastically with the $\tilde{\chi}_1^\pm/\tilde{\chi}_1^0$ mass. At low mass, the $\tilde{\chi}_1^\pm\tilde{\chi}_1^\mp/\tilde{\chi}_1^\pm\tilde{\chi}_1^0$ pairs are boosted and recoil against each other. As a result, the decay products of each $\tilde{\chi}_1^\pm/\tilde{\chi}_1^0$ are collimated. At high mass, the $\tilde{\chi}_1^\pm\tilde{\chi}_1^\mp/\tilde{\chi}_1^\pm\tilde{\chi}_1^0$ pairs are produced almost at rest, so the *direct* lepton and Z boson from the $\tilde{\chi}_1^\pm \to Z\ell$ decay recoil against each other instead.

To maximize the sensitivity over a range of possible $\tilde{\chi}_1^\pm/\tilde{\chi}_1^0$ masses, an SR4ℓ-specific matching algorithm was developed. The goal was to find a kinematic variable to serve as a proxy for the $\tilde{\chi}_1^\pm/\tilde{\chi}_1^0$ mass, allowing separate matching algorithms at low and high mass. This proxy mass has to be appropriate for the full range of final states targeted by SR4ℓ. The common feature of all these targeted final states is the presence of at least four leptons. Consequently, the scalar p_T-sum of all the leptons in the event, L_T, was used as the proxy for the $\tilde{\chi}_1^\pm/\tilde{\chi}_1^0$ mass:

$$L_T = \sum_{\text{leps}} p_T. \tag{5.2}$$

If an event has $L_T < 550$ GeV, it is assumed to be a low mass signal event, and the lepton that minimizes $\Delta R(Z, \ell)$ is chosen to reconstruct the $\tilde{\chi}_1^\pm \to Z\ell \to \ell\ell\ell$ decay. If an event has $L_T > 550$ GeV, it is assumed to be a high mass signal event, and the lepton that maximizes $m_{Z\ell}$ is chosen instead.

To determine the optimal L_T value at which to switch between the $\min[\Delta R(Z, \ell)]$ and $\max[m_{Z\ell}]$ methods for selecting the *direct* lepton, several factors must be considered. By maximizing the efficiency for choosing the correct three leptons to reconstruct the $\tilde{\chi}_1^\pm \to Z\ell \to \ell\ell\ell$ decay, the signal $m_{Z\ell}$ distribution becomes more strongly peaked at the true $\tilde{\chi}_1^\pm$ mass. However, this does not necessarily lead to the optimal sensitivity, as various matching algorithms may shape the background $m_{Z\ell}$ distribution differently. Finally, since a shape-fit is performed in the signal regions, all $m_{Z\ell}$ bins contribute to the sensitivity. As a result, even the mismatched signal events in the combinatorial tails of the $m_{Z\ell}$ distribution can contribute. Various matching algorithms were evaluated using `HistFitter` [197] to perform the shape-fit, with the algorithm described above providing the best sensitivity over the probed $\tilde{\chi}_1^\pm/\tilde{\chi}_1^0$ mass range. These studies are summarized in Appendix A.

Branching Fraction Scan and Signal Event Reweighting

When setting limits on the $\tilde{\chi}_1^\pm \tilde{\chi}_1^\mp + \tilde{\chi}_1^\pm \tilde{\chi}_1^0$ signal, a scan is performed over the $\tilde{\chi}_1^\pm / \tilde{\chi}_1^0$ mass and branching fractions to the various leptons and bosons. For these limits, it is assumed that the branching fractions are fully correlated between the $\tilde{\chi}_1^\pm$ and $\tilde{\chi}_1^0$. Four points in the lepton branching fraction space are considered: equal branching fractions to the three flavors, 100% to electrons, 100% to muons, and 100% to tau leptons. A finer scan is performed over the boson branching fractions.

As described in Section 5.2, the $\tilde{\chi}_1^\pm \tilde{\chi}_1^\mp$ samples are produced with equal branching fractions to the various leptons and bosons, while the $\tilde{\chi}_1^\pm \tilde{\chi}_1^0$ samples force the $\tilde{\chi}_1^\pm$ to decay via $\tilde{\chi}_1^\pm \to Z\ell \to \ell\ell\ell$. After reweighting the $\tilde{\chi}_1^\pm \tilde{\chi}_1^0$ events by a factor of 1/3, both sets of signal samples are weighted properly to test the equal branching fractions hypothesis. To obtain the expected signal yields for some other $\tilde{\chi}_1^\pm / \tilde{\chi}_1^0$ branching fraction hypothesis, each simulated signal event is further reweighted by the following factor:

$$\omega = 3^{(N_Z + N_W + N_H)} \mathcal{B}(Z)^{N_Z} \mathcal{B}(W)^{N_W} \mathcal{B}(H)^{N_H} \times 3^{(N_e + N_\mu + N_\tau)} \mathcal{B}(e)^{N_e} \mathcal{B}(\mu)^{N_\mu} \mathcal{B}(\tau)^{N_\tau}, \qquad (5.3)$$

where N_e, for example, is the number of electrons produced directly from a $\tilde{\chi}_1^\pm / \tilde{\chi}_1^0$ decay vertex at truth-level.[25]

For example, consider a simulated $\tilde{\chi}_1^\pm \tilde{\chi}_1^0$ event that decays via $\tilde{\chi}_1^\pm \tilde{\chi}_1^0 \to Z e W \mu$ at truth-level. This event will be reweighted by

$$\omega = 3^{(1+1+0)} \mathcal{B}(Z)^1 \mathcal{B}(W)^1 \mathcal{B}(H)^0 \times 3^{(1+1+0)} \mathcal{B}(e)^1 \mathcal{B}(\mu)^1 \mathcal{B}(\tau)^0. \qquad (5.4)$$

As a sanity check, one can choose equal branching fractions to each lepton and boson. This results in $\omega = 1$, as expected, since these samples are already weighted for equal branching fractions. However, when testing signal hypotheses with $\mathcal{B}(H)$ or $\mathcal{B}(\tau)$ approaching 100%, this particular event will be weighted to zero.

Alongside SR3ℓ, SR4ℓ, and SRFR, two additional sets of signal regions are defined with identical selections except the chosen *direct* leptons are required to be either electrons (SR3ℓ_e, SR4ℓ_e, SRFR$_e$) or muons (SR3ℓ_μ, SR4ℓ_μ, SRFR$_\mu$). In SR3ℓ and SR4ℓ, the direct lepton is the one paired with the Z boson to reconstruct the $\tilde{\chi}_1^\pm \to Z\ell \to \ell\ell\ell$ decay. As the fourth lepton in SR4ℓ may or may not be produced directly from the second $\tilde{\chi}_1^\pm / \tilde{\chi}_1^0$ decay, it is not subjected to the flavor requirement. In SRFR, both leptons that are paired with bosons to reconstruct $\tilde{\chi}_1^\pm / \tilde{\chi}_1^0$ decays are considered *direct* and are subjected to the flavor requirements. These flavor-specific SRs are used when setting limits

---

[25]Note that this equation assumes that the $\tilde{\chi}_1^\pm$ and $\tilde{\chi}_1^0$ branching bractions are 100% correlated. While $(N_Z + N_W + N_H) = 2$ in all events, $(N_e + N_\mu + N_\tau)$ can vary depending on the number of $\tilde{\chi}_1^\pm / \tilde{\chi}_1^0$ decays to neutrinos.

on $\tilde{\chi}_1^\pm \tilde{\chi}_1^\mp + \tilde{\chi}_1^\pm \tilde{\chi}_1^0$ signals with 100% branching fractions to electrons or muons. When setting limits under the lepton universal or 100% tau assumptions, the nominal SRs are used. More information on the limit setting procedure is provided in Section 5.8.3.

Signal Region Shape-fit Details

To search for a trilepton mass resonance above a smoothly falling background, a shape-fit is performed in the three signal regions. The trilepton mass distributions are binned and fit simultaneously. If a $\tilde{\chi}_1^\pm \tilde{\chi}_1^\mp + \tilde{\chi}_1^\pm \tilde{\chi}_1^0$ signal exists with even a small branching fraction to Z bosons, a resonance should be seen near the same mass in all three signal regions.

Instead of using the trilepton mass directly, the shape-fit is performed in $m_{Z\ell}^{\mathrm{shifted}}$, defined as:

$$m_{Z\ell}^{\mathrm{shifted}} = m_{Z\ell} - m_{\ell\ell} + 91.2 \text{ GeV}, \tag{5.5}$$

where $m_{Z\ell}$ is the reconstructed $\tilde{\chi}_1^\pm$ mass, and $m_{\ell\ell}$ is the reconstructed Z mass. Subtracting $m_{\ell\ell}$ from $m_{Z\ell}$ cancels resolution effects, resulting in narrower signal resonances, while adding the true Z mass re-centers the variable at the $\tilde{\chi}_1^\pm$ mass. The binning of the $m_{Z\ell}^{\mathrm{shifted}}$ distributions in the signal regions is given in Table 5.6. This binning is chosen to maximize the sensitivity while maintaining sufficient background statistics and computation feasibility. The increasing bin widths at higher mass reflect both the decrease in background statistics and the increase in the signal width due to resolution effects. The full details of the statistical interpretation, including the likelihood definition, fitting procedure, and hypothesis testing are presented in Sections 5.7 and 5.8. For the sake of notational simplicity, $m_{Z\ell}$ will always refer to $m_{Z\ell}^{\mathrm{shifted}}$ unless otherwise stated.

Bin Width [GeV]	$m_{Z\ell}^{\mathrm{shifted}}$ Range [GeV]
20	[90, 270)
30	[270, 360)
40	[360, 440)
140	[440, 580)
inclusive	[580, ∞)

Table 5.6: The binning used for the shape-fit of the signal region $m_{Z\ell}^{\mathrm{shifted}}$ distributions.

Suppressing Combinatorial Standard Model Backgrounds

While no Standard Model particle resonantly decays to three leptons, various background processes can produce events capable of passing the signal region criteria described above. To mitigate such

processes entering the signal regions, additional requirements are placed on the event kinematics and object multiplicities.

The ZZ process can enter either SR4ℓ or SRFR if both bosons decay leptonically. In the latter case, two jets from initial state radiation or pileup must coincidentally form a dijet pair with an invariant mass in the boson mass window. To reject this background, both signal regions veto events containing exactly four leptons that form two SFOS pairs if the mass of the second pair satisfies $|m_{\ell\ell,2} - m_Z| < 20$ GeV. To further reduce the ZZ background in SR4ℓ, which targets signal events where the second $\tilde{\chi}_1^\pm / \tilde{\chi}_1^0$ decay includes neutrinos, events with a second pair of same-flavor leptons must satisfy $E_{\mathrm{T}}^{\mathrm{miss}} > 80$ GeV.

The $t\bar{t}Z$ process can enter all three signal regions, depending on the decays of the two top quarks. If both decay leptonically, the event may enter either SR4ℓ or SRFR. The latter case requires a pair of jets that accidentally reconstructs a second boson. This is not uncommon in leptonic $t\bar{t}Z$ events, as the two b-quark initiated jets are usually tagged. Consequently, the relaxed dijet mass requirement of $71.2 < m_{jj} < 150$ GeV is applied when attempting to reconstruct a second boson. If only one top quark decays leptonically, the event can only enter SR3ℓ (barring any fake or non-prompt leptons).

The presence of well-separated b-tagged jets in $t\bar{t}Z$ events provides a handle for managing the background. While signal events may contain $Z/H \to bb$ decays, the two b-jets are often collimated due to the boost of the boson. Therefore, to reject $t\bar{t}Z$ events, all three signal regions veto events with at least two b-jets that satisfy $\Delta R(b_1, b_2) > 1.5$.

To further reduce the background from ZZ, $t\bar{t}Z$, and other rarer processes, SRFR again exploits the mass degeneracy of the $\tilde{\chi}_1^\pm \tilde{\chi}_1^\mp / \tilde{\chi}_1^\pm \tilde{\chi}_1^0$ pair. If reconstructed properly, the mass asymmetry between the two $\tilde{\chi}_1^\pm / \tilde{\chi}_1^0$ decay chains should be small. By requiring $m_{Z\ell}^{\mathrm{asym}} < 0.1$, the more evenly distributed combinatorial background is effectively rejected.

The WZ process is the dominant background in SR3ℓ, which targets signal events where the second $\tilde{\chi}_1^\pm / \tilde{\chi}_1^0$ decay provides no additional leptons. Both the signal and WZ background events contain three leptons and at least one neutrino, with two of the leptons originating from a Z boson. Despite the similar lepton and neutrino multiplicities, the kinematics of the two samples differ. In WZ events, the third lepton and neutrino are produced resonantly from the W boson decay. Using $\boldsymbol{p}_{\mathrm{T}}^{\mathrm{miss}}$ as a proxy for the neutrino momentum, the transverse mass of the W boson can be reconstructed from the third lepton $\boldsymbol{p}_{\mathrm{T}}$ and $\boldsymbol{p}_{\mathrm{T}}^{\mathrm{miss}}$ as:

$$m_{\mathrm{T}} = \sqrt{2p_{\mathrm{T}} E_{\mathrm{T}}^{\mathrm{miss}}(1 - \cos(\Delta\phi))}, \tag{5.6}$$

where $\Delta\phi$ is the azimuthal separation between the third lepton $\boldsymbol{p}_{\mathrm{T}}$ and $\boldsymbol{p}_{\mathrm{T}}^{\mathrm{miss}}$. While the WZ

m_{T} distribution has a kinematic edge at the W mass, the signal m_{T} distribution has no such feature, since the third lepton and neutrino are produced non-resonantly from separate $\tilde{\chi}_1^\pm/\tilde{\chi}_1^0$ decays.[26] By cutting on m_{T}, the WZ background can be effectively rejected.

When all three leptons are of the same flavor, there are two possible SFOS pairs that can be considered when reconstructing the Z decay. Choosing the pair that minimizes $|m_{\ell\ell} - m_Z|$ has a very high efficiency in signal events ($> 95\%$) since the third lepton is produced directly from a $\tilde{\chi}_1^\pm$ decay and typically has a larger momentum. However, this method for determining the Z leptons is less efficient for the WZ background since the three leptons are of similar momenta. When the wrong two Z leptons are chosen, the third lepton and $\boldsymbol{p}_{\mathrm{T}}^{\mathrm{miss}}$ will not correctly reconstruct the W, and the resulting m_{T} value may exceed m_W. Consequently, better WZ background rejection is achieved by cutting on the minimum m_{T} of all lepton and $\boldsymbol{p}_{\mathrm{T}}^{\mathrm{miss}}$ pairings for which the remaining two leptons form a SFOS pair. Labeled $m_{\mathrm{T}}^{\mathrm{min}}$, all SR3$\ell$ events must satisfy $m_{\mathrm{T}}^{\mathrm{min}} > 125$ GeV. Finally, Standard Model backgrounds without neutrinos are suppressed in SR3ℓ by requiring $E_{\mathrm{T}}^{\mathrm{miss}} > 150$ GeV. This includes Z+jets events where a jet produces a *fake* or non-prompt lepton.

The full definitions of the signal regions and the other analysis regions are summarized in Section 5.5. The SR distributions of the important kinematic variables will be shown in Section 5.8. All cut values mentioned above were chosen to optimize the sensitivity to the $\tilde{\chi}_1^\pm\tilde{\chi}_1^\mp + \tilde{\chi}_1^\pm\tilde{\chi}_1^0$ signal. Occasionally, this required sacrificing some sensitivity to the low mass signals in favor of the intermediate and high mass signals, as the lower mass signals had sensitivity to spare due to their large production cross sections. The truth-level acceptances and reconstruction efficiencies are provided in Appendix D as a function of the $\tilde{\chi}_1^\pm/\tilde{\chi}_1^0$ mass and branching fractions to the leptons and bosons.

5.5 Background Estimation and Validation

Presented in this section are the methods used to estimate the various Standard Model backgrounds. The primary WZ, ZZ, and $t\bar{t}Z$ backgrounds are estimated via a semi-data-driven method, with control regions (CRs) defined for each by inverting a small number of SR requirements. Designed to be pure in the targeted background and high in statistics, these CRs can be fit simultaneously with the SRs to constrain the normalization and systematic uncertainties related to the dominant backgrounds. Validation regions (VRs) are defined in the intermediate phase space between the CRs and SRs, and are used to test the extrapolation over the inverted selections. The kinematic selections applied to each CR and VR are described in Section 5.5.1. The remaining prompt lepton

---

[26]Signal events in SR3ℓ may even contain multiple neutrinos contributing to $\boldsymbol{p}_{\mathrm{T}}^{\mathrm{miss}}$ (e.g. $\tilde{\chi}_1^\pm\tilde{\chi}_1^0 \to Z\ell Z\nu \to \ell\ell\ell\nu\nu\nu$).

backgrounds are minor, and their yields in the various analysis regions are taken directly from simulation. Finally, the background from *fake* and non-prompt leptons is estimated via the data-driven fake factor method, presented in Section 5.5.2. While this method requires an additional CR and VR, the CR is not included in the fit. More information on the fit procedure is provided in Sections 5.7 and 5.8.

Events in all analysis regions are required to contain at least three leptons, two of which form a SFOS pair satisfying $|m_{\ell\ell} - m_Z| < 10$ GeV. Additionally, an $m_{Z\ell} > 90$ GeV selection is applied in all regions, in line with the lowest probed $\tilde{\chi}_1^{\pm}/\tilde{\chi}_1^0$ mass of 100 GeV. This selection also mitigates $Z \to 4\ell$ events where one lepton may avoid reconstruction, which are difficult to estimate. While the SRs are binned in $m_{Z\ell}$, the CRs and VRs are defined inclusively, as this variable is well-modeled by the simulation. The selections used to define the CRs, VRs, and SRs are summarized in Table 5.7.

Table 5.7: Selection criteria for the various signal, control, and validation regions used in the analysis. All regions require a pair of leptons with the same flavor and opposite sign of their electric charge whose invariant mass is between 81.2 GeV and 101.2 GeV. Additionally, they require a third lepton and a trilepton invariant mass above 90 GeV. The 2nd boson requirement indicates the presence of two additional jets or leptons consistent with a W, Z, or Higgs boson decay. The asterisk (*) in the SR4ℓ $E_{\mathrm{T}}^{\mathrm{miss}}$ requirement indicates that this selection is only considered for events with two pairs of same-flavor leptons. The $\Delta R(b_1, b_2)$ selection is only considered for events with at least two b-jets.

Region	N_{lep}	$E_{\mathrm{T}}^{\mathrm{miss}}$ [GeV]	$m_{\mathrm{T}}^{\mathrm{min}}$ [GeV]	2nd boson	2nd leptonic Z; $|m_{\ell\ell,2} - m_Z|$ [GeV]	$N_{\mathrm{b\text{-}jet}}$	$\Delta R(b_1, b_2)$	$m_{Z\ell}^{\mathrm{asym}}$
SRFR	≥ 4	-	-	Yes	veto; <20	-	<1.5	<0.1
SR4ℓ	≥ 4	>80*	-	No	veto; <20	-	<1.5	-
CRZZ	=4	-	-	-	require; <5	-	<1.5	-
VRZZ	=4	-	-	-	require; [5,20]	-	<1.5	-
CR$t\bar{t}Z$	≥ 3	>40	-	-	veto; <20	≥ 2	>2.5	-
VR$t\bar{t}Z$	≥ 3	>40	-	-	veto; <20	≥ 2	[1.5,2.5]	-
SR3ℓ	=3	>150	>125	-	-	-	<1.5	-
CRWZ	=3	<80	[50,100]	-	-	-	<1.5	-
VR$E_{\mathrm{T}}^{\mathrm{miss}}$	=3	>80	<100	-	-	-	<1.5	-
VR$m_{\mathrm{T}}^{\mathrm{min}}$	=3	<80	>125	-	-	-	<1.5	-
CRFake	=3	<30	<30	-	-	-	<1.5	-
VRFake	=3	[30,80]	<30	-	-	-	<1.5	-

5.5.1 Primary Prompt Backgrounds

Control and validation regions are defined to estimate the primary WZ, ZZ, and $t\bar{t}Z$ backgrounds. The remaining prompt backgrounds, including the Higgs, triboson, tWZ, $t\bar{t}W$, and tZ processes, are minor and estimated directly from simulation.

The dominant background in SR3ℓ is the WZ process. As explained in Section 5.4, the $m_T^{\min}$ distribution of the WZ background has a kinematic edge at the W mass, while the signal distribution is smooth. Additionally, both the E_T^{miss} and $m_T^{\min}$ distributions are softer in WZ events, especially compared to the higher $\tilde{\chi}_1^\pm/\tilde{\chi}_1^0$ mass signals. To define CRWZ, the E_T^{miss} and $m_T^{\min}$ requirements of SR3ℓ are inverted. By requiring $E_T^{\mathrm{miss}} < 80$ GeV and $50 < m_T^{\min} < 100$ GeV, the WZ process is enhanced while the signal contamination is minimized. Two validation regions, VRE_T^{miss} and VR$m_T^{\min}$, are defined between CRWZ and SR3ℓ to test the extrapolation over the two variables.

The contamination in CRWZ from possible low mass $\tilde{\chi}_1^\pm \tilde{\chi}_1^\mp + \tilde{\chi}_1^\pm \tilde{\chi}_1^0$ signals is large, which can inflate the WZ normalization factor obtained from a background-only fit should the signal exist. Consequently, the post-fit WZ background would be over-estimated in the signal regions, reducing the sensitivity to the signal. However, the production cross-sections are so large for the low mass signals that this slight decrease in sensitivity is acceptable. Expressed as a percentage of the expected total background yield before the fit, the signal contamination from $\tilde{\chi}_1^\pm \tilde{\chi}_1^\mp + \tilde{\chi}_1^\pm \tilde{\chi}_1^0$ signals with democratic branching fractions starts at about 25% for $m_{\tilde{\chi}_1} = 100$ GeV, dropping rapidly to 13% for $m_{\tilde{\chi}_1} = 150$ GeV, 4% for $m_{\tilde{\chi}_1} = 200$ GeV, and 0.5% for $m_{\tilde{\chi}_1} = 300$ GeV.

The ZZ process is an important background in both SR4ℓ and SRFR. CRZZ is defined by requiring exactly four leptons with a second SFOS pair satisfying $|m_{\ell\ell,2} - m_Z| < 5$ GeV. While extremely pure in ZZ events, CRZZ also has significant contamination from low mass signals. However, the contamination drops rapidly from 40% to just 2% between $m_{\tilde{\chi}_1} = 100$ and 200 GeV. VRZZ is then defined by loosening this second Z boson mass window to $5 < |m_{\ell\ell,2} - m_Z| < 20$ GeV, falling between the CRZZ requirement and the $m_{\ell\ell,2}$ vetoes of SR4ℓ and SRFR.

Finally, the $t\bar{t}Z$ background is significant in SR4ℓ and SRFR, and is often characterized by two well-separated b-jets. While the signal may produce two b-jets via $Z/H \to bb$ decays, the two jets tend to be collimated due to the boost of the boson. CR$t\bar{t}Z$ and VR$t\bar{t}Z$ are therefore defined by requiring at least three leptons and two $b-$tagged jets satisfying $\Delta R(b_1, b_2) > 2.5$ and $1.5 < \Delta R(b_1, b_2) < 2.5$, respectively. All other analysis regions veto events with two b-tagged jets with $\Delta R(b_1, b_2) > 1.5$ to reduce the $t\bar{t}Z$ contribution and to maintain orthogonality with CR$t\bar{t}Z$ and VR$t\bar{t}Z$. Lastly, to mitigate contamination from the Z+jets process, both regions require $E_T^{\mathrm{miss}} > 40$ GeV. The signal contamination peaks at about 15% for the $m_{\tilde{\chi}_1} = 200$ GeV signal point, decreasing to just 3% for $m_{\tilde{\chi}_1} = 300$ GeV.

A background-only fit to the observed data in the CRs and SRs is performed to evaluate the background modeling.[27] In the fit, the normalization factors for the WZ, ZZ, and $t\bar{t}Z$ processes

---

[27]When designing the analysis, only the CRs were used in the fit since the SRs were blinded.

Background	NF
WZ	1.03 ± 0.01
ZZ	1.12 ± 0.03
$t\bar{t}Z$	1.05 ± 0.11

Table 5.8: Normalization factors after a background-only fit to the observed data in the CRs & SRs.

are allowed to float, and are mostly constrained by the CRs due to their high statistics and purity for the targeted process. The post-fit normalization factors are summarized in Table 5.8. The post-fit CR and VR distributions for all variables relevant in the extrapolation to the SRs are shown in Figure 5.3. The $m_{Z\ell}$ distributions in each CR and VR are shown in Figures 5.4 and 5.5, respectively. No significant shape disagreement is seen in the $m_{Z\ell}$ distributions, justifying the choice to normalize the primary backgrounds inclusively in $m_{Z\ell}$ to benefit from the improved statistics.
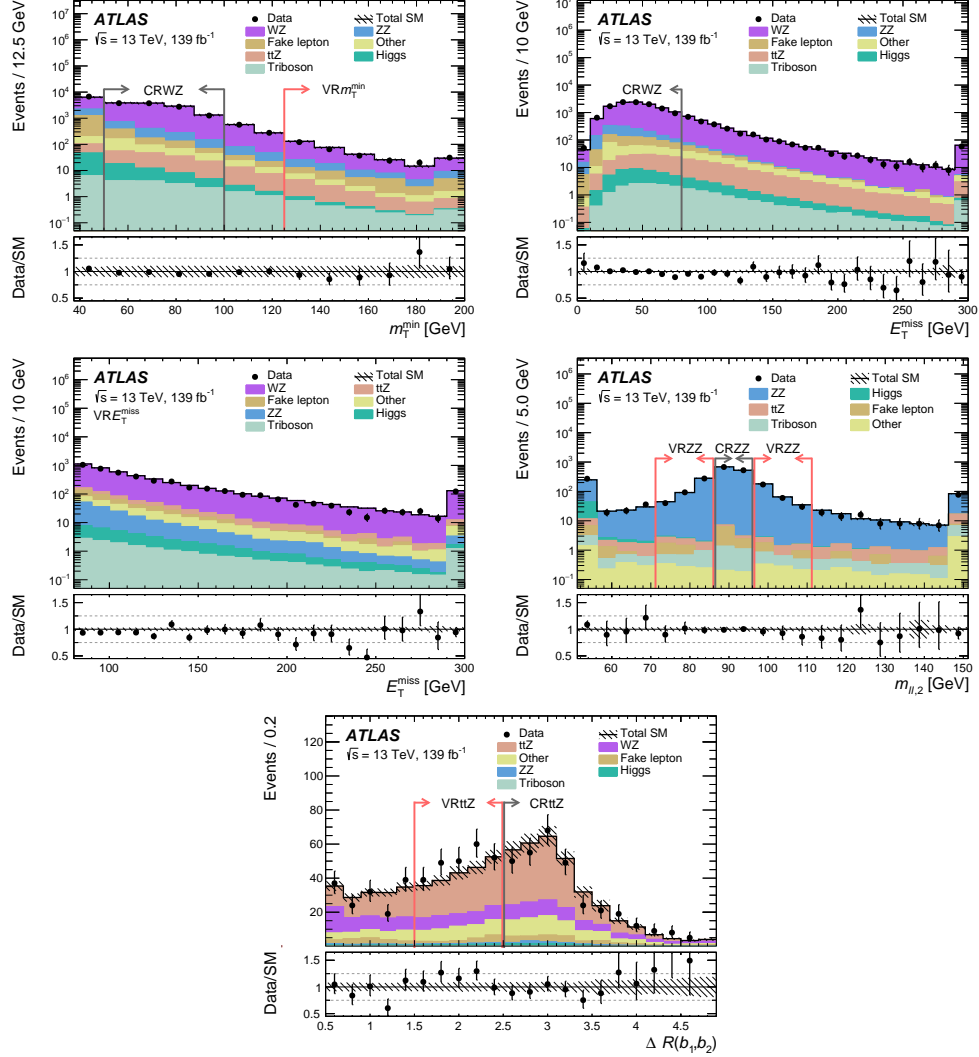
Figure 5.3: Distributions of the data and post-fit background in the CRs and VRs that are relevant in the extrapolation to the SRs, including (top left) $m_\mathrm{T}^\mathrm{min}$ in CRWZ and VR$m_\mathrm{T}^\mathrm{min}$, (top right) $E_\mathrm{T}^\mathrm{miss}$ in CRWZ, (middle left) $E_\mathrm{T}^\mathrm{miss}$ in VR$E_\mathrm{T}^\mathrm{miss}$, (middle right), $m_{\ell\ell,2}$ in CRZZ and VRZZ, and (bottom) $\Delta R(b_1, b_2)$ in CR$t\bar{t}Z$ and VR$t\bar{t}Z$. Black (red) arrows indicate the CR (VR) selection on the variable shown, with all other region selections applied. The first (last) bin includes underflow (overflow) events. The "Other" category consists mostly of the tWZ, $t\bar{t}W$ and tZ processes. The hatched bands indicate the combined theoretical, experimental, and MC statistical uncertainties in the background prediction. The bottom panel shows the ratio of the data to the background prediction.
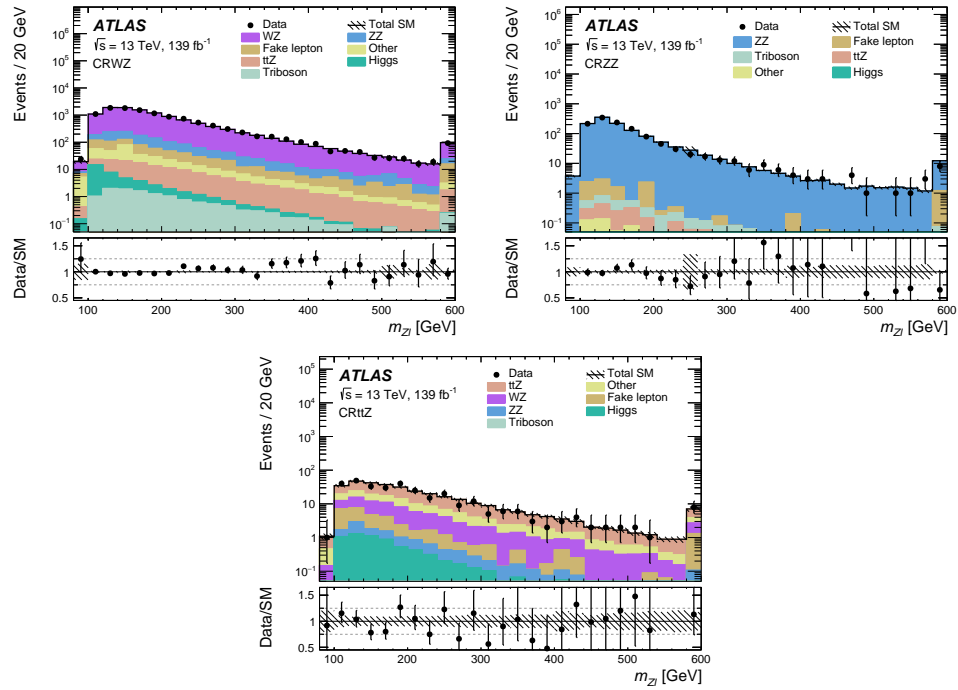
Figure 5.4: The $m_{Z\ell}$ distributions of the data and post-fit background in the CRWZ, CRZZ and CR$t\bar{t}Z$ regions, respectively. The first (last) bin includes underflow (overflow) events. The "Other" category consists mostly of the tWZ, $t\bar{t}W$ and tZ processes. The hatched bands indicate the combined theoretical, experimental, and MC statistical uncertainties in the background prediction. The bottom panel shows the ratio of the data to the background prediction.
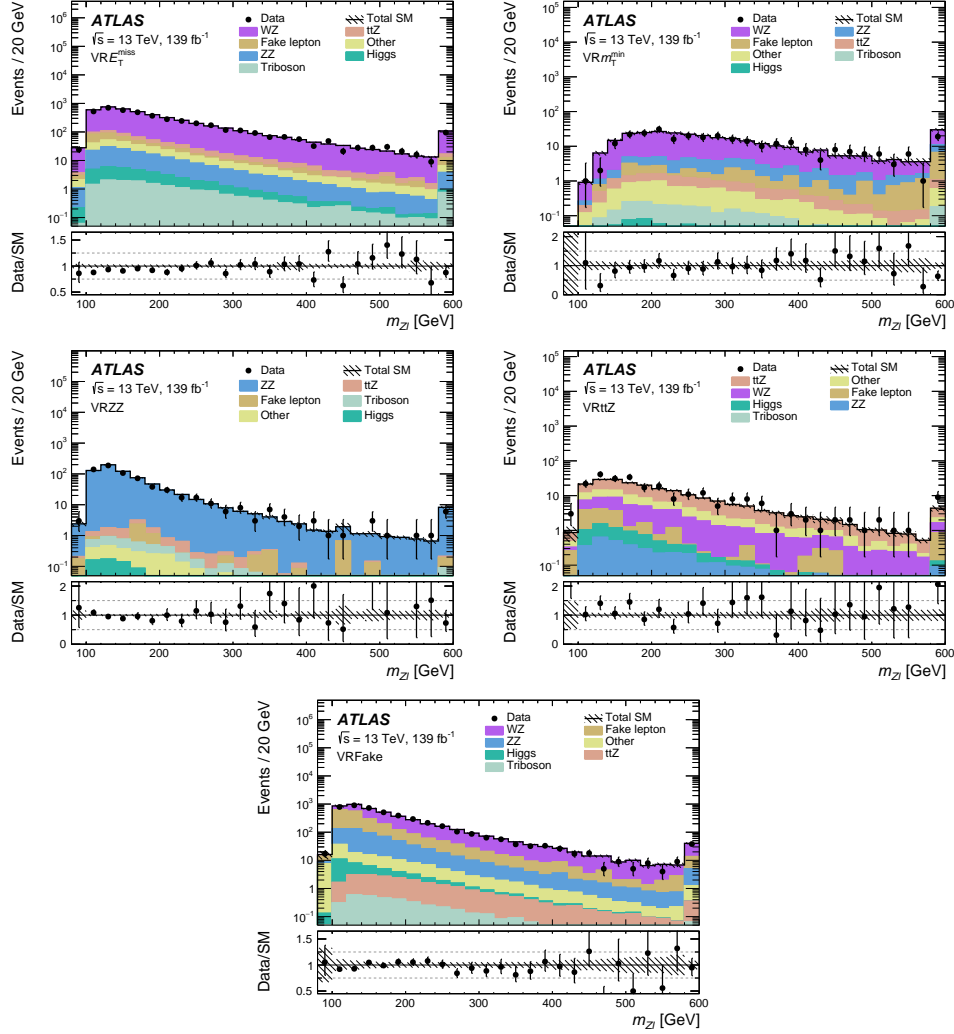
Figure 5.5: The $m_{\mathrm{Z}\ell}$ distributions of the data and post-fit background in the VR$E_{\mathrm{T}}^{\mathrm{miss}}$, VR$m_{\mathrm{T}}^{\mathrm{min}}$, VR$ZZ$, VR$t\bar{t}Z$ and VRFake regions, respectively. The first (last) bin includes underflow (overflow) events. The "Other" category consists mostly of the tWZ, $t\bar{t}W$ and tZ processes. The hatched bands indicate the combined theoretical, experimental, and MC statistical uncertainties in the background prediction. The bottom panel shows the ratio of the data to the background prediction.

A summary of the observed data and expected background estimates in each CR and VR is shown in Figure 5.6. The background estimates shown here are pre-fit for the CRs and post-fit for the VRs. In the bottom panel, the pre-fit relative difference between the data and expected background yields are shown for each CR, and the post-fit significances are shown for each VR. A nearly 2σ overestimate is seen in VR$E_{\mathrm{T}}^{\mathrm{miss}}$, however, no major mismodeling is observed in the shapes of the $m_{\mathrm{Z}\ell}$ (Figure 5.5) or $E_{\mathrm{T}}^{\mathrm{miss}}$ (Figure 5.3) distributions in the region. In VR$t\bar{t}Z$, a 1.5σ excess is observed. Again, no feature is seen in the $m_{\mathrm{Z}\ell}$ distribution (Figure 5.5). Additionally, decent agreement is seen in the $\Delta R(b_1, b_2)$ distribution (Figure 5.3) on either side of VR$t\bar{t}Z$, which is defined over $1.5 < \Delta R(b_1, b_2) < 2.5$.
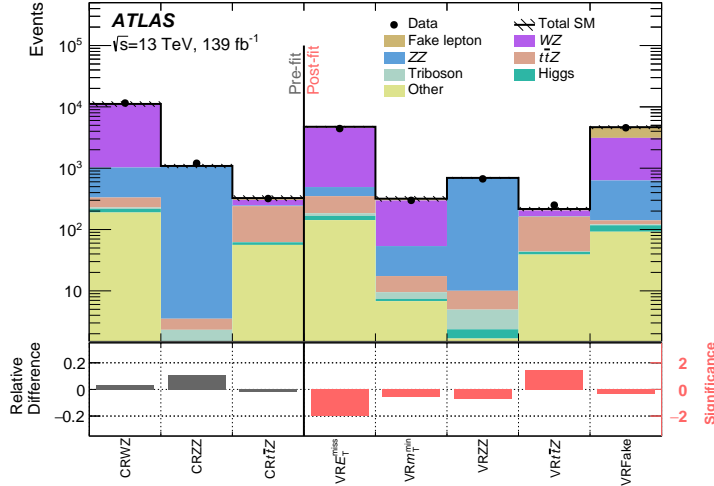
Figure 5.6: The observed data and the SM background expectation in the CRs (pre-fit) and VRs (post-fit). The bottom panel shows the fractional difference between the observed data and expected yields for the CRs and the significance of the difference for the VRs, calculated following the recommendation [198].

5.5.2 Fake & Non-Prompt Background

Fake and non-prompt leptons are the result of misidentified light flavor (LF) jets, semi-leptonic decays of heavy flavor (HF) hadrons, and photon conversions. While the non-prompt leptons from heavy flavor decays and photon conversions are real, all three sources are collectively labeled *fake* and estimated via the data-driven fake factor method.

The processes contributing to the fake background vary significantly between the various analysis regions. Some processes that are almost entirely prompt backgrounds in the $3l$ regions contribute

to the fake background in the $4l$ regions (e.g. WZ). The relative contributions of each process to the total fake background in the various analysis regions is shown in Table 5.9. Also shown is the fake background as a percent of the total background. These percentages are measured in MC simulation.

fake process	CRWZ	VR$E_\mathrm{T}^\mathrm{miss}$	VR$m_\mathrm{T}^\mathrm{min}$	CR$t\bar{t}Z$	VR$t\bar{t}Z$	SR3ℓ	SR4ℓ	SRFR
Z+jets/$Z+\gamma$	74%	47%	63%	37%	23%	41%	22%	5%
WZ	-	-	-	-	-	-	45%	21%
ZZ	-	-	-	-	-	-	15%	19%
$t\bar{t}Z$	-	-	-	-	-	-	-	40%
top-like	20%	43%	28%	54%	69%	48%	3%	10%
tot. fake / tot. bkgd	4%	5%	8%	12%	11%	7%	5%	2%

Table 5.9: The relative contributions of each process to the fake and total background in the various analysis regions. The "top-like" background includes $t\bar{t}$, single top, and WW. The ZZ regions are very pure in real ZZ events and are not included in the table.

Fake Factor Method

The data-driven fake factor method is used to estimate the fake and non-prompt lepton background, as the rate at which these leptons pass the signal requirements is not modeled well by the simulation. In addition to the signal (aka *tight* or *ID*) leptons defined in Section 5.3, the fake factor method uses a second, disjoint set of leptons referred to as *anti-ID* (or *loose*) leptons. These anti-ID leptons are required to pass the baseline lepton requirements and overlap removal, but fail at least one signal lepton requirement. Consequently, the anti-ID leptons are enriched in fakes. The anti-ID electron and muon requirements are summarized in Table 5.10.

Electrons	Muons
fail `MediumLLH` identification	-
–or– $|d_0$-significance$| > 5$	$|d_0$-significance$| > 3$
–or– fail `FCTight` isolation	–or– fail `FCTight_FixedRad` isolation

Table 5.10: Anti-ID electron and muon definitions used for the fake estimate. These leptons must pass the baseline requirements and overlap removal. However, by satisfying one of the conditions listed in the table, they must fail at least one signal requirement.

The fake factor F is defined as the ratio of signal to anti-ID leptons, as measured in data in a kinematic region enriched in fake leptons. Typically, the fake factor is binned in some kinematic

variable(s), as the probability of a fake lepton passing the signal criteria is kinematic-dependent. Ideally, the composition of the fake leptons in this region matches the other analysis regions in both process (e.g. Z+jets vs. top-like) and source (HF vs. LF vs. conversions). Alternatively, the fake factors can be binned in some variable that provides a handle on the composition (e.g. $N_{\text{b-jets}}$), or the signal and anti-ID definitions can be tuned such that the fake factors are robust against composition changes (i.e. the LF, HF, and conversion fake factors are the same). Any contamination from events with only real leptons is removed using MC, thus ensuring only fake leptons are considered in the measurement of the fake factors. The fake factors are of the form:

$$F(i) = \frac{N_{\text{ID, data}}(i) - N_{\text{ID, prompt MC}}(i)}{N_{\text{anti-ID, data}}(i) - N_{\text{anti-ID, prompt MC}}(i)} \tag{5.7}$$

where N is the number of events and i refers to the ith bin.

Once measured, the fake factors can be used to estimate the fake background in the various analysis regions. For each region, a corresponding anti-ID region is defined with identical requirements, except at least one signal lepton is replaced with an anti-ID lepton. For the 3ℓ regions, the number of events with at least one fake lepton can then be estimated with the following equation:

$$N_{\text{TTT}}^{\text{Fake}} = N_{\text{TTT}} - N_{\text{TTT}}^{\text{RRR}} = F_1(N_{\text{LTT}} - N_{\text{LTT}}^{\text{RRR}}) + F_2(N_{\text{TLT}} - N_{\text{TLT}}^{\text{RRR}}) + F_3(N_{\text{TTL}} - N_{\text{TTL}}^{\text{RRR}})$$
$$-F_1 F_2(N_{\text{LLT}} - N_{\text{LLT}}^{\text{RRR}}) - F_1 F_3(N_{\text{LTL}} - N_{\text{LTL}}^{\text{RRR}}) - F_2 F_3(N_{\text{TLL}} - N_{\text{TLL}}^{\text{RRR}}) \tag{5.8}$$
$$+F_1 F_2 F_3(N_{\text{LLL}} - N_{\text{LLL}}^{\text{RRR}})$$

where "RRR" denotes events with three real leptons, and F_i is the fake factor for the ith lepton. N_{LTT}, N_{LLT}, and N_{LLL} (plus all permutations) are measured in data, and their "RRR" analogs are determined from MC. While this equation holds for regions with exactly three leptons, analogous equations can be found for any number of leptons.

Measuring Fake Factors

The fake factors for this analysis are derived in a region dominated by Z+jets events with fake leptons. Events in this region must contain exactly three baseline leptons. Two of these leptons, known as the *tag* leptons, must also pass the signal lepton requirements and together form a Z boson candidate (SFOS pair with $|m_{ll} - m_Z| < 10$ GeV). Additionally, one of the two tag leptons must also fire a single lepton trigger and pass its associated offline p_{T} cut, as described in Section 5.3. The remaining baseline lepton, known as the *probe* lepton, is used for the fake factor measurement.

To increase the Z+jets purity and reduce prompt contamination (mostly WZ), the fake factor measurement region CRFake is defined with $m_T^{\min} < 30$ GeV and $E_T^{\text{miss}} < 30$ GeV. To reduce the number of $Z \to 4l$ events (with one lost lepton), events must satisfy $m_{Z\ell} > 105$ GeV. All selections used to define CRFake are summarized in Table 5.11.

Three baseline leptons
SFOS pair of signal leptons with $\lvert m_{ll} - m_Z \rvert < 10$ GeV, one of which fires a single lepton trigger and passes its associated offline p_T cut.
$m_T^{\min} < 30$ GeV
$E_T^{\text{miss}} < 30$ GeV
$m_{Z\ell} > 105$ GeV

Table 5.11: Selection criteria used to define the Z+jets dominated fake factor measurement region, CRFake.

While the processes contributing to the fake background vary significantly across the analysis regions, the Z+jets fake factors will be used to estimate fakes from all processes. Consequently, the chosen fake factor parameterization must be reasonable for all processes. Any residual differences or non-closure will be covered by systematic uncertainties.

After studying multiple possible fake factor parameterizations, p_T^{cone} was chosen. Defined as:

$$p_T^{\text{cone}} = p_T + p_T^{\text{iso}}, \tag{5.9}$$

p_T^{cone} includes the scalar p_T-sum of all tracks in the lepton's track-based isolation cone (p_T^{iso}), which varies in radius as described in Section 5.3. In general, p_T^{cone} provides a better handle on the momentum of the underlying jet giving rise to the fake/non-prompt lepton. Fake leptons passing the signal requirements tend to carry a larger fraction of the underlying jet momentum than those that fail, particularly due to the isolation requirement. As a result, when the fake factors are binned in p_T, a signal and an anti-ID lepton falling in the same bin may originate from jets with significantly different momenta. By including the isolation cone momentum, p_T^{cone} helps correct for this. While the effect of adding the cone is negligible for the well isolated signal leptons, it significantly increases the momenta of the anti-ID leptons. By binning in p_T^{cone} instead, signal and anti-ID fake leptons falling in the same bin originate from more similarly boosted jets. More pragmatically, these fake factors provided the best agreement between the expected background and observed data in the fake factor validation region and other analysis regions.

The p_T^{cone}-binned fake factors measured in CRFake are shown in Figure 5.7. These fake factors are used for all fake estimates in this analysis. The fake factors are cutoff at 100 (50) GeV for

electrons (muons) due to a lack of statistics above these values. Events with anti-ID leptons above the cutoff have the fake factor from the highest bin applied. The data and MC fake factors are not necessarily expected to agree, since the processes giving rise to fake leptons are not well-modeled by the MC. Alternative parameterizations of the fake factors can be found in Appendix B.1.
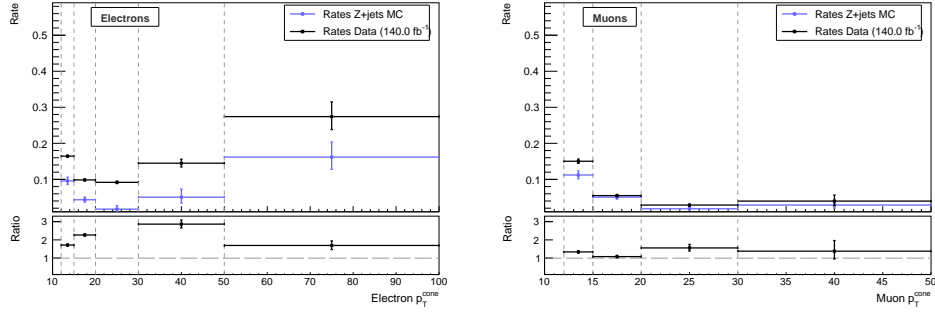
Figure 5.7: Data and Z+jets MC fake factors for electrons (left) and muons (right), binned in $p_\mathrm{T}^\mathrm{cone}$.

Validating Fake Factors

The fake estimate is validated in an intermediate $E_\mathrm{T}^\mathrm{miss}$ region. The goal when designing this region was to move closer to the other analysis regions while maintaining Z+jets purity. The definition of the fake factor validation region, VRFake, is summarized in Table 5.12.

Various kinematic distributions in the validation region are shown in Fig. 5.8-5.12, with decent agreement seen in most distributions. Figures 5.8 and 5.9 show the kinematics of the lepton not assigned to the Z boson, which is most likely the fake in Z+jets events. The kinematics of the leading, subleading, and third leptons are shown in Figures 5.10 and 5.11, split by flavor. The object multiplicities and additional event-level distributions are shown in Figure 5.12 and 5.13, respectively. All distributions are shown before the background-only fit to the observed data in the CRs and SRs, and all uncertainties are statistical only.

Exactly three signal leptons, no additional leptons
SFOS pair of signal leptons with $|m_{ll} - m_Z| < 10$ GeV, $m_\mathrm{T}^\mathrm{min} < 30$ GeV
$30 < E_\mathrm{T}^\mathrm{miss} < 80$ GeV

Table 5.12: Selection criteria used to define the Z+jets fake factor validation region, VRFake.

To better understand any discrepancies between the data and the estimated background in the validation region, the fake factors were measured in the VRFake. These are shown and discussed in Appendix B.2. In general, the fake factors are lower in the validation region, suggesting that it is harder for a baseline lepton to pass the signal requirements. This is consistent with the slight over-prediction of the background in the validation region seen in Figures 5.8-5.12. A systematic uncertainty is assessed to cover this non-closure in VRFake.
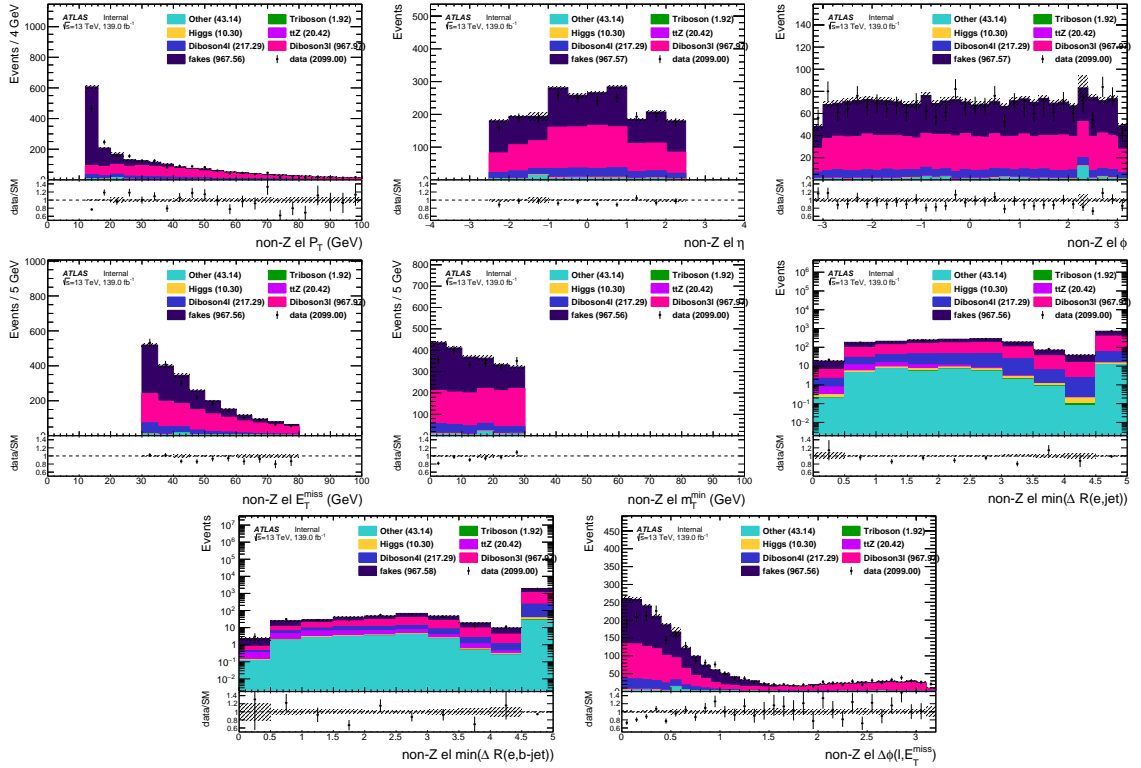
Figure 5.8: Various kinematic distributions in the fake factor validation region when the non-Z lepton is an electron. This lepton is most likely the fake in the Z+jets events. In the $\min\Delta R(e, \text{jet})$ and $\min\Delta R(e, b\text{-jet})$ distributions, events without a (b-tagged) jet are added to the overflow. All uncertainties shown are statistical only.
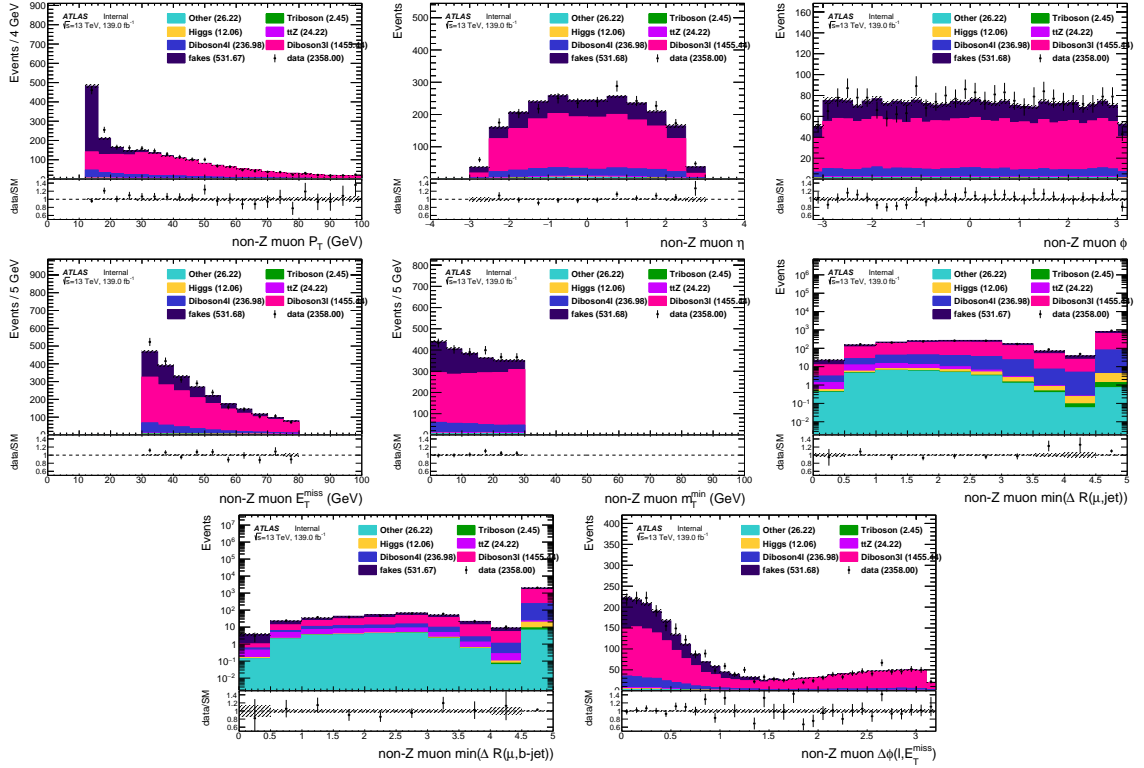
Figure 5.9: Various kinematic distributions in the fake factor validation region when the non-Z lepton is a muon. This lepton is most likely the fake in the Z+jets events. In the min$\Delta R(\mu, \mathrm{jet})$ and min$\Delta R(\mu, b\text{-jet})$ distributions, events without a (b-tagged) jet are added to the overflow. All uncertainties shown are statistical only.
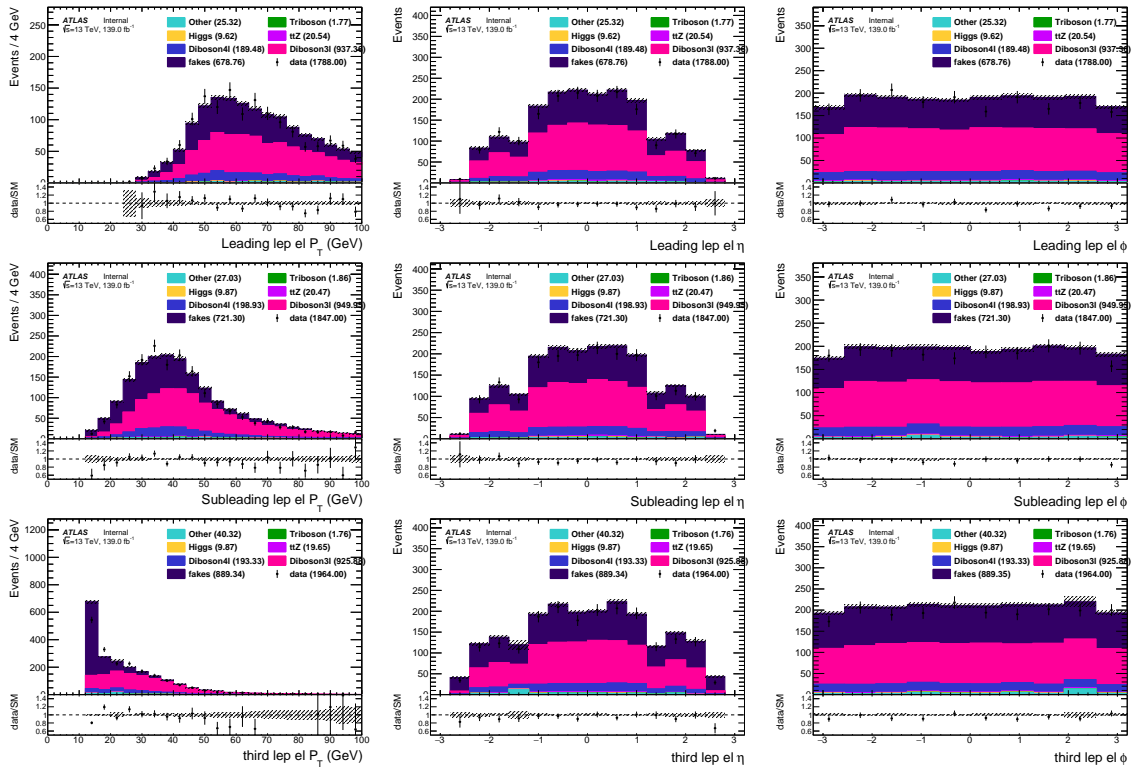
Figure 5.10: The p_T, η, and ϕ distributions of the leading, subleading, and third leptons in VRFake when they are electrons. All uncertainties shown are statistical only.
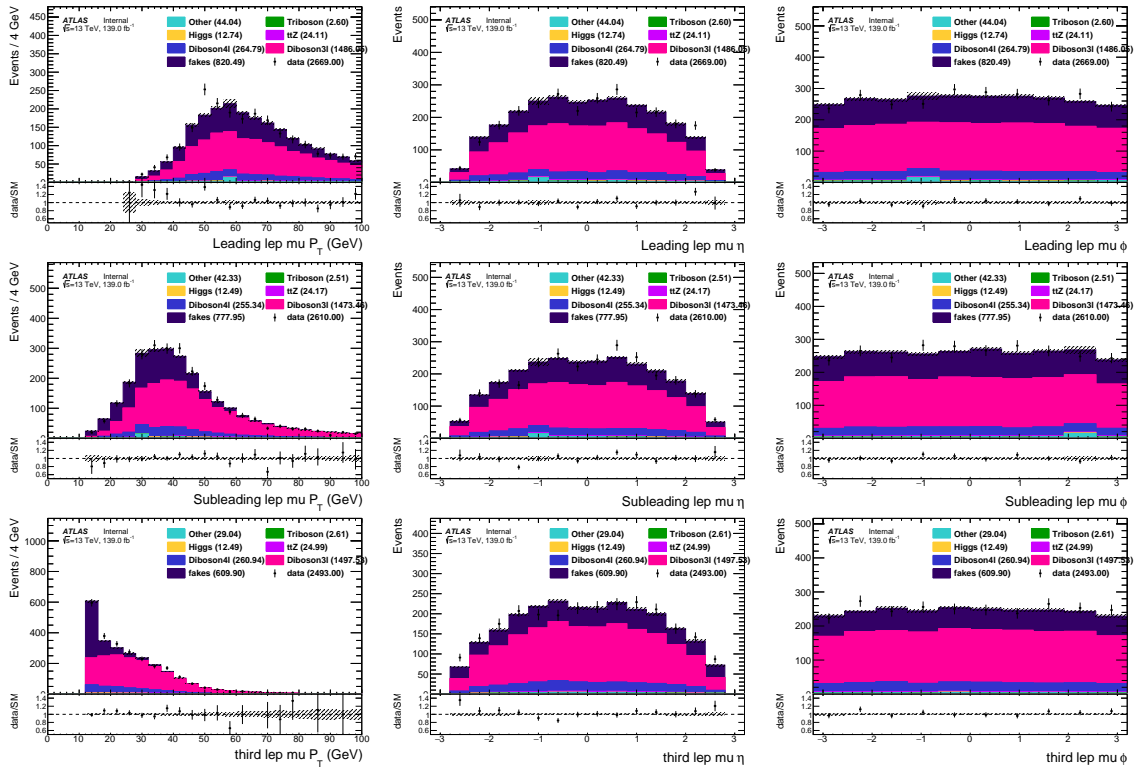
Figure 5.11: The p_T, η, and ϕ distributions of the leading, subleading, and third leptons in VRFake when they are muons. All uncertainties shown are statistical only.
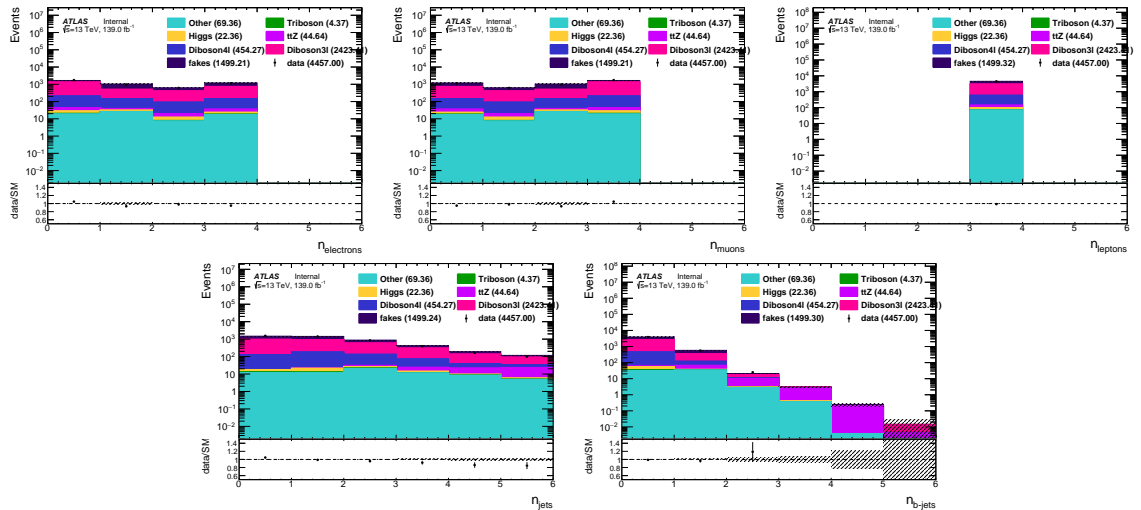
Figure 5.12: Object multiplicity distributions in the fake factor validation region. All uncertainties shown are statistical only.
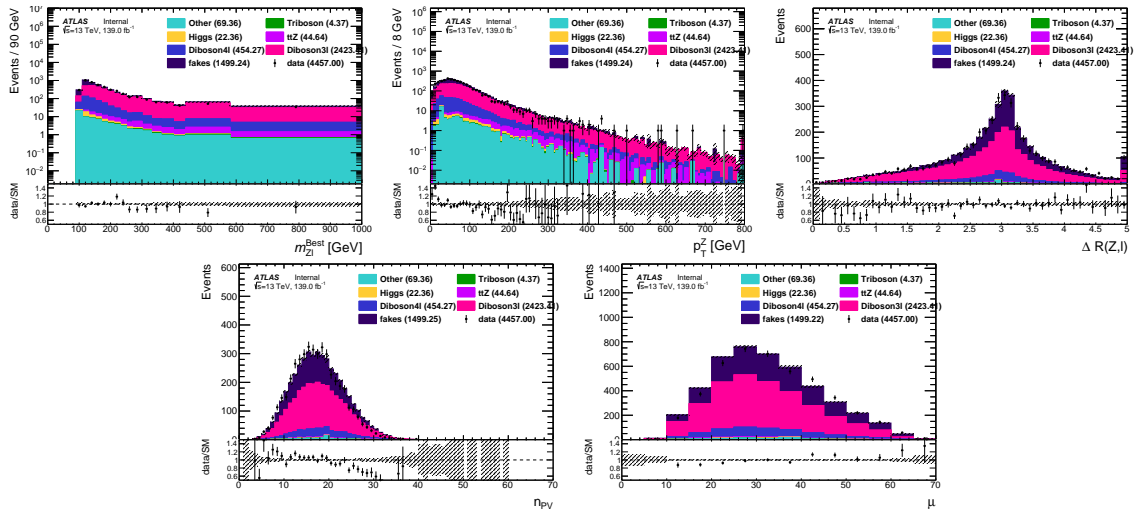
Figure 5.13: Additional distributions in the fake factor validation region. All uncertainties shown are statistical only.

5.6   Systematic Uncertainties

Systematic uncertainties on the signal and background estimates include those associated with the data-driven background estimation methods, as well as the statistical uncertainties from the simulated MC samples, experimental uncertainties on detector measurements, and theoretical uncertainties in the MC simulation. For each systematic effect, a parametric model is defined. The model and its parameters may be theoretical (e.g. a Lagrangian parameter like α_S), phenomenological (e.g. the factorization scale in a MC generator), empirical (e.g. the jet energy scale), or statistical (e.g. the Poisson error for some MC sample in some bin). These *nuisance parameters* are not of particular interest to the analysis, but they must be incorporated in the statistical model (see Section 5.7).

Many of the nuisance parameters are constrained by auxiliary measurements, which may be performed specifically for this analysis (e.g. fake systematics), by combined performance groups for general use on ATLAS (e.g. jet energy scale), or even by outside collaborations (e.g. parton distribution functions). These auxiliary measurements provide central values and some uncertainty band for the nuisance parameters, allowing their incorporation in the statistical model through constraint terms.[28] Each nuisance parameter is assumed to be independent and Gaussian distributed with a mean and width determined from an auxiliary measurement. Correlated uncertainties are described by the same nuisance parameter, while uncorrelated uncertainties are given separate nuisance parameters.

When propagating the systematic uncertainties to the signal and background estimates, each nuisance parameter is varied independently. The expected yields for all values of the nuisance parameters are then interpolated from the nominal estimate and the $\pm 1\sigma$ variations. While the nuisance parameters are assumed to be Gaussian (and therefore symmetrically) distributed about their means, the corresponding variations in the expected signal and background yields need not be. The systematic variations on the estimates are implemented either as additional event weights (when the same events are used in all variations) or alternative `ROOT` trees (when the events may vary).

The relative systematic uncertainties on the expected background yields in the signal regions are shown in Figure 5.14. The various sources of uncertainty are grouped into categories: *experimental*, *theoretical*, *fake lepton*, *MC statistics*, and *normalization*. The *MC statistics* category includes all uncertainties resulting from the finite statistics of the simulated samples used to estimate the

---

[28]Some parameters, like the factorization and renormalization scales, cannot be constrained by auxiliary measurements and are instead given *reasonable* uncertainties.

prompt backgrounds, while the *normalization* category includes the uncertainties related to the normalization procedure used to estimate the primary WZ, ZZ, and $t\bar{t}Z$ backgrounds. The remaining categories will be discuss in detail below.

The jagged bin-to-bin fluctuations in the total uncertainty are primarily driven by the systematic uncertainties associated with the fake estimate. As explained in the upcoming discussion, a conservative uncertainty is applied to any bin with no observed anti-ID events in data, resulting in large relative uncertainties in the more statistically-limited SR bins. In particular, the highest $m_{Z\ell}$ bin in SRFR has a 200% uncertainty on a total post-fit background expectation of about 0.1 event due to the fake systematics. However, the effect of a fluctuation in a particular SR bin is mitigated due to the complementary nature of the three SRs; all three SRs contribute to the signal sensitivity.
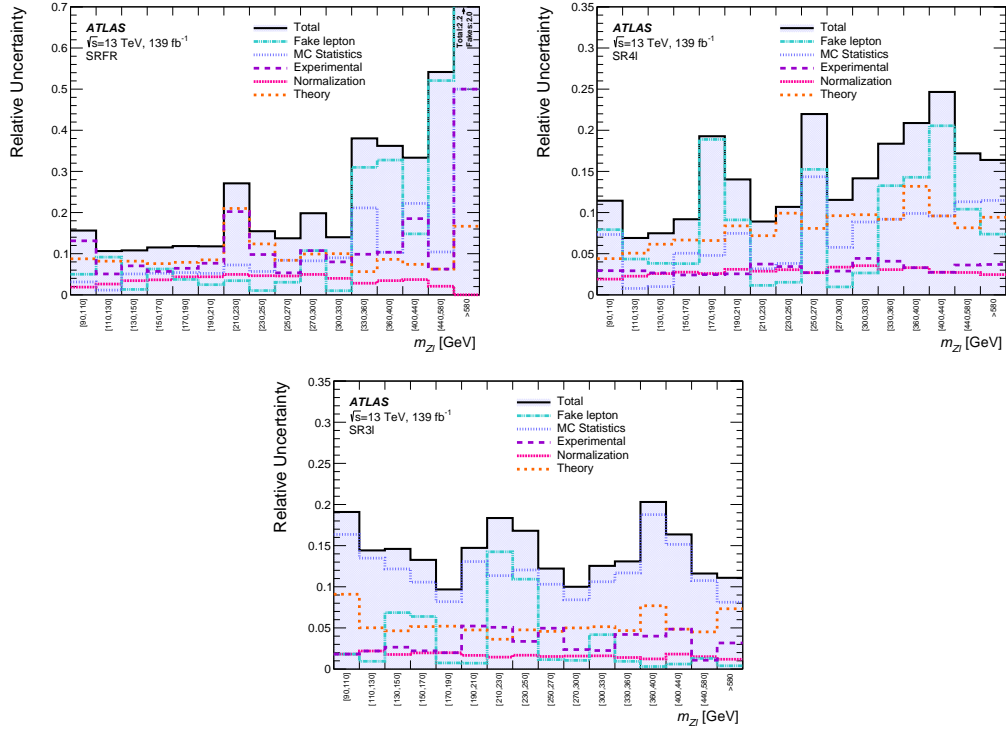
Figure 5.14: The relative uncertainties in the post-fit SM background prediction as a function of $m_{Z\ell}$ from the background-only fit for the (top left) SRFR, (top right) SR4ℓ, and (bottom) SR3ℓ regions. Sources of uncertainty are grouped into experimental, theoretical, and MC statistical categories. Separate categories are provided for the fake/non-prompt backgrounds and for the normalization procedure of the major WZ, ZZ, and $t\bar{t}Z$ backgrounds. The individual uncertainties can be correlated and do not necessarily contribute in quadrature to the total uncertainty.

Experimental Uncertainties

Included in the experimental uncertainties are those related to the limited precision of the detector, for example, the energy/momentum scales and resolutions of the leptons and jets. Varying these within their uncertainties will modify the event kinematics, and possibly the signal object and reconstructed boson multiplicities as well. Consequently, these variations may cause an event to migrate between analysis regions. The jet energy scale and resolution uncertainties [199, 200] in particular constitute a large fraction of the total experimental uncertainty. They are derived as a function of the jet p_T and η, while also accounting for the flavor and pileup dependence of the energy measurement. Similar scale and resolution uncertainties are included for electrons [201] and muons [191]. These per-object uncertainties are propagated through the E_T^{miss} calculation, with additional uncertainties accounting for the scale and resolution of the E_T^{miss} soft term [196].

Also included in the experimental uncertainties are those related to the MC simulation mismodeling electron [201] and muon [191] efficiencies for passing trigger, identification, reconstruction, and isolation requirements. They also include modeling uncertainties for the identification and rejection of pileup jets by the jet vertex tagger [192] and the identification of b-jets by the flavor-tagging algorithm [202]. Finally, there is a 1.7% experimental uncertainty on the total integrated luminosity, as measured primarily by the LUCID-2 detector [203]. The experimental uncertainties are fully correlated across the analysis regions.

Theoretical Uncertainties

Theoretical uncertainties account for potential mismodeling in both the shape and cross section of the simulated backgrounds. For the major diboson, triboson, and $t\bar{t}Z$ backgrounds, the shape uncertainties are derived using MC simulation with varied generator parameters. A 1% variation in the strong coupling constant, α_S, is propagated to the event yields, while uncertainties related to the choice of PDF sets, CT14NNLO [204] or MMHT2014NNLO [205], are derived by taking the envelope of 100 propagated uncertainties [173]. Uncertainties due to the choice of QCD renormalization and factorization scales [206] are assessed by varying the relevant generator parameters up and down by a factor of two around the nominal values, allowing for both independent and correlated variations of the two scales but prohibiting anti-correlated variations. Each QCD variation is kept separate and is treated as correlated across analysis regions. For the other minor backgrounds, a conservative 20% uncertainty is applied.

Additional sample-specific theoretical uncertainties are assessed for the primary WZ, ZZ, and

$t\bar{t}Z$ backgrounds. These are related to assumptions made in the event generators and parton shower (PS) models, which can affect both the event kinematics and the cross section of the physics process. For the WZ and ZZ backgrounds, the SHERPA parameters related to the PS matching scale and resummation scale are varied up and down by a factor of two around the nominal values, and an alternative recoil scheme is studied. For the $t\bar{t}Z$ background, the uncertainties in the hard scatter and in the PS are derived through a comparison with the SHERPA and MADGRAPH5_AMC@NLO +HERWIG7 predictions, respectively. Additional uncertainties in the amount of initial-state radiation (ISR) in the $t\bar{t}Z$ background are assessed by varying the related generator parameters.

Finally, theoretical uncertainties on the signal cross section are applied, ranging from 4.5% at 100 GeV to 16% at 1500 GeV. Uncertainties related to the QCD scale, PS matching scale, and amount of ISR are derived by varying the related generator parameters of the A14 tune [163].

Fake Background Uncertainties

The derivation of the systematic uncertainties related to the fake factor method are described in detail in Appendix C. These uncertainties are summarized in Table 5.13 and account for the following:

- Fake factor statistics:

  The statistical uncertainties on fake factors themselves are propagated to the fake estimates. A separate nuisance parameter is assigned to each fake factor bin, so events using the same (different) fake factors are correlated (uncorrelated) across all analysis regions.

- Magnitude of prompt subtraction:

  When deriving the fake factors in CRFake, any contamination from (real) prompt events must be subtracted using MC simulation. The magnitude of the prompt subtraction is varied by the cross-section uncertainty when deriving the fake factors. While the impact of this variation depends on which fake factor bin is used, the uncertainty is correlated across all fake events.

- Parametrization:

  While the fake factors are parameterized in $p_{\mathrm{T}}^{\mathrm{cone}}$, they may have a residual dependence on other kinematic variables, such as η or $N_{\text{b-jets}}$. Alternative fake estimates are derived using various 2D parameterizations and are treated as one-sided systematic variations.

- Composition:

  The composition of the fake lepton background varies in both process (e.g. Z+jets vs. $t\bar{t}$) and source (e.g. heavy flavor vs. light flavor). To account for this, region-specific MC fake factors

are derived by taking a weighted average of the heavy and light flavor fake factors, matching the composition of each region. It is assumed that the heavy and light flavor fake factors, when binned in p_T^{cone}, are process universal. The difference between the region-specific and nominal MC fake factors is applied as an uncertainty.

- Closure:

  The fake factor method may suffer from non-closure, mostly due to kinematic dependencies that are not covered by the nominal p_T^{cone} parameterization of the fake factors. A data-driven closure systematic is derived in the fake factor validation region, VRFake, by analyzing the data vs. background agreement, assuming all non-closure is due to error in the fake estimate.

An additional conservative systematic uncertainty is applied when the fake estimate in a signal region $m_{Z\ell}$ bin is negative. This can occur when the number of data events with anti-ID leptons is very low. More details on this systematic can be found in Appendix C.

Fake Systematic	Relative Weight	Comment
Statistical	3 - 31%	The statistical errors on the fake factors themselves. Events using the same (different) FFs are correlated (uncorrelated) across the analysis regions.
Prompt Subtraction	0.5 - 34%	The magnitude of the prompt subtraction is varied by 5% when deriving the FFs. Value depends on which FFs are used. Correlated across all fake factors and analysis regions.
Parameterization	0.1 - 35%	Derived alternative fake estimates using 2D fake factor parameterizations: p_T^{cone} vs. η and p_T^{cone} vs. $N_{\text{b-jets}}$. Applied as a one-sided systematic on the fake yields, and uncorrelated across analysis regions.
Composition	14-53%	Derived region-specific MC FFs by matching the heavy vs. light flavor fake composition. Only applied to events with anti-ID electrons. Value depends on the analysis region. Uncorrelated across the analysis regions.
Kinematic/Closure	23% (e), 27% (μ)	A data-driven flat uncertainty derived in the fake factor validation region, VRFake. Value depends on the flavor of the anti-ID lepton. Uncorrelated across the analysis regions.

Table 5.13: Summary of the fake factor method systematics. The relative errors on the fake factors are shown for the weight-based systematics. The parameterization systematic is the only tree-based uncertainty, requiring alternative fake estimates. Detailed information on the derivation of these systematics can be found in Appendix C.

5.7   Statistical Framework

In this section, the statistical model and methods used in the analysis are presented. The statistical inference is performed using a software framework known as `HistFitter` [197]. Built around `HistFactory` [207] and `RooStats` [208], `HistFitter` facilitates statistical model building, bookkeeping, fitting, and hypothesis testing.

Statistical Model

Let $\boldsymbol{n}$ and $\boldsymbol{\lambda}$ be the set of observed and expected data yields in the 48 SR $m_{Z\ell}$ bins and the three CRs. The number of events in any given bin, n_i, is distributed according to a Poisson distribution with expectation $\lambda_i = \mu_{\mathrm{sig}} s_i(\boldsymbol{\theta}) + b_i(\boldsymbol{\theta})$, where $s_i(\boldsymbol{\theta})$ and $b_i(\boldsymbol{\theta})$ are the expected number of signal and background events in the bin, respectively. The signal strength, $\mu_{\mathrm{sig}} = \sigma/\sigma_{\mathrm{theory}}$, is the *parameter of interest*. It is defined such that $\mu_{\mathrm{sig}} = 1$ corresponds to the nominal signal production cross section. Note both the signal and background yields depend on the values of additional parameters, $\boldsymbol{\theta}$, referred to as *nuisance parameters*.

These nuisance parameters include the normalization factors for the three primary backgrounds (μ_{WZ}, μ_{ZZ}, and $\mu_{t\bar{t}Z}$), as well as the parameters used to model the systematic effects described in Section 5.6. Correlated systematic uncertainties are described by the same nuisance parameter, while uncorrelated uncertainties are given separate nuisance parameters. The nuisance parameters are constrained by auxiliary measurements and assumed to be independent. Consequently, their joint probability density function $C_{\mathrm{syst}}(\boldsymbol{\theta}^0, \boldsymbol{\theta})$ is taken to be the product of individual Gaussians centered at the central values of the auxiliary measurements, $\boldsymbol{\theta}^0$, with widths reflecting the uncertainty bands.[29] The effects of varying the nuisance parameters on the signal and background expectations are described by $s(\boldsymbol{\theta})$ and $b(\boldsymbol{\theta})$. These estimates are determined explicitly for the nominal and $\pm 1\sigma$ variations of the nuisance parameters, and interpolated for all other values. While the probability density function of any nuisance parameter is symmetric, its impact on the expected yields need not be.

The statistical model for this analysis is defined as:

$$f(\boldsymbol{n}, \boldsymbol{\theta}^0 | \mu_{\mathrm{sig}}, \boldsymbol{\theta}) = \prod_{i \in \mathrm{SRs}} \mathrm{Pois}(n_i | \lambda_i^{(\mathrm{SR})}) \times \prod_{j \in \mathrm{CRs}} \mathrm{Pois}(n_j | \lambda_j^{(\mathrm{CR})}) \times C_{\mathrm{syst}}(\boldsymbol{\theta}^0, \boldsymbol{\theta}),$$

$$\lambda_i = \mu_{\mathrm{sig}} s_i(\boldsymbol{\theta}) + b_i(\boldsymbol{\theta}), \quad C_{\mathrm{syst}}(\boldsymbol{\theta}^0, \boldsymbol{\theta}) = \prod_{k \in S} G(\theta_k^0 - \theta_k).$$

(5.10)

---

[29]In practice, the Gaussian constraint on each NP is transformed into a unit width Gaussian centered at zero. As a result, $\theta_k = 0$ and $\theta_k = \pm 1$ correspond to the central and $\pm 1\sigma$ values of the auxiliary measurement.

This equation can be interpreted as a probability density function (PDF), which is a function of the data $\boldsymbol{n}$ and auxiliary measurements $\boldsymbol{\theta}^0$ under some hypothesis specified by fixed values of μ_{sig} and $\boldsymbol{\theta}$. Alternatively, it can be interpreted as a likelihood, which is a function of μ_{sig} and $\boldsymbol{\theta}$ given some fixed observed data $\boldsymbol{n}$ and auxiliary measurements $\boldsymbol{\theta}^0$.

Profile Likelihood and CL$_{\mathrm{s}}$ Methods

According to the Neyman-Pearson lemma, the most powerful test between two *simple* hypotheses with no free parameters is the likelihood ratio test. The likelihood ratio is defined as

$$\Lambda(\boldsymbol{x}) = \frac{\mathcal{L}(H_0|\boldsymbol{x})}{\mathcal{L}(H_1|\boldsymbol{x})}, \tag{5.11}$$

where H_0 and H_1 are the null and alternative hypotheses, and $\mathcal{L}$ is the likelihood for the hypothesis given some observed data $\boldsymbol{x}$. The *test statistic* $\Lambda(\boldsymbol{x})$ follows some distribution under the null hypothesis, but once the data is observed, a specific value for the test statistic is obtained, $\Lambda_{\mathrm{obs}}(\boldsymbol{x})$. The null hypothesis is rejected in favor of the alternative if the probability of obtaining $\Lambda(\boldsymbol{x}) \leq \Lambda_{\mathrm{obs}}(\boldsymbol{x})$ under the null hypothesis (the *p*-value) is below some threshold.

Now consider the case of *composite* hypotheses, where the null and alternative are differentiated by a continuous parameter, μ_{sig}. A null hypothesis defined by a specific μ_{sig} value (μ'_{sig}) should be tested against an alternative hypothesis where μ_{sig} takes on any other value. This is accomplished by performing a likelihood ratio test with the alternative hypothesis defined using the value of μ_{sig} that maximizes the likelihood given the observed data ($\hat{\mu}_{\mathrm{sig}}$):

$$\Lambda_{\mu'_{\mathrm{sig}}}(\boldsymbol{x}) = \frac{\mathcal{L}(\mu'_{\mathrm{sig}}|\boldsymbol{x})}{\mathcal{L}(\hat{\mu}_{\mathrm{sig}}|\boldsymbol{x})}. \tag{5.12}$$

Such statistical models, where the simpler null can be specified by constraining some parameters of the more complex alternative, are considered nested.

Finally, consider the statistical model specified in Equation 5.10, which contains a parameter of interest and many nuisance parameters. While a straightforward extension of the likelihood ratio in Equation 5.12 could be used to perform hypothesis testing, this would require either specifying or scanning over all values the nuisance parameters. The profile likelihood method addresses this issue.

The profile likelihood method [209, 210] defines a new test statistic, $\tilde{q}_\mu$, that follows a distribution $f(\tilde{q}_\mu|\mu_{\mathrm{sig}})$ that is approximately independent of the nuisance parameters. This is achieved by using the (un)conditional maximum likelihood estimates (MLEs) of the nuisance parameters. The

unconditional MLEs of the model parameters, denoted $\hat{\mu}_{\text{sig}}$ and $\hat{\boldsymbol{\theta}}$, are the values that maximize the likelihood function given the observed data. The conditional MLEs of the nuisance parameters, denoted $\hat{\hat{\boldsymbol{\theta}}}(\mu_{\text{sig}})$, are the values that maximize the likelihood function given some fixed value of μ_{sig}.

The profile likelihood ratio is then given by

$$\lambda(\mu'_{\text{sig}}) = \frac{\mathcal{L}(\mu'_{\text{sig}}, \hat{\hat{\boldsymbol{\theta}}}(\mu'_{\text{sig}}))}{\mathcal{L}(\hat{\mu}_{\text{sig}}, \hat{\boldsymbol{\theta}})} \tag{5.13}$$

where μ'_{sig} is the value of μ_{sig} to be tested. In the above equation, $\hat{\mu}_{\text{sig}}$ may be negative due to a deficit of events with respect to the background-only expectation. While some models of new physics may predict deficits (e.g. due to interference effects), the $\tilde{\chi}_1^{\pm}\tilde{\chi}_1^{\mp} + \tilde{\chi}_1^{\pm}\tilde{\chi}_1^0$ signal targeted by this analysis can only add events over the background in any region or bin. Therefore, a constraint is placed on the test statistic:

$$\tilde{\lambda}(\mu'_{\text{sig}}) = \begin{cases} \frac{\mathcal{L}(\mu'_{\text{sig}}, \hat{\hat{\boldsymbol{\theta}}}(\mu'_{\text{sig}}))}{\mathcal{L}(\hat{\mu}_{\text{sig}}, \hat{\boldsymbol{\theta}})} & \hat{\mu}_{\text{sig}} \geq 0, \\ \frac{\mathcal{L}(\mu'_{\text{sig}}, \hat{\hat{\boldsymbol{\theta}}}(\mu'_{\text{sig}}))}{\mathcal{L}(0, \hat{\hat{\boldsymbol{\theta}}}(0))} & \hat{\mu}_{\text{sig}} < 0. \end{cases} \tag{5.14}$$

When performing a discovery hypothesis test, the background-only null hypothesis is tested against an alternative with $\mu_{\text{sig}} > 0$. The discovery test statistic $\tilde{q}_0$ is used, defined as

$$\tilde{q}_0 = \begin{cases} -2 \log \tilde{\lambda}(0) & \hat{\mu}_{\text{sig}} > 0, \\ 0 & \hat{\mu}_{\text{sig}} \leq 0. \end{cases} \tag{5.15}$$

The log-likelihood (multiplied by a factor of -2) has the same MLEs as the likelihood, and its use is motivated by the nice mathematical properties of logarithms in multiplication, division and exponentiation.[30] Since $\tilde{\lambda}(\mu'_{\text{sig}})$ is bounded between 0 and 1, the discovery test statistic $\tilde{q}_0$ ranges from 0 to infinity, with larger $\tilde{q}_0$ implying increased incompatibility between the data and the $\mu_{\text{sig}} = 0$ hypothesis. Notice this test statistic has no power in the case of a deficit, since only an excess of events is taken as evidence for the signal.

The level of agreement between the data and background-only null hypothesis is quantified by the p-value:

$$p_0 = \int_{\tilde{q}_{0,\text{obs}}}^{\infty} f(\tilde{q}_0|0, \boldsymbol{\theta}) \, d\tilde{q}_0, \tag{5.16}$$

where $f(\tilde{q}_0|0, \boldsymbol{\theta})$ is the probability density function of the discovery test statistic under the $\mu_{\text{sig}} = 0$ hypothesis. Notice the PDF, and therefore the p-value, depends on the values of the nuisance parameters. As these are unknown, a strict frequentist would only exclude the null hypothesis

---

[30] Also, Wilks [211] and Wald [212] showed that its probability distribution has a nice asymptotic form.

if the p-value is below the chosen threshold for all values of the nuisance parameters. With the large number of systematic uncertainties in this analysis, any reasonable sampling of the nuisance parameter space would be incredibly computationally expensive.

Fortunately, the set of nuisance parameters that give the maximal p-value can be estimated using the conditional MLEs, $\hat{\hat{\boldsymbol{\theta}}}(0)$. The approximately maximal p-value is then given by:

$$p_0 = \int_{\tilde{q}_{0,\mathrm{obs}}}^{\infty} f(\tilde{q}_0|0, \hat{\hat{\boldsymbol{\theta}}}(0)) \, d\tilde{q}_0. \tag{5.17}$$

This use of the conditional MLEs of the nuisance parameters is known as the *profile construction* [210]. The p-value can be translated into a quantile of the standard Gaussian, or *significance*, using:

$$Z_0 = \Phi^{-1}(1 - p_0), \tag{5.18}$$

where Φ is the cumulative distribution of the standard Gaussian, and Φ^{-1} is its inverse. The background-only hypothesis is rejected and a discovery is claimed if the significance exceeds 5σ, or equivalently, the p-value is below 2.87×10^{-7}.

To set limits on possible signals (i.e. possible μ_{sig} values), the following test statistic is used:

$$\tilde{q}_{\mu'_{\mathrm{sig}}} = \begin{cases} -2\log\tilde{\lambda}(\mu'_{\mathrm{sig}}) & \hat{\mu}_{\mathrm{sig}} \leq \mu'_{\mathrm{sig}} \\ 0 & \hat{\mu}_{\mathrm{sig}} > \mu'_{\mathrm{sig}}. \end{cases} = \begin{cases} -2\log\frac{\mathcal{L}(\mu'_{\mathrm{sig}}, \hat{\hat{\boldsymbol{\theta}}}(\mu'_{\mathrm{sig}}))}{\mathcal{L}(0, \boldsymbol{\theta}(\hat{0}))} & \hat{\mu}_{\mathrm{sig}} < 0, \\ -2\log\frac{\mathcal{L}(\mu'_{\mathrm{sig}}, \hat{\hat{\boldsymbol{\theta}}}(\mu'_{\mathrm{sig}}))}{\mathcal{L}(\hat{\mu}_{\mathrm{sig}}, \hat{\boldsymbol{\theta}})} & 0 \leq \hat{\mu}_{\mathrm{sig}} \leq \mu'_{\mathrm{sig}}, \\ 0 & \hat{\mu}_{\mathrm{sig}} > \mu'_{\mathrm{sig}}. \end{cases} \tag{5.19}$$

Again, since $\tilde{\lambda}(\mu'_{\mathrm{sig}})$ is bounded between 0 and 1, the limit setting test statistic $\tilde{q}_{\mu'_{\mathrm{sig}}}$ ranges from 0 to infinity, with larger $\tilde{q}_{\mu'_{\mathrm{sig}}}$ implying increased incompatibility between the data and the μ'_{sig} hypothesis. Notice that this test statistic has no power when testing a signal strength hypothesis smaller than the best fit value. Again using the profile construction, the p-value under the μ'_{sig} hypothesis is given by:

$$p_{\mu'_{\mathrm{sig}}} = \int_{\tilde{q}_{\mu'_{\mathrm{sig}},\mathrm{obs}}}^{\infty} f(\tilde{q}_{\mu'_{\mathrm{sig}}}|\mu'_{\mathrm{sig}}, \hat{\hat{\boldsymbol{\theta}}}(\mu'_{\mathrm{sig}})) \, d\tilde{q}_{\mu'_{\mathrm{sig}}}. \tag{5.20}$$

Notice a downward fluctuation in the data can create arbitrarily small $p_{\mu'_{\mathrm{sig}}}$-values. Consequently, a p-value under the signal-plus-background hypothesis alone is insufficient for rejecting signal hypotheses. To insulate against downward fluctuations, the CL_s method [213] is used to determine if the μ'_{sig} hypothesis is excluded at some confidence level. The CL_s statistic is defined as:

$$CL_s = \frac{p_{\mu'_{\mathrm{sig}}}}{1 - p_b}, \tag{5.21}$$

where p_b is the p-value derived from $\tilde{q}_{\mu'_{\text{sig}},\text{obs}}$, but under the background-only hypothesis:

$$p_b = 1 - \int_{\tilde{q}_{\mu'_{\text{sig}},\text{obs}}}^{\infty} f(\tilde{q}_{\mu'_{\text{sig}}}|0, \hat{\hat{\boldsymbol{\theta}}}(0))\, d\tilde{q}_{\mu'_{\text{sig}}}. \tag{5.22}$$

The μ'_{sig} hypothesis is excluded at 95% confidence level if the CL_s falls below 5%. An upper limit on the signal strength given the observed data can be set at 95% confidence level by finding the value of μ'_{sig} for which the CL_s is exactly 5%. The CL_s method is conservative and overcovers the targeted confidence level, since the denominator is less than unity. At 95% confidence level, the coverage can range from 95% to 100%.

The CL_s method and its relevant p-values are illustrated in Figure 5.15 for two different toy experiments. In the first experiment, the test statistic PDFs under the background-only and signal hypotheses are well-separated. The observed data agrees well with the background-only hypothesis, and the signal hypothesis is excluded. In the second experiment, the two hypotheses are less separated, and a downward fluctuation is observed in the data. Despite a small $p_{\mu'_{\text{sig}}}$, the CL_s method prevents the exclusion of the signal hypothesis due to the large p_b.

(a) Signal hypothesis excluded. (b) Signal hypothesis not excluded.
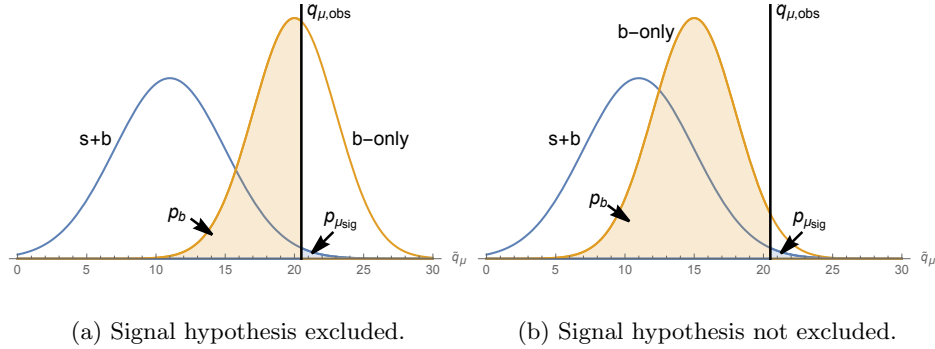
Figure 5.15: Illustration of the CL_s method for two different experiments. In (a), the PDFs of the test statistic under the two hypotheses are well-separated, and the observed data agrees well with the background-only hypothesis. In (b), the two hypotheses are less separated, and a downward fluctuation is observed. Despite the small $p_{\mu_{\text{sig}}}$, the CL_s method prevents the exclusion of the signal-plus-background hypothesis due to the large p_b.

Finally, when attempting to reject the background-only hypothesis and discover new physics, a p-value must be calculated from $\tilde{q}_{0,\text{obs}}$ and its probability density function under the background-only hypothesis. When setting limits on the signal strength via the CL_s method, a p-value must be calculated using $\tilde{q}_{\mu'_{\text{sig}},\text{obs}}$ and its PDFs under both the $\mu_{\text{sig}} = 0$ and $\mu_{\text{sig}} = \mu'_{\text{sig}}$ hypotheses. These PDFs can be obtained by generating a large ensemble of pseudo-experiments and calculating the

test statistic in each. The pseudo-experiments are generated via Monte Carlo methods using the model in Equation 5.10. Again, the ideal frequentist approach would be to scan over all possible nuisance parameter values, generating an ensemble of pseudo-experiments for each set of values and calculating the p-value for each. The largest (i.e. most conservative) p-value would then be used to determine if the μ'_{sig} hypothesis is rejected. However, this method is incredibly computationally intensive. Instead, in the profile construction, the profiled values are used when generating pseudo-experiments. The resulting p-value is approximately equal to the maximal value.

Alternatively, if the data yields are sufficiently large, the PDFs of the test statistics follow asymptotic formulae that are obtained through the application of both Wilks' and Wald's theorems [211, 212, 214]. In this asymptotic regime, the PDFs are approximately independent of the nuisance parameters — an attractive feature of the profile likelihood ratio method.

5.8   Results

Presented in this section are the unblinded signal region yields and the statistical inference. First, the results of a background-only fit to the observed data in the control and signal regions are shown. Afterwards, model-independent limits are set on generic signals that may populate the SR bins. Finally, limits are set on the targeted $\tilde{\chi}_1^{\pm}\tilde{\chi}_1^{\mp} + \tilde{\chi}_1^{\pm}\tilde{\chi}_1^0$ signal while scanning over the $\tilde{\chi}_1^{\pm}/\tilde{\chi}_1^0$ mass and branching fractions to the leptons and bosons.

5.8.1   Signal Region Observation and Background-Only Fit

The observed data and expected background yields in the signal regions are shown in Table 5.14. The background expectations are obtained by simultaneously fitting the model in Equation 5.10 to the observed yields in the three CRs and all 48 SR bins with the signal strength parameter fixed at zero.[31] As previously shown in Figures 5.3-5.6, the post-fit background distributions and yields are well-modeled, showing good agreement with the data in the CRs and VRs.

As discussed in Section 5.4, two additional sets of signal regions are defined alongside SR3ℓ, SR4ℓ, and SRFR with identical selections except the chosen *direct* leptons are required to be either electrons (SR3ℓ_e, SR4ℓ_e, SRFR$_e$) or muons (SR3ℓ_μ, SR4ℓ_μ, SRFR$_\mu$). These flavor-specific SRs are eventually used when setting limits on $\tilde{\chi}_1^{\pm}\tilde{\chi}_1^{\mp} + \tilde{\chi}_1^{\pm}\tilde{\chi}_1^0$ signals with 100% branching fractions to

---

[31]To be more precise, the conditional MLEs of the nuisance parameters are found. The background expectations in each region are then given by $\boldsymbol{b}_i(\hat{\hat{\boldsymbol{\theta}}}(\mu_{\mathrm{sig}} = 0))$.

electrons or muons. When observed inclusively in $m_{Z\ell}$, there are slight excesses in SR4ℓ, SR4ℓ_e, SR3ℓ, and SR3ℓ_μ.

Note that in SR3ℓ and SR4ℓ, the sum of observed data yields in the electron and muon flavor channels is equal to the flavor-inclusive yield. This is not the case in SRFR, as the flavor requirements are applied to both direct leptons. As a result, SRFR events with different flavor direct leptons ($e\mu/\mu e$) are not included in either SRFR$_e$ or SRFR$_\mu$. In all SRs, the flavor-inclusive post-fit background yields are not equal in the sum of the electron and muon flavor channels, as the yields for the three flavor channels are obtained from separate fits.

The signal region $m_{Z\ell}$ distributions are shown in Figure 5.16 with the shape-fit binning. Also included are the distributions for three possible $\tilde{\chi}_1^\pm \tilde{\chi}_1^\mp + \tilde{\chi}_1^\pm \tilde{\chi}_1^0$ signals, with $m_{\tilde{\chi}_1} = 200$, 500, and 800 GeV. Each signal peaks strongly in the corresponding $m_{Z\ell}$ bin of all three SRs. Notice the yields are normalized by the bin widths, which increases at higher $m_{Z\ell}$. The statistical significance of the observation in each bin is shown in the bottom panel, with no bin reaching $Z_0 \geq 2\sigma$. Additionally, no coherent excess is seen near the same $m_{Z\ell}$ value across all three SRs. These post-fit $m_{Z\ell}$ distributions are also shown in Figure 5.17, but with uniform 20 GeV binning. Here, the bottom panel shows the ratio of the data to the background prediction. The signal distributions have longer tails in SR4ℓ and SRFR due to events where the wrong third lepton is paired with the Z boson to reconstruct the $\tilde{\chi}_1^\pm \rightarrow Z\ell \rightarrow \ell\ell\ell$ decay.

Finally, the distributions for the important kinematic variables used to define the signal regions are shown in Figure 5.18. Good agreement is seen between the data and post-fit background expectation, both inside and outside the signal regions.

Table 5.14: The observed yields and post-fit background expectations in SRFR, SR4ℓ and SR3ℓ, shown inclusively and when the direct lepton from a $\tilde{\chi}_1^\pm / \tilde{\chi}_1^0$ decay is required to be an electron or muon. The "Other" category consists mostly of the tWZ, $t\bar{t}W$ and tZ processes. Uncertainties in the background expectation include combined statistical and systematic uncertainties. The individual uncertainties may be correlated and do not necessarily combine in quadrature to give the total background uncertainty.

Region	SRFR	SRFR$_e$	SRFR$_\mu$	SR4ℓ	SR4ℓ_e	SR4ℓ_μ
Observed yield	42	15	17	89	48	41
Expected background yield	39.3 ± 3.5	13.8 ± 2.1	15.7 ± 2.6	76 ± 5	36 ± 4	38.4 ± 2.9
WZ yield	$-$	$-$	$-$	$-$	$-$	$-$
ZZ yield	19.5 ± 2.8	7.2 ± 1.7	10.4 ± 2.5	21.0 ± 1.1	9.6 ± 0.7	11.2 ± 0.8
$t\bar{t}Z$ yield	12.3 ± 2.4	2.5 ± 0.7	3.0 ± 0.7	18 ± 5	9.1 ± 3.2	8.6 ± 1.6
Triboson yield	1.3 ± 0.4	0.26 ± 0.09	0.32 ± 0.12	12.2 ± 2.4	5.7 ± 1.4	5.9 ± 1.5
Higgs yield	2.7 ± 0.5	0.73 ± 0.18	1.17 ± 0.25	11.2 ± 1.7	5.2 ± 1.0	5.5 ± 1.1
Other yield	2.2 ± 0.4	0.25 ± 0.17	0.39 ± 0.16	7.9 ± 1.3	4.0 ± 0.8	3.5 ± 0.8
$Fake$ yield	1.3 ± 0.7	2.9 ± 1.5	0.5 ± 0.5	6.4 ± 2.1	2.1 ± 1.1	3.6 ± 1.7

Region	SR3ℓ	SR3ℓ_e	SR3ℓ_μ
Observed yield	61	28	33
Expected background yield	55.1 ± 3.0	27.6 ± 2.4	28.0 ± 2.3
WZ yield	33.7 ± 2.1	16.6 ± 1.8	17.7 ± 1.9
ZZ yield	0.93 ± 0.23	0.11 ± 0.04	0.79 ± 0.25
$t\bar{t}Z$ yield	7.5 ± 1.6	4.1 ± 1.4	3.5 ± 0.7
Triboson yield	5.6 ± 1.2	2.7 ± 0.8	2.7 ± 0.7
Higgs yield	0.51 ± 0.09	0.25 ± 0.06	0.23 ± 0.06
Other yield	4.2 ± 0.7	2.0 ± 0.4	2.0 ± 0.5
$Fake$ yield	2.6 ± 1.1	1.9 ± 1.1	1.0 ± 0.8
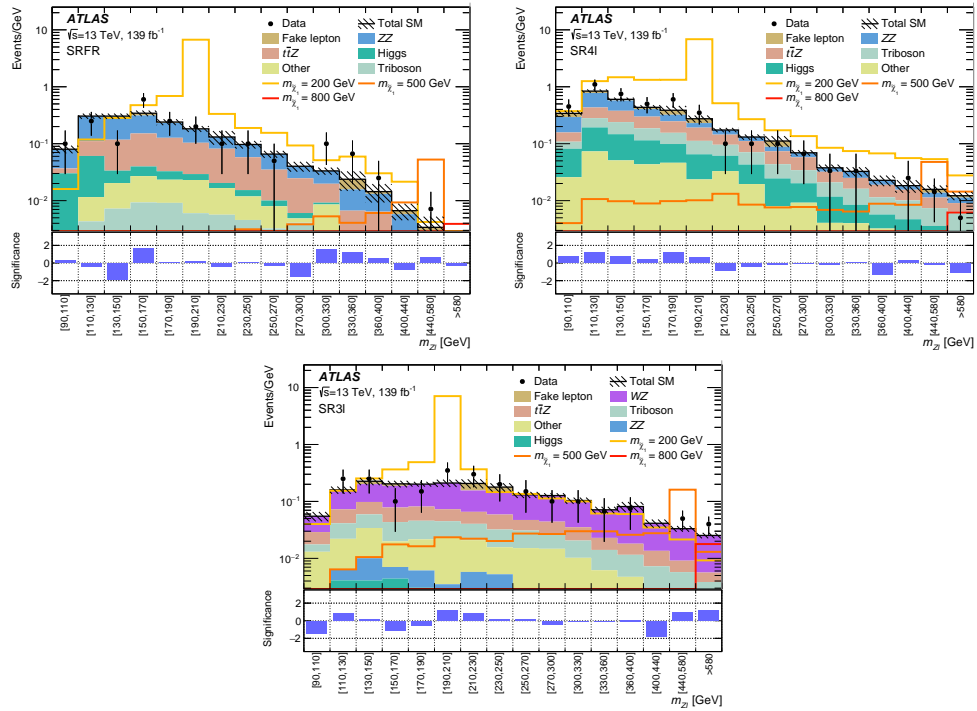
Figure 5.16: The observed data and post-fit SM background expectation as a function of $m_{Z\ell}$ in (top left) SRFR, (top right) SR4ℓ, and (bottom) SR3ℓ. The $m_{Z\ell}$ binning is the same as that used in the fit and the yield is normalized to the bin width, with the last bin normalized using a width of 200 GeV. The "Other" category consists mostly of the tWZ, $t\bar{t}W$ and tZ processes. The hatched bands indicate the combined theoretical, experimental, and MC statistical uncertainties in the background prediction. The bottom panel shows the significance of the differences between the observed data and expected yields.
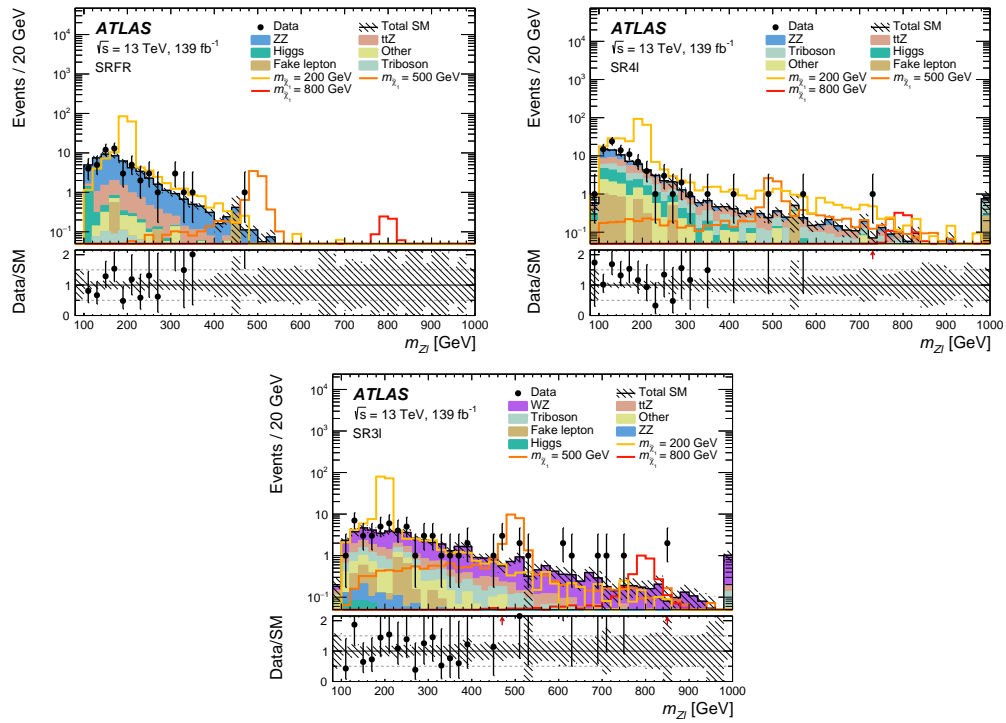
Figure 5.17: The observed data and post-fit SM background expectation as a function of $m_{Z\ell}$ with uniform binning in (top left) SRFR, (top right) SR4ℓ, and (bottom) SR3ℓ. The last bin includes overflow events. The "Other" category consists mostly of the tWZ, $t\bar{t}W$ and tZ processes. The hatched bands indicate the combined theoretical, experimental, and MC statistical uncertainties in the background prediction. The bottom panel shows the ratio of the data to the background prediction.
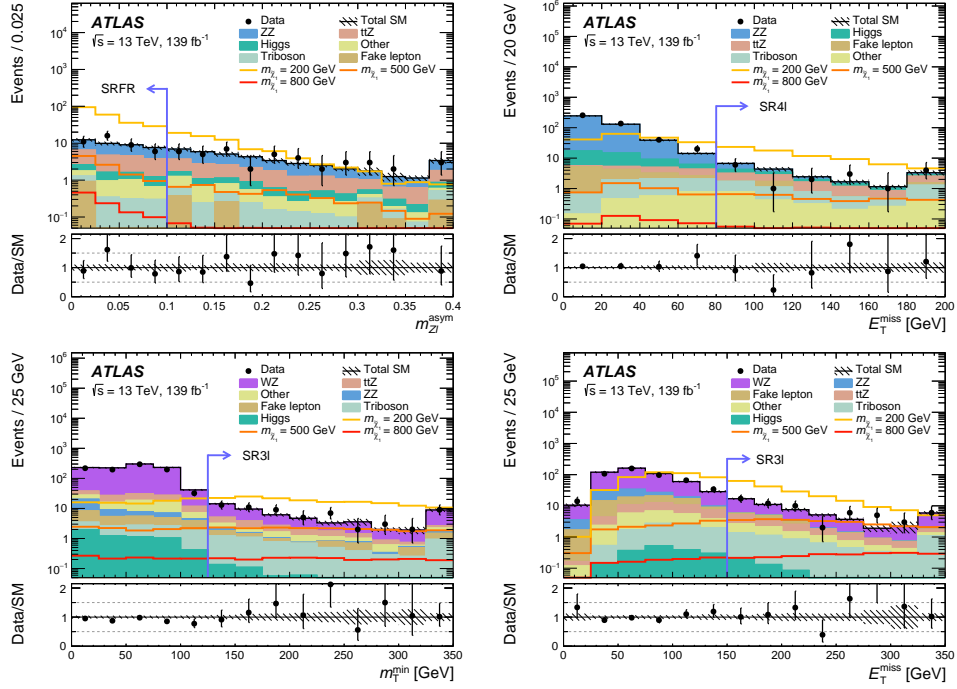
Figure 5.18: Example kinematic distributions in the signal regions showing the data and the post-fit background expectation, including (top left) $m_{Z\ell}$ asymmetry in SRFR, (top right) E_T^{miss} in SR4ℓ, and (bottom left) m_T^{min} and (bottom right) E_T^{miss} in SR3ℓ. The fit uses all CRs and SRs, and the distributions are shown inclusively in $m_{Z\ell}$. The full event selection for each of the corresponding regions is applied except for the variable shown, where the selection is indicated by a blue arrow. The last bin includes overflow events. The "Other" category consists mostly of the tWZ, $t\bar{t}W$ and tZ processes. The hatched bands indicate the combined theoretical, experimental, and MC statistical uncertainties in the background prediction. The bottom panel shows the ratio of the data to the background prediction.

5.8.2 Model-Independent Limits

Before setting limits set on the targeted $\tilde{\chi}_1^\pm \tilde{\chi}_1^\mp + \tilde{\chi}_1^\pm \tilde{\chi}_1^0$ signal, model-independent limits are set on generic signals in each SR $m_{Z\ell}$ bin. Hypothesis tests are performed by fitting the control regions and a single SR $m_{Z\ell}$ bin at a time, as fitting multiple SR bins would require some knowledge of the signal shape. For the same reason, the signal contamination in the control regions is assumed to be zero. If a real signal happens to populate both the CRs and the SR bin, the excess of events in the CRs will be covered primarily by the background normalization factors, increasing the background expectation in the SR bin and reducing the sensitivity to the signal. The limits resulting from this hypothesis testing procedure are therefore conservative. The generic signal is assumed to populate the SR bin with a single event when $\mu_{\text{sig}} = 1$, so the signal strength is also the number of expected signal events. No systematic uncertainties are associated with the generic signal except the uncertainty on the recorded luminosity.

For each SR bin, upper limits on the number of generic signal events S_{obs}^{95} are set at 95% confidence level using the CL_s method. These limits are powerful and particularly useful for the physics community, as any new physics model can be excluded if it predicts more signal events than S_{obs}^{95} in any SR bin. These results are translated to upper limits on the generic signal's visible cross section $\langle \epsilon\sigma \rangle_{\text{obs}}^{95}$, which incorporates the reconstruction efficiency, acceptance, and production cross section of the generic signal. Additionally, the discovery p-value under the background-only hypothesis is calculated and converted to an equivalent significance Z.[32] Due to the limited number of events in the SR bins, the PDFs of the $\tilde{q}_0$ and $\tilde{q}_{\mu_{\text{sig}}}$ test statistics are obtained from ensembles of simulated pseudo-experiments, as opposed to asymptotic formulae. The full results from the model-independent hypothesis testing are shown in Table 5.15.

Three SR bins have excesses with $Z \geq 2\sigma$, the largest of which ($Z = 2.2\sigma$) is seen in the SRFR bin between 150 and 170 GeV. Notice the significance values differ from those previously shown in Figure 5.16. The significance values in Table 5.15 are calculated from the discovery p-values (p_0), which were obtained by performing hypothesis tests. The p-values are calculated using Equation 5.17, with the discovery test statistic PDF determined from an ensemble of pseudo-data. When performing the hypothesis tests, only a single SR bin is included with the three CRs in the likelihood.

In contrast, the significance values in Figure 5.16 are calculated not from p-values, but instead from an approximate formula that relies on the asymptotic behavior of the profile likelihood ra-

---

[32]Note the discovery p-value uses the $\tilde{q}_0$ test statistic. It is not the p-value calculated using $\tilde{q}_{\mu_{\text{sig}}}$ under the background-only hypothesis, which is used for the CL_s calculation.

tio [198]. The formula is derived for a simple Poisson statistical model with one SR and one CR. The uncertainty on the total background in the SR is constrained by the auxiliary measurement in the CR. In the asymptotic limit of many observed events, the significance is given by a simple formula that depends only on the observed data, the total post-fit background, and the total post-fit background uncertainty. When applying this formula to a particular SR bin, the total background and its uncertainty are obtained from a background-only fit that includes all SR bins in the likelihood.

Table 5.15: Model-independent results where each row targets one $m_{Z\ell}$ bin of one SR and probes scenarios where a generic beyond-the-SM process is assumed to contribute only to that $m_{Z\ell}$ bin. The first two columns refer to the signal region and $m_{Z\ell}$ bin probed, while the third and fourth columns show the observed ($N_{\rm obs}$) and expected ($N_{\rm exp}$) event yields. The expected yields are obtained using a background-only fit of all the CRs, and the errors include statistical and systematic uncertainties. The fifth and sixth columns show the observed 95% CL upper limit on the visible cross section ($\langle\epsilon\sigma\rangle^{95}_{\rm obs}$) and on the number of signal events ($S^{95}_{\rm obs}$), while the seventh column shows the expected 95% CL upper limit on the number of signal events ($S^{95}_{\rm exp}$) with the associated $1\,\sigma$ uncertainties. The last column provides the discovery p-value and significance (Z) of any excess of data above background expectation. Cases for which the observed yield is less than the expected yield are capped at a p-value of 0.5.

Region	Range of $m_{Z\ell}$ [GeV]	$N_{\rm obs}$	$N_{\rm exp}$	$\langle\epsilon\sigma\rangle^{95}_{\rm obs}$ [fb]	$S^{95}_{\rm obs}$	$S^{95}_{\rm exp}$	$p(s=0)$ (Z)
SRFR	[90, 110]	2	1.6 ± 0.3	0.03	4.2	$4.0^{+1.7}_{-0.7}$	0.43 (0.2)
	[110, 130]	5	5.9 ± 1.0	0.04	5.7	$6.4^{+2.5}_{-1.7}$	0.50 (0.0)
	[130, 150]	2	6.0 ± 1.1	0.03	4.2	$6.2^{+2.3}_{-1.5}$	0.50 (0.0)
	[150, 170]	12	6.1 ± 1.1	0.10	14.2	$7.9^{+2.7}_{-1.3}$	0.01 (2.2)
	[170, 190]	5	4.5 ± 0.8	0.05	6.4	$5.6^{+2.5}_{-1.2}$	0.31 (0.5)
	[190, 210]	4	3.4 ± 0.6	0.04	6.1	$5.2^{+2.0}_{-1.4}$	0.26 (0.7)
	[210, 230]	2	2.6 ± 1.5	0.03	4.7	$4.9^{+1.9}_{-1.4}$	0.50 (0.0)
	[230, 250]	2	1.8 ± 0.3	0.03	4.6	$4.0^{+1.7}_{-0.9}$	0.42 (0.2)
	[250, 270]	1	1.2 ± 0.2	0.03	3.9	$3.7^{+1.6}_{-0.7}$	0.50 (0.0)
	[270, 300]	0	1.2 ± 0.3	0.03	3.6	$3.7^{+1.5}_{-0.7}$	0.50 (0.0)
	[300, 330]	3	0.9 ± 0.2	0.05	6.6	$4.2^{+0.7}_{-0.5}$	0.02 (2.1)
	[330, 360]	2	0.5 ± 0.2	0.04	5.6	$3.5^{+0.8}_{-0.1}$	0.03 (1.9)
	[360, 400]	1	0.5 ± 0.2	0.03	4.0	$3.4^{+0.8}_{-0.1}$	0.18 (0.9)
	[400, 440]	0	0.3 ± 0.1	0.03	3.7	$3.1^{+0.8}_{-0.1}$	0.50 (0.0)
	[440, 580]	1	0.3 ± 0.2	0.03	4.4	$3.3^{+0.9}_{-0.1}$	0.12 (1.2)
	>580	0	$0.1^{+0.2}_{-0.1}$	0.02	3.2	$3.0^{+0.1}_{-0.0}$	0.50 (0.0)
SR4ℓ	[90, 110]	9	6.1 ± 0.9	0.07	9.7	$7.1^{+2.3}_{-1.1}$	0.14 (1.1)
	[110, 130]	22	15.4 ± 1.3	0.12	16.0	$10.2^{+4.2}_{-2.1}$	0.05 (1.6)
	[130, 150]	15	10.9 ± 0.9	0.09	12.7	$8.5^{+3.7}_{-1.2}$	0.09 (1.3)
	[150, 170]	10	7.9 ± 0.9	0.07	9.9	$7.7^{+2.8}_{-1.4}$	0.18 (0.9)
	[170, 190]	12	5.9 ± 0.6	0.10	14.3	$8.5^{+3.2}_{-0.8}$	0.02 (2.0)
	[190, 210]	7	4.9 ± 0.9	0.06	8.4	$6.6^{+2.2}_{-1.2}$	0.16 (1.0)
	[210, 230]	2	3.2 ± 0.3	0.03	4.3	$4.8^{+2.2}_{-1.4}$	0.50 (0.0)
	[230, 250]	2	2.4 ± 0.3	0.03	4.2	$4.4^{+2.7}_{-1.4}$	0.50 (0.0)
	[250, 270]	2	2.1 ± 0.6	0.03	4.5	$4.5^{+1.9}_{-1.0}$	0.50 (0.0)
	[270, 300]	2	1.9 ± 0.2	0.03	4.9	$4.8^{+1.6}_{-1.2}$	0.48 (0.1)
	[300, 330]	1	1.0 ± 0.2	0.03	4.7	$4.2^{+1.6}_{-0.9}$	0.50 (0.0)
	[330, 360]	1	0.9 ± 0.2	0.03	3.9	$3.6^{+1.6}_{-0.5}$	0.30 (0.5)
	[360, 400]	0	0.8 ± 0.2	0.03	3.6	$3.6^{+1.1}_{-0.5}$	0.50 (0.0)
	[400, 440]	1	0.6 ± 0.2	0.03	4.2	$3.2^{+1.1}_{-0.2}$	0.17 (1.0)
	[440, 580]	2	2.0 ± 0.4	0.03	4.7	$4.5^{+1.7}_{-1.2}$	0.50 (0.0)
	>580	1	2.3 ± 0.5	0.03	3.5	$4.5^{+1.7}_{-1.2}$	0.50 (0.0)
SR3ℓ	[90, 110]	0	1.1 ± 0.2	0.02	3.0	$3.5^{+2.2}_{-0.5}$	0.50 (0.0)
	[110, 130]	5	2.8 ± 0.6	0.06	7.8	$5.7^{+1.3}_{-1.1}$	0.09 (1.3)
	[130, 150]	5	4.1 ± 0.8	0.05	6.8	$5.7^{+2.3}_{-1.2}$	0.27 (0.6)
	[150, 170]	2	4.0 ± 0.7	0.03	3.8	$5.3^{+2.4}_{-1.5}$	0.50 (0.0)
	[170, 190]	3	3.9 ± 0.5	0.04	4.9	$5.4^{+2.2}_{-1.7}$	0.50 (0.0)
	[190, 210]	7	3.7 ± 0.8	0.07	9.1	$6.2^{+1.8}_{-1.6}$	0.12 (1.2)
	[210, 230]	6	3.5 ± 0.9	0.06	8.9	$6.2^{+2.0}_{-1.1}$	0.09 (1.4)
	[230, 250]	4	3.3 ± 0.7	0.04	6.0	$5.4^{+1.8}_{-1.2}$	0.29 (0.6)
	[250, 270]	3	2.5 ± 0.4	0.04	5.4	$4.8^{+1.8}_{-1.3}$	0.37 (0.3)
	[270, 300]	3	3.7 ± 0.5	0.04	5.1	$5.4^{+2.0}_{-1.7}$	0.50 (0.0)
	[300, 330]	3	3.0 ± 0.5	0.04	5.0	$4.9^{+2.1}_{-1.2}$	0.50 (0.0)
	[330, 360]	2	2.1 ± 0.4	0.03	4.7	$4.4^{+1.7}_{-1.1}$	0.50 (0.0)
	[360, 400]	3	3.2 ± 0.9	0.04	5.4	$5.6^{+2.0}_{-1.8}$	0.50 (0.0)
	[400, 440]	0	1.7 ± 0.3	0.02	3.0	$4.0^{+1.2}_{-0.6}$	0.50 (0.0)
	[440, 580]	7	4.3 ± 0.7	0.06	8.7	$6.3^{+1.5}_{-1.6}$	0.11 (1.2)
	>580	8	4.6 ± 0.7	0.07	10.0	$6.6^{+2.3}_{-1.6}$	0.08 (1.4)

5.8.3   Model-Dependent Limits

With no significant excess observed, limits are set on the targeted $\tilde{\chi}_1^{\pm}\tilde{\chi}_1^{\mp} + \tilde{\chi}_1^{\pm}\tilde{\chi}_1^0$ signal by performing a simultaneous shape-fit of the $m_{\mathrm{Z}\ell}$ distribution in the three signal regions. The three control regions are also included in the fit to constrain the nuisance parameters associated with the primary backgrounds, particularly their normalization factors. Limits are set at 95% confidence level via the profile likelihood and CL_s methods using the statistical model defined in Equation 5.10, as described in Section 5.7. Since every SR $m_{\mathrm{Z}\ell}$ bin is fit simultaneously, every bin contributes to the limit on a particular signal; even bins with very low expected signal yields are useful in constraining the background in the signal region phase space. Due to the higher effective data statistics from fitting all 48 SR bins, asymptotic formulae are used instead of simulated pseudo-data to calculate the necessary p-values.

Limits are set on the $\tilde{\chi}_1^{\pm}\tilde{\chi}_1^{\mp} + \tilde{\chi}_1^{\pm}\tilde{\chi}_1^0$ signal as a function of the $\tilde{\chi}_1^{\pm}/\tilde{\chi}_1^0$ mass and branching fractions to the different leptons and bosons. These branching fractions are assumed to be fully correlated between the $\tilde{\chi}_1^{\pm}$ and $\tilde{\chi}_1^0$. The expected number of signal events from each branching fraction hypothesis is determined by reweighting the simulated events, as described in Section 5.4. The branching fractions to leptons and bosons can be specified by two parameters each, since all three decay probabilities must sum to unity. With the $\tilde{\chi}_1^{\pm}/\tilde{\chi}_1^0$ mass taken as a free parameter as well, this results in a 5-dimensional scan over signal parameter space. At each point in the scan, the observed and expected CL_s values are calculated for the nominal signal strength ($\mu_{\mathrm{sig}} = 1$),[33] from which a 5-dimensional 95% CL_s exclusion contour can be interpolated. In the upcoming results, the exclusion contour is projected to lower dimensions by holding some signal parameters constant.

For the $\tilde{\chi}_1^{\pm}/\tilde{\chi}_1^0$ branching fractions to leptons, four points are considered: equal branching fractions to the three flavors, 100% to electrons, 100% to muons, and 100% to tau leptons. When setting limits on signals with 100% branching fractions to electrons or muons, the signal regions that constrain the direct lepton flavor are used (e.g. SRFR_e and SRFR_μ); otherwise, the nominal SRs are used. For each of the four points in lepton branching fraction space, the $\tilde{\chi}_1^{\pm}/\tilde{\chi}_1^0$ mass and branching fractions to bosons are then scanned more finely.

In Figure 5.19, the exclusion contours are shown for each lepton branching fraction hypothesis as a function of the $\tilde{\chi}_1^{\pm}$ mass and branching fraction to Z bosons. For these exclusion contours, the remaining boson branching fraction space is split evenly between the W and H decay channels if the latter is kinematically possible. For example, if the Z branching fraction is 50% and the $\tilde{\chi}_1^{\pm}/\tilde{\chi}_1^0$

---

[33]When setting upper limits on μ_{sig}, the scan becomes 6-dimensional. See Appendix D for these results.

mass is above 125 GeV, the W and H branching fractions are each set to 25%. The decision to reduce the dimensionality of the exclusion contours in this way will be justified shortly.

As expected, the $\tilde{\chi}_1^\pm / \tilde{\chi}_1^0$ mass exclusions become stronger as the Z branching fraction increases, reaching 1100 GeV and 1050 GeV for the electron and muon channels, respectively. This limit is slightly weaker for the lepton universal contour due to the increase in τ-leptons, reaching 975 GeV at 100% branching fraction to Z. When the $\tilde{\chi}_1^\pm$ and $\tilde{\chi}_1^0$ both decay purely to τ-leptons, $\tilde{\chi}_1^\pm / \tilde{\chi}_1^0$ masses are excluded up to 625 GeV. In all cases, the mass limits become weaker as the branching fraction to Z bosons is reduced. At 1% branching fraction to Z bosons, the observed mass limit drops to 350 GeV, 375 GeV, and 175 GeV for the electron, muon, and lepton universal scenarios, respectively. No limits are set for Z branching fractions below 11% when the $\tilde{\chi}_1^\pm$ and $\tilde{\chi}_1^0$ decay purely to τ-leptons. Due to the slight excesses seen, particularly in high $m_{Z\ell}$ events where the direct lepton is a muon, the observed limits are slightly weaker than expected.

For a limited number of interesting mass points, the full boson branching fraction space is explored. Shown in Figures 5.20-5.23 are the exclusion contours drawn as a function of the $\tilde{\chi}_1^\pm / \tilde{\chi}_1^0$ branching fractions to Higgs and Z bosons. For each contour, the $\tilde{\chi}_1^\pm / \tilde{\chi}_1^0$ mass and lepton branching fractions are fixed. As the mass is increased, the limits in the boson branching fraction plane become weaker, shifting towards higher branching fractions to Z bosons. In most cases, the exclusion contours are fairly vertical, and are therefore dominated by the $\tilde{\chi}_1^\pm / \tilde{\chi}_1^0$ branching fractions to Z bosons. This is expected, as the signal region selections are optimized to target $\tilde{\chi}_1^\pm \to Z\ell \to \ell\ell\ell$ decays. As a result, the exclusion contours shown in Figure 5.19 are expected to be stable under changes in how the remaining branching fraction space is divided between the W and Higgs decay channels.

To better understand how each signal region contributes to the combined limits, the expected and observed CL_s values were calculated for the 700 GeV mass point using only a single SR at a time. The resulting 95% CL_s exclusion contours are shown in Figure 5.24 for the electron, muon, and lepton universal scenarios.

In general, SR3ℓ provides the strongest expected limits of the three SRs, and the contour (dashed blue) is mostly independent of the W and Higgs branching fractions. The expected SR4ℓ contours (dashed red) are usually the weakest, but they improve drastically as the Higgs branching fraction is decreased in favor of decays involving W bosons. The opposite behavior is seen in the expected contours from SRFR (dashed green), which become slightly stronger as the Higgs branching fraction is increased at the expense of the W branching fraction. Finally, the limits are improved by combining the signal regions. While the relative sensitivities of the individual signal regions may

depend on how the non-Z branching fraction space is split between the W and H decay channels, the complementarity of the signal regions results in limits that are mostly dependent on the Z branching fraction only.

Additional results can be found in Appendix D, including the expected and observed upper limits on the $\tilde{\chi}_1^\pm \tilde{\chi}_1^\mp + \tilde{\chi}_1^\pm \tilde{\chi}_1^0$ cross section. Also included are the $\tilde{\chi}_1^\pm \tilde{\chi}_1^\mp + \tilde{\chi}_1^\pm \tilde{\chi}_1^0$ truth-level acceptances and reconstruction efficiencies in the SRs, as well as detailed cutflows showing the number of signal events remaining after each SR requirement is applied sequentially.
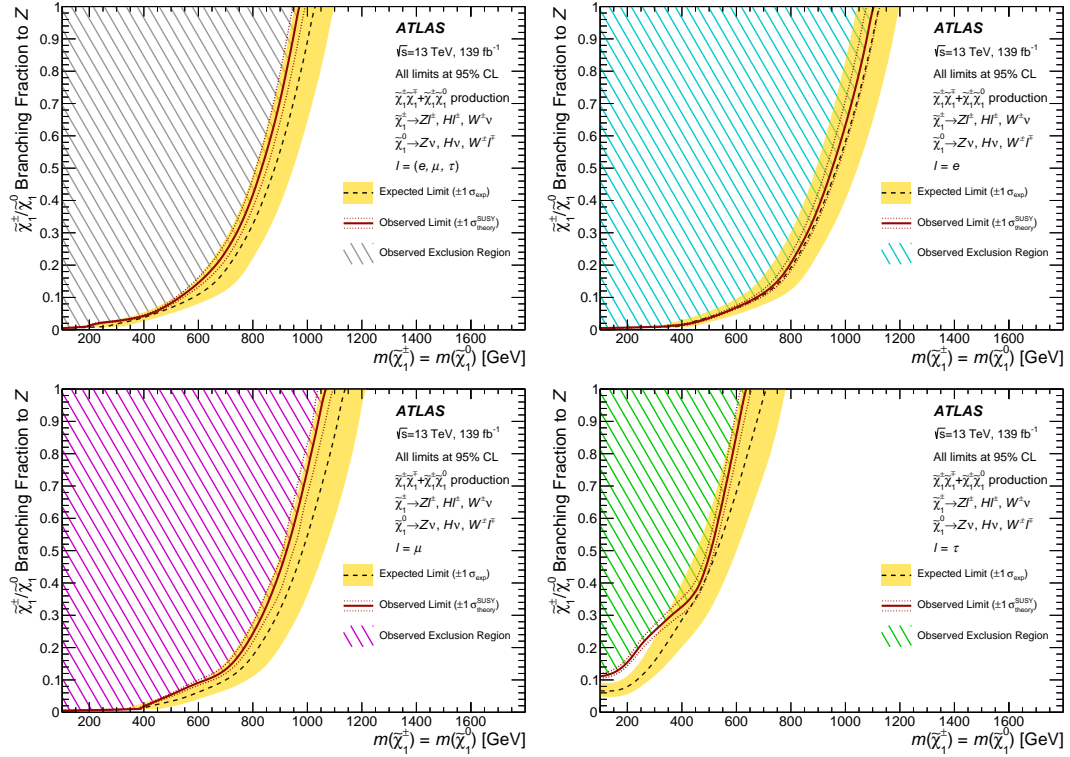
Figure 5.19: Exclusion curves for the simplified model of $\tilde{\chi}_1^\pm \tilde{\chi}_1^\mp + \tilde{\chi}_1^\pm \tilde{\chi}_1^0$ production as a function of $\tilde{\chi}_1^\pm / \tilde{\chi}_1^0$ mass and branching fraction to Z bosons. Curves are derived separately when requiring that the charged-lepton decays of $\tilde{\chi}_1^\pm / \tilde{\chi}_1^0$ are into (top left) any leptons with equal probability, (top right) electrons only, (bottom left) muons only, or (bottom right) τ-leptons only. The expected 95% CL exclusion (dashed black line) is shown with $\pm 1\,\sigma_{\mathrm{exp}}$ variations (shaded yellow band) from systematic and statistical uncertainties in the expected yields. The observed 95% CL exclusion (solid red line) is shown with $\pm 1\,\sigma_{\mathrm{theory}}^{\mathrm{SUSY}}$ variations (dotted red lines) from cross-section uncertainties for the signal models. The phase-space excluded by the search is shown in the hatched regions. The sum of the $\tilde{\chi}_1^\pm / \tilde{\chi}_1^0$ branching fractions to W, Z, and Higgs bosons is unity for each point, and the branching fractions to W and Higgs bosons are chosen so as to be equal everywhere.

Figure 5.20: Exclusion curves for the simplified model of $\tilde{\chi}_1^\pm \tilde{\chi}_1^\mp + \tilde{\chi}_1^\pm \tilde{\chi}_1^0$ production as a function of the branching fractions to Z and Higgs bosons, assuming equal branching fractions to each lepton flavor. Results are shown for the charged-lepton decays of $\tilde{\chi}_1^\pm / \tilde{\chi}_1^0$ into any leptons with equal probability for $\tilde{\chi}_1^\pm / \tilde{\chi}_1^0$ masses of (top left) 600, (top right) 700, (bottom left) 800, and (bottom right) 900 GeV. The expected 95% CL exclusion (dashed black line) is shown with $\pm 1\,\sigma_{\mathrm{exp}}$ variations (shaded yellow band) from systematic and statistical uncertainties in the expected yields. The observed 95% CL exclusion (solid red line) is shown with $\pm 1\,\sigma_{\mathrm{theory}}^{\mathrm{SUSY}}$ variations (dotted red lines) from cross-section uncertainties for the signal models. The phase-space excluded by the search is shown in the hatched regions.

Figure 5.21: Exclusion curves for the simplified model of $\tilde{\chi}_1^\pm \tilde{\chi}_1^\mp + \tilde{\chi}_1^\pm \tilde{\chi}_1^0$ production as a function of the branching fractions to Z and Higgs bosons. Results are shown for the charged-lepton decays of $\tilde{\chi}_1^\pm / \tilde{\chi}_1^0$ into electrons only for $\tilde{\chi}_1^\pm / \tilde{\chi}_1^0$ masses of (top left) 600, (top right) 700, (bottom left) 800, and (bottom right) 900 GeV. The expected 95% CL exclusion (dashed black line) is shown with $\pm 1\,\sigma_{\mathrm{exp}}$ variations (shaded yellow band) from systematic and statistical uncertainties in the expected yields. The observed 95% CL exclusion (solid red line) is shown with $\pm 1\,\sigma_{\mathrm{theory}}^{\mathrm{SUSY}}$ variations (dotted red lines) from cross-section uncertainties for the signal models. The phase-space excluded by the search is shown in the hatched regions.

Figure 5.22: Exclusion curves for the simplified model of $\tilde{\chi}_1^\pm \tilde{\chi}_1^\mp + \tilde{\chi}_1^\pm \tilde{\chi}_1^0$ production as a function of the branching fractions to Z and Higgs bosons. Results are shown for the charged-lepton decays of $\tilde{\chi}_1^\pm / \tilde{\chi}_1^0$ into muons only for $\tilde{\chi}_1^\pm / \tilde{\chi}_1^0$ masses of (top left) 600, (top right) 700, (bottom left) 800, and (bottom right) 900 GeV. The expected 95% CL exclusion (dashed black line) is shown with $\pm 1\,\sigma_{\mathrm{exp}}$ variations (shaded yellow band) from systematic and statistical uncertainties in the expected yields. The observed 95% CL exclusion (solid red line) is shown with $\pm 1\,\sigma_{\mathrm{theory}}^{\mathrm{SUSY}}$ variations (dotted red lines) from cross-section uncertainties for the signal models. The phase-space excluded by the search is shown in the hatched regions.

Figure 5.23: Exclusion curves for the simplified model of $\tilde{\chi}_1^\pm \tilde{\chi}_1^\mp + \tilde{\chi}_1^\pm \tilde{\chi}_1^0$ production as a function of the branching fractions to Z and Higgs bosons. Results are shown for the charged-lepton decays of $\tilde{\chi}_1^\pm / \tilde{\chi}_1^0$ into τ-leptons only for $\tilde{\chi}_1^\pm / \tilde{\chi}_1^0$ masses of (top left) 200, (top right) 300, (bottom left) 400, and (bottom right) 500 GeV. The expected 95% CL exclusion (dashed black line) is shown with $\pm 1\,\sigma_{\mathrm{exp}}$ variations (shaded yellow band) from systematic and statistical uncertainties in the expected yields. The observed 95% CL exclusion (solid red line) is shown with $\pm 1\,\sigma_{\mathrm{theory}}^{\mathrm{SUSY}}$ variations (dotted red lines) from cross-section uncertainties for the signal models. The phase-space excluded by the search is shown in the hatched regions.
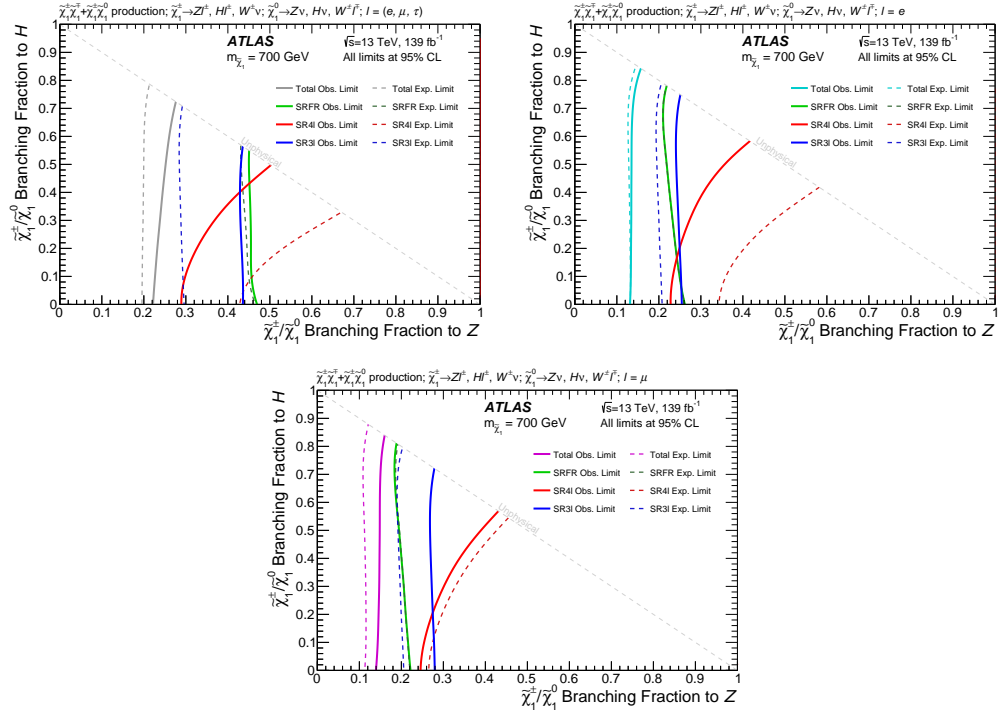
Figure 5.24: Exclusion curves for the simplified model of $\tilde{\chi}_1^\pm \tilde{\chi}_1^\mp + \tilde{\chi}_1^\pm \tilde{\chi}_1^0$ production as a function of the branching fractions to Z and Higgs bosons. Results are shown for the (green) SRFR, (red) SR4ℓ, and (blue) SR3ℓ regions separately as well as for the total from the regions combined for $\tilde{\chi}_1^\pm / \tilde{\chi}_1^0$ masses of 700 GeV. Results are shown for the charged-lepton decays of $\tilde{\chi}_1^\pm / \tilde{\chi}_1^0$ into (top left) any leptons with equal probability, (top right) electrons only, and (bottom) muons only. Both the observed 95% CL exclusion (solid line) and expected 95% CL exclusion (dashed line) are shown.

5.8.4 Public Likelihoods and pyhf

To preserve the statistical model and to facilitate reinterpretations of the results, the full likelihoods are made public on HEPData [215]. As mentioned in Section 5.7, the likelihoods are specified using the `HistFactory` [207] model. Based on the `RooFit/RooStats` [208] framework, `HistFactory` was developed for measurements based on binned data. Instead of interacting with `HistFactory` directly, this analysis uses a tool known as `HistFitter` [197] for the statistical model building, book-keeping, fitting, and hypothesis testing.

To build the statistical model, `HistFactory` requires a set of XML files that specify the form of the likelihood. The user must also provide `ROOT` files containing histograms of the observed data and expected background yields in the various channels. With a separate histogram for each channel, sample, and systematic variation, these `ROOT` files are large and difficult to publish. Additionally, since the histograms are stored in the binary `ROOT` format, the observed and expected yields are not human-readable. Finally, `HistFactory` is tied to `ROOT`, which is not as widely used or actively developed as Python or R.

Therefore, this search explored a new tool for performing statistical analysis in high energy physics: `pyhf`. A pure Python implementation of `HistFactory`, `pyhf` uses a likelihood specification based solely on the human-readable JSON format, which is ubiquitous in the software industry. Due to the small file sizes, the `pyhf` likelihoods are much easier to publish. With both a Python and command line Application Programming Interface (API), statistical analysis is easy in `pyhf`. For example, CL_s values can be calculated from the likelihoods via a single command or a couple lines of Python code. Additionally, `pyhf` benefits from all the useful libraries and active development of Python. By leveraging machine learning frameworks for tensor computations, `pyhf` can often perform fitting and hypothesis testing far quicker than the `ROOT`-based frameworks like `HistFitter`.

Before publishing the likelihoods for this analysis, they must be re-implemented in the `pyhf` framework and validated. This must be done for all signal models, as well as the background-only model. First, the `HistFactory` XML files and `ROOT` histograms were built using the nominal `HistFitter` setup. Afterwards, these files were converted to the `pyhf` JSON format using a built-in functionality of `pyhf`. As part of the verification process, the CL_s values for the $\tilde{\chi}_1^\pm/\tilde{\chi}_1^0$ signals were recalculated using `pyhf`. An overlay of the exclusion contours calculated using `HistFitter` and `pyhf` is shown in Figure 5.25. Additionally, the percent differences in the CL_s values are shown in Figure 5.26. The two frameworks produce very similar results, although the `pyhf` exclusions are slightly stronger.
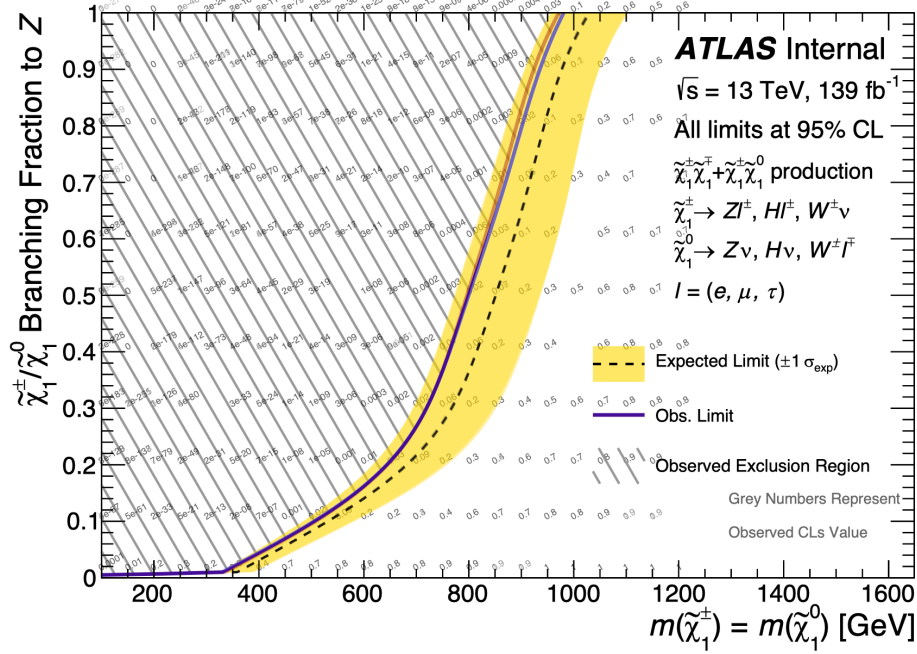
Figure 5.25: Overlay of the exclusions contours calculated using `HistFitter` (red) and `pyhf` (blue) for equal branching fractions to electrons, muons, and tau leptons.
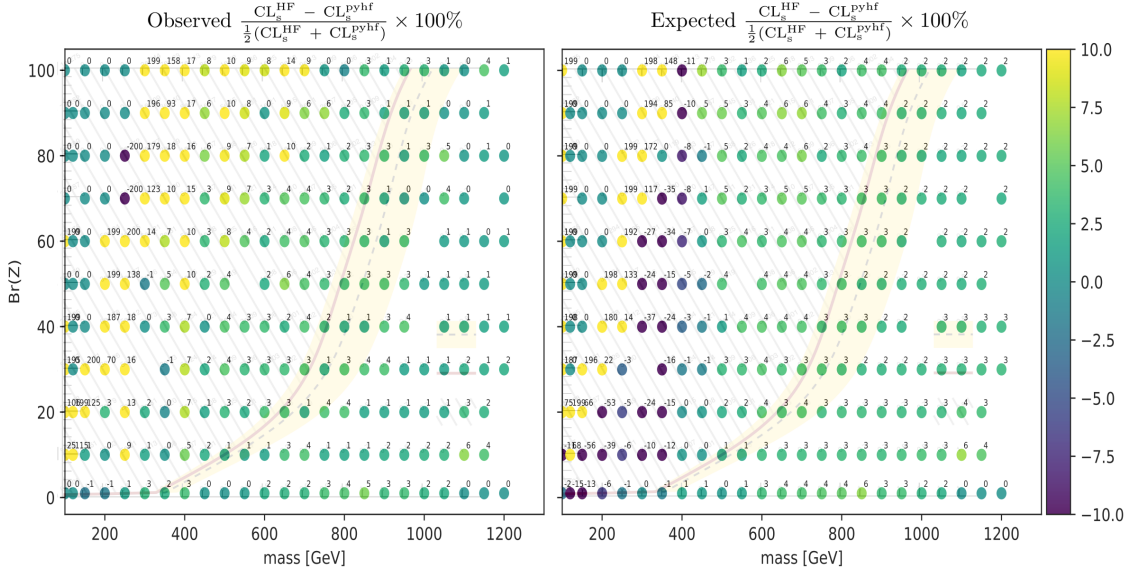
Figure 5.26: The percent difference between the CL_s values calculated by `HistFitter` and `pyhf`. The observed and expected CL_s percent differences are shown on the left and right, respectively. The two methods agree near the contour at the level of a few percent, with the `pyhf` exclusions being slightly stronger. Farther from the contour, where the CL_s values are extremely small, the differences can be large; however, these points are heavily excluded.

Instead of publishing separate likelihood specifications for the background-only model and the thousands of signal models, only the full background-only specification is uploaded. Separate JSON patches [216] are then created for each signal point and uploaded as well. When applied to the background-only JSON specification, these patches insert the expected signal yields in each channel and any associated systematics. With the background-only specification and signal patches, maximum likelihood estimation and hypothesis testing can be performed easily through either the command line or Python API. For example, the CL_s value for a particular signal model can be calculated from the command line using

```
$ pyhf cls bkgonly_LH_spec.json --patch signal_patch.json
```

This command will return the observed CL_s value, as well as the expected CL_s value with the $\pm 1\sigma$ and $\pm 2\sigma$ bands.

With `pyhf`, reinterpretations can be performed by patching in any new signal. However, the expected yields from this new signal must first be found. This typically involves reproducing the analysis selections and algorithms from the paper text, which can be difficult. These selections are then applied to a simulated sample of signal events, which must be corrected from truth-level to reconstruction-level in order to accurately estimate the signal yields in each channel. To ease this process, cutflow tables, signal acceptance and efficiency maps, and analysis code are also included in the HEPData entry [215]. The cutflows show the number of signal events that pass each analysis selection as they are applied sequentially. The truth-level signal acceptances and reconstruction efficiencies are provided in each signal region as a function of the $\tilde{\chi}_1^\pm / \tilde{\chi}_1^0$ mass and branching fractions. Finally, the analysis code demonstrate how the kinematic variables are calculated and event selections are applied. Some of the auxiliary results for the HEPData entry are reproduced in Appendix D.

5.9 Outlook

With no significant deviation from the Standard Model observed, this search provides strong limits on wino charginos and neutralinos in the $B - L$ MSSM, especially at high branching fractions to Z bosons and light leptons. With the limited statistics in some signal region $m_{Z\ell}$ bins, this analysis would benefit from the Run 3 dataset. Also, including reconstructed tau leptons in the analysis would help the sensitivity, as the current sensitivity to events with taus relies on their leptonic decays.

The limits on this model can also be improved by designing a new analysis targeting the hadronic decays of the bosons. These final states are particularly interesting for high mass signals, since the decay products of the bosons are collimated in large-radius jets. These bosonic jets could be distinguished from the background using jet substructure variables and boson tagging [217,218]. By requiring a lepton and a boson-tagged large-radius jet, the fully visible $\tilde{\chi}_1^\pm \to Z\ell \to qq\ell$, $\tilde{\chi}_1^\pm \to H\ell \to bb\ell$, and $\tilde{\chi}_1^0 \to W\ell \to qq\ell$ decays can be targeted. The $\tilde{\chi}_1^\pm/\tilde{\chi}_1^0$ signal would then produce a resonance in the $m_{J\ell}$ distribution. Like the trilepton resonance analysis, information from the second $\tilde{\chi}_1^\pm/\tilde{\chi}_1^0$ decay can be used to discriminate the signal from the background. Three signal regions can be similarly defined, with the reconstructed bosons replaced by a boson-tagged large-radius jet. While the $\tilde{\chi}_1^\pm/\tilde{\chi}_1^0$ mass resolution would be worse than in the trilepton analysis, this new search would cover many more $\tilde{\chi}_1^\pm \tilde{\chi}_1^\mp/\tilde{\chi}_1^\pm \tilde{\chi}_1^0$ final states while also benefiting from the higher hadronic branching fractions of the bosons. With sensitivity to all three bosons, the results of this new analysis would be more robust to variations in the $\tilde{\chi}_1^\pm/\tilde{\chi}_1^0$ branching fractions. The increased sensitivity to $\tilde{\chi}_1^\pm \to H\ell$ decays is particularly interesting, as this decay channel is favored by the parameter space scan discussed in Chapter 2.

Finally, the results from the trilepton resonance search can be maximized by performing reinterpretations for other signals. For example, the type-III seesaw mechanism predicts the existence of isospin triplets of heavy leptons $(\Sigma^+, \Sigma^0, \Sigma^-)$ that mix with the active neutrinos, generating their small masses [219]. While their production cross sections differ, the $\Sigma^\pm$ and Σ^0 have the same decay paths as the $\tilde{\chi}_1^\pm$ and $\tilde{\chi}_1^0$, particularly $\Sigma^\pm \to Z\ell \to \ell\ell\ell$. Alternatively, the trilepton results can be reinterpreted for vector-like lepton signals, like those in composite Higgs models [220]. These vector-like leptons are non-chiral and can have mass terms in the Lagrangian without violating the gauge symmetries. Instead of acquiring mass through the Higgs mechanism, the Standard Model leptons become massive by mixing with the vector-like leptons. These models are appealing as they may explain the observed hierarchy in the lepton masses. The heavy vector-like leptons again have decays similar to the charginos and neutralinos targeted by this analysis. As discussed in Section 5.8.4, these reinterpretations are facilitated by the publication of the full likelihoods, cutflows, truth acceptances, reconstruction efficiencies, and sample analysis code to HEPData.

CHAPTER 6

Conclusion

This dissertation has presented the performance of the Transition Radiation Tracker compression algorithm under the strenuous conditions of Run 2, as well as a search for trilepton resonances from the R-parity violating decays of charginos in the $B - L$ MSSM. The theoretical framework of the SM and $B - L$ MSSM was established in Chapter 2, followed by a brief introduction to the LHC and the ATLAS detector in Chapter 3.

Chapter 4 focused on the readout bandwidth limitations of the TRT and the upgrades performed in Run 2. To operate the TRT at high trigger rates, the straw data must be compressed before it is sent off the detector. While the lossless Huffman algorithm drastically reduces the data size, it proved insufficient under the harsher conditions of Run 2. As the pileup, detector occupancy, and Level-1 trigger rate increased, the TRT approached its bandwidth limit. Therefore, a new lossy compression scheme was developed which improved the compression performance at the expense of some information loss. This lossy scheme was designed such that the tracking capabilties of the TRT were unaffected. While the compression performance was significantly improved by the lossy scheme, the more complicated logic was difficult to implement in the firmware. Ultimately, the original Huffman algorithm was reoptimized on the new high pileup data. In parallel, a hardware upgrade was performed to increase the total available bandwidth. With the increased bandwidth and improved compression, the TRT successfully collected the high pileup Run 2 data at the maximum trigger rate of 100 kHz.

Presented in Chapter 5 is the first trilepton resonance search at the LHC in Run 2. This analysis was inspired by the $B - L$ MSSM with spontaneous R-parity violation, where the LSPs are the mass-degenerate wino chargino and neutralino. Targeting charginos decaying via $\tilde{\chi}_1^{\pm} \to Z\ell \to \ell\ell\ell$, a search was performed for resonances in the trilepton invariant mass spectrum. Unfortunately, no significant

deviation from the Standard Model was observed. Limits were set on the $\tilde{\chi}_1^\pm \tilde{\chi}_1^\mp + \tilde{\chi}_1^\pm \tilde{\chi}_1^0$ signal as a function of the $\tilde{\chi}_1^\pm / \tilde{\chi}_1^0$ mass and branching fractions to SM bosons and leptons. Additionally, model-independent limits were set on generic signals in each individual mass bin. Finally, to facilitate reinterpretations of these results, the full likelihoods were published to HEPData in the `pyhf` format.

While compelling evidence of physics beyond the Standard Model has yet to be observed, much of the LHC data remains unexplored. Supersymmetry is an extremely rich framework with many possible low-energy manifestations. SUSY may present itself through new particles, anomalous rates, modified couplings, or new interactions. Therefore, the LHC experiments benefit from a diverse program of precision measurements and searches for new physics. While the simplest and most easily discoverable supersymmetric models were not found, SUSY may still be lurking in the Run 2 dataset. With Run 3 starting in the coming years, followed by the High-Luminosity LHC, the discovery potential of ATLAS and CMS will only increase. Perhaps new physics, whatever it may be, is waiting just around the corner.

Appendices

SR4ℓ Optimization

In SR4ℓ, the second $\tilde{\chi}_1^\pm/\tilde{\chi}_1^0$ decay cannot be fully reconstructed. Therefore, the mass asymmetry cannot be used to choose the correct three leptons to reconstruct the $\tilde{\chi}_1^\pm \to Z\ell \to \ell\ell\ell$ decay. Each event contains at least four leptons, two of which reconstruct a Z boson. Choosing the correct third lepton to pair with the Z is difficult, as the event kinematics change drastically with the $\tilde{\chi}_1^\pm/\tilde{\chi}_1^0$ mass. At low mass, the $\tilde{\chi}_1^\pm\tilde{\chi}_1^\mp/\tilde{\chi}_1^\pm\tilde{\chi}_1^0$ pair are boosted and recoil against each other. As a result, the decay products of each $\tilde{\chi}_1^\pm/\tilde{\chi}_1^0$ are collimated. At high mass, the $\tilde{\chi}_1^\pm\tilde{\chi}_1^\mp/\tilde{\chi}_1^\pm\tilde{\chi}_1^0$ pair are produced almost at rest, so the *direct* lepton and Z boson from the $\tilde{\chi}_1^\pm \to Z\ell$ decay are well-separated.

To maximize the sensitivity over a range of possible $\tilde{\chi}_1^\pm/\tilde{\chi}_1^0$ masses, an SR4ℓ-specific matching algorithm was developed. The goal was to find a kinematic variable to serve as a proxy for the $\tilde{\chi}_1^\pm/\tilde{\chi}_1^0$ mass, allowing separate matching algorithms at low and high mass. This proxy mass has to be appropriate for the full range of final states targeted by SR4ℓ. The common feature of all these targeted final states is the presence of at least four leptons. Consequently, the scalar p_T-sum of all the leptons in the event, L_T, was used as the proxy for the $\tilde{\chi}_1^\pm/\tilde{\chi}_1^0$ mass:

$$L_\mathrm{T} = \sum_{\mathrm{leps}} p_\mathrm{T}. \tag{A.1}$$

The observed data and pre-fit background L_T distributions are shown in Figure A.1, and the unit-normalized $\tilde{\chi}_1^\pm\tilde{\chi}_1^\mp$ signal distributions are shown in Figure A.2 for a range of $\tilde{\chi}_1^\pm$ masses. While the background peaks at low L_T, the signal distribution peaks above the $\tilde{\chi}_1^\pm$ mass, becoming harder and more broad as the $\tilde{\chi}_1^\pm$ mass increases.

After studying many methods for selecting the correct *direct* lepton, the following algorithm was chosen. If an event has $L_\mathrm{T} < 550$ GeV, it is assumed to be a low mass signal, and the lepton that minimizes $\Delta R(Z, \ell)$ is chosen to reconstruct the $\tilde{\chi}_1^\pm \to Z\ell \to \ell\ell\ell$ decay. If an event has $L_\mathrm{T} > 550$
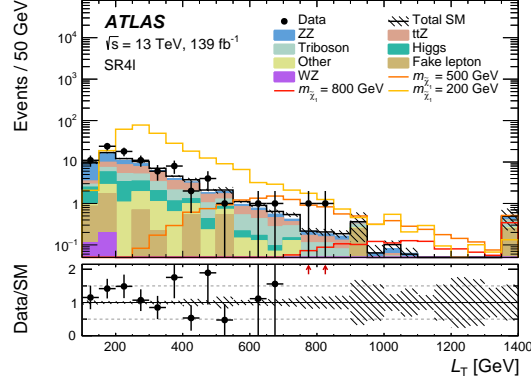
Figure A.1: The observed data and pre-fit SM background expectation as a function of L_T in SR4ℓ. The last bin includes overflow events. The "Other" category consists mostly of the tWZ, $t\bar{t}W$ and tZ processes. Only statistical uncertainties on the data and background expectation are shown. The bottom panel shows the ratio between the data and the pre-fit background prediction.
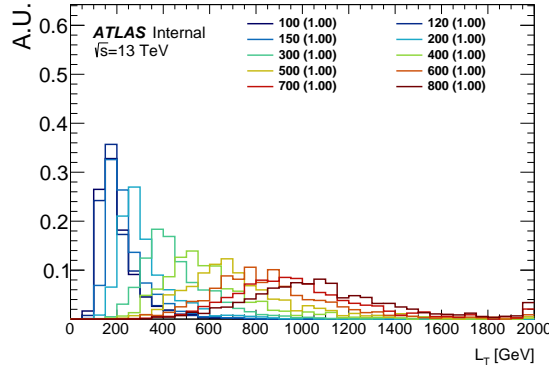
Figure A.2: The unit-normalized L_T distributions in SR4ℓ for $\tilde{\chi}_1^\pm \tilde{\chi}_1^\mp$ signals.

GeV, it is assumed to be a high mass signal, and the lepton that maximizes $m_{\mathrm{Z}\ell}$ is chosen instead. The efficiency for choosing the correct three leptons to reconstruct the $\tilde{\chi}_1^\pm \to Z\ell \to \ell\ell\ell$ decay under this algorithm is shown in Figure A.3 as a function of the $\tilde{\chi}_1^\pm$ mass on the x-axis and the L_T value used to switch between the two methods on the y-axis.

To determine the optimal L_T value at which to switch between the $\min\left[\Delta R(Z, \ell)\right]$ and $\max\left[m_{\mathrm{Z}\ell}\right]$ methods for selecting the *direct* lepton, several factors must be considered. By maximizing the efficiency for choosing the correct three leptons to reconstruct the $\tilde{\chi}_1^\pm \to Z\ell \to \ell\ell\ell$ decay, the signal $m_{\mathrm{Z}\ell}$ distribution becomes more strongly peaked at the true $\tilde{\chi}_1^\pm$ mass. However, this does not necessarily lead to the optimal sensitivity, as various matching algorithms may shape the background $m_{\mathrm{Z}\ell}$ distribution differently. Additionally, since a shape-fit is performed in the signal regions, all $m_{\mathrm{Z}\ell}$

Hybrid Eff (minDR or maxMZI)
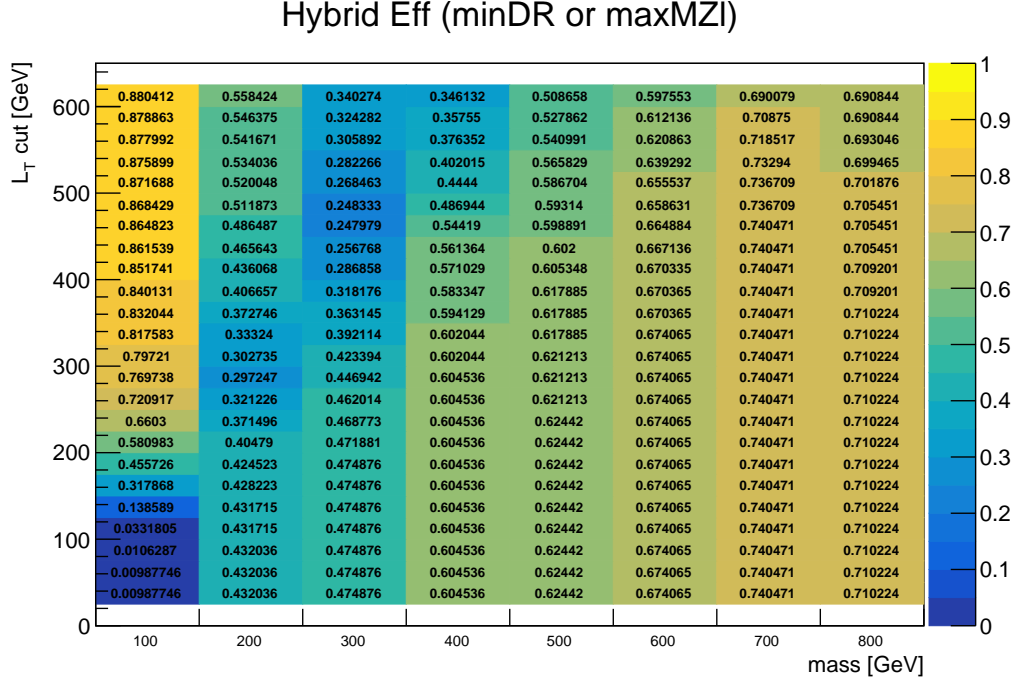
Figure A.3: The correct lepton selection efficiency in SR4ℓ. The efficiency only considers events where all three leptons from a chargino decay are reconstructed and pass the signal lepton requirements. Below the L_T cut on the y-axis, the *direct* lepton is chosen via minimizing $\Delta R(Z, l)$. Otherwise, the *direct* lepton is chosen via maximizing $m_{Z\ell}$.

bins contribute to the sensitivity. As a result, even the mismatched signal events in the combinatorial tails of the $m_{Z\ell}$ distribution can contribute to the sensitivity.

Various matching algorithms were evaluated using `HistFitter` [197] to perform the shape-fit, with the algorithm described above providing the best sensitivity over the probed $\tilde{\chi}_1^\pm/\tilde{\chi}_1^0$ mass range. Shown in Figure A.4 are the expected CL_s upper limits on μ_{sig} for a wide range of methods for selecting the *direct* lepton. The tested methods include:

- *minDR*: choose lepton closest in ΔR to the reconstructed Z boson.

- *min*: choose lepton that minimizes $m_{Z\ell}$.

- *max*: choose lepton that maximizes $m_{Z\ell}$.

- *hybrid_*[L_T^{switch}]: if $L_T < L_T^{\text{switch}}$, use *minDR*, else use *max*.

- *hybrid_minmax_*[L_T^{switch}]: if $L_T < L_T^{\text{switch}}$, use *min*, else use *max*.
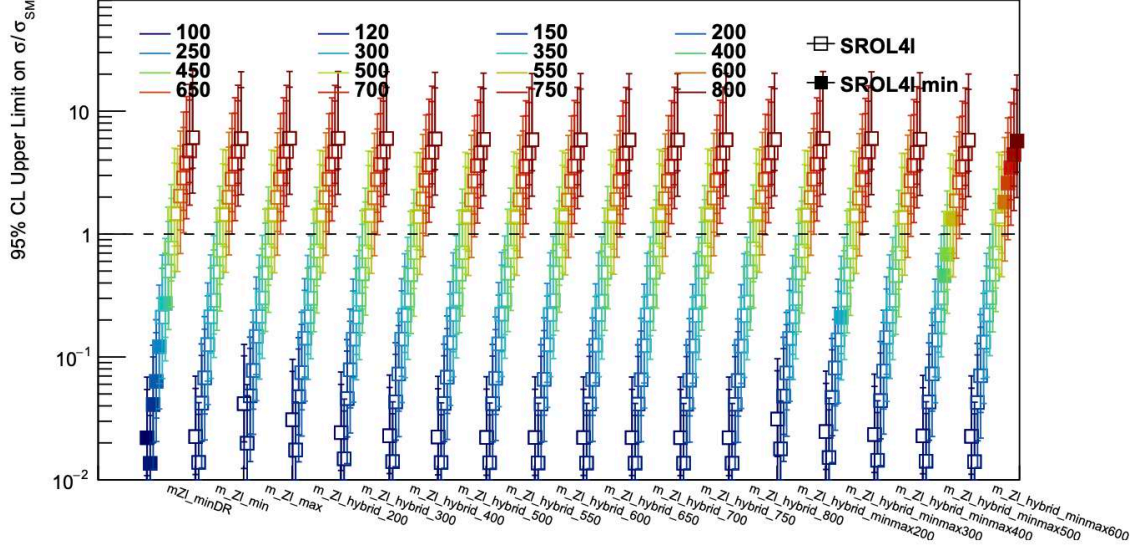
Figure A.4: Upper limit on μ_{sig} for each mass point in SR4ℓ, for various lepton matching schemes. The numbers in some labels represent the L_{T} value used for this scheme. On each plot there is one filled point for each mass point. This filled point marks the lowest limit achieved for this mass point.

Various values are also tested for $L_{\text{T}}^{\text{switch}}$ in the *hybrid* and *hybrid_minmax* methods, ranging from 200 to 800 GeV. There are two sets of error bars on each point in the plot, $\pm 1\sigma$ and $\pm 2\sigma$, which only include statistical uncertainties. For each $\tilde{\chi}_1^{\pm}/\tilde{\chi}_1^0$ mass tested, there is one filled marker indicating the lowest limit achieved for this mass.

In Figure A.5, the relative differences between the limit achieved from a given method and the best limit achieved from any method is shown. The method with the lowest spread was chosen for the analysis: *hybrid_550*. For all tested mass points, the expected upper limits on the signal strength when using *hybrid_550* are within 10% of the best limits from any method.
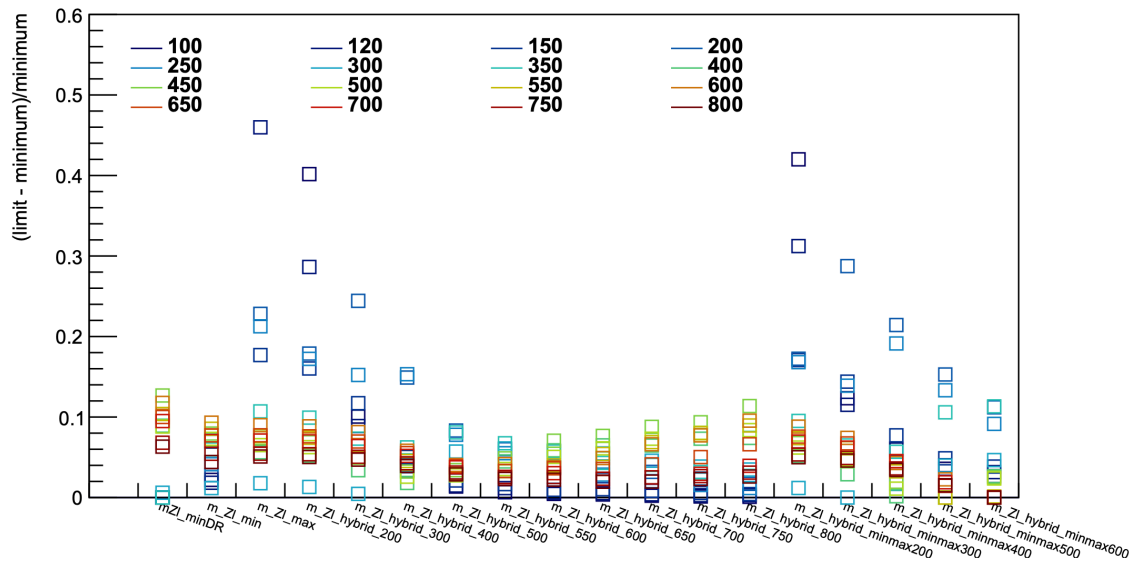
Figure A.5: Relative difference between each lepton matching scheme and the best performing scheme for each mass point.

Fake Studies

This appendix presents additional studies regarding the fake lepton background and its estimation. First, alternative parameterization of the fake factors are shown in Appendix B.1. Afterwards, to better understand the dependence on event-level kinematic requirements, these fake factors are derived in VRFake and shown in Appendix B.2. In Appendices B.3 and B.4, the data vs. expected background agreement in VRFake is studied, but using the p_{T}-binned fake factors or Z+jets MC instead. Next, the fake lepton composition in each analysis region is shown in Appendix B.5. Finally, the light and heavy flavor MC fake factors are presented in Appendix B.6.

B.1 Alternative Fake Factor Parameterizations

As described in Section 5.5.2, the nominal fake factors used for this analysis are binned in $p_{\mathrm{T}}^{\mathrm{cone}}$. Other choices for the parameterization of the fake factors are shown in Figures B.1-B.2. The fake factors are independent of the variable chosen in some cases (η, ϕ, N_{jets}) but clearly depend on the variable in other cases (lepton p_{T}, $E_{\mathrm{T}}^{\mathrm{miss}}$). This is only concerning if the nominal $p_{\mathrm{T}}^{\mathrm{cone}}$ parameterization does not already account for this dependence. For example, a clear downward trend can be seen in the $E_{\mathrm{T}}^{\mathrm{miss}}$-binned fake factors, especially for electrons. If this information isn't captured in our nominal parameterization (i.e. if $E_{\mathrm{T}}^{\mathrm{miss}}$ isn't correlated with $p_{\mathrm{T}}^{\mathrm{cone}}$), this may lead to worse agreement in analysis regions that require significant $E_{\mathrm{T}}^{\mathrm{miss}}$. A systematic uncertainty associated with the choice of fake factor parameterization is assessed (see Appendix C).

The data and MC fake factor agreement is generally worse for electrons than muons, possibly due to the more complicated fake electron composition. While the fake muons are almost always the result of a heavy flavor decay, the electrons are a mix of heavy and light flavor fakes (see B.5).
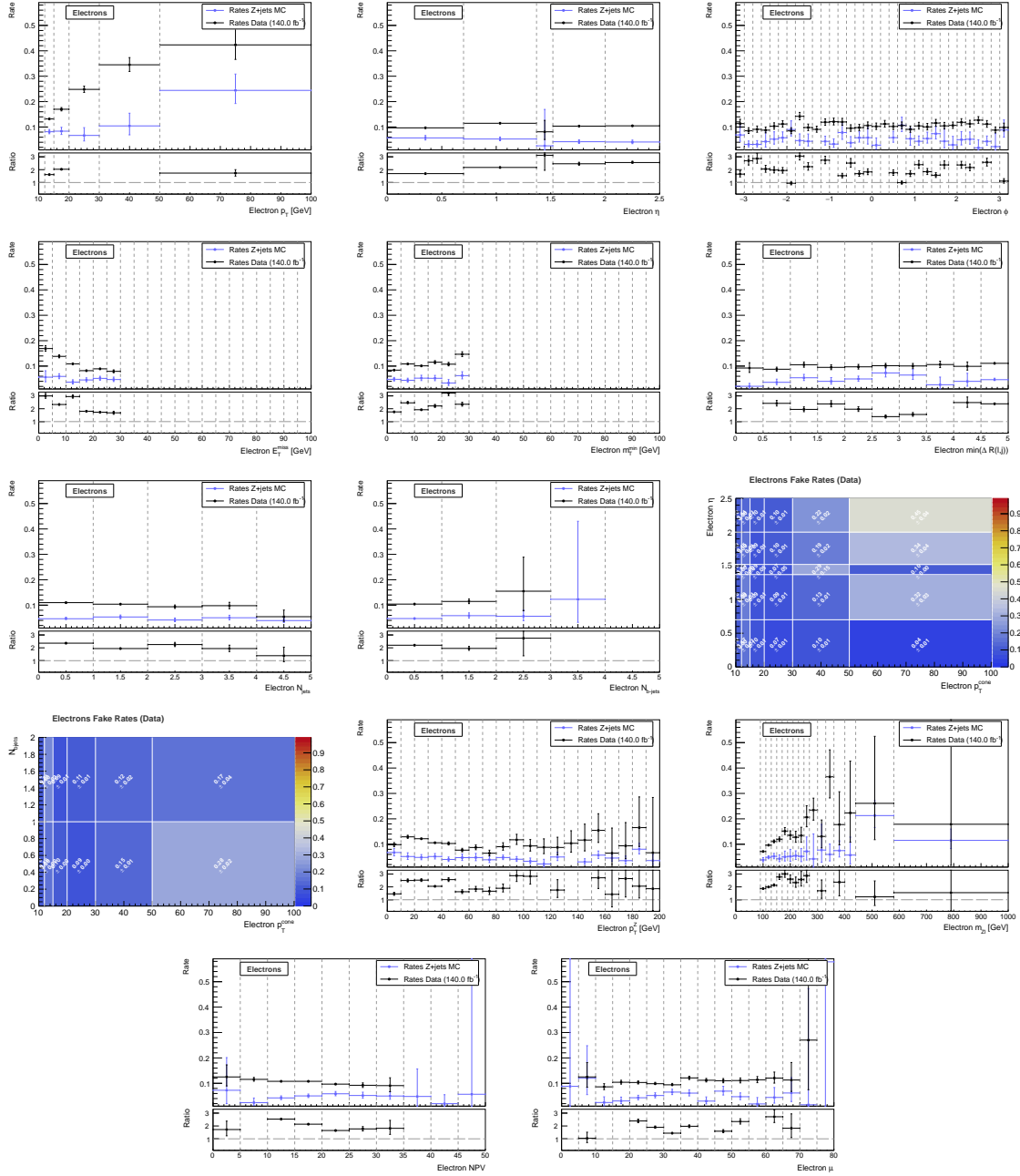
Figure B.1: Various parameterizations of the electron Z+jets fake factors. All uncertainties shown are only statistical.
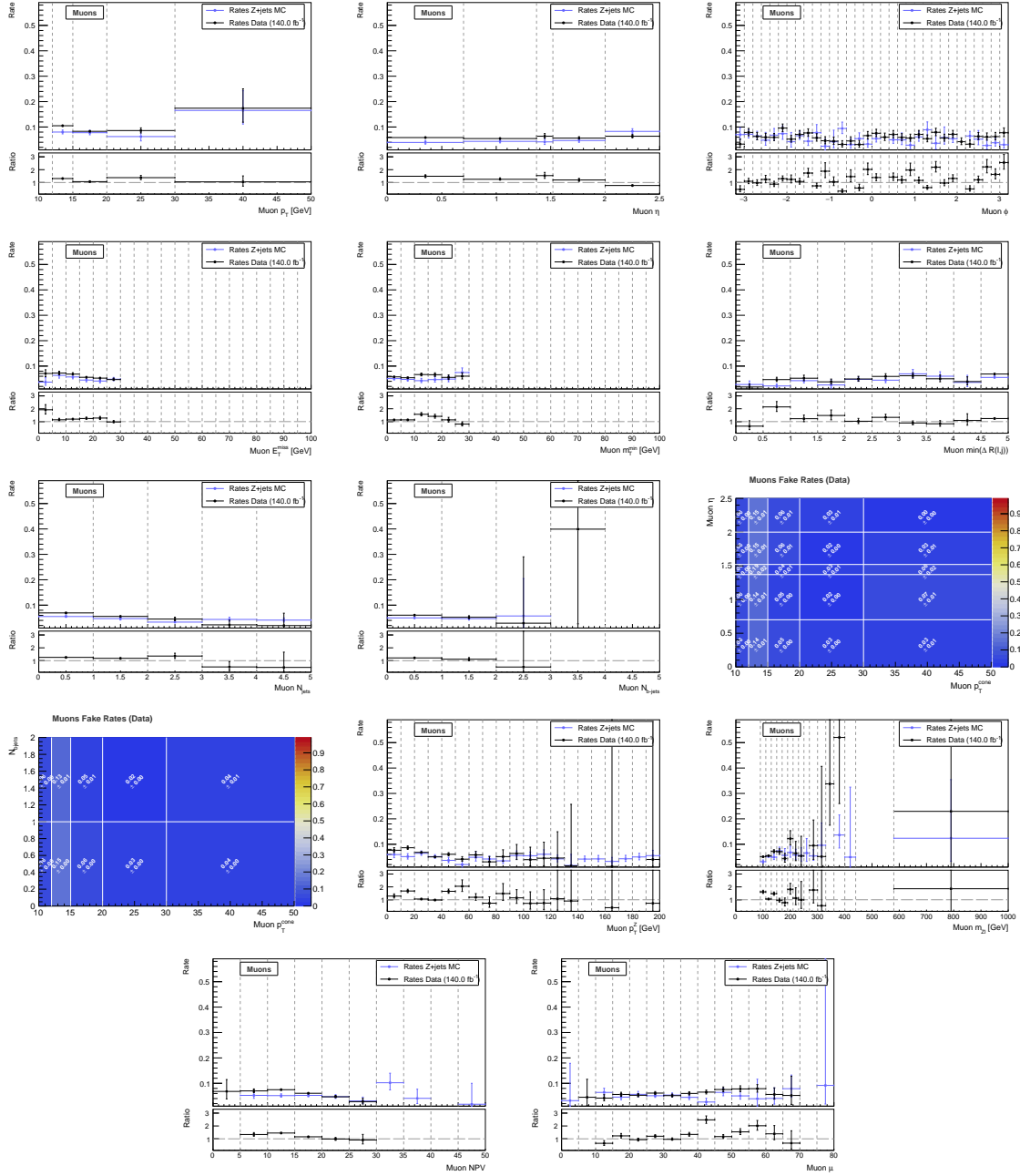
Figure B.2: Various parameterizations of the muon Z+jets fake factors. All uncertainties shown are only statistical.

B.2   Fake Factors Derived in the Validation Region

To better understand any discrepancies between the data and the estimated background in the validation region (VRFake), the fake factors were measured in VRFake. While the control region (CRFake) requires $E_T^{miss} < 30$ GeV, VRFake requires 30 GeV $< E_T^{miss} < 80$ GeV. The fake factors measured in VRFake are shown in Figures B.3 and B.4. In general, the fake factors are lower in the validation region, suggesting that it is harder for a baseline lepton to pass the signal requirements. This is consistent with the slight over-prediction of the background in the validation region seen in Fig. 5.8- 5.12. The over-prediction is a bit worse for fake electrons, as seen in the lowest lepton p_T bin in Fig. 5.8. This can also be seen in the $n_e = 1$ or $n_e = 3$ bins in Fig. 5.12, since the non-Z (and likely fake) lepton in these events is an electron.

As shown in Appendix B.1, the E_T^{miss}-binned fake factors decrease quickly with increasing E_T^{miss} in CRFake. Here in VRFake, the fake factors continue to decrease, but more gradually. This suggests that the higher E_T^{miss} requirement of VRFake is the cause of the lower fake factors. As will be shown in Appendix B.5, the higher E_T^{miss} requirement shifts the Z+jets fake composition towards heavy flavor (HF) fakes, which are produced alongside neutrinos in the semileptonic decays of HF hadrons. Also, the E_T^{miss} may be correlated with the p_T of the HF hadron giving rise to the non-prompt lepton. The higher E_T^{miss} requirement may therefore bias the selection towards harder HF jets, which have more collimated decay products and larger d_0-significance values. As a result, the non-prompt leptons produced in the HF hadron decays may fail the signal impact parameter and isolation requirements at higher rates, reducing the fake factors.

Via an analogous argument, one would expect the fake factors to decrease with increasing lepton p_T, as the non-prompt lepton p_T is also correlated with the boost of the underlying jet. Indeed, the heavy flavor MC fake factors decrease with p_T, as shown in Appendix B.6. The p_T of the reconstructed Z boson might also be a handle on the underlying jet p_T if the two recoil against each other; however, the inclusive jet selection may decrease the correlation. In both the measurement and validation regions, the p_T^Z-binned fake factors decrease with the Z boson momentum.

The observed sensitivity to the underlying jet momentum motivated the parameterization of the fake factors in p_T^{cone}. Initially, the more conventional p_T parameterization was attempted, and the validation region distributions are shown in Appendix B.3. The over-prediction of the fake background was much worse using the p_T-binned fake factors, presumably because it is a worse estimate of the underlying jet momentum. Also, the validation region distributions using MC for all background estimates are shown in Appendix B.4.

It is possible that binning the FFs in both p_T^{cone} and E_T^{miss} would improve the agreement in this Z+jets dominated fake factor validation region. However, this is problematic for two reasons:

1. The fake factor region is defined with $E_T^{\text{miss}} < 30$ GeV, while the validation region has $30 < E_T^{\text{miss}} < 80$. As a result, only the fake factors from the highest E_T^{miss} bin would be applied to all anti-ID events in the validation region. Additionally, all other analysis regions have significant portions of their phase-space at $E_T^{\text{miss}} > 30$ GeV.

2. The fake factor estimate must cover fakes from other processes (e.g. leptonic $t\bar{t}$). These can have sources of E_T^{miss} other than the neutrino from the HF decay. As a result, fakes from other processes will have a different E_T^{miss} profile.

In conclusion, since p_T^{cone} is a lepton-level variable, unlike the event-level E_T^{miss}, the p_T^{cone}-binned fake factors should be more applicable to processes other than Z+jets.
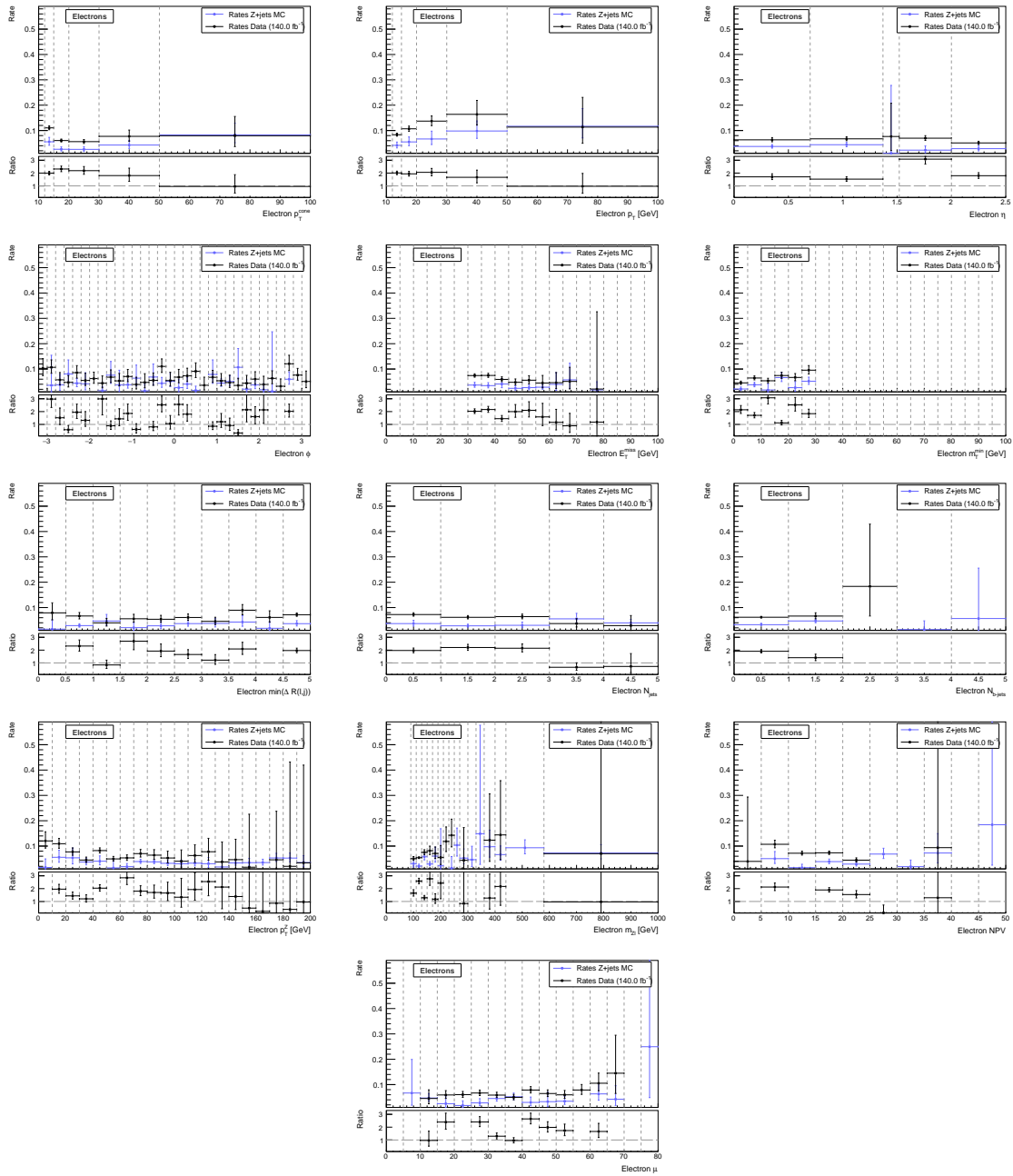
Figure B.3: Various parameterizations of the electron Z+jets fake factors, **but measured in the validation region.** All uncertainties shown are only statistical. The fake factors measured here are lower in general compared to those measured in the fake factor measurement region, which is consistent with the over-prediction of the background in the validation region shown in Fig. 5.8-5.12.
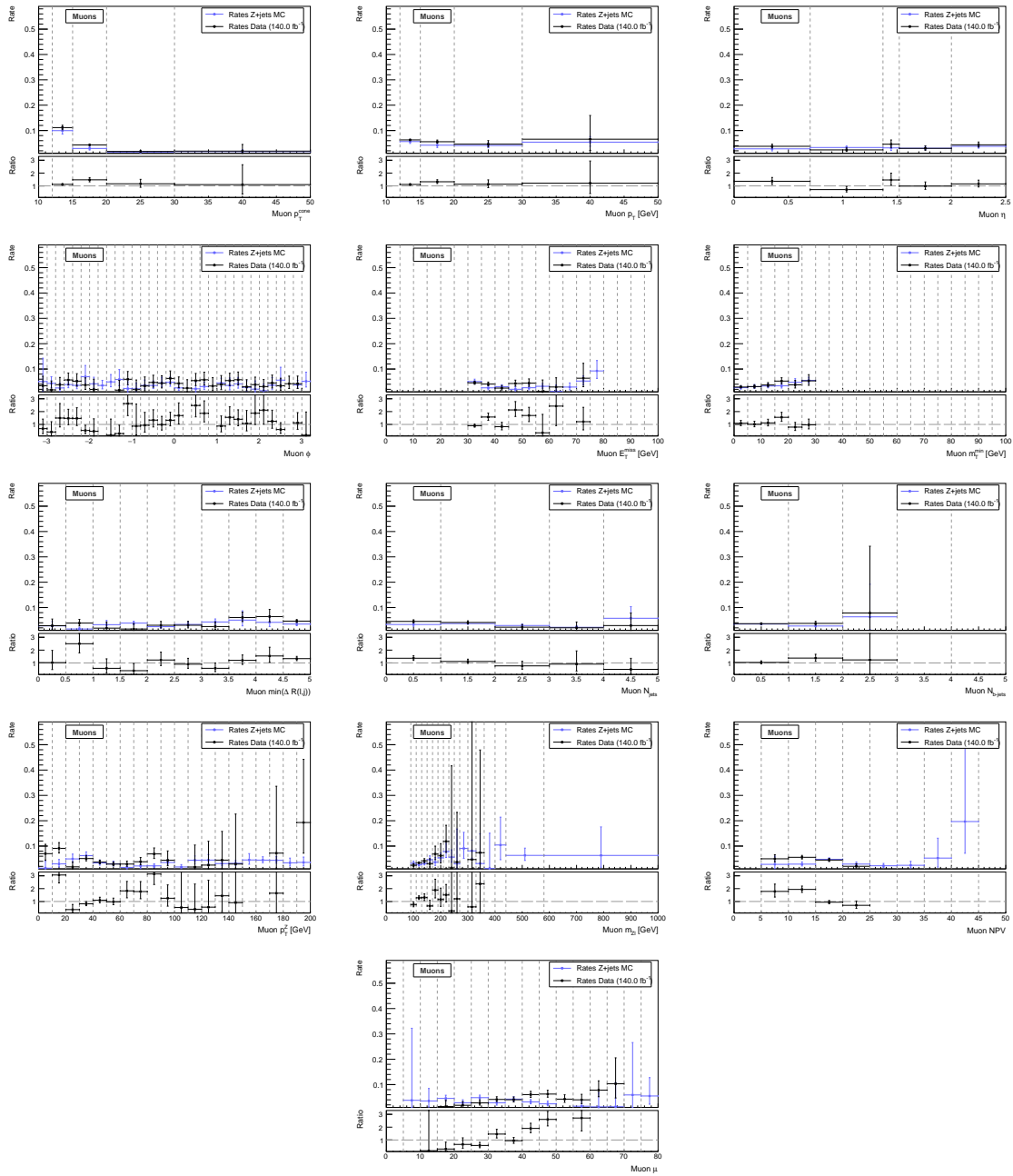
Figure B.4: Various parameterizations of the muon $Z+$jets fake factors, **but measured in the validation region.** All uncertainties shown are only statistical. The fake factors measured here are lower in general compared to those measured in the fake factor measurement region, which is consistent with the over-prediction of the background in the validation region shown in Fig. 5.8-5.12.

B.3 Validation Region Agreement Using p_T-binned Fake Factors

The following figures show the kinematic distributions in the fake factor validation region, but using the p_T-binned fake factors instead. The data vs. estimated background agreement is noticeably worse than that achieved using the nominal p_T^{cone} fake factor parameterization (Section 5.5.2).
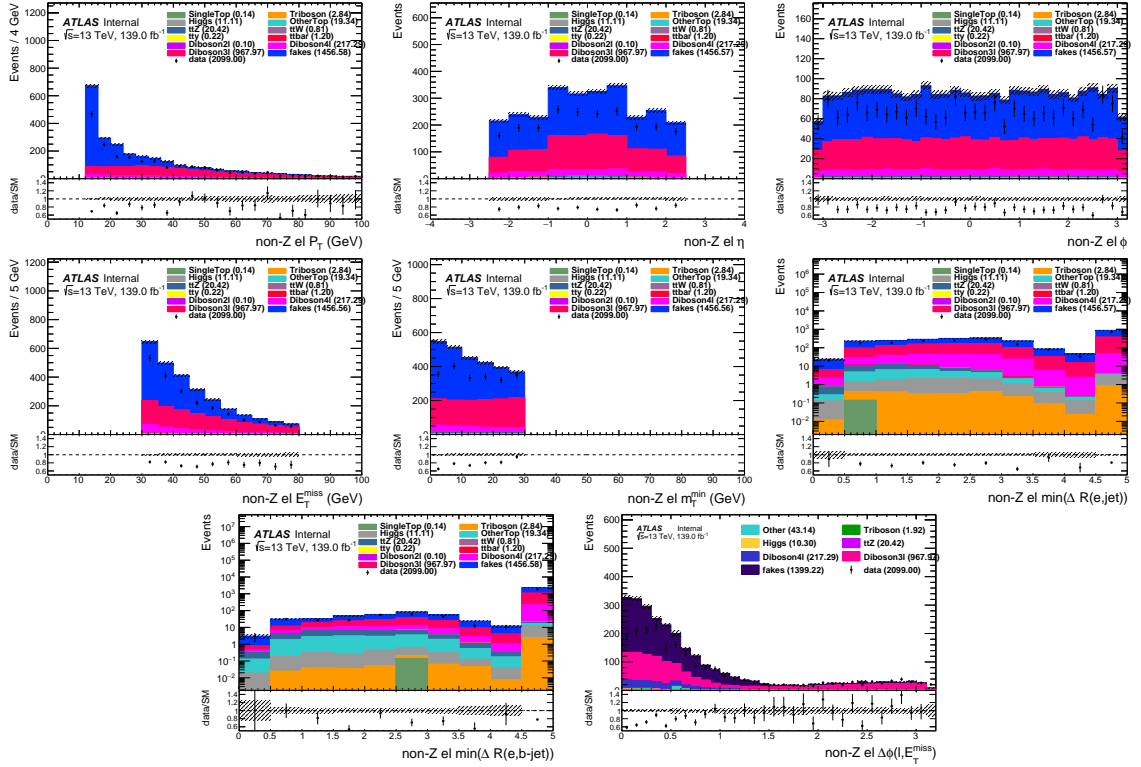
Figure B.5: Various kinematics in the fake factor validation region when the non-Z lepton is an electron, **but using the p_T-binned fake factors instead**. This lepton is most likely the fake in the Z+jets events. In the $\min\Delta R(e, \text{jet})$ and $\min\Delta R(e, \text{b-jet})$ distributions, events without a (b-tagged) jet are added to the overflow. All uncertainties shown are only statistical.
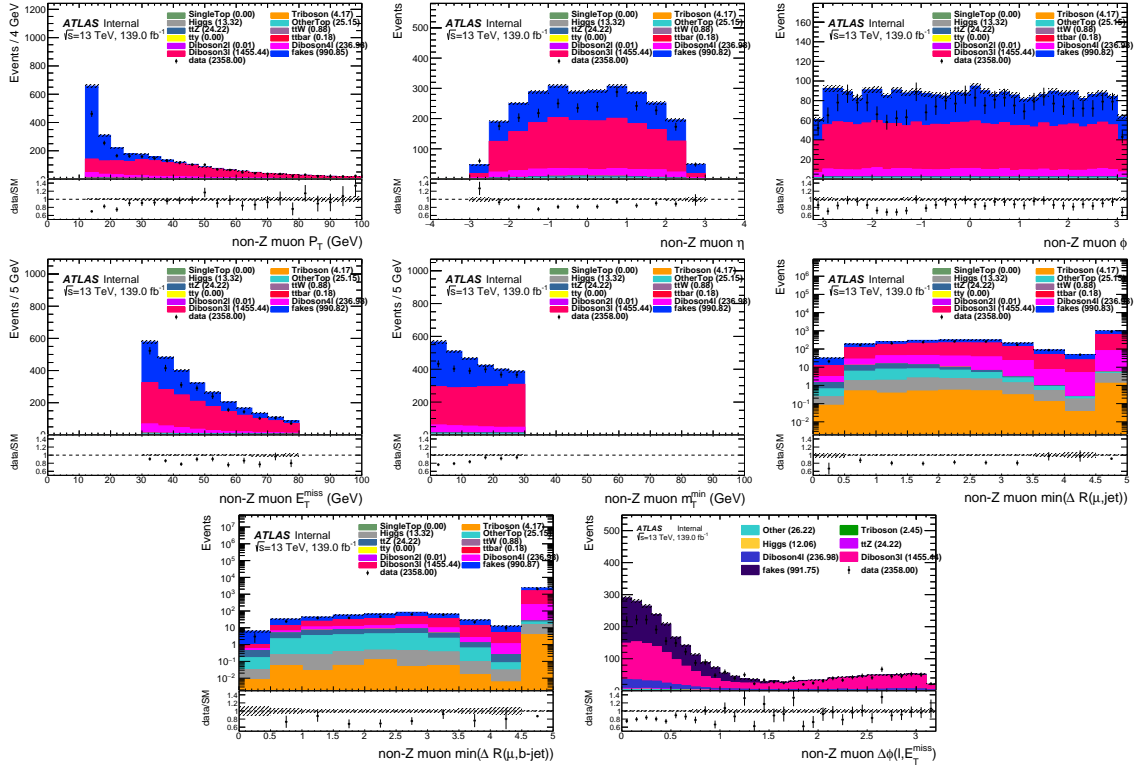
Figure B.6: Various kinematics in the fake factor validation region when the non-Z lepton is a muon, **but using the p_T-binned fake factors instead**. This lepton is most likely the fake in the Z+jets events. In the min$\Delta R(\mu, \text{jet})$ and min$\Delta R(\mu, \text{b-jet})$ distributions, events without a (b-tagged) jet are added to the overflow. All uncertainties shown are only statistical.

Figure B.7: The p_T, η, and ϕ distributions of the leading, subleading, and third leptons in VRFake when they are electrons, **but using the p_T-binned fake factors instead**. All uncertainties shown are only statistical.
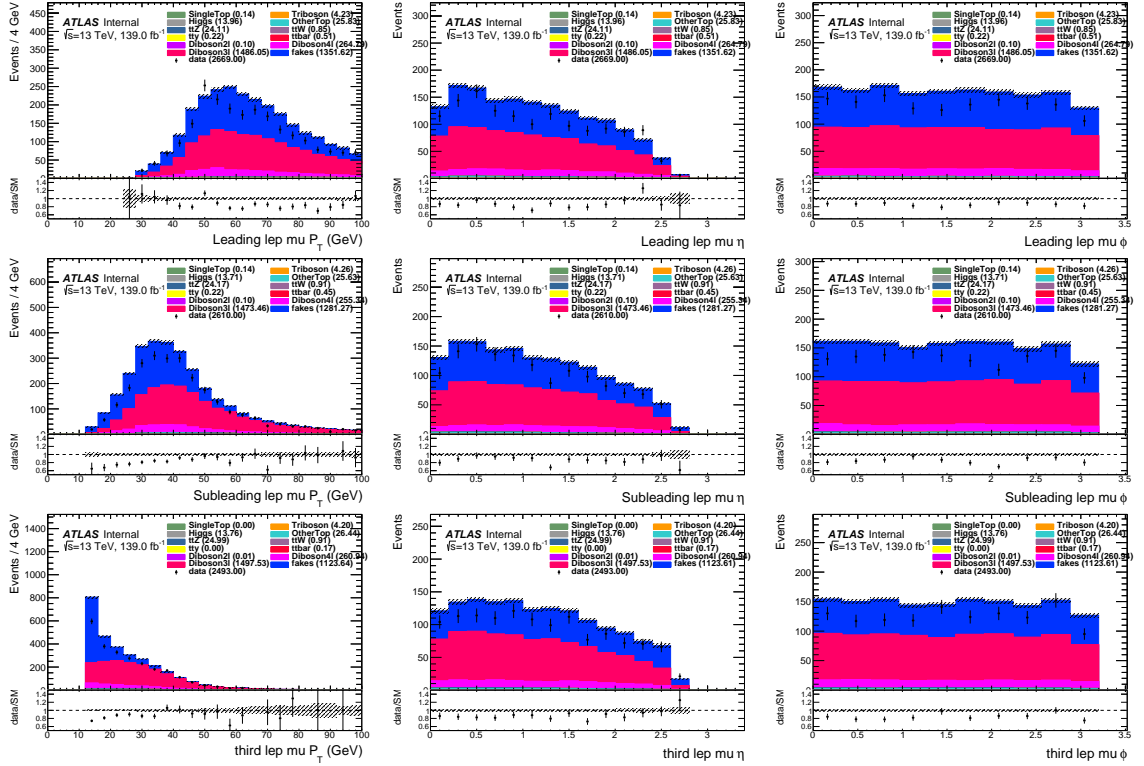
Figure B.8: The p_T, η, and ϕ distributions of the leading, subleading, and third leptons in VRFake when they are muons, **but using the p_T-binned fake factors instead**. All uncertainties shown are only statistical.
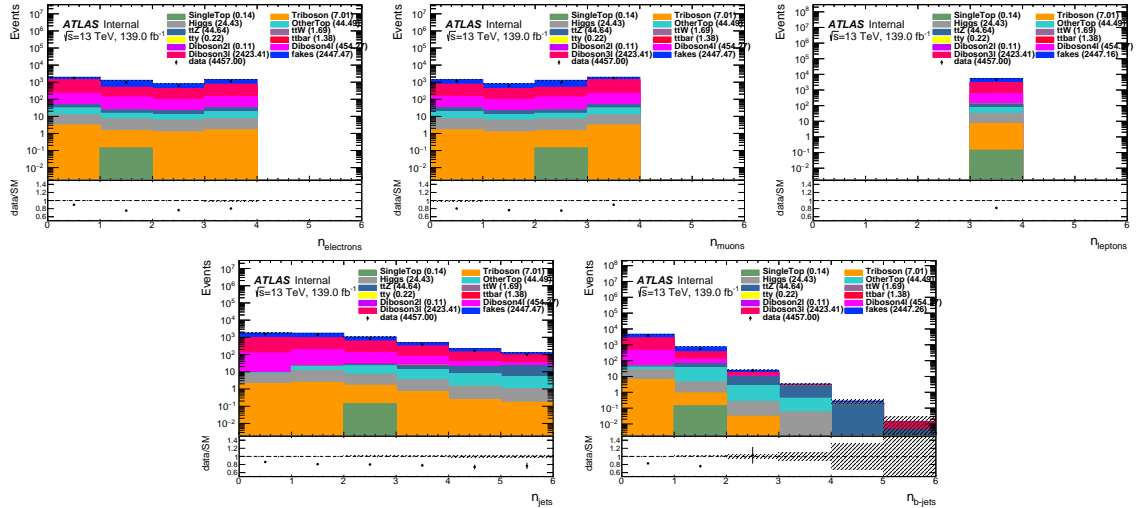
Figure B.9: Object multiplicity distributions in the fake factor validation region, **but using the p_T-binned fake factors instead**. All uncertainties shown are only statistical.
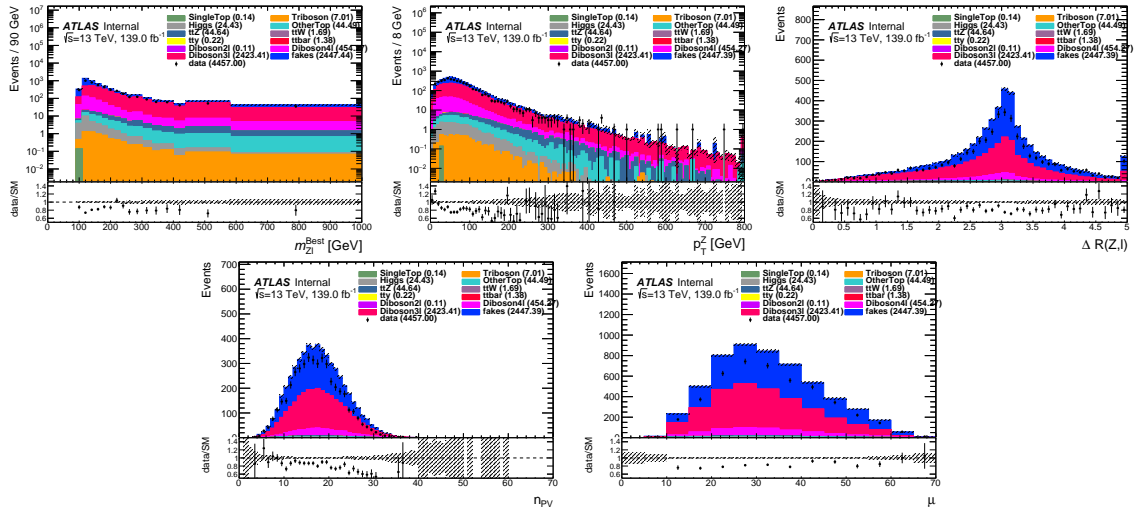
Figure B.10: Additional event level variable distributions in VRFake, **but using the p_T-binned fake factors instead**. All uncertainties shown are only statistical.

B.4 Validation Region Agreement Using MC Only

The following figures show the kinematic distributions in the fake factor validation region using only MC for all background estimates. Instead of the fake factor method, the fake estimates is taken directly from MC. The data vs. estimated background agreement is noticeably worse than that achieved using the data-driven fake factor method with the $p_{\mathrm{T}}^{\mathrm{cone}}$ fake factor parameterization (Section 5.5.2). Additionally, the Z+jets MC statistical errors are much larger than those of the fake factor estimate.
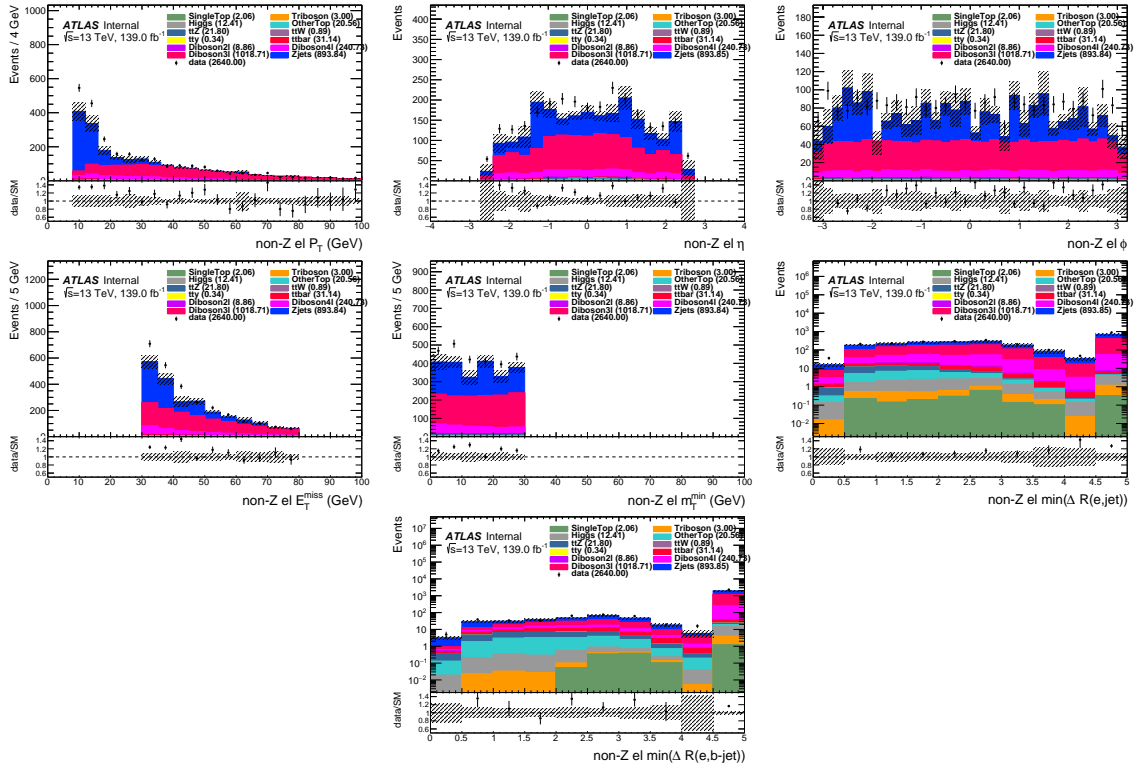
Figure B.11: Various kinematics in the fake factor validation region when the non-Z lepton is an electron, **but using only MC to estimate the backgrounds instead**. This lepton is most likely the fake in the Z+jets events. In the $\min\Delta R(e, \mathrm{jet})$ and $\min\Delta R(e, \mathrm{b\text{-}jet})$ distributions, events without a (b-tagged) jet are added to the overflow. All uncertainties shown are only statistical.
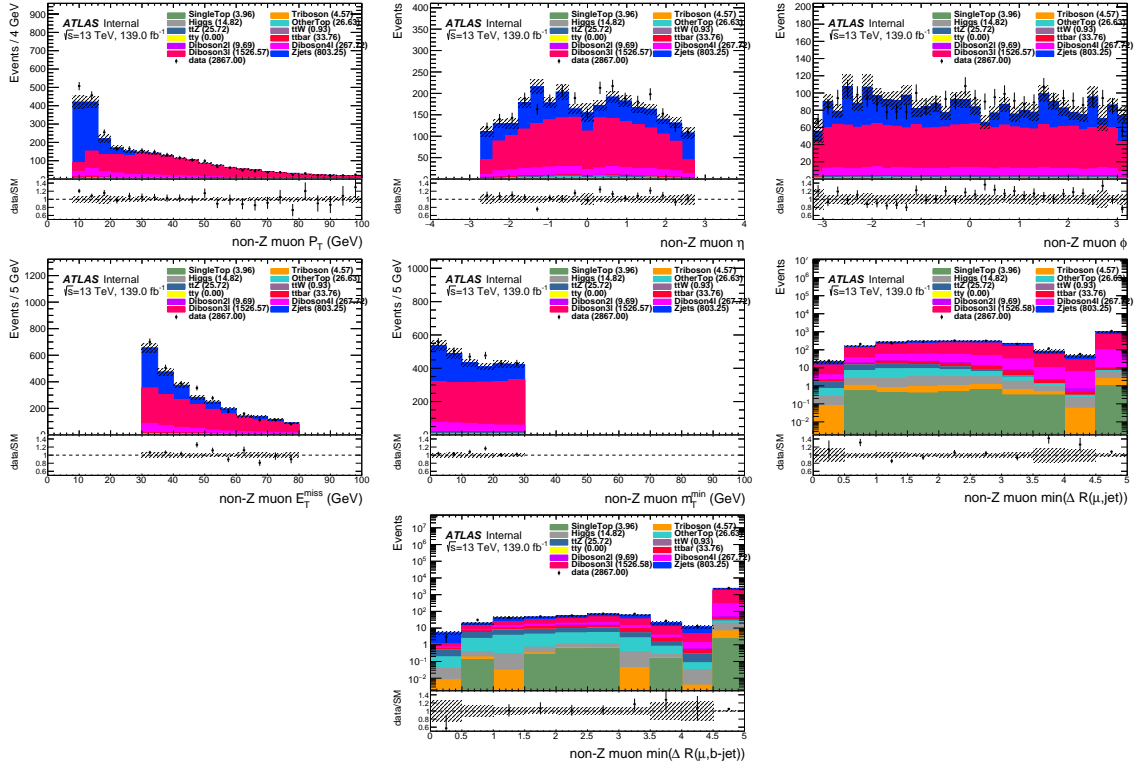
Figure B.12: Various kinematics in the fake factor validation region when the non-Z lepton is a muon, **but using only MC to estimate the backgrounds instead**. This lepton is most likely the fake in the Z+jets events. In the $\min\Delta R(\mu, \text{jet})$ and $\min\Delta R(\mu, \text{b-jet})$ distributions, events without a (b-tagged) jet are added to the overflow. All uncertainties shown are only statistical.
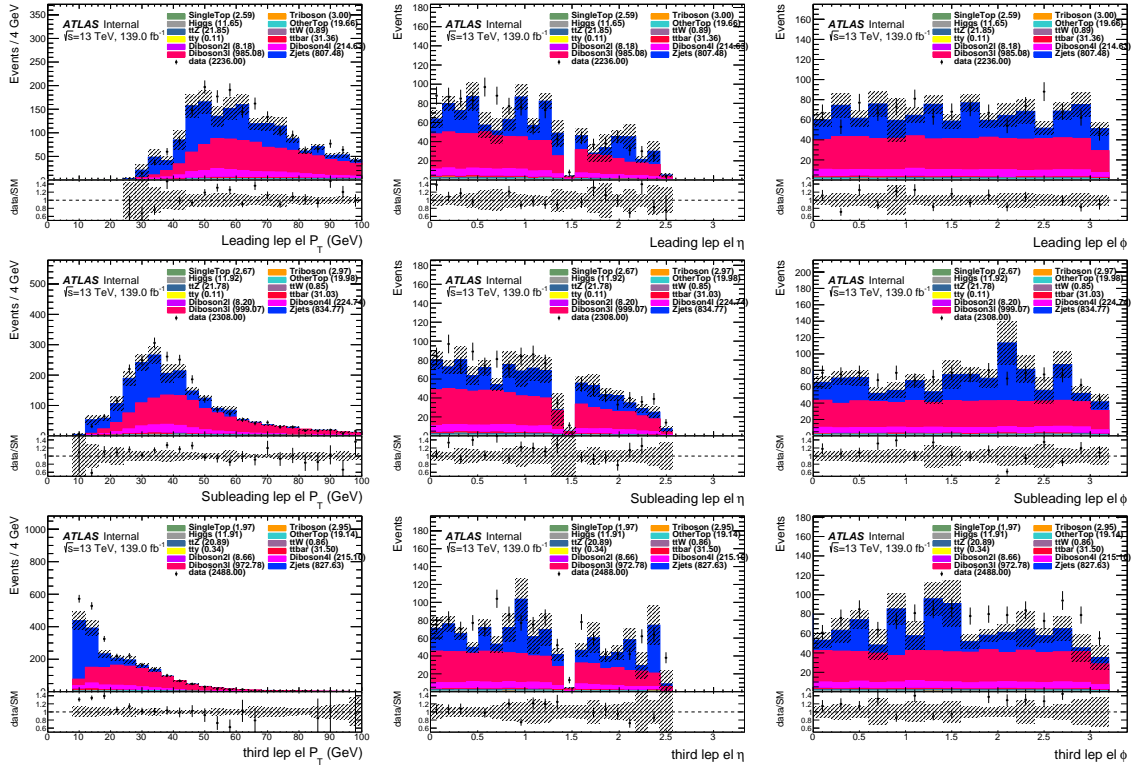
Figure B.13: The p_T, η, and ϕ distributions of the leading, subleading, and third leptons in VRFake when they are electrons, **but using only MC to estimate the backgrounds instead**. All uncertainties shown are only statistical.
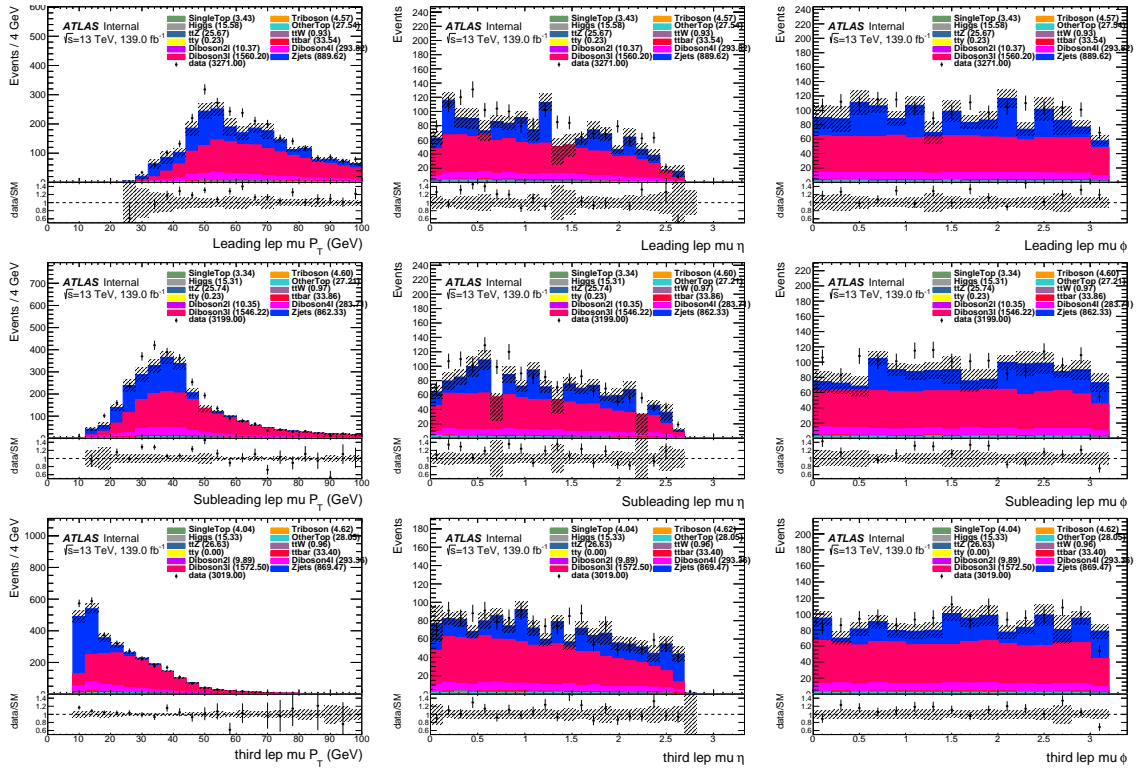
Figure B.14: The p_T, η, and ϕ distributions of the leading, subleading, and third leptons in VRFake when they are muons, **but using only MC to estimate the backgrounds instead**. All uncertainties shown are only statistical.
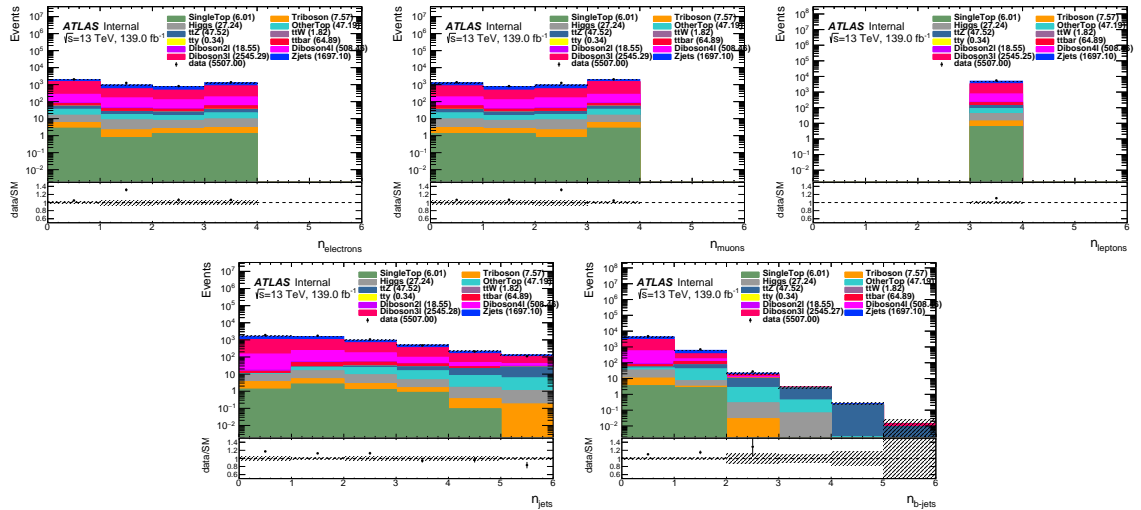
Figure B.15: Object multiplicity distributions in the fake factor validation region, **but using only MC to estimate the backgrounds instead**. All uncertainties shown are only statistical.
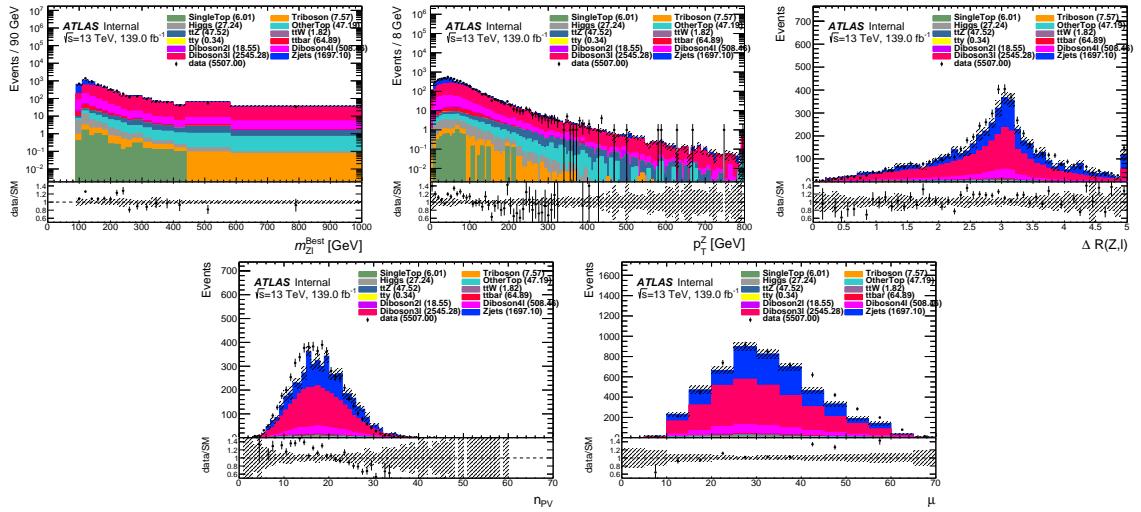
Figure B.16: Additional event level variable distributions in VRFake, **but using only MC to estimate the backgrounds instead**. All uncertainties shown are only statistical.

B.5   Fake Lepton Composition

Signal leptons

The fake **signal** lepton sources (heavy flavor, light flavor, etc.) are shown Fig. B.17-B.20, split by analysis region. The classification of the leptons is performed using the IFFTruthClassifier tool on MC simulation. While muon fakes are dominated by HF decays, the primary source of fake electrons varies across the regions. The processes giving rise to fake leptons (Z+jets, $t\bar{t}$, etc.) also vary. There is an issue with the truth record in the triboson samples causing the muons to be classified as "unknown". Since triboson is expected to be almost entirely real, it is treated as always prompt.

Focusing on the fake regions, the fake factor measurement region has more LF fake electrons, while the validation region has more HF electrons. The higher $E_{\mathrm{T}}^{\mathrm{miss}}$ requirement in the validation region biases the fake composition towards HF fakes, which are produced alongside neutrinos in the semileptonic decays of HF hadrons.

Interestingly, there are no fake electrons from conversions seen from the Z+jets samples, which overlap with the $Z + \gamma$ samples due to the inclusion of diagrams with ISR and FSR photons. In the analysis regions, some $Z \rightarrow 3e$ events are expected (a prompt electron from a $Z \rightarrow ee$ decay undergoes bremsstrahlung and radiates a photon, which converts to two electrons with only one reconstructed). While the fake factor measurement region has an $m_{\mathrm{Z}\ell} > 105$ GeV cut to remove these events, the other regions have no such cut. These Z+jets "conversion" electrons are not seen in these distributions because the IFFTruthClassifier tool classifies these electrons from FSR as isolated, since they are collinear with the prompt electron. As a result, these Z+jets events are considered to have three prompt electrons and are not included in the fake estimate. These "prompt" events must be estimated from the Z+jets MC. This applies similarly to $t\bar{t} \rightarrow ee\mu/eee$ and $WZ \rightarrow eeee/\mu eee$ events where an electron produces an FSR photon that converts.
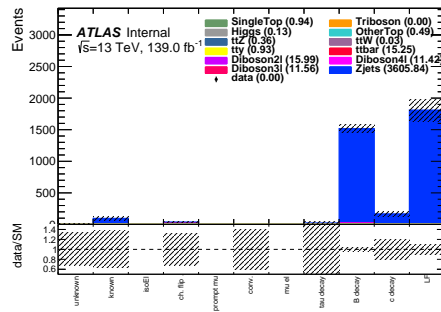
(a) CRFake fake signal electrons
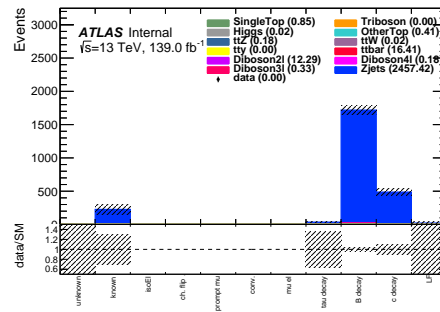
(b) CRFake fake signal muons
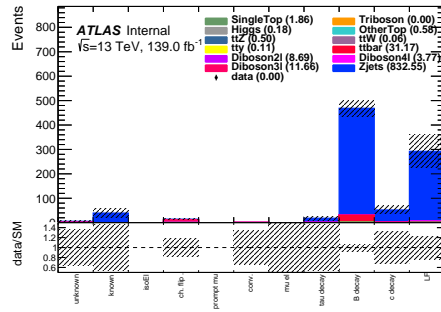
(c) VRFake fake signal electrons
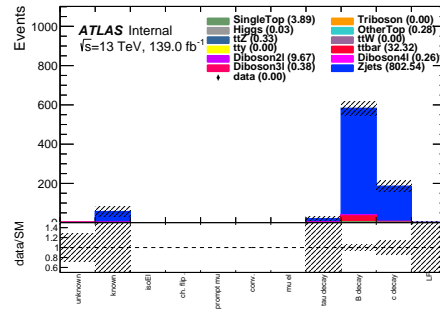
(d) VRFake fake signal muons

Figure B.17: Sources of fake signal electrons and muons in CRFake and VRFake, the FF measurement and validation regions. Only fake leptons are included in the distributions. The classification of the leptons is done using the `IFFTruthClassifier` tool.
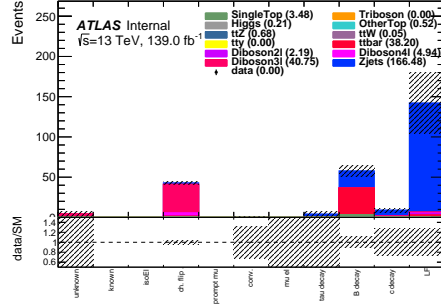
(a) CRWZ fake signal electrons
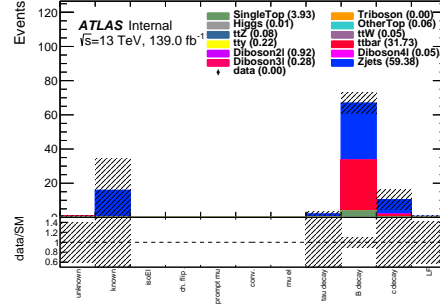
(b) CRWZ fake signal muons
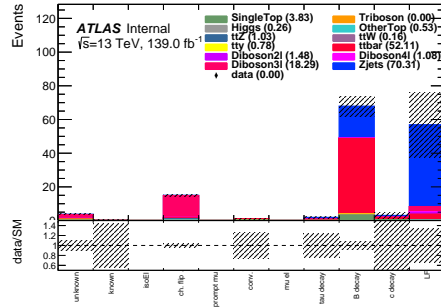
(c) VRE_T^{miss} fake signal electrons
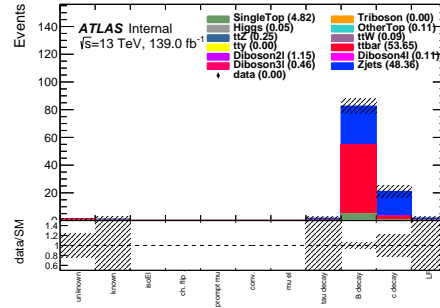
(d) VRE_T^{miss} fake signal muons
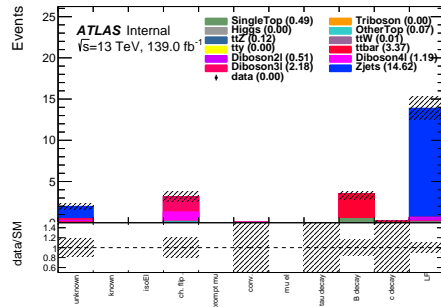
(e) VRm_T^{min} fake signal electrons
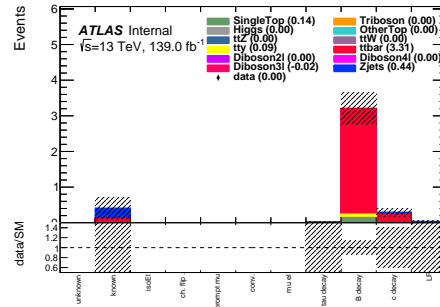
(f) VRm_T^{min} fake signal muons

Figure B.18: Sources of fake signal electrons and muons in CRWZ, VRE_T^{miss}, and VRm_T^{min}. Only fake leptons are included in the distributions. The classification of the leptons is done using the `IFFTruthClassifier` tool.
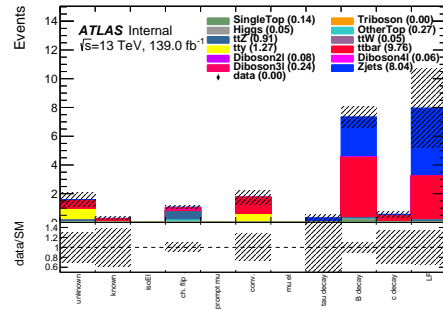
(a) CR$t\bar{t}Z$ fake signal electrons
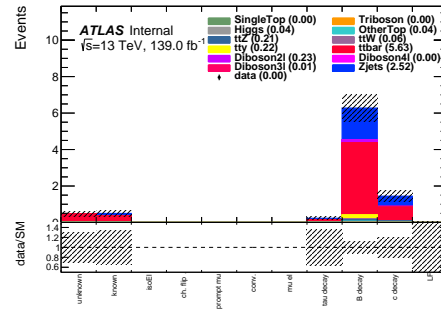
(b) CR$t\bar{t}Z$ fake signal muons
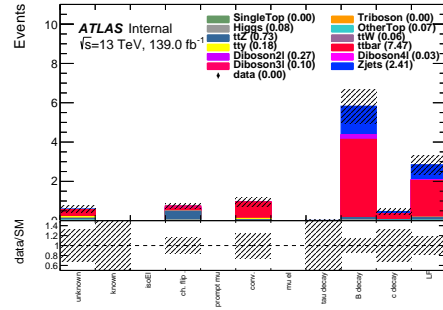
(c) VR$t\bar{t}Z$ fake signal electrons
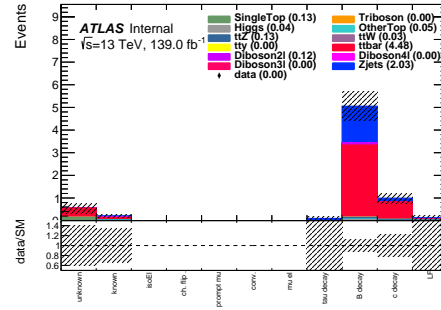
(d) VR$t\bar{t}Z$ fake signal muons

Figure B.19: Sources of fake signal electrons and muons in CR$t\bar{t}Z$ and VR$t\bar{t}Z$. Only fake leptons are included in the distributions. The classification of the leptons is done using the `IFFTruthClassifier` tool.
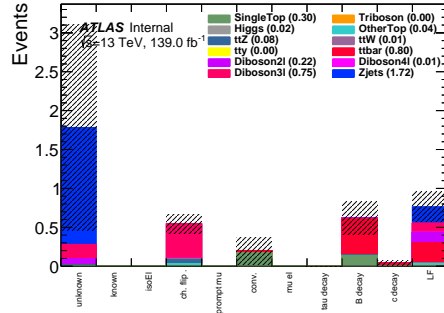
(a) SR3ℓ fake signal electrons
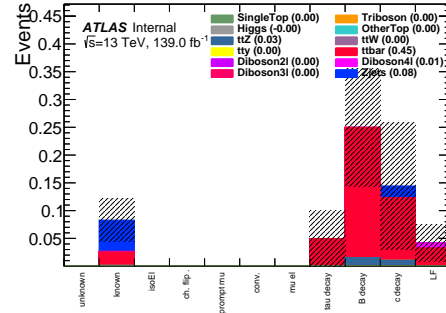
(b) SR3ℓ fake signal muons
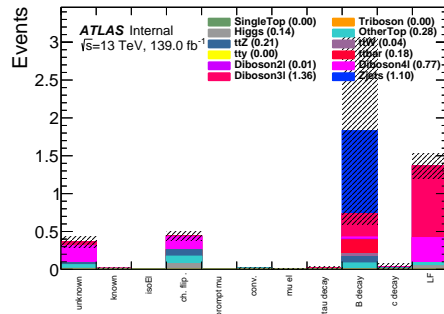
(c) SR4ℓ fake signal electrons
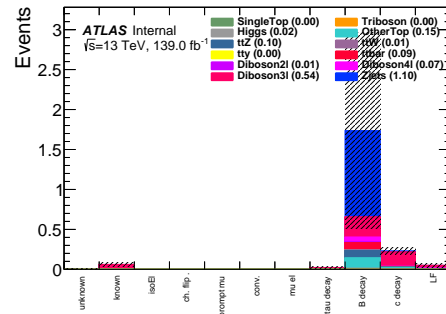
(d) SR4ℓ fake signal muons
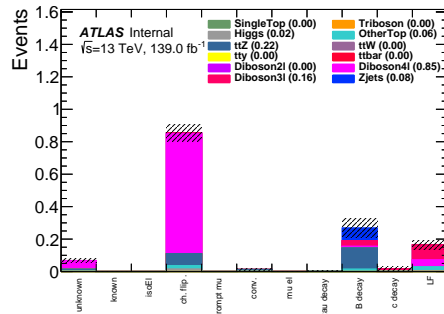
(e) SRFR fake signal electrons
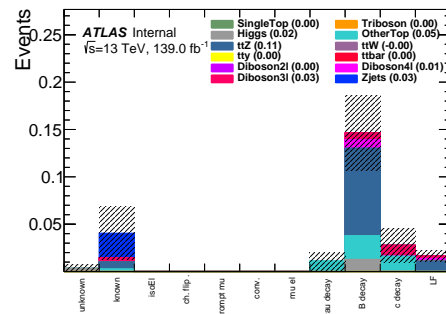
(f) SRFR fake signal muons

Figure B.20: Sources of fake signal electrons and muons in the signal regions. Only fake leptons are included in the distributions. The classification of the leptons is done using the `IFFTruthClassifier` tool.

Anti-ID leptons

The fake **anti-ID** lepton sources (HF, LF, etc.) are shown Fig. B.21-B.24, split by analysis region. The composition of anti-ID electrons shifts drastically across the various regions, and the systematic uncertainty derived to cover these shifts is detailed in Appendix C.

While the source of fake electrons passing the signal requirements in CRFake is split somewhat evenly between HF and LF jets (Figure B.17), the anti-ID electrons are much more biased towards LF jets. As a result, the average fake factor is smaller for LF fake electrons (see Appendix B.6).

(a) CRFake fake anti-ID electrons

(b) CRFake fake anti-ID muons

(c) VRFake fake anti-ID electrons

(d) VRFake fake anti-ID muons
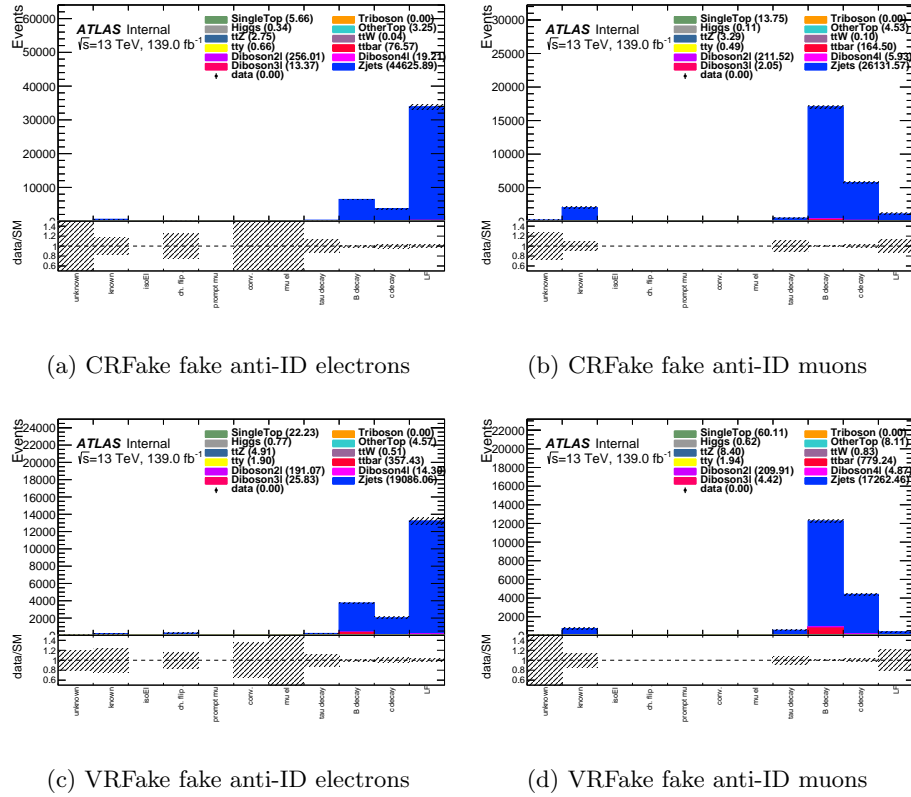
Figure B.21: Sources of fake anti-ID electrons and muons in CRFake and VRFake, the FF measurement and validation regions. Only fake leptons are included in the distributions. The classification of the leptons is done using the `IFFTruthClassifier` tool.
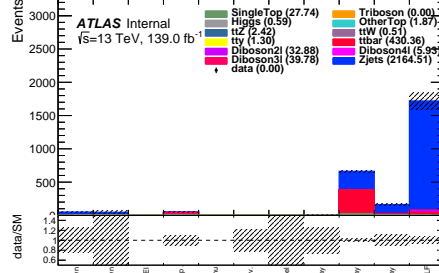
(a) CRWZ fake anti-ID electrons
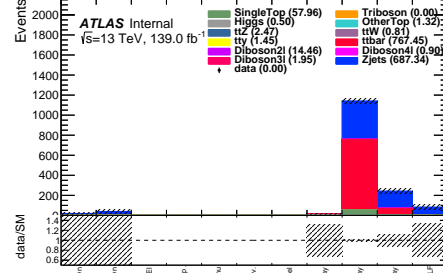
(b) CRWZ fake anti-ID muons
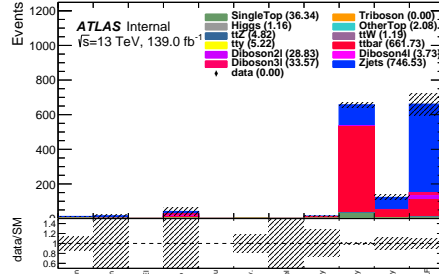
(c) VRE_T^{miss} fake anti-ID electrons
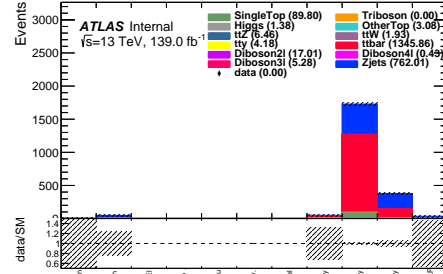
(d) VRE_T^{miss} fake anti-ID muons
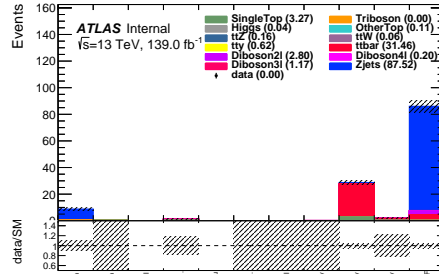
(e) VRm_T^{min} fake anti-ID electrons
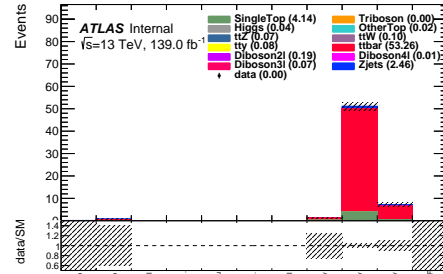
(f) VRm_T^{min} fake anti-ID muons

Figure B.22: Sources of fake anti-ID electrons and muons in CRWZ, VRE_T^{miss} and VRm_T^{min}. Only fake leptons are included in the distributions. The classification of the leptons is done using the `IFFTruthClassifier` tool.
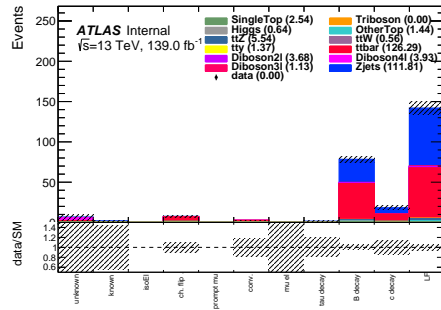
(a) CR$t\bar{t}Z$ fake anti-ID electrons
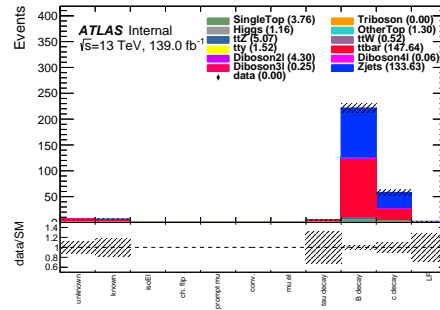
(b) CR$t\bar{t}Z$ fake anti-ID muons
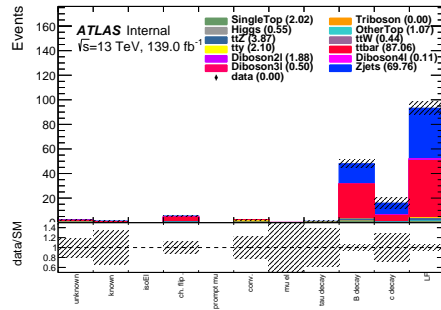
(c) VR$t\bar{t}Z$ fake anti-ID electrons
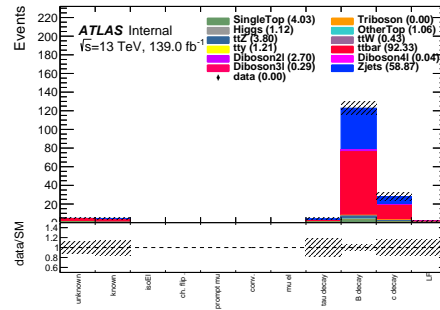
(d) VR$t\bar{t}Z$ fake anti-ID muons

Figure B.23: Sources of fake anti-ID electrons and muons in CR$t\bar{t}Z$ and VR$t\bar{t}Z$. Only fake leptons are included in the distributions. The classification of the leptons is done using the `IFFTruthClassifier` tool.
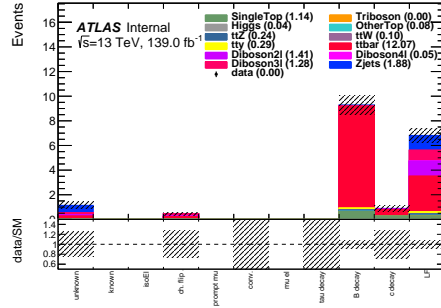
(a) SR3ℓ fake anti-ID electrons
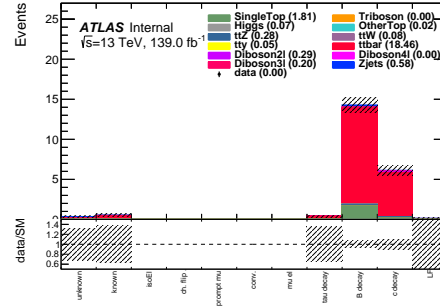
(b) SR3ℓ fake anti-ID muons
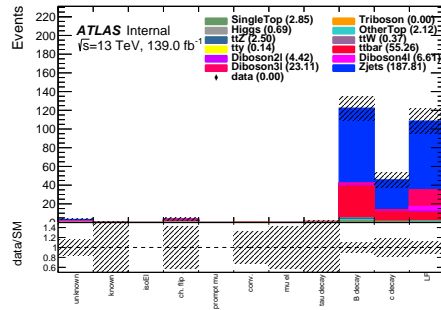
(c) SR4ℓ fake anti-ID electrons
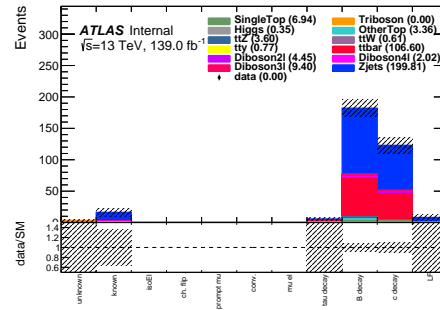
(d) SR4ℓ fake anti-ID muons
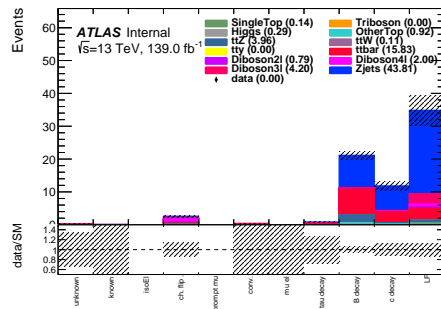
(e) SRFR fake anti-ID electrons
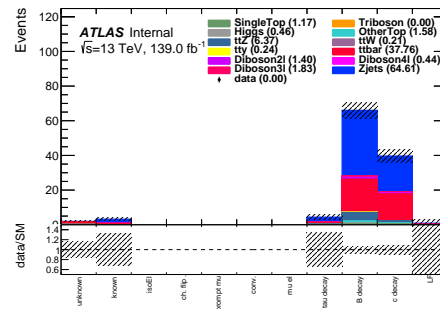
(f) SRFR fake anti-ID muons

Figure B.24: Sources of fake anti-ID electrons and muons in the signal regions. Only fake leptons are included in the distributions. The classification of the leptons is done using the `IFFTruthClassifier` tool.

B.6   Heavy vs. Light Flavor Fake Factors

As shown in Appendix B.5, the composition of the fake signal and anti-ID electrons varies across the analysis regions. Therefore, it is interesting to examine the electron heavy flavor and light flavor fake factors individually using the Z+jets MC. These MC fake factors are shown in Fig. B.25.

While the LF fake factors increase with p_T, the HF fake factors decrease. As mentioned in Appendix B.2, the HF fake factors may decrease with p_T due to a larger boost of the heavy flavor hadron producing the non-prompt electron. A more boosted HF hadron may have a longer decay length and more collimated decay products. As a result, the non-prompt electron produced in the decay may have a large d_0-significance and more energy in its isolation cone. Since the non-prompt electron p_T is correlated with the boost of the parent HF hadron, the non-prompt electron may be more likely to fail the signal electron requirements at higher p_T.

For comparison, Fig. B.26 shows the HF and LF fake factors derived in the fake factor validation region (VRFake) instead. While the fake factor trends here are similar to those in the measurement region, the fake factors are smaller in general, likely due to the higher E_T^{miss} requirement.

As the dominant source of fake muons is heavy flavor decays, the muon versions of the plots shown in Fig. B.25-B.26 are not included.
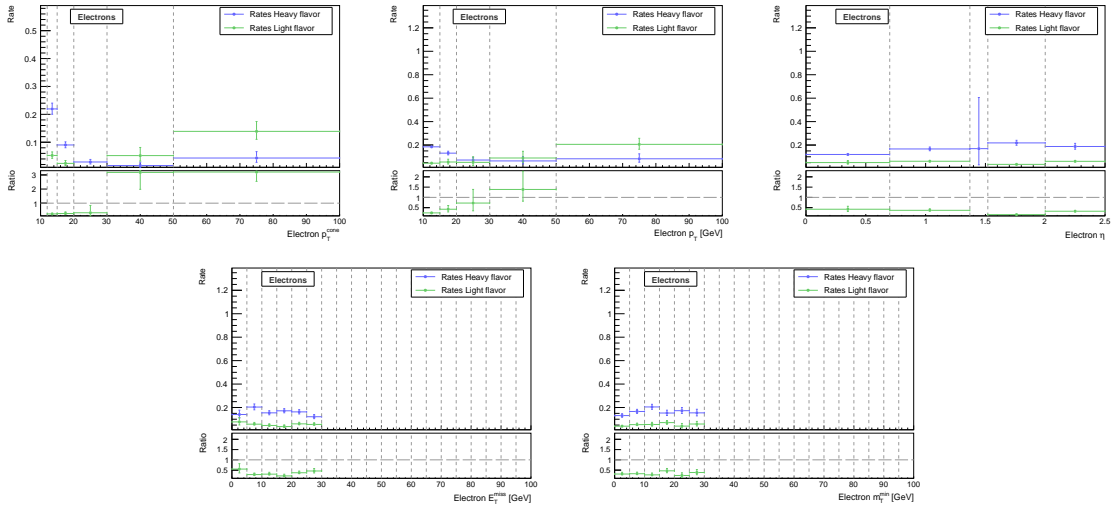
Figure B.25: Various parameterizations of the HF and LF electron Z+jets fake factors, derived in MC in the fake factor measurement region (CRFake). All uncertainties shown are statistical only.
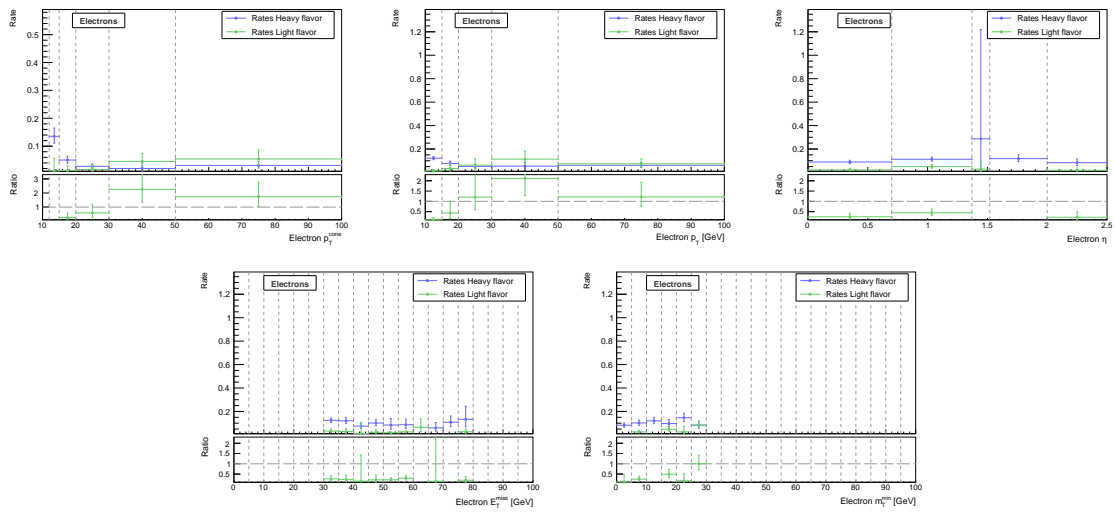
Figure B.26: Various parameterizations of the HF and LF electron Z+jets fake factors, derived in MC in the fake factor validation region (VRFake) instead. All uncertainties shown are statistical only.

Derivation of Fake Systematics

This section details the derivation and implementation of the systematic uncertainties associated with the fake background estimate.

C.1 Fake Factor Statistical Systematic

The statistical uncertainties on the fake factors themselves are propagated to the fake event weight. The uncertainty on a given fake factor bin is independent from those on all other bins; however, events using the same fake factor bins should be correlated. This is accomplished by associating a nuisance parameter with each fake factor bin. In practice, each bin is assigned 1σ up and down weight systematics that are set to non-unity for the event if that particular bin is used. These statistical systematics are correlated accross the analysis regions.

C.2 Prompt Subtraction Systematic

When measuring the fake factors in data, the prompt contamination must be subtracted using MC. A systematic uncertainty associated with this prompt subtraction is derived by varying the normalization of the prompt MC in the fake factor measurement region by 5%. The amount by which the prompt MC is varied is informed by the recent ATLAS WZ [221] and ZZ [222] cross section measurement with 36.1 fb^{-1} at 13 TeV. Additionally, this 5% is consistent with typical observed normalization factors on WZ and ZZ background estimates.

The $p_{\mathrm{T}}^{\mathrm{cone}}$ distributions of the tight probe leptons in the fake factor measurement region are shown in Fig. C.1. The binning of these distributions matches that of the fake factors. These plots are populated with the numerator leptons from the fake factor calculation. The prompt contamination

(a) Signal probe electrons   (b) Signal probe muons
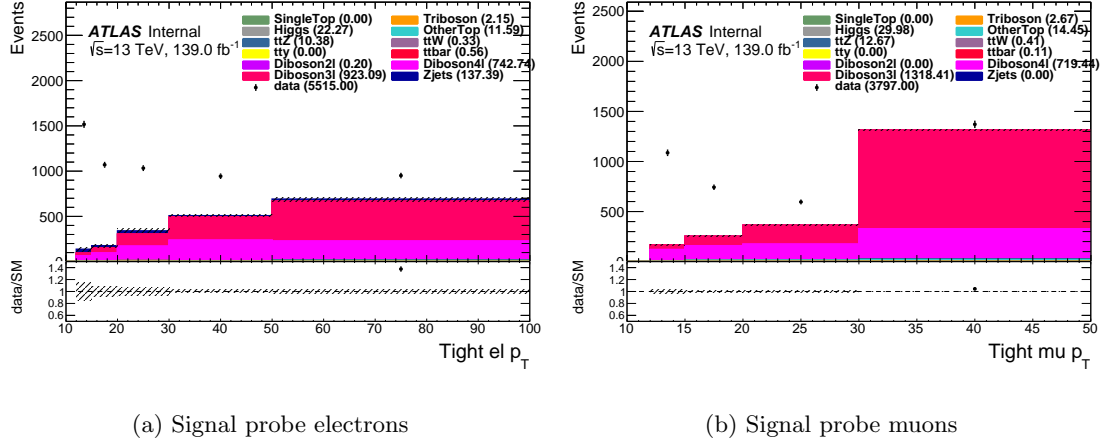
Figure C.1: The data and prompt MC p_T^{cone} distributions for the probe leptons in the fake factor measurement region (CRFake) when the signal lepton requirements are passed. The binning matches that of the fake factors. The difference in each bin between the data and the prompt MC is the numerator of the fake factor. The prompt contamination is worse at higher values of p_T^{cone}, particularly for muons.

becomes more significant at higher values of p_T^{cone}, particularly for muons. The denominator (anti-ID) lepton version of these plots are dominated by fake events, so the variation in the prompt subtraction is negligible.

The fake factors derived with the 5% up and down fluctuations in the prompt subtraction are shown in Fig. C.2, along with the nominal fake factors. Note that the statistical error bars are correlated, as each set of fake factors uses the exact same events. As expected from the p_T^{cone} distributions, the relative variation of the fake factors grows with p_T^{cone}, with the muon fake factors being more sensitive.

Since the prompt subtraction systematic is a reflection of the uncertainty on the WZ and ZZ cross sections, only one nuisance parameter is used. The values assigned to the 1σ up and down weights are determined by which FF bins are used, pulling from the ratios in the bottom panel in Figure C.2. The relative uncertainty for each FF bin can be seen in Table C.1. The prompt systematic is also correlated across analysis regions. With this statistical treatment, as the NP is varied, the fake factors are constrained to pull in the same direction, across p_T^{cone} bins, lepton flavor, and analysis region.

(a) Electrons   (b) Muons
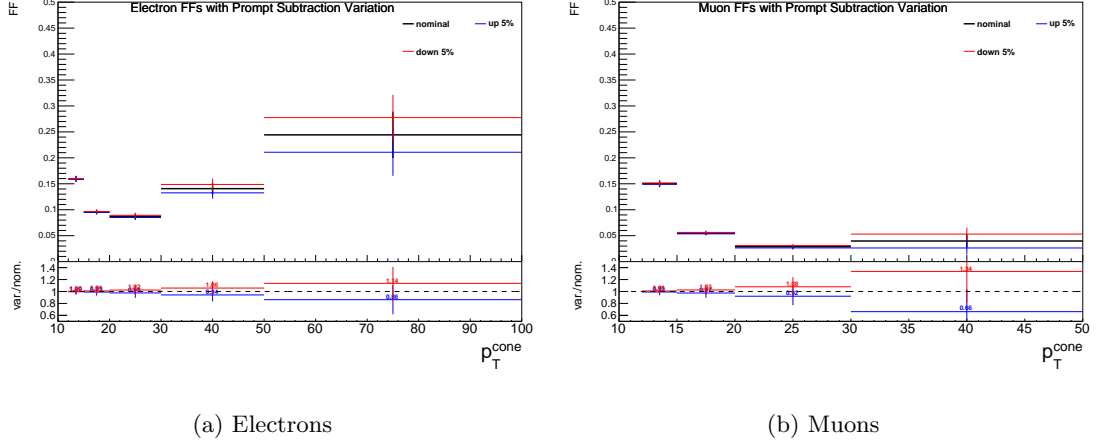
Figure C.2: The effect of varying the prompt subtraction normalization up and down by 5% when deriving the fake factors. The prompt contamination becomes more significant in the higher p_T^{cone} bins, especially for muons, resulting in larger deviations from the nominal fake factors.

FF bin [GeV]	12-15	15-20	20-30	30-50	50-100
electron rel. uncert.	0.5%	1.0%	2.4%	5.7%	14%
muon rel. uncert.	0.9%	2.6%	8.0%	34%	-

Table C.1: The relative uncertainty on the fake factors due to prompt subtraction systematic.

C.3 Parameterization Systematic

The parameterization systematic is assessed by creating alternative fake estimates using other reasonable fake factor parameterizations. The two alternative parameterizations to the nominal p_T^{cone}-binning are p_T^{cone} vs. η and p_T^{cone} vs. $N_{\text{b-jets}}$. The three sets of fake factors can be seen in Fig C.3. These 2D parameterizations contain extra information relative to the nominal, but the statistical errors are worse. The nominal and two alternative fake estimate trees are all passed to HistFitter, with the alternative estimates used as one-sided systematic uncertainties.

(a) Electron p_T^{cone} (nominal)   (b) Electron p_T^{cone} vs. η (c) Electron p_T^{cone} vs. $N_{\text{b-jets}}$

(d) Muon p_T^{cone} (nominal)   (e) Muon p_T^{cone} vs. η (f) Muon p_T^{cone} vs. $N_{\text{b-jets}}$
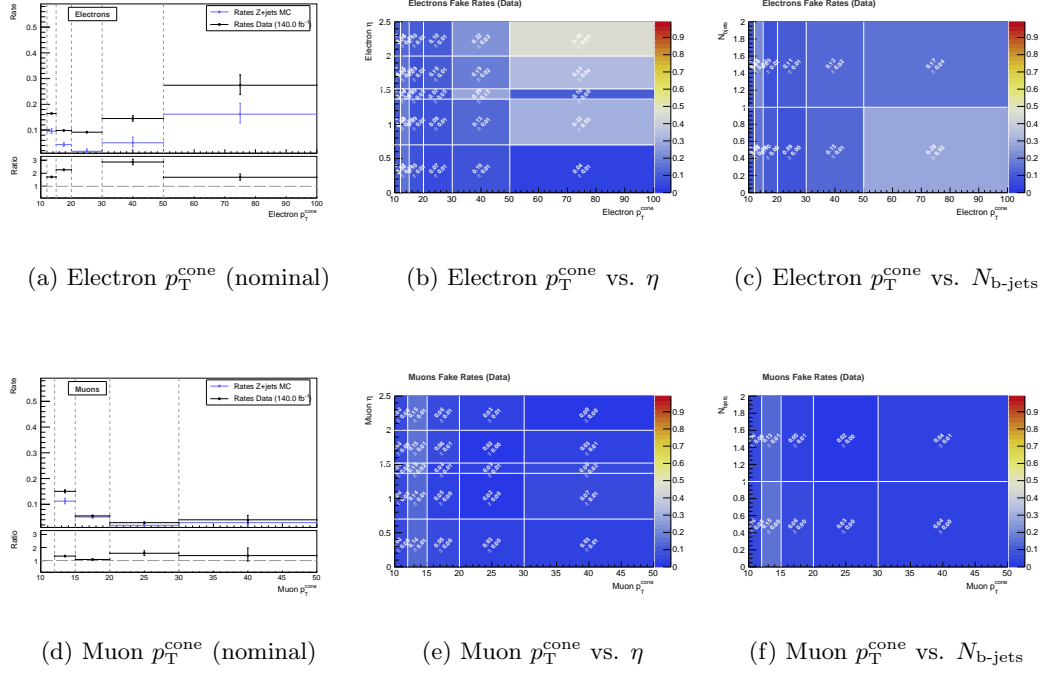
Figure C.3: Fake factor parameterizations. The 1D p_T^{cone} parameterization is used for the nominal fake estimate, and the two 2D parameterization are used to derive the parameterization systematic.

C.4   Composition Systematic

As shown in Table 5.9 in Section 5.5, the processes giving rise to the fake background vary across the analysis regions. The light flavor vs. heavy flavor fake composition varies as well, as shown in Appendix B.5.

To assess a systematic uncertainty to cover these variations, it is assumed that the fake factors only depend on the source (HF vs. LF) and not the process (Z+jets vs. $t\bar{t}$, etc.). In other words, the HF and LF fake factors are assumed to be process universal. The validity of this assumption can be assessed from Fig. C.4, which shows the fake factors derived from Z+jets and $t\bar{t}$ MC in the preselection region (the only region with enough $t\bar{t}$ stats), split by fake source. Only the HF fake factors are shown for muons, as the fake muons are dominated by heavy flavor decays. It is also assumed that the HF and LF fake factors are region independent, however, a separate systematic is derived to cover any residual kinematic dependence (see Appendix C.5).

Region specific fake factors are then derived by taking a weighted average of the HF and LF fake

(a) Electron heavy flavor   (b) Electron light flavor   (c) Muon heavy flavor
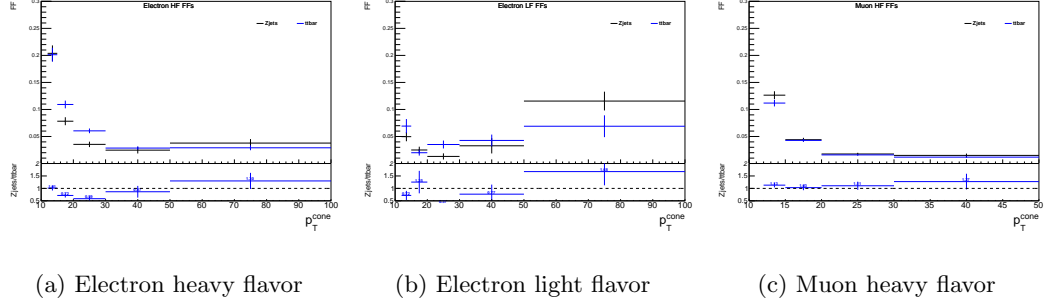
Figure C.4: Comparing Z+jets vs $t\bar{t}$ MC fake factors, binned in p_T^{cone}, and separated by heavy flavor and light flavor. These fake factors are measured in the preselection region to achieve enough $t\bar{t}$ stats. Only the heavy flavor fake factors are shown for muons due to the lack of light flavor statistic.

factors, where the weights match the composition of the anti-ID leptons in that region. If the HF fake fraction in a given region is X_{HF}, the region specific fake factor for the ith p_T^{cone}-bin is:

$$F(i) = X_{\text{HF}} \cdot F_{\text{HF}}(i) + (1 - X_{\text{HF}}) \cdot F_{\text{LF}}(i). \tag{C.1}$$

The HF fake fractions are measured inclusively, not bin-by-bin. The sources of the fake anti-ID leptons in the various analysis regions are shown in Figures B.21-B.24. Note the ZZ regions are very pure in real ZZ events and are not shown.

As a test of this method, the nominal Z+jets MC electron fake factors were recreated from the HF and LF fake factors using Eq. C.1. The results can be seen in Fig. C.5. Included are the nominal (solid black), LF (green), HF (blue), and recreated fake factors (dotted black). The ratios of the recreated fake factors to the nominal are shown in the bottom pad, and good agreement is seen. The use of inclusive HF fake fractions, as opposed to bin-by-bin, introduces some error. As the statistics are much higher in the low p_T^{cone} bins, these bins dominate X_{HF}, resulting in better agreement at low p_T^{cone}. An additional source of error is the omission of all fake sources other than HF and LF in Eq. C.1. As shown in Fig. B.21-B.24, fake electrons occasionally fall in other categories.

The region-specific fake factors are shown in Fig. C.6-C.7, plotted in red. The lower pad shows the ratio of the region-specific fake factors to the nominal Z+jets MC ones from the fake factor measurement region. The deviation from the nominal fake factors is greatest in SR3ℓ and SR4ℓ, where the HF fraction is the largest. A region-specific relative weight systematic is derived by taking
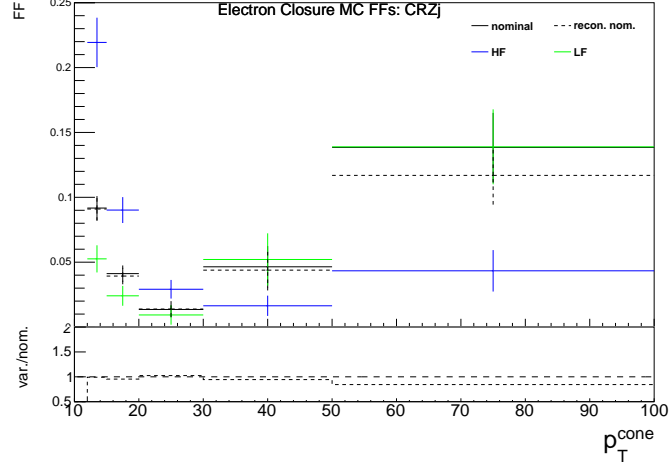
Figure C.5: The nominal (solid black), heavy flavor (blue), light flavor (green), and recreated (dotted black) MC fake factors, derived in the fake factor measurement region (CRFake). The recreated fake factor is derived by taking a weighted average of the HF and LF fake factors, matching the composition of the fake factor measurement region. Good agreement is seen between the nominal and recreated fake factors.

the RMS of the bin-by-bin percent errors:

$$\sigma_{\text{comp}}^{\text{rel}} = \sqrt{\frac{1}{n} \sum_{i=1}^{n} (1 - \frac{F_{\text{region}}(i)}{F_{\text{nominal}}(i)})^2} \tag{C.2}$$

The 1σ up and down relative weights are set to $(1 \pm \sigma_{\text{comp}}^{\text{rel}})^k$ where k is the number of anti-ID electrons in the event. The fake anti-ID muons are dominantly produced in heavy flavor decays, so no composition systematic is applied for fake events where all anti-ID leptons are muons. The values of $\sigma_{\text{comp}}^{\text{rel}}$ for each region are contained in Table C.2. By using the RMS, only one number needs to be derived and applied for each region. Alternatively, the systematic could be assessed based on which fake factor bins were used in the event, but this would require a systematic uncertainty derived for every bin in every region. The composition systematic is not correlated across the analysis regions.

	VRFake	CRWZ	VR$E_{\text{T}}^{\text{miss}}$	VR$m_{\text{T}}^{\text{min}}$	CR$t\bar{t}Z$	VR$t\bar{t}Z$	SR3ℓ	SR4ℓ	SRFR
relative comp. syst.	14%	16%	44%	10%	26%	26%	52%	53%	37%

Table C.2: Relative systematic uncertainty on the electron fake factors due to HF vs LF composition differences across the analysis regions. Note the ZZ regions are very pure in real ZZ events and are not assigned a composition systematic.

(a) VRFake

(b) CRWZ

(c) VRE_T^{miss}

(d) VRm_T^{min}

(e) CR$t\bar{t}Z$

(f) VR$t\bar{t}Z$
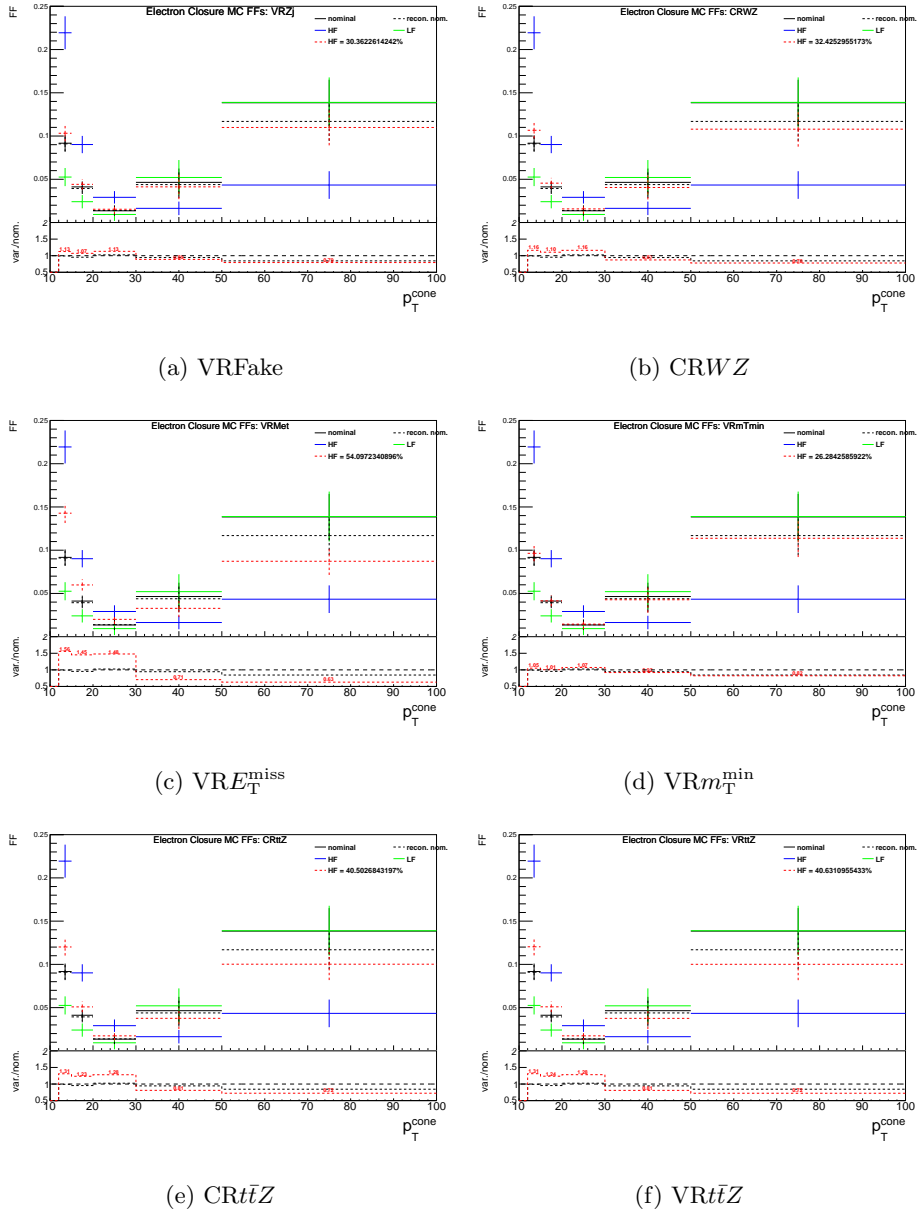
Figure C.6: The region-specific MC fake factors (red) compared with the nominal (solid black), heavy flavor (blue), and light flavor (green) fake factors. These region-specifc fake factors are found by taking a weighted average of the HF and LF fake factors, matching the composition of the region. The ratio of the region-specific fake factors to the nominal, shown in the ratio plot, are used to derive region-specific composition systematics.

(a) SR3ℓ (b) SR4ℓ
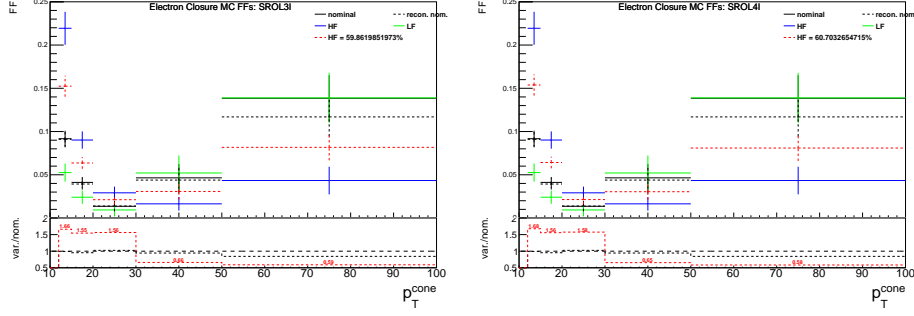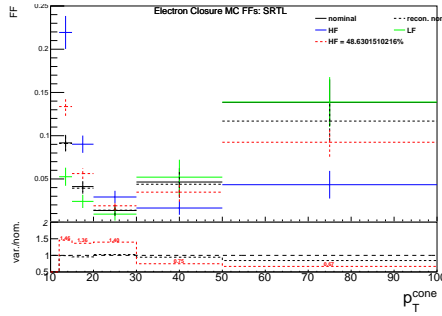
(c) SRFR

Figure C.7: The region-specific MC fake factors (red) compared with the nominal (solid black), heavy flavor (blue), and light flavor (green) fake factors. These region-specifc fake factors are found by taking a weighted average of the HF and LF fake factors, matching the composition of the region. The ratio of the region-specific fake factors to the nominal, shown in the ratio plot, are used to derive region-specific composition systematics.

C.5   Kinematic and Closure Systematic

A systematic uncertainty is derived to cover any remaining kinematic dependence of the fake factors and any non-closure of the fake factor method. To do so, the $p_{\mathrm{T}}^{\mathrm{cone}}$ distribution of the non-Z lepton in the fake factor validation region is used, as this lepton is most likely the fake. By examining the distribution with the same binning as the fake factors, data-driven systematics can be derived for each FF bin. For each bin, the factor by which the fake yield must change for data vs. background closure is calculated, accounting for the data and prompt background statistical errors only. This factor, labeled f, is the value closest to 1 for which the following relation holds:

$$|N_{\mathrm{data}} - N_{\mathrm{prompt}} - f \cdot N_{\mathrm{fake}}| \leq \sqrt{\sigma_{\mathrm{data,stat}}^2 + \sigma_{\mathrm{prompt,stat}}^2}, \qquad (\mathrm{C}.3)$$

where N_{data} is the data yield in the bin, N_{prompt} is the prompt background yield, N_{fake} is the fake yield, and $\sigma_{\text{data,stat}}$ and $\sigma_{\text{prompt,stat}}$ are the absolute statistical errors on the data and prompt background yields, respectively. One can think of $N_{\text{data}} - N_{\text{prompt}}$ as the "observed" fake yield in the bin, and f as a normalization factor on the expected fake yield in the bin, and therefore on the corresponding fake factor. Instead of requiring perfect agreement, the observed and expected must only agree within the statistical errors of the observed yield. For some bins, the observed and expected fake yields already agree within the statistical errors before any scaling (i.e. for $f = 1$). The $p_{\text{T}}^{\text{cone}}$ distributions of the non-Z electrons and muons are shown in Figure C.8.

(a) Non-Z Electron   (b) Non-Z Muon
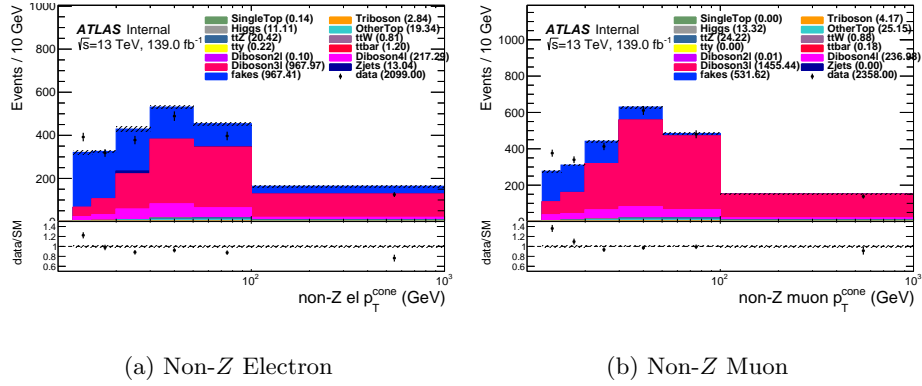
Figure C.8: The $p_{\text{T}}^{\text{cone}}$ distributions of the non-Z electrons and muons in the fake factor validation region. These distributions have the same binning as the fake factors and are used to derive a kinematic and closure systematic.

Once f has been calculated for every bin, the following equation is used to obtain a combined relative error:

$$\sigma_{\text{closure}}^{\text{rel}} = \sqrt{\frac{1}{n} \sum_{i=1}^{n} (1 - f(i))^2}.$$ \hfill (C.4)

This $\sigma_{\text{closure}}^{\text{rel}}$ is calculated separately for electrons and muons, and all bins that cover before any scaling of the expected fake yield are skipped in the sum. The values are found to be 23% for electrons and 27% for muons. By combining the relative errors this way, only two nuisance parameters are needed, as opposed to separate nuisance parameters for every fake factor bin. The pairs of 1σ up and down relative weights corresponding to the two nuisance parameters are set to $(1 \pm \sigma_{\text{closure, el}}^{\text{rel}})^k$ and $(1 \pm \sigma_{\text{closure},\mu}^{\text{rel}})^j$, where k and j are the number of anti-ID electrons and muons in the event, respectively. Notice this method does not consider any other sources of error on the fake estimate and is therefore conservative. Also, it only considers the statistical errors on the observed data and

prompt MC.

C.6   Negative Yields Systematic

With the fake factor method, it is possible to obtain a fake estimate with negative yields in some regions or bins. Typically, this occurs when the statistics are low for data events with anti-ID leptons. Momentarily ignoring all events with multiple fake leptons, the fake estimate in a three lepton region is given by the following:

$$
\begin{aligned}
N_{\text{TTT}}^{\text{fake}} &= N_{\text{TTT}} - N_{\text{TTT}}^{\text{RRR}} \\
&= F_1(N_{\text{LTT}} - N_{\text{LTT}}^{\text{RRR}}) + F_2(N_{\text{TLT}} - N_{\text{TLT}}^{\text{RRR}}) + F_3(N_{\text{TTL}} - N_{\text{TTL}}^{\text{RRR}}) + ...,
\end{aligned}
\tag{C.5}
$$

where "RRR" denotes events with three real leptons, and F_i is the fake factor for the ith lepton. N_{LTT} and its permutations are measured in data, and their "RRR" analogs are determined from MC. Notice that if the prompt subtraction is larger than the number of data events with an anti-ID lepton, the fake estimate will be negative.

Once multiple anti-ID leptons are allowed, a new source of negative fake yields appears. Below is the full equation for the fake estimate in a three lepton region:

$$
\begin{aligned}
N_{\text{TTT}}^{\text{fake}} = N_{\text{TTT}} - N_{\text{TTT}}^{\text{RRR}} = {}& F_1(N_{\text{LTT}} - N_{\text{LTT}}^{\text{RRR}}) + F_2(N_{\text{TLT}} - N_{\text{TLT}}^{\text{RRR}}) + F_3(N_{\text{TTL}} - N_{\text{TTL}}^{\text{RRR}}) \\
& - F_1 F_2(N_{\text{LLT}} - N_{\text{LLT}}^{\text{RRR}}) - F_1 F_3(N_{\text{LTL}} - N_{\text{LTL}}^{\text{RRR}}) - F_2 F_3(N_{\text{TLL}} - N_{\text{TLL}}^{\text{RRR}}) \\
& + F_1 F_2 F_3(N_{\text{LLL}} - N_{\text{LLL}}^{\text{RRR}}).
\end{aligned}
\tag{C.6}
$$

Now, data events with two anti-ID leptons contribute negatively to the fake yield, and prompt MC events with two real anti-ID leptons contribute positively (so "prompt subtraction" is a bit of a misnomer). Finally, when all three leptons are anti-ID, the data (prompt MC) contributes positively (negatively) again. As the fake factors are smaller than unity, events with two or three anti-ID leptons have smaller contributions to the total fake yields than events with just a single anti-ID lepton.

This analysis did observe negative fake estimates in some signal region bins, particularly at high $m_{\text{Z}\ell}$. This was primarily driven by very low statistics for data events with anti-ID leptons. After setting the negative yields to zero and recentering the uncertainties about zero, an additional systematic uncertainty was assessed using the following algorithm:

1. **If no anti-ID events are observed in data:**
   Apply an additional systematic uncertainty of $\lambda_{68} \times F_{\text{max}}$, where F_{max} is the largest fake factor

(0.28) and λ_{68} is the quantile of order 0.68 for a Poisson distribution with zero observed events, given by: $\int_0^{\lambda_{68}} \text{Poisson}(0|\lambda)d\lambda = 0.68 \implies \lambda_{68} \approx 1.14$.

2. **If at least one anti-ID event is observed in data AND the negative fake yield is consistent with zero when considering the statistical uncertainty:**
   Do not apply any additional systematic uncertainty.

3. **If at least one anti-ID events is observed in data AND the negative fake yield is inconsistent with zero when considering the statistical uncertainty:**
   Apply the magnitude of the negative yield as an additional systematic uncertainty.

Auxiliary Results for HEPData

D.1 Event Displays
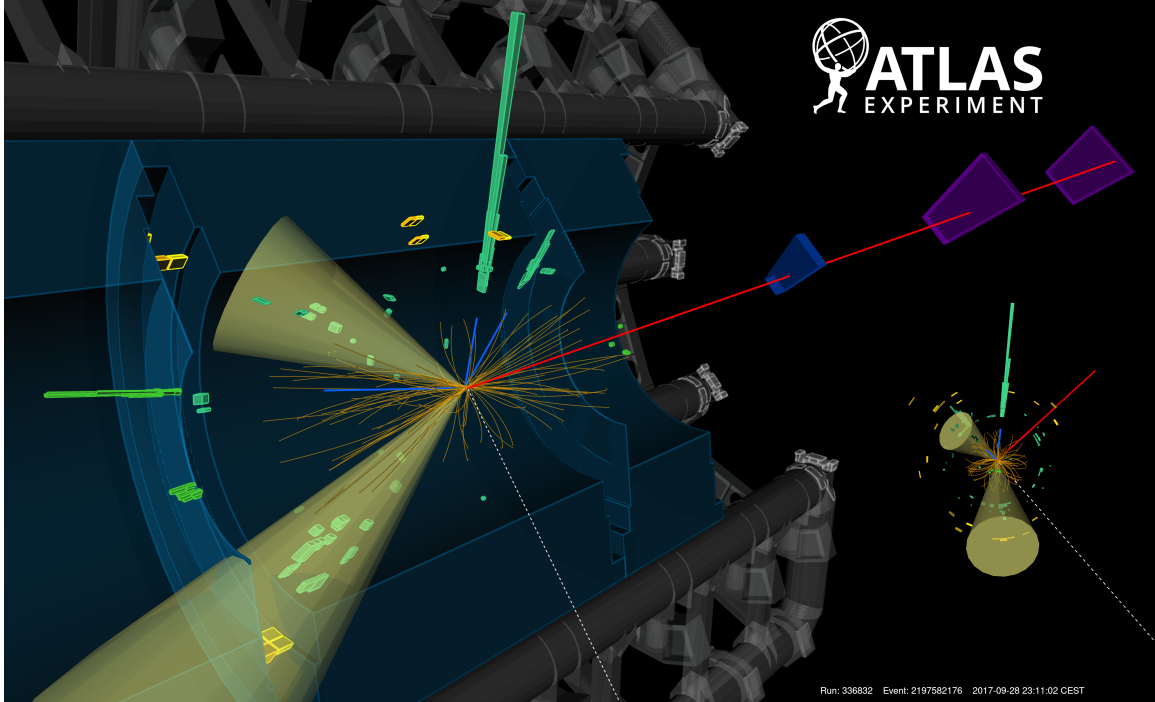
Figure D.1: The event display shows a data event recorded in September of 2017 which falls into the fully reconstructed signal region (SRFR). The event consists of three electrons (blue lines), one muon (red line) and two jets (yellow cones), neither of which are b-tagged. Two electrons with kinematic properties (p_{T}, η, ϕ) of (46.5 GeV, 1.14, 0.52) and (61.8 GeV, -2.14, 0.42) form an invariant mass of $m_{\ell\ell} = 93.2$ GeV, consistent with a Z boson. They are paired with a third electron (103.4 GeV, 0.09, 1.31), with $m_{Z\ell} = 365.8$ GeV. The first jet (77.9 GeV, -1.17, -2.00) and second jet (32.3 GeV, -0.76, 0.26) are used to reconstruct a second Z boson candidate of $m_{jj} = 94.7$ GeV. The jets are paired with the muon (44.7 GeV, 2.33, 2.04), with $m_{Z\ell} = 403.0$ GeV. The event has a missing transverse energy of $E_{\text{T}}^{\text{miss}} = 116.49$ GeV, which is represented as a dashed white line at $\phi = -2.40$.
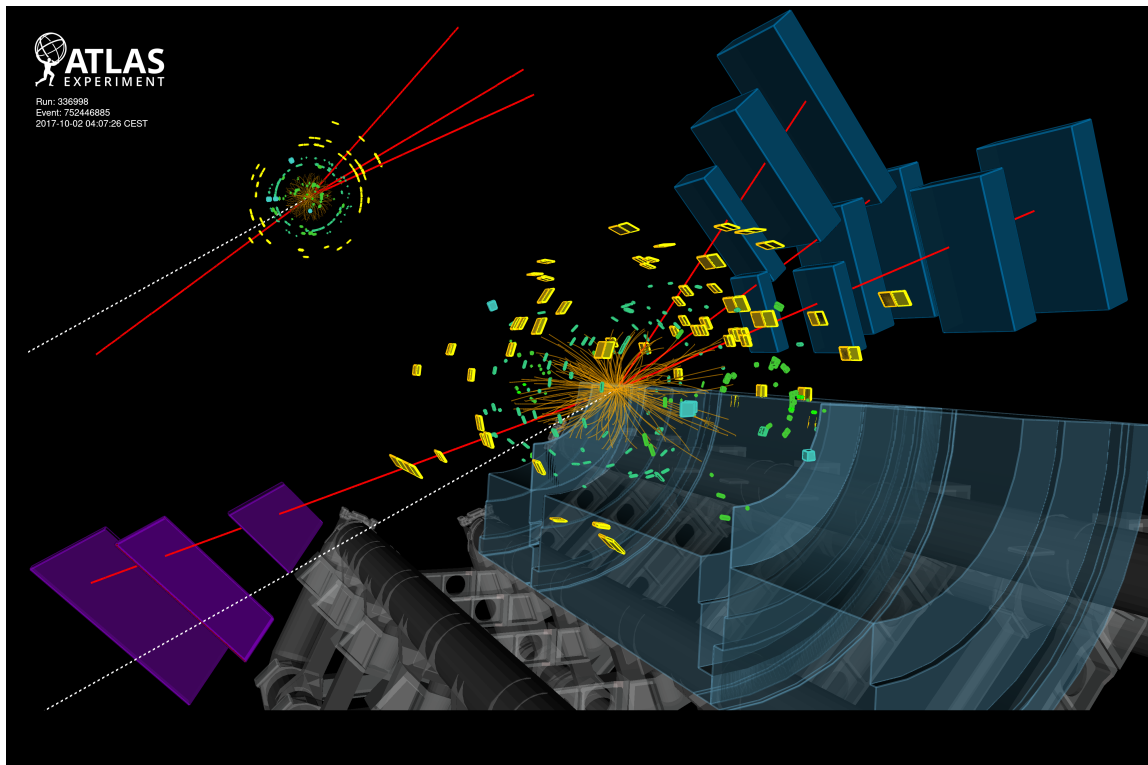
Figure D.2: The event display shows a data event recorded in October of 2017 which falls into the four lepton signal region (SR4ℓ). This event consists of four muons (red lines). Two muons with kinematic properties (p_{T}, η, ϕ) of (179.0 GeV, -0.26, 0.53) and (292.9 GeV, 0.10, 0.43) form an invariant mass of $m_{\ell\ell} = 88.4$ GeV, consistent with a Z boson. They are paired with a third muon (206.8 GeV, -1.08, -2.50), with $m_{Z\ell} = 719.4$ GeV. There is a fourth muon (126.6 GeV, -0.29, 0.85) that is unpaired. The event has a missing transverse energy of $E_{\text{T}}^{\text{miss}} = 390.6$ GeV, which is represented as a dashed white line at $\phi = -2.66$.
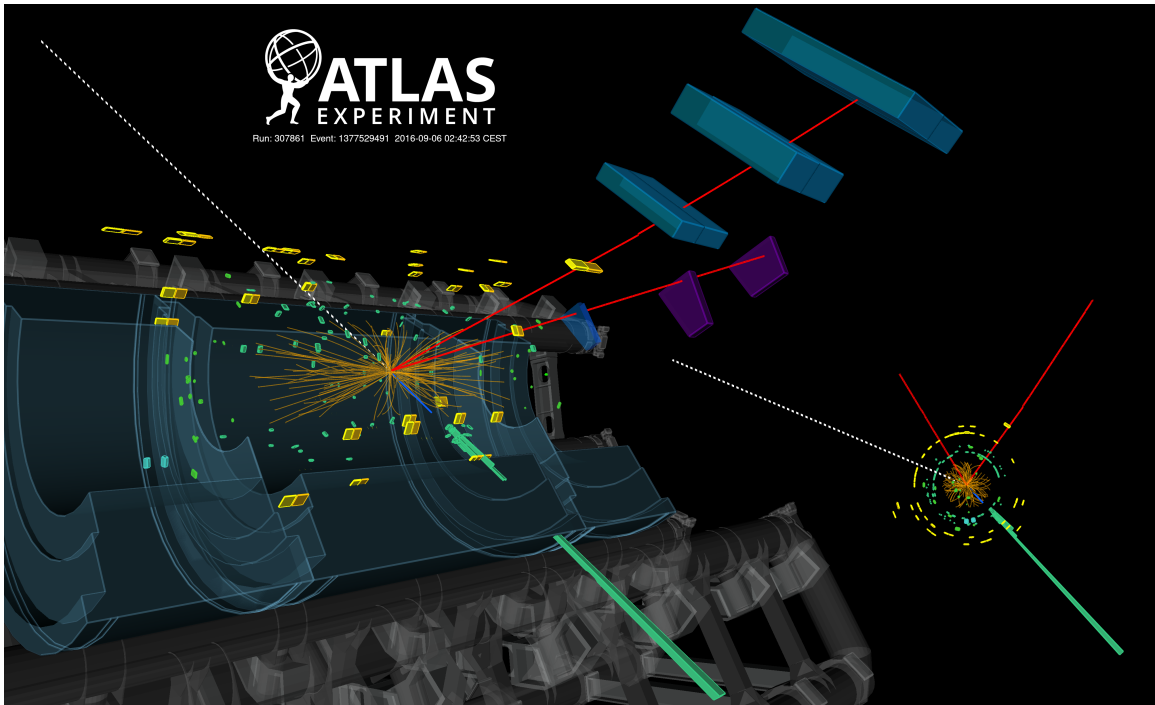
Figure D.3: The event display shows a data event recorded in September of 2016 which falls into the three lepton signal region (SR3ℓ). This event consists of two muons (red lines) and one electron (blue line). The muons with kinematic properties (p_{T}, η, ϕ) of (217.0 GeV, -2.05, 1.87) and (14.4 GeV, -0.97, 0.74) form an invariant mass of of $m_{\ell\ell} = 87.0$ GeV, consistent with a Z boson. The muons are paired with the electron (362.2 GeV, -0.53, -1.06), with $m_{\mathrm{Z}\ell} = 742.7$ GeV. The event has a missing transverse energy of $E_{\mathrm{T}}^{\mathrm{miss}} = 172.5$ GeV, which is represented as a dashed white line at $\phi = 2.51$.

D.2 Upper Limits on Signal Production Cross Section
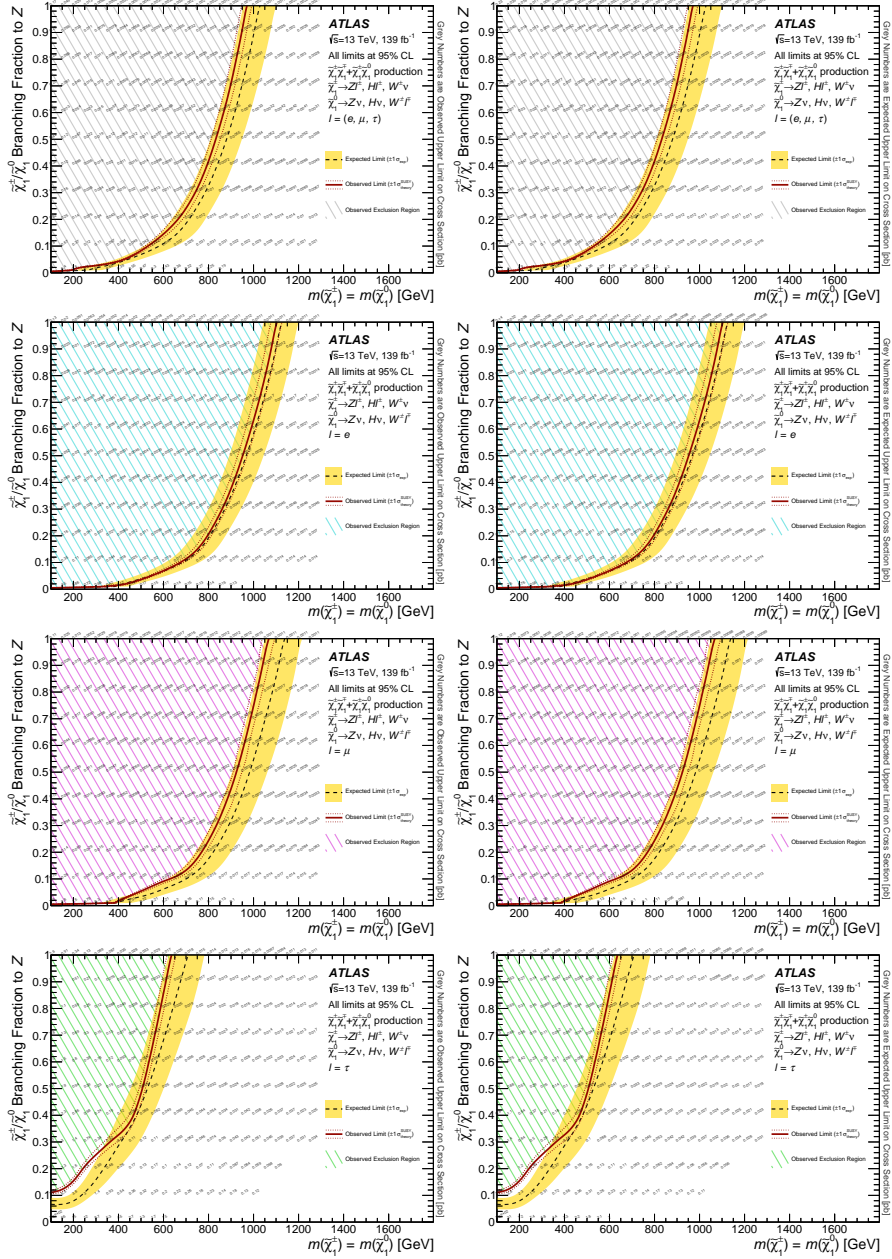
Figure D.4: Exclusion curves for the simplified model of $\tilde{\chi}_1^\pm \tilde{\chi}_1^\mp + \tilde{\chi}_1^\pm \tilde{\chi}_1^0$ production as a function of $\tilde{\chi}_1^\pm / \tilde{\chi}_1^0$ mass and branching fraction to Z bosons. Curves are derived separately when requiring that the charged-lepton decays of $\tilde{\chi}_1^\pm / \tilde{\chi}_1^0$ are into (top) any leptons with equal probability, (second row) electrons only, (third row) muons only, or (bottom) τ-leptons only. The expected 95% CL exclusion (dashed black line) is shown with $\pm 1\,\sigma_{\text{exp}}$ variations (shaded yellow band) from systematic and statistical uncertainties in the expected yields. The observed 95% CL exclusion (solid red line) is shown with $\pm 1\,\sigma_{\text{theory}}^{\text{SUSY}}$ variations (dotted red lines) from cross-section uncertainties for the signal models. The phase-space excluded by the search is shown in the hatched regions. The sum of the $\tilde{\chi}_1^\pm / \tilde{\chi}_1^0$ branching fractions to W, Z, and Higgs bosons is unity for each point, and the branching fractions to W and Higgs bosons are chosen so as to be equal everywhere. Grey numbers represent the observed (left) and expected (right) upper cross-section limits.

Table D.1: Upper limits on the (left) observed and (right) expected cross section of the $\tilde{\chi}_1^\pm\tilde{\chi}_1^\mp + \tilde{\chi}_1^\pm\tilde{\chi}_1^0$ processes as a function of $\tilde{\chi}_1^\pm/\tilde{\chi}_1^0$ mass and branching fraction to Z bosons. Upper limits are derived when requiring that the charged-lepton decays of $\tilde{\chi}_1^\pm/\tilde{\chi}_1^0$ are into any leptons with equal probability. The sum of the $\tilde{\chi}_1^\pm/\tilde{\chi}_1^0$ branching fractions to W, Z, and Higgs bosons is unity for each point, and the branching fractions to W and Higgs bosons are chosen so as to be equal everywhere.

$l = (e,\,\mu,\,\tau)$

$m_{\tilde{\chi}_1^\pm/\tilde{\chi}_1^0}$	Z b.f.	$\sigma^{95}_{\mathrm{obs}}$ [pb]	$\sigma^{95}_{\mathrm{exp}}$ [pb]	$m_{\tilde{\chi}_1^\pm/\tilde{\chi}_1^0}$	Z b.f.	$\sigma^{95}_{\mathrm{obs}}$ [pb]	$\sigma^{95}_{\mathrm{exp}}$ [pb]	$m_{\tilde{\chi}_1^\pm/\tilde{\chi}_1^0}$	Z b.f.	$\sigma^{95}_{\mathrm{obs}}$ [pb]	$\sigma^{95}_{\mathrm{exp}}$ [pb]
100	1.0	0.17	0.23	500	1.0	0.0049	0.0033	900	1.0	0.0024	0.0017
100	0.9	0.25	0.24	500	0.9	0.0056	0.0038	900	0.9	0.0027	0.002
100	0.8	0.22	0.25	500	0.8	0.0064	0.0043	900	0.8	0.0032	0.0023
100	0.7	0.25	0.26	500	0.7	0.0075	0.0051	900	0.7	0.0028	0.0027
100	0.6	0.36	0.28	500	0.6	0.0089	0.0061	900	0.6	0.0045	0.0033
100	0.5	0.42	0.31	500	0.5	0.011	0.0075	900	0.5	0.0055	0.0041
100	0.4	0.38	0.36	500	0.4	0.014	0.0096	900	0.4	0.007	0.0053
100	0.3	0.49	0.45	500	0.3	0.019	0.013	900	0.3	0.0096	0.0074
100	0.2	0.92	0.63	500	0.2	0.028	0.02	900	0.2	0.015	0.012
100	0.1	1.8	1.2	500	0.1	0.043	0.041	900	0.1	0.022	0.024
100	0.01	17	11	500	0.01	0.47	0.36	950	1.0	0.0018	0.0018
150	1.0	0.049	0.039	550	1.0	0.0034	0.003	950	0.9	0.0028	0.002
150	0.9	0.056	0.045	550	0.9	0.0051	0.0034	950	0.8	0.0032	0.0023
150	0.8	0.066	0.052	550	0.8	0.0059	0.0039	950	0.7	0.0037	0.0028
150	0.7	0.061	0.061	550	0.7	0.0053	0.0046	950	0.6	0.0045	0.0033
150	0.6	0.073	0.071	550	0.6	0.0083	0.0055	950	0.5	0.0055	0.0042
150	0.5	0.12	0.087	550	0.5	0.0077	0.0068	950	0.4	0.0053	0.0054
150	0.4	0.12	0.11	550	0.4	0.0098	0.0087	950	0.3	0.0096	0.0074
150	0.3	0.16	0.15	550	0.3	0.013	0.012	950	0.2	0.011	0.012
150	0.2	0.25	0.23	550	0.2	0.02	0.018	950	0.1	0.022	0.023
150	0.1	0.67	0.47	550	0.1	0.052	0.037	1000	1.0	0.0024	0.0017
150	0.01	6.4	4	550	0.01	0.3	0.29	1000	0.9	0.0027	0.002
200	1.0	0.029	0.016	600	1.0	0.0036	0.0025	1000	0.8	0.0031	0.0023
200	0.9	0.033	0.018	600	0.9	0.0041	0.0029	1000	0.7	0.0037	0.0027
200	0.8	0.029	0.021	600	0.8	0.0048	0.0034	1000	0.6	0.0033	0.0033
200	0.7	0.045	0.025	600	0.7	0.0042	0.004	1000	0.5	0.0054	0.0041
200	0.6	0.054	0.03	600	0.6	0.0068	0.0048	1000	0.4	0.0069	0.0053
200	0.5	0.067	0.036	600	0.5	0.0084	0.006	1000	0.3	0.0093	0.0072
200	0.4	0.086	0.047	600	0.4	0.0081	0.0077	1000	0.2	0.011	0.011
200	0.3	0.088	0.064	600	0.3	0.011	0.011	1000	0.1	0.029	0.023
200	0.2	0.14	0.098	600	0.2	0.023	0.017	1050	1.0	0.0017	0.0016
200	0.1	0.37	0.2	600	0.1	0.047	0.034	1050	0.9	0.002	0.0019
200	0.01	3.6	1.9	600	0.01	0.43	0.29	1050	0.8	0.003	0.0022
250	1.0	0.013	0.011	650	1.0	0.0031	0.0022	1050	0.7	0.0035	0.0026
250	0.9	0.011	0.013	650	0.9	0.0035	0.0025	1050	0.6	0.0032	0.0032
250	0.8	0.017	0.015	650	0.8	0.003	0.0029	1050	0.5	0.0052	0.0039
250	0.7	0.015	0.018	650	0.7	0.0048	0.0035	1050	0.4	0.0066	0.0051
250	0.6	0.023	0.021	650	0.6	0.0057	0.0042	1050	0.3	0.0091	0.0071
250	0.5	0.022	0.026	650	0.5	0.0052	0.0051	1050	0.2	0.014	0.011
250	0.4	0.036	0.033	650	0.4	0.0089	0.0066	1050	0.1	0.028	0.023
250	0.3	0.038	0.045	650	0.3	0.009	0.0091	1100	1.0	0.0017	0.0016
250	0.2	0.076	0.07	650	0.2	0.014	0.014	1100	0.9	0.0026	0.0019
250	0.1	0.12	0.14	650	0.1	0.037	0.029	1100	0.8	0.003	0.0022
250	0.01	1.5	1.3	650	0.01	0.36	0.26	1100	0.7	0.0035	0.0026
300	1.0	0.0088	0.0081	700	1.0	0.0021	0.002	1100	0.6	0.0042	0.0031
300	0.9	0.0075	0.009	700	0.9	0.0032	0.0023	1100	0.5	0.0039	0.0039
300	0.8	0.011	0.011	700	0.8	0.0037	0.0027	1100	0.4	0.0066	0.0051
300	0.7	0.013	0.012	700	0.7	0.0043	0.0032	1100	0.3	0.0069	0.0071
300	0.6	0.016	0.015	700	0.6	0.0052	0.0038	1100	0.2	0.014	0.011
300	0.5	0.019	0.018	700	0.5	0.0064	0.0048	1100	0.1	0.021	0.023
300	0.4	0.019	0.024	700	0.4	0.0082	0.0062	1150	1.0	0.0023	0.0017
300	0.3	0.034	0.032	700	0.3	0.0084	0.0085	1150	0.9	0.002	0.0019
300	0.2	0.04	0.05	700	0.2	0.013	0.013	1150	0.8	0.003	0.0022
300	0.1	0.11	0.1	700	0.1	0.025	0.027	1150	0.7	0.0027	0.0026
300	0.01	0.7	0.88	700	0.01	0.22	0.23	1150	0.6	0.0042	0.0032
350	1.0	0.0052	0.0049	750	1.0	0.002	0.0019	1150	0.5	0.004	0.0039
350	0.9	0.0078	0.0056	750	0.9	0.0031	0.0022	1150	0.4	0.0051	0.0051
350	0.8	0.0069	0.0065	750	0.8	0.0026	0.0026	1150	0.3	0.0091	0.0071
350	0.7	0.011	0.0077	750	0.7	0.0041	0.003	1150	0.2	0.014	0.011
350	0.6	0.0097	0.0092	750	0.6	0.0037	0.0036	1150	0.1	0.027	0.023
350	0.5	0.012	0.011	750	0.5	0.006	0.0045	1200	1.0	0.0022	0.0016
350	0.4	0.02	0.015	750	0.4	0.0076	0.0058	1200	0.9	0.0026	0.0019
350	0.3	0.028	0.02	750	0.3	0.0077	0.0079	1200	0.8	0.003	0.0022
350	0.2	0.043	0.031	750	0.2	0.012	0.012	1200	0.7	0.0035	0.0026
350	0.1	0.067	0.064	750	0.1	0.031	0.025	1200	0.6	0.0041	0.0031
350	0.01	0.66	0.56	750	0.01	0.27	0.22	1200	0.5	0.0052	0.0039
400	1.0	0.0039	0.0046	800	1.0	0.0026	0.0019	1200	0.4	0.0066	0.0051
400	0.9	0.0044	0.0052	800	0.9	0.003	0.0021	1200	0.3	0.0069	0.007
400	0.8	0.0037	0.006	800	0.8	0.0026	0.0025	1200	0.2	0.01	0.011
400	0.7	0.0059	0.007	800	0.7	0.004	0.0029	1200	0.1	0.021	0.022
400	0.6	0.0051	0.0085	800	0.6	0.0047	0.0035	1250	1.0	0.0021	0.0016
400	0.5	0.0063	0.01	800	0.5	0.0058	0.0044	1250	0.9	0.0025	0.0018
400	0.4	0.011	0.013	800	0.4	0.0074	0.0057	1250	0.8	0.0028	0.0022
400	0.3	0.015	0.019	800	0.3	0.01	0.0078	1250	0.7	0.0033	0.0026
400	0.2	0.017	0.029	800	0.2	0.015	0.012	1250	0.6	0.0031	0.0031
400	0.1	0.034	0.058	800	0.1	0.031	0.025	1250	0.5	0.0038	0.0039
400	0.01	0.39	0.51	800	0.01	0.25	0.2	1250	0.4	0.0049	0.005
450	1.0	0.0051	0.0039	850	1.0	0.0018	0.0018	1250	0.3	0.0067	0.007
450	0.9	0.0058	0.0044	850	0.9	0.0028	0.002	1250	0.2	0.013	0.011
450	0.8	0.0067	0.0051	850	0.8	0.0024	0.0024	1250	0.1	0.021	0.016
450	0.7	0.0079	0.0061	850	0.7	0.0038	0.0028				
450	0.6	0.0073	0.0073	850	0.6	0.0034	0.0034				
450	0.5	0.012	0.009	850	0.5	0.0056	0.0043				
450	0.4	0.015	0.012	850	0.4	0.0072	0.0055				
450	0.3	0.02	0.016	850	0.3	0.0075	0.0076				
450	0.2	0.031	0.025	850	0.2	0.015	0.012				
450	0.1	0.049	0.051	850	0.1	0.031	0.024				
450	0.01	0.55	0.44	850	0.01	0.19	0.2				

Table D.2: Upper limits on the (left) observed and (right) expected cross section of the $\tilde{\chi}_1^\pm \tilde{\chi}_1^\mp + \tilde{\chi}_1^\pm \tilde{\chi}_1^0$ processes as a function of $\tilde{\chi}_1^\pm/\tilde{\chi}_1^0$ mass and branching fraction to Z bosons. Upper limits are derived when requiring that the charged-lepton decays of $\tilde{\chi}_1^\pm/\tilde{\chi}_1^0$ are into electrons only. The sum of the $\tilde{\chi}_1^\pm/\tilde{\chi}_1^0$ branching fractions to W, Z, and Higgs bosons is unity for each point, and the branching fractions to W and Higgs bosons are chosen so as to be equal everywhere.

$l = e$

$m_{\tilde{\chi}_1^\pm/\tilde{\chi}_1^0}$	Z b.f.	σ_{obs}^{95} [pb]	σ_{exp}^{95} [pb]	$m_{\tilde{\chi}_1^\pm/\tilde{\chi}_1^0}$	Z b.f.	σ_{obs}^{95} [pb]	σ_{exp}^{95} [pb]	$m_{\tilde{\chi}_1^\pm/\tilde{\chi}_1^0}$	Z b.f.	σ_{obs}^{95} [pb]	σ_{exp}^{95} [pb]
100	1.0	0.13	0.14	500	1.0	0.0018	0.0018	900	1.0	0.0011	0.00098
100	0.9	0.15	0.15	500	0.9	0.0021	0.002	900	0.9	0.0013	0.0011
100	0.8	0.17	0.16	500	0.8	0.0024	0.0023	900	0.8	0.0015	0.0013
100	0.7	0.19	0.17	500	0.7	0.0028	0.0028	900	0.7	0.0018	0.0016
100	0.6	0.21	0.19	500	0.6	0.0033	0.0033	900	0.6	0.0021	0.0019
100	0.5	0.25	0.21	500	0.5	0.0041	0.0041	900	0.5	0.0026	0.0024
100	0.4	0.31	0.25	500	0.4	0.0052	0.0052	900	0.4	0.0034	0.0031
100	0.3	0.4	0.31	500	0.3	0.007	0.0071	900	0.3	0.0047	0.0043
100	0.2	0.58	0.44	500	0.2	0.011	0.011	900	0.2	0.0073	0.0067
100	0.1	1.1	0.83	500	0.1	0.021	0.022	900	0.1	0.015	0.014
100	0.01	11	7.9	500	0.01	0.17	0.19	900	0.01	0.13	0.12
150	1.0	0.02	0.022	550	1.0	0.0018	0.0017	950	1.0	0.0012	0.001
150	0.9	0.023	0.026	550	0.9	0.002	0.0019	950	0.9	0.0013	0.0012
150	0.8	0.028	0.03	550	0.8	0.0023	0.0023	950	0.8	0.0016	0.0014
150	0.7	0.033	0.035	550	0.7	0.0027	0.0026	950	0.7	0.0018	0.0016
150	0.6	0.041	0.042	550	0.6	0.0032	0.0031	950	0.6	0.0022	0.002
150	0.5	0.052	0.053	550	0.5	0.0039	0.0039	950	0.5	0.0027	0.0025
150	0.4	0.069	0.068	550	0.4	0.0049	0.0049	950	0.4	0.0036	0.0033
150	0.3	0.099	0.094	550	0.3	0.0066	0.0067	950	0.3	0.0049	0.0045
150	0.2	0.16	0.15	550	0.2	0.0099	0.01	950	0.2	0.0076	0.0071
150	0.1	0.35	0.3	550	0.1	0.02	0.02	950	0.1	0.015	0.015
150	0.01	4.5	2.6	550	0.01	0.15	0.15	1000	1.0	0.0011	0.00095
200	1.0	0.0091	0.008	600	1.0	0.0015	0.0014	1000	0.9	0.0012	0.0011
200	0.9	0.01	0.0091	600	0.9	0.0017	0.0016	1000	0.8	0.0014	0.0013
200	0.8	0.012	0.011	600	0.8	0.0019	0.0018	1000	0.7	0.0017	0.0015
200	0.7	0.014	0.012	600	0.7	0.0023	0.0021	1000	0.6	0.0021	0.0019
200	0.6	0.017	0.014	600	0.6	0.0027	0.0026	1000	0.5	0.0026	0.0023
200	0.5	0.02	0.018	600	0.5	0.0033	0.0032	1000	0.4	0.0033	0.003
200	0.4	0.026	0.023	600	0.4	0.0043	0.004	1000	0.3	0.0046	0.0042
200	0.3	0.036	0.031	600	0.3	0.0059	0.0055	1000	0.2	0.0072	0.0066
200	0.2	0.055	0.047	600	0.2	0.0091	0.0086	1000	0.1	0.015	0.014
200	0.1	0.11	0.096	600	0.1	0.019	0.017	1050	1.0	0.0011	0.00097
200	0.01	0.86	0.76	600	0.01	0.17	0.14	1050	0.9	0.0012	0.0011
250	1.0	0.0063	0.0052	650	1.0	0.0013	0.0012	1050	0.8	0.0015	0.0013
250	0.9	0.0072	0.0059	650	0.9	0.0015	0.0014	1050	0.7	0.0017	0.0016
250	0.8	0.0084	0.0069	650	0.8	0.0017	0.0016	1050	0.6	0.0021	0.0019
250	0.7	0.0099	0.0081	650	0.7	0.002	0.0019	1050	0.5	0.0026	0.0024
250	0.6	0.012	0.0097	650	0.6	0.0024	0.0022	1050	0.4	0.0034	0.0031
250	0.5	0.015	0.012	650	0.5	0.0029	0.0028	1050	0.3	0.0048	0.0044
250	0.4	0.019	0.015	650	0.4	0.0038	0.0036	1050	0.2	0.0074	0.0068
250	0.3	0.026	0.021	650	0.3	0.0053	0.005	1050	0.1	0.015	0.014
250	0.2	0.041	0.033	650	0.2	0.0081	0.0076	1100	1.0	0.0011	0.00096
250	0.1	0.085	0.068	650	0.1	0.017	0.016	1100	0.9	0.0012	0.0011
250	0.01	0.72	0.56	650	0.01	0.14	0.14	1100	0.8	0.0014	0.0013
300	1.0	0.0054	0.0036	700	1.0	0.0012	0.0011	1100	0.7	0.0017	0.0015
300	0.9	0.0062	0.0042	700	0.9	0.0014	0.0013	1100	0.6	0.002	0.0019
300	0.8	0.0073	0.0048	700	0.8	0.0016	0.0015	1100	0.5	0.0025	0.0023
300	0.7	0.0086	0.0057	700	0.7	0.0019	0.0018	1100	0.4	0.0033	0.003
300	0.6	0.01	0.0068	700	0.6	0.0024	0.0022	1100	0.3	0.0045	0.0042
300	0.5	0.013	0.0084	700	0.5	0.0029	0.0027	1100	0.2	0.007	0.0065
300	0.4	0.017	0.011	700	0.4	0.0038	0.0035	1100	0.1	0.014	0.013
300	0.3	0.024	0.015	700	0.3	0.0052	0.0049	1150	1.0	0.0011	0.00095
300	0.2	0.037	0.023	700	0.2	0.0082	0.0075	1150	0.9	0.0012	0.0011
300	0.1	0.076	0.047	700	0.1	0.017	0.016	1150	0.8	0.0014	0.0013
300	0.01	0.68	0.4	700	0.01	0.15	0.15	1150	0.7	0.0017	0.0015
350	1.0	0.0032	0.0025	750	1.0	0.0011	0.001	1150	0.6	0.0021	0.0018
350	0.9	0.0037	0.0029	750	0.9	0.0013	0.0012	1150	0.5	0.0026	0.0023
350	0.8	0.0043	0.0033	750	0.8	0.0015	0.0014	1150	0.4	0.0033	0.003
350	0.7	0.0051	0.0039	750	0.7	0.0018	0.0016	1150	0.3	0.0046	0.0042
350	0.6	0.0061	0.0047	750	0.6	0.0021	0.002	1150	0.2	0.0071	0.0066
350	0.5	0.0076	0.0058	750	0.5	0.0026	0.0024	1150	0.1	0.014	0.014
350	0.4	0.0099	0.0075	750	0.4	0.0034	0.0032	1200	1.0	0.0011	0.00096
350	0.3	0.014	0.01	750	0.3	0.0047	0.0044	1200	0.9	0.0013	0.0011
350	0.2	0.021	0.016	750	0.2	0.0073	0.0068	1200	0.8	0.0015	0.0013
350	0.1	0.044	0.032	750	0.1	0.015	0.014	1200	0.7	0.0017	0.0015
350	0.01	0.42	0.28	750	0.01	0.13	0.12	1200	0.6	0.0021	0.0019
400	1.0	0.0014	0.0021	800	1.0	0.0011	0.001	1200	0.5	0.0026	0.0023
400	0.9	0.0016	0.0024	800	0.9	0.0013	0.0012	1200	0.4	0.0034	0.003
400	0.8	0.0018	0.0028	800	0.8	0.0015	0.0014	1200	0.3	0.0046	0.0042
400	0.7	0.0021	0.0033	800	0.7	0.0018	0.0016	1200	0.2	0.0071	0.0066
400	0.6	0.0025	0.004	800	0.6	0.0021	0.002	1200	0.1	0.014	0.014
400	0.5	0.0031	0.0049	800	0.5	0.0026	0.0024	1250	1.0	0.0011	0.00095
400	0.4	0.004	0.0063	800	0.4	0.0034	0.0032	1250	0.9	0.0012	0.0011
400	0.3	0.0055	0.0087	800	0.3	0.0047	0.0043	1250	0.8	0.0014	0.0013
400	0.2	0.0085	0.013	800	0.2	0.0072	0.0066	1250	0.7	0.0017	0.0015
400	0.1	0.018	0.027	800	0.1	0.015	0.014	1250	0.6	0.0021	0.0019
400	0.01	0.17	0.24	800	0.01	0.14	0.12	1250	0.5	0.0026	0.0023
450	1.0	0.002	0.002	850	1.0	0.0011	0.00098	1250	0.4	0.0033	0.003
450	0.9	0.0023	0.0023	850	0.9	0.0012	0.0011	1250	0.3	0.0046	0.0042
450	0.8	0.0026	0.0027	850	0.8	0.0014	0.0013	1250	0.2	0.007	0.0066
450	0.7	0.0031	0.0032	850	0.7	0.0017	0.0016	1250	0.1	0.014	0.014
450	0.6	0.0037	0.0038	850	0.6	0.0021	0.0019				
450	0.5	0.0046	0.0047	850	0.5	0.0026	0.0024				
450	0.4	0.0058	0.0061	850	0.4	0.0035	0.0032				
450	0.3	0.008	0.0084	850	0.3	0.0049	0.0044				
450	0.2	0.012	0.013	850	0.2	0.0077	0.007				
450	0.1	0.025	0.027	850	0.1	0.016	0.015				
450	0.01	0.19	0.21	850	0.01	0.16	0.14				

Table D.3: Upper limits on the (left) observed and (right) expected cross section of the $\tilde{\chi}_1^{\pm}\tilde{\chi}_1^{\mp} + \tilde{\chi}_1^{\pm}\tilde{\chi}_1^0$ processes as a function of $\tilde{\chi}_1^{\pm}/\tilde{\chi}_1^0$ mass and branching fraction to Z bosons. Upper limits are derived when requiring that the charged-lepton decays of $\tilde{\chi}_1^{\pm}/\tilde{\chi}_1^0$ are into muons only. The sum of the $\tilde{\chi}_1^{\pm}/\tilde{\chi}_1^0$ branching fractions to W, Z, and Higgs bosons is unity for each point, and the branching fractions to W and Higgs bosons are chosen so as to be equal everywhere.

$l = \mu$

$m_{\tilde{\chi}_1^{\pm}/\tilde{\chi}_1^0}$	Z b.f.	σ_{obs}^{95} [pb]	σ_{exp}^{95} [pb]	$m_{\tilde{\chi}_1^{\pm}/\tilde{\chi}_1^0}$	Z b.f.	σ_{obs}^{95} [pb]	σ_{exp}^{95} [pb]	$m_{\tilde{\chi}_1^{\pm}/\tilde{\chi}_1^0}$	Z b.f.	σ_{obs}^{95} [pb]	σ_{exp}^{95} [pb]
100	1.0	0.11	0.12	500	1.0	0.0026	0.0014	900	1.0	0.0012	0.00092
100	0.9	0.11	0.12	500	0.9	0.0026	0.0017	900	0.9	0.0016	0.0011
100	0.8	0.12	0.13	500	0.8	0.0035	0.0019	900	0.8	0.0018	0.0012
100	0.7	0.13	0.13	500	0.7	0.0036	0.0023	900	0.7	0.0022	0.0015
100	0.6	0.17	0.14	500	0.6	0.0051	0.0027	900	0.6	0.0022	0.0018
100	0.5	0.19	0.16	500	0.5	0.0054	0.0034	900	0.5	0.0032	0.0022
100	0.4	0.19	0.19	500	0.4	0.007	0.0043	900	0.4	0.004	0.0028
100	0.3	0.28	0.23	500	0.3	0.011	0.0059	900	0.3	0.0055	0.0039
100	0.2	0.35	0.32	500	0.2	0.018	0.0092	900	0.2	0.0071	0.0061
100	0.1	0.75	0.61	500	0.1	0.03	0.019	900	0.1	0.017	0.012
100	0.01	7.2	5.8	500	0.01	0.22	0.14	900	0.01	0.1	0.081
150	1.0	0.025	0.018	550	1.0	0.0025	0.0013	950	1.0	0.0012	0.00092
150	0.9	0.028	0.02	550	0.9	0.0029	0.0015	950	0.9	0.0014	0.0011
150	0.8	0.032	0.023	550	0.8	0.0034	0.0017	950	0.8	0.0018	0.0012
150	0.7	0.037	0.028	550	0.7	0.0035	0.002	950	0.7	0.0018	0.0015
150	0.6	0.044	0.033	550	0.6	0.0042	0.0024	950	0.6	0.0022	0.0018
150	0.5	0.054	0.041	550	0.5	0.0052	0.0031	950	0.5	0.0031	0.0022
150	0.4	0.069	0.052	550	0.4	0.0067	0.0039	950	0.4	0.004	0.0028
150	0.3	0.094	0.072	550	0.3	0.0092	0.0055	950	0.3	0.0055	0.0039
150	0.2	0.14	0.11	550	0.2	0.014	0.0084	950	0.2	0.0083	0.006
150	0.1	0.26	0.23	550	0.1	0.034	0.017	950	0.1	0.017	0.012
150	0.01	2.8	1.9	550	0.01	0.21	0.13	1000	1.0	0.0015	0.00099
200	1.0	0.013	0.0073	600	1.0	0.0021	0.0012	1000	0.9	0.0014	0.0011
200	0.9	0.013	0.0084	600	0.9	0.002	0.0014	1000	0.8	0.0019	0.0013
200	0.8	0.017	0.0097	600	0.8	0.0028	0.0017	1000	0.7	0.0022	0.0015
200	0.7	0.017	0.011	600	0.7	0.0028	0.002	1000	0.6	0.0022	0.0018
200	0.6	0.021	0.014	600	0.6	0.0034	0.0024	1000	0.5	0.0031	0.0022
200	0.5	0.029	0.017	600	0.5	0.0042	0.003	1000	0.4	0.0039	0.0028
200	0.4	0.038	0.021	600	0.4	0.0054	0.0038	1000	0.3	0.0045	0.0038
200	0.3	0.045	0.029	600	0.3	0.0074	0.0053	1000	0.2	0.0068	0.0059
200	0.2	0.069	0.045	600	0.2	0.011	0.0083	1000	0.1	0.014	0.012
200	0.1	0.17	0.093	600	0.1	0.028	0.017	1050	1.0	0.0011	0.0009
200	0.01	1.6	0.89	600	0.01	0.21	0.14	1050	0.9	0.0013	0.001
250	1.0	0.0052	0.0051	650	1.0	0.0017	0.0011	1050	0.8	0.0015	0.0012
250	0.9	0.0053	0.0058	650	0.9	0.0016	0.0013	1050	0.7	0.0018	0.0014
250	0.8	0.007	0.0068	650	0.8	0.0022	0.0014	1050	0.6	0.0025	0.0017
250	0.7	0.0081	0.0078	650	0.7	0.0026	0.0017	1050	0.5	0.0031	0.0022
250	0.6	0.0086	0.0093	650	0.6	0.0026	0.002	1050	0.4	0.0034	0.0028
250	0.5	0.011	0.012	650	0.5	0.0037	0.0025	1050	0.3	0.0046	0.0039
250	0.4	0.014	0.015	650	0.4	0.0047	0.0032	1050	0.2	0.0083	0.0061
250	0.3	0.021	0.02	650	0.3	0.0063	0.0044	1050	0.1	0.014	0.013
250	0.2	0.029	0.031	650	0.2	0.0081	0.0068	1100	1.0	0.0011	0.00088
250	0.1	0.061	0.065	650	0.1	0.016	0.014	1100	0.9	0.0012	0.001
250	0.01	0.79	0.62	650	0.01	0.2	0.14	1100	0.8	0.0017	0.0012
300	1.0	0.0029	0.0035	700	1.0	0.0016	0.001	1100	0.7	0.0017	0.0014
300	0.9	0.0033	0.004	700	0.9	0.0018	0.0012	1100	0.6	0.0024	0.0017
300	0.8	0.0038	0.0047	700	0.8	0.0018	0.0014	1100	0.5	0.0026	0.0021
300	0.7	0.0038	0.0054	700	0.7	0.0021	0.0016	1100	0.4	0.0033	0.0028
300	0.6	0.0046	0.0065	700	0.6	0.0029	0.0019	1100	0.3	0.0054	0.0039
300	0.5	0.0056	0.008	700	0.5	0.0036	0.0024	1100	0.2	0.0083	0.0061
300	0.4	0.0083	0.01	700	0.4	0.0046	0.0031	1100	0.1	0.017	0.013
300	0.3	0.011	0.014	700	0.3	0.0062	0.0043	1150	1.0	0.0011	0.00088
300	0.2	0.015	0.021	700	0.2	0.0079	0.0067	1150	0.9	0.0012	0.001
300	0.1	0.036	0.044	700	0.1	0.019	0.014	1150	0.8	0.0014	0.0012
300	0.01	0.3	0.38	700	0.01	0.16	0.1	1150	0.7	0.0017	0.0014
350	1.0	0.0018	0.0023	750	1.0	0.0016	0.001	1150	0.6	0.002	0.0017
350	0.9	0.0024	0.0026	750	0.9	0.0018	0.0012	1150	0.5	0.0025	0.0021
350	0.8	0.0024	0.0031	750	0.8	0.0021	0.0013	1150	0.4	0.0032	0.0028
350	0.7	0.0027	0.0036	750	0.7	0.0024	0.0016	1150	0.3	0.0044	0.0037
350	0.6	0.0039	0.0043	750	0.6	0.0024	0.0019	1150	0.2	0.0079	0.0058
350	0.5	0.0047	0.0053	750	0.5	0.003	0.0023	1150	0.1	0.014	0.012
350	0.4	0.006	0.0069	750	0.4	0.0044	0.003	1200	1.0	0.0011	0.0009
350	0.3	0.007	0.0095	750	0.3	0.005	0.0041	1200	0.9	0.0013	0.001
350	0.2	0.011	0.015	750	0.2	0.0075	0.0063	1200	0.8	0.0018	0.0012
350	0.1	0.023	0.03	750	0.1	0.015	0.013	1200	0.7	0.0021	0.0014
350	0.01	0.27	0.23	750	0.01	0.11	0.1	1200	0.6	0.0025	0.0017
400	1.0	0.0016	0.0022	800	1.0	0.0012	0.00095	1200	0.5	0.0026	0.0022
400	0.9	0.0021	0.0025	800	0.9	0.0014	0.0011	1200	0.4	0.0034	0.0029
400	0.8	0.002	0.0029	800	0.8	0.0019	0.0013	1200	0.3	0.0046	0.004
400	0.7	0.0024	0.0034	800	0.7	0.0022	0.0015	1200	0.2	0.0084	0.0063
400	0.6	0.0033	0.0041	800	0.6	0.0023	0.0018	1200	0.1	0.015	0.013
400	0.5	0.0034	0.005	800	0.5	0.0028	0.0022	1250	1.0	0.0011	0.00089
400	0.4	0.0052	0.0065	800	0.4	0.0035	0.0029	1250	0.9	0.0014	0.001
400	0.3	0.007	0.0089	800	0.3	0.0056	0.004	1250	0.8	0.0017	0.0012
400	0.2	0.0089	0.014	800	0.2	0.0073	0.0062	1250	0.7	0.0017	0.0014
400	0.1	0.018	0.028	800	0.1	0.015	0.013	1250	0.6	0.002	0.0017
400	0.01	0.22	0.25	800	0.01	0.15	0.11	1250	0.5	0.0025	0.0022
450	1.0	0.003	0.002	850	1.0	0.0012	0.00094	1250	0.4	0.0033	0.0028
450	0.9	0.003	0.0022	850	0.9	0.0014	0.0011	1250	0.3	0.0046	0.004
450	0.8	0.004	0.0026	850	0.8	0.0019	0.0012	1250	0.2	0.0083	0.0062
450	0.7	0.004	0.003	850	0.7	0.0018	0.0015	1250	0.1	0.015	0.013
450	0.6	0.0056	0.0036	850	0.6	0.0022	0.0018				
450	0.5	0.0069	0.0044	850	0.5	0.0032	0.0022				
450	0.4	0.0088	0.0057	850	0.4	0.0041	0.0028				
450	0.3	0.012	0.0077	850	0.3	0.0047	0.0039				
450	0.2	0.018	0.012	850	0.2	0.0071	0.0061				
450	0.1	0.031	0.024	850	0.1	0.017	0.012				
450	0.01	0.31	0.22	850	0.01	0.13	0.095				

Table D.4: Upper limits on the (left) observed and (right) expected cross section of the $\tilde{\chi}_1^\pm \tilde{\chi}_1^\mp + \tilde{\chi}_1^\pm \tilde{\chi}_1^0$ processes as a function of $\tilde{\chi}_1^\pm/\tilde{\chi}_1^0$ mass and branching fraction to Z bosons. Upper limits are derived when requiring that the charged-lepton decays of $\tilde{\chi}_1^\pm/\tilde{\chi}_1^0$ are into τ-leptons only. The sum of the $\tilde{\chi}_1^\pm/\tilde{\chi}_1^0$ branching fractions to W, Z, and Higgs bosons is unity for each point, and the branching fractions to W and Higgs bosons are chosen so as to be equal everywhere.

$l = \tau$

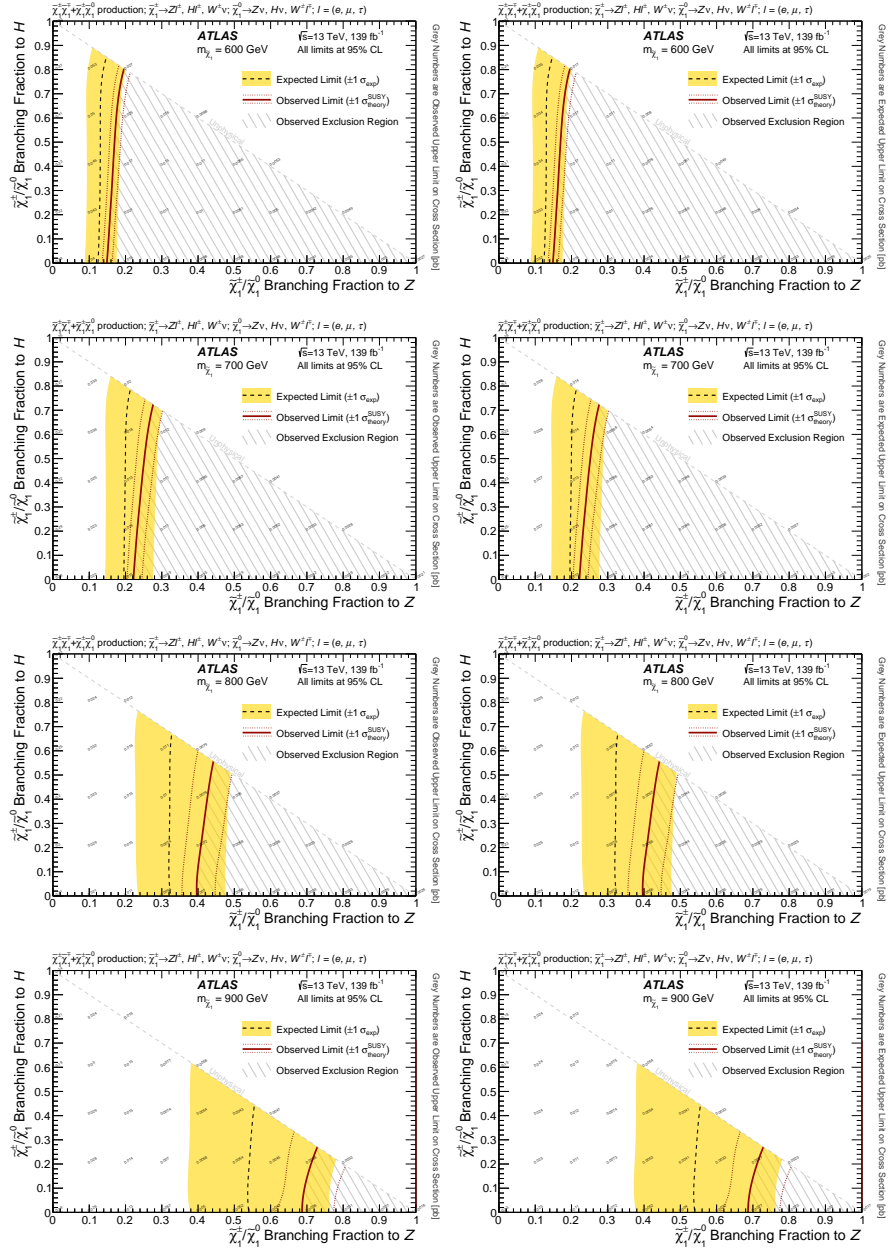| $m_{\tilde{\chi}_1^\pm/\tilde{\chi}_1^0}$	Z b.f.	σ^{95}_{obs} [pb]	σ^{95}_{exp} [pb]	$m_{\tilde{\chi}_1^\pm/\tilde{\chi}_1^0}$	Z b.f.	σ^{95}_{obs} [pb]	σ^{95}_{exp} [pb]	$m_{\tilde{\chi}_1^\pm/\tilde{\chi}_1^0}$	Z b.f.	σ^{95}_{obs} [pb]	σ^{95}_{exp} [pb]
100	1.0	2.6	3	500	1.0	0.033	0.027	900	1.0	0.013	0.0098
100	0.9	2.3	3.5	500	0.9	0.038	0.031	900	0.9	0.012	0.011
100	0.8	3	3.9	500	0.8	0.043	0.036	900	0.8	0.018	0.013
100	0.7	3.8	4.3	500	0.7	0.05	0.042	900	0.7	0.021	0.016
100	0.6	6.5	4.9	500	0.6	0.059	0.05	900	0.6	0.02	0.019
100	0.5	8.1	5.7	500	0.5	0.055	0.061	900	0.5	0.024	0.023
100	0.4	10	6.8	500	0.4	0.088	0.078	900	0.4	0.031	0.03
100	0.3	10	8.6	500	0.3	0.12	0.1	900	0.3	0.043	0.042
100	0.2	15	12	500	0.2	0.13	0.16	900	0.2	0.087	0.065
100	0.1	39	23	500	0.1	0.32	0.31	900	0.1	0.18	0.13
100	0.01	2.8e+02	2.2e+02	500	0.01	1.3	1.8	950	1.0	0.016	0.011
150	1.0	0.91	0.49	550	1.0	0.029	0.023	950	0.9	0.014	0.012
150	0.9	1	0.53	550	0.9	0.033	0.026	950	0.8	0.016	0.014
150	0.8	1.1	0.59	550	0.8	0.038	0.03	950	0.7	0.024	0.016
150	0.7	1.3	0.66	550	0.7	0.045	0.035	950	0.6	0.028	0.019
150	0.6	1.5	0.75	550	0.6	0.053	0.042	950	0.5	0.025	0.023
150	0.5	1.9	0.88	550	0.5	0.05	0.051	950	0.4	0.042	0.029
150	0.4	2.3	1.1	550	0.4	0.082	0.065	950	0.3	0.043	0.039
150	0.3	3	1.4	550	0.3	0.11	0.088	950	0.2	0.084	0.06
150	0.2	3.3	2	550	0.2	0.17	0.13	950	0.1	0.13	0.12
150	0.1	6.5	3.8	550	0.1	0.33	0.26	1000	1.0	0.015	0.01
150	0.01	66	31	550	0.01	1.7	2.1	1000	0.9	0.016	0.011
200	1.0	0.34	0.24	600	1.0	0.017	0.017	1000	0.8	0.014	0.013
200	0.9	0.51	0.27	600	0.9	0.025	0.019	1000	0.7	0.016	0.015
200	0.8	0.59	0.31	600	0.8	0.029	0.023	1000	0.6	0.025	0.018
200	0.7	0.69	0.36	600	0.7	0.034	0.027	1000	0.5	0.03	0.022
200	0.6	0.8	0.42	600	0.6	0.031	0.032	1000	0.4	0.038	0.027
200	0.5	0.94	0.51	600	0.5	0.05	0.041	1000	0.3	0.051	0.037
200	0.4	0.86	0.64	600	0.4	0.049	0.053	1000	0.2	0.059	0.056
200	0.3	1.4	0.84	600	0.3	0.067	0.073	1000	0.1	0.12	0.11
200	0.2	1.6	1.2	600	0.2	0.1	0.11	1050	1.0	0.0097	0.0085
200	0.1	3.8	2.3	600	0.1	0.2	0.23	1050	0.9	0.011	0.0096
200	0.01	15	7.2	600	0.01	1.5	2	1050	0.8	0.016	0.011
250	1.0	0.13	0.12	650	1.0	0.025	0.017	1050	0.7	0.014	0.013
250	0.9	0.21	0.14	650	0.9	0.022	0.02	1050	0.6	0.022	0.015
250	0.8	0.25	0.16	650	0.8	0.025	0.023	1050	0.5	0.02	0.019
250	0.7	0.3	0.19	650	0.7	0.029	0.027	1050	0.4	0.026	0.024
250	0.6	0.39	0.23	650	0.6	0.045	0.032	1050	0.3	0.045	0.032
250	0.5	0.39	0.29	650	0.5	0.055	0.04	1050	0.2	0.068	0.049
250	0.4	0.68	0.37	650	0.4	0.069	0.051	1100	1.0	0.0094	0.0086
250	0.3	0.74	0.5	650	0.3	0.093	0.07	1100	0.9	0.014	0.0099
250	0.2	1.5	0.76	650	0.2	0.14	0.11	1100	0.8	0.016	0.011
250	0.1	3	1.5	650	0.1	0.22	0.21	1100	0.7	0.019	0.013
250	0.01	12	7.4	700	1.0	0.018	0.013	1100	0.6	0.023	0.016
300	1.0	0.089	0.064	700	0.9	0.021	0.015	1100	0.5	0.028	0.02
300	0.9	0.1	0.074	700	0.8	0.019	0.018	1100	0.4	0.037	0.026
300	0.8	0.12	0.089	700	0.7	0.023	0.021	1100	0.3	0.039	0.036
300	0.7	0.15	0.11	700	0.6	0.036	0.026	1100	0.2	0.06	0.056
300	0.6	0.18	0.13	700	0.5	0.044	0.033	1150	1.0	0.011	0.0091
300	0.5	0.23	0.16	700	0.4	0.045	0.043	1150	0.9	0.012	0.01
300	0.4	0.24	0.21	700	0.3	0.062	0.06	1150	0.8	0.014	0.012
300	0.3	0.34	0.29	700	0.2	0.12	0.093	1150	0.7	0.021	0.014
300	0.2	0.69	0.45	700	0.1	0.26	0.19	1150	0.6	0.024	0.016
300	0.1	1.4	0.91	750	1.0	0.015	0.011	1150	0.5	0.022	0.02
300	0.01	8.7	4.8	750	0.9	0.017	0.013	1150	0.4	0.037	0.025
350	1.0	0.087	0.058	750	0.8	0.02	0.015	1150	0.3	0.037	0.034
350	0.9	0.076	0.067	750	0.7	0.023	0.017	1200	1.0	0.013	0.0081
350	0.8	0.088	0.092	750	0.6	0.028	0.021	1200	0.9	0.011	0.0091
350	0.7	0.13	0.092	750	0.5	0.027	0.026	1200	0.8	0.012	0.01
350	0.6	0.12	0.11	750	0.4	0.044	0.033	1200	0.7	0.013	0.012
350	0.5	0.19	0.14	750	0.3	0.046	0.045	1200	0.6	0.021	0.014
350	0.4	0.19	0.18	750	0.2	0.07	0.07	1200	0.5	0.025	0.017
350	0.3	0.32	0.24	750	0.1	0.18	0.14	1200	0.4	0.023	0.021
350	0.2	0.48	0.37	800	1.0	0.014	0.012	1200	0.3	0.031	0.028
350	0.1	0.93	0.72	800	0.9	0.021	0.014	1250	1.0	0.011	0.008
350	0.01	5.3	4.4	800	0.8	0.024	0.016	1250	0.9	0.013	0.0091
400	1.0	0.035	0.04	800	0.7	0.028	0.02	1250	0.8	0.015	0.01
400	0.9	0.052	0.047	800	0.6	0.026	0.024	1250	0.7	0.017	0.012
400	0.8	0.049	0.055	800	0.5	0.032	0.029	1250	0.6	0.021	0.015
400	0.7	0.075	0.066	800	0.4	0.054	0.038	1250	0.5	0.025	0.018
400	0.6	0.093	0.081	800	0.3	0.074	0.053	1250	0.4	0.025	0.023
400	0.5	0.093	0.1	800	0.2	0.11	0.082	1250	0.3	0.034	0.031
400	0.4	0.12	0.13	800	0.1	0.23	0.17				
400	0.3	0.21	0.18	850	1.0	0.012	0.011				
400	0.2	0.26	0.28	850	0.9	0.013	0.012				
400	0.1	0.54	0.56	850	0.8	0.02	0.014				
400	0.01	4.5	3.3	850	0.7	0.023	0.017				
450	1.0	0.028	0.03	850	0.6	0.022	0.02				
450	0.9	0.032	0.034	850	0.5	0.035	0.024				
450	0.8	0.038	0.04	850	0.4	0.034	0.031				
450	0.7	0.044	0.047	850	0.3	0.06	0.042				
450	0.6	0.04	0.056	850	0.2	0.071	0.064				
450	0.5	0.065	0.069	850	0.1	0.14	0.13				
450	0.4	0.063	0.087								
450	0.3	0.11	0.12								
450	0.2	0.17	0.18								
450	0.1	0.36	0.36								
450	0.01	2.7	2.2								

Figure D.5: Exclusion curves for the simplified model of $\tilde{\chi}_1^{\pm}\tilde{\chi}_1^{\mp} + \tilde{\chi}_1^{\pm}\tilde{\chi}_1^0$ production as a function of the branching fractions to Z and Higgs bosons. Results are shown for the charged-lepton decays of $\tilde{\chi}_1^{\pm}/\tilde{\chi}_1^0$ into any leptons with equal probability for $\tilde{\chi}_1^{\pm}/\tilde{\chi}_1^0$ masses of (top) 600, (second row) 700, (third row) 800, and (bottom) 900 GeV. The expected 95% CL exclusion (dashed black line) is shown with $\pm 1\,\sigma_{\text{exp}}$ variations (shaded yellow band) from systematic and statistical uncertainties in the expected yields. The observed 95% CL exclusion (solid red line) is shown with $\pm 1\,\sigma_{\text{theory}}^{\text{SUSY}}$ variations (dotted red lines) from cross-section uncertainties for the signal models. The phase-space excluded by the search is shown in the hatched regions. Grey numbers represent the observed (left) and expected (right) upper cross-section limits.
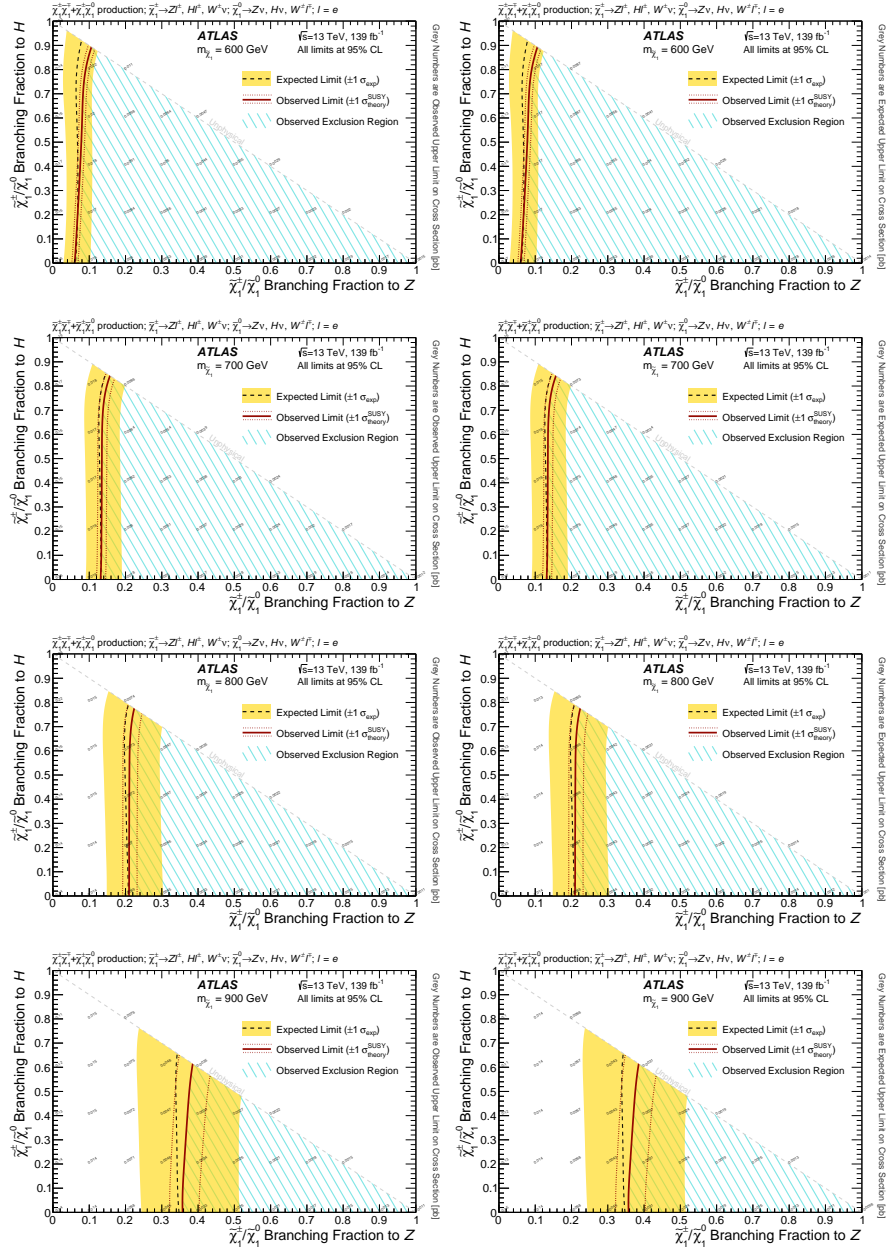
Figure D.6: Exclusion curves for the simplified model of $\tilde{\chi}_1^\pm \tilde{\chi}_1^\mp + \tilde{\chi}_1^\pm \tilde{\chi}_1^0$ production as a function of the branching fractions to Z and Higgs bosons. Results are shown for the charged-lepton decays of $\tilde{\chi}_1^\pm / \tilde{\chi}_1^0$ into electrons only for $\tilde{\chi}_1^\pm / \tilde{\chi}_1^0$ masses of (top) 600, (second row) 700, (third row) 800, and (bottom) 900 GeV. The expected 95% CL exclusion (dashed black line) is shown with $\pm 1\,\sigma_{\rm exp}$ variations (shaded yellow band) from systematic and statistical uncertainties in the expected yields. The observed 95% CL exclusion (solid red line) is shown with $\pm 1\,\sigma_{\rm theory}^{\rm SUSY}$ variations (dotted red lines) from cross-section uncertainties for the signal models. The phase-space excluded by the search is shown in the hatched regions. Grey numbers represent the observed (left) and expected (right) upper cross-section limits.
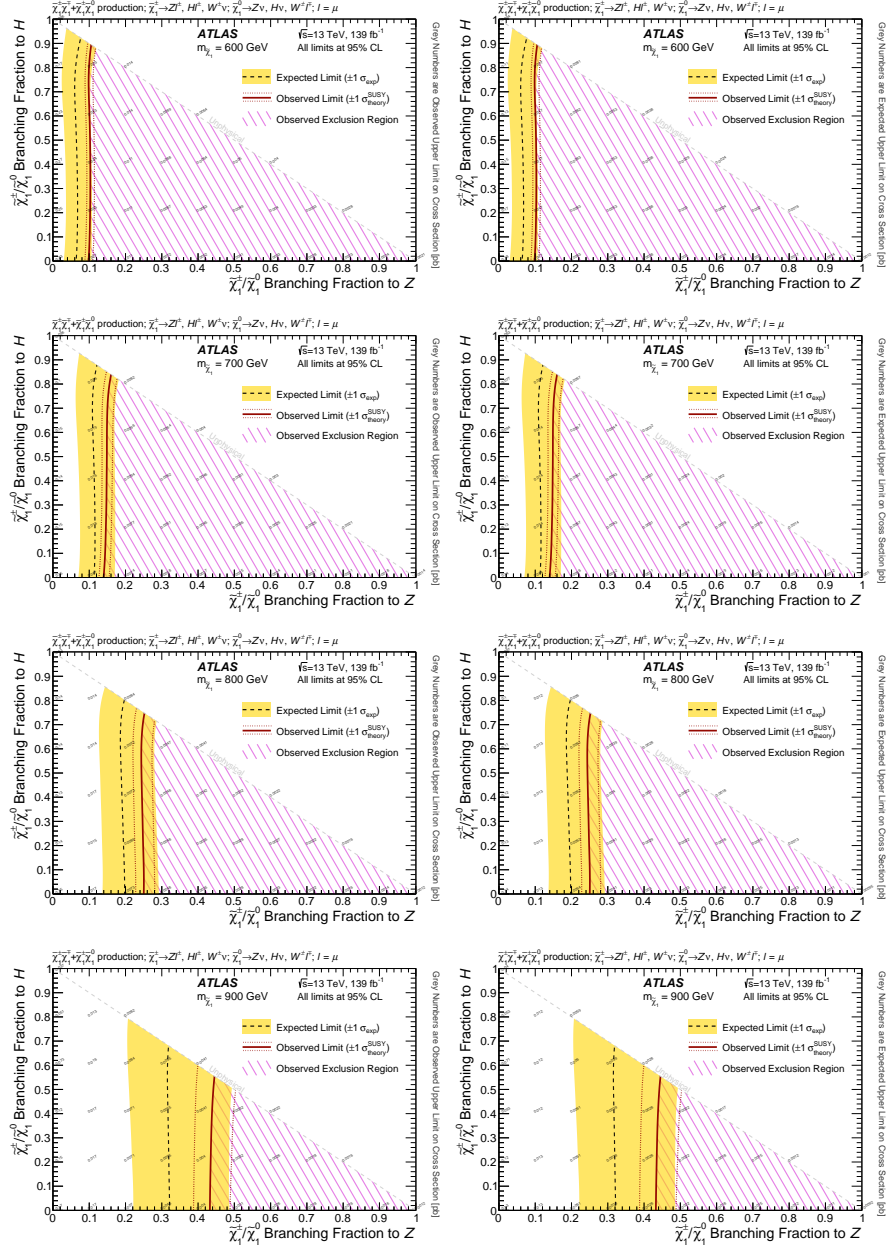
Figure D.7: Exclusion curves for the simplified model of $\tilde{\chi}_1^\pm \tilde{\chi}_1^\mp + \tilde{\chi}_1^\pm \tilde{\chi}_1^0$ production as a function of the branching fractions to Z and Higgs bosons. Results are shown for the charged-lepton decays of $\tilde{\chi}_1^\pm / \tilde{\chi}_1^0$ into muons only for $\tilde{\chi}_1^\pm / \tilde{\chi}_1^0$ masses of (top) 600, (second row) 700, (third row) 800, and (bottom) 900 GeV. The expected 95% CL exclusion (dashed black line) is shown with $\pm 1\,\sigma_{\rm exp}$ variations (shaded yellow band) from systematic and statistical uncertainties in the expected yields. The observed 95% CL exclusion (solid red line) is shown with $\pm 1\,\sigma_{\rm theory}^{\rm SUSY}$ variations (dotted red lines) from cross-section uncertainties for the signal models. The phase-space excluded by the search is shown in the hatched regions. Grey numbers represent the observed (left) and expected (right) upper cross-section limits.
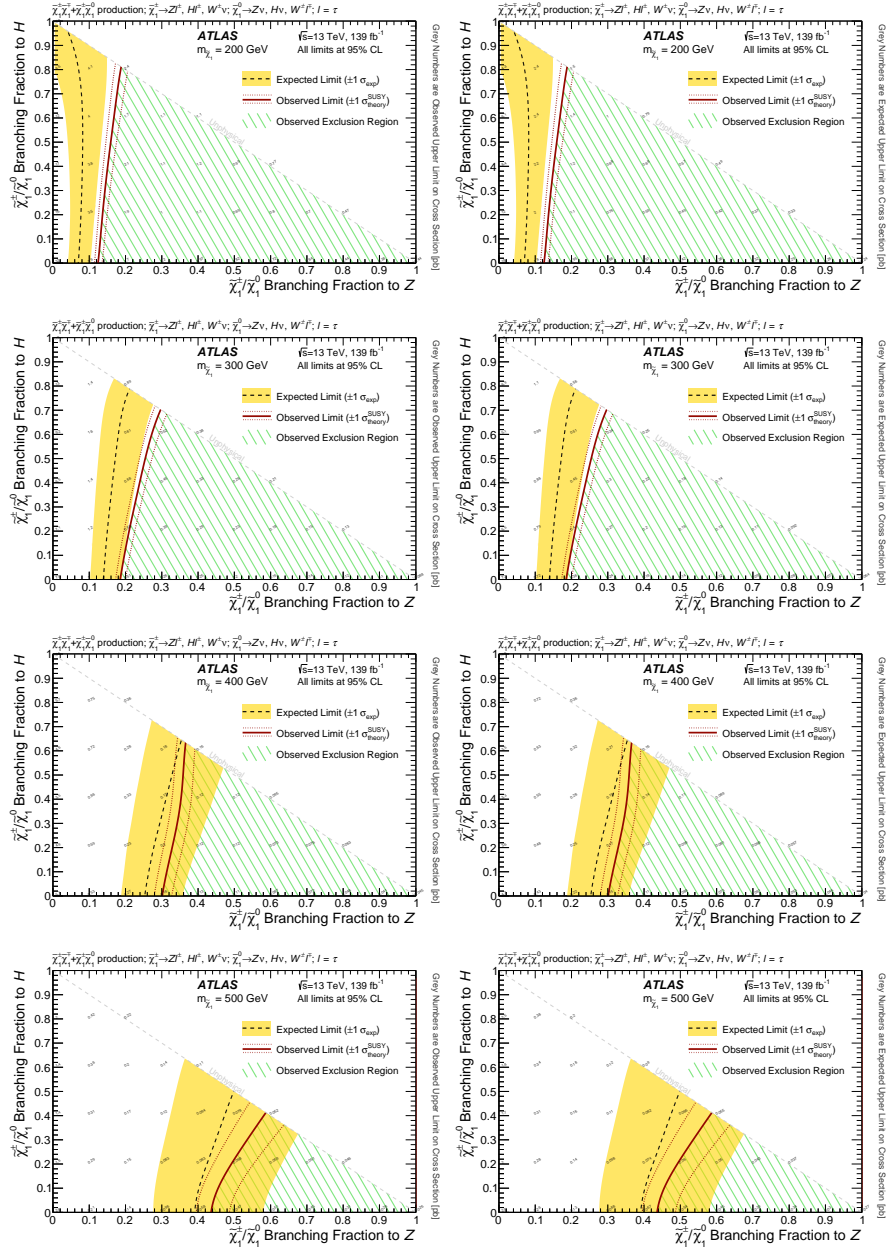
Figure D.8: Exclusion curves for the simplified model of $\tilde{\chi}_1^\pm \tilde{\chi}_1^\mp + \tilde{\chi}_1^\pm \tilde{\chi}_1^0$ production as a function of the branching fractions to Z and Higgs bosons. Results are shown for the charged-lepton decays of $\tilde{\chi}_1^\pm / \tilde{\chi}_1^0$ into τ-leptons only for $\tilde{\chi}_1^\pm / \tilde{\chi}_1^0$ masses of (top) 200, (second row) 300, (third row) 400, and (bottom) 500 GeV. The expected 95% CL exclusion (dashed black line) is shown with $\pm 1\,\sigma_{\mathrm{exp}}$ variations (shaded yellow band) from systematic and statistical uncertainties in the expected yields. The observed 95% CL exclusion (solid red line) is shown with $\pm 1\,\sigma_{\mathrm{theory}}^{\mathrm{SUSY}}$ variations (dotted red lines) from cross-section uncertainties for the signal models. The phase-space excluded by the search is shown in the hatched regions. Grey numbers represent the observed (left) and expected (right) upper cross-section limits.

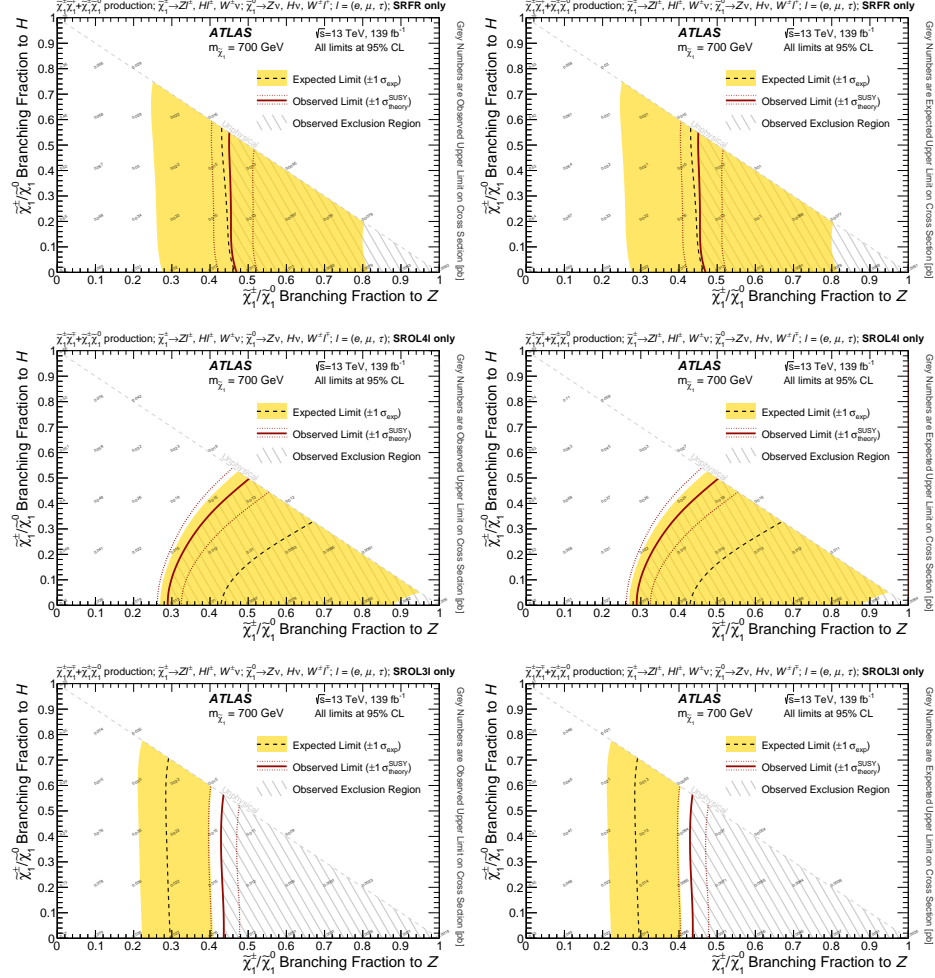## D.3 Upper Limits on Signal Production Cross Section by Individual SR

Figure D.9: Exclusion curves for the simplified model of $\tilde{\chi}_1^\pm \tilde{\chi}_1^\mp + \tilde{\chi}_1^\pm \tilde{\chi}_1^0$ production as a function of the branching fractions to Z and Higgs bosons. Results are shown for the (top) SRFR, (middle) SR4ℓ, and (bottom) SR3ℓ regions separately for $\tilde{\chi}_1^\pm/\tilde{\chi}_1^0$ masses of 700 GeV for the charged-lepton decays of $\tilde{\chi}_1^\pm/\tilde{\chi}_1^0$ into any leptons with equal probability. The expected 95% CL exclusion (dashed black line) is shown with $\pm 1\,\sigma_{\mathrm{exp}}$ variations (shaded yellow band) from systematic and statistical uncertainties in the expected yields. The observed 95% CL exclusion (solid red line) is shown with $\pm 1\,\sigma_{\mathrm{theory}}^{\mathrm{SUSY}}$ variations (dotted red lines) from cross-section uncertainties for the signal models. The phase-space excluded by the search is shown in the hatched regions. Grey numbers represent the observed (left) and expected (right) upper cross-section limits.
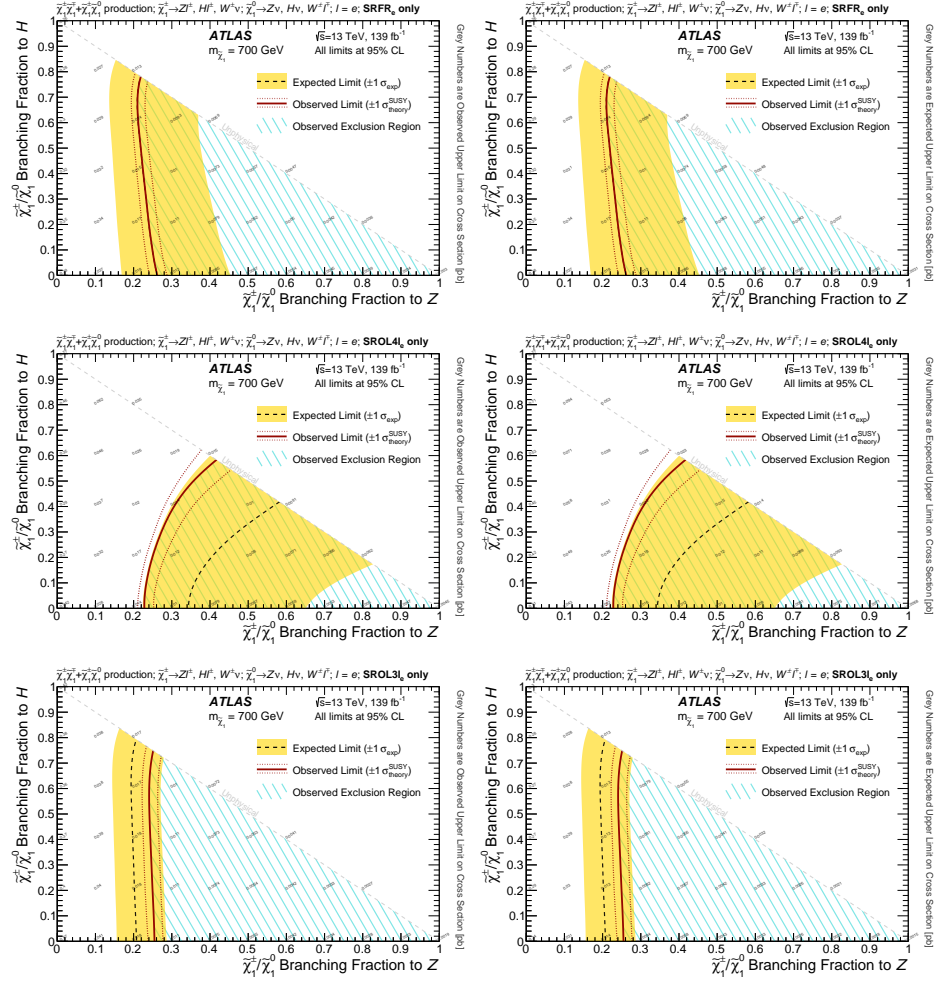
Figure D.10:   Exclusion curves for the simplified model of $\tilde{\chi}_1^\pm \tilde{\chi}_1^\mp + \tilde{\chi}_1^\pm \tilde{\chi}_1^0$ production as a function of the branching fractions to Z and Higgs bosons. Results are shown for the (top) SRFR, (middle) SR4ℓ, and (bottom) SR3ℓ regions separately for $\tilde{\chi}_1^\pm / \tilde{\chi}_1^0$ masses of 700 GeV for the charged-lepton decays of $\tilde{\chi}_1^\pm / \tilde{\chi}_1^0$ into electrons. The expected 95% CL exclusion (dashed black line) is shown with $\pm 1\, \sigma_{\mathrm{exp}}$ variations (shaded yellow band) from systematic and statistical uncertainties in the expected yields. The observed 95% CL exclusion (solid red line) is shown with $\pm 1\, \sigma_{\mathrm{theory}}^{\mathrm{SUSY}}$ variations (dotted red lines) from cross-section uncertainties for the signal models. The phase-space excluded by the search is shown in the hatched regions. Grey numbers represent the observed (left) and expected (right) upper cross-section limits.
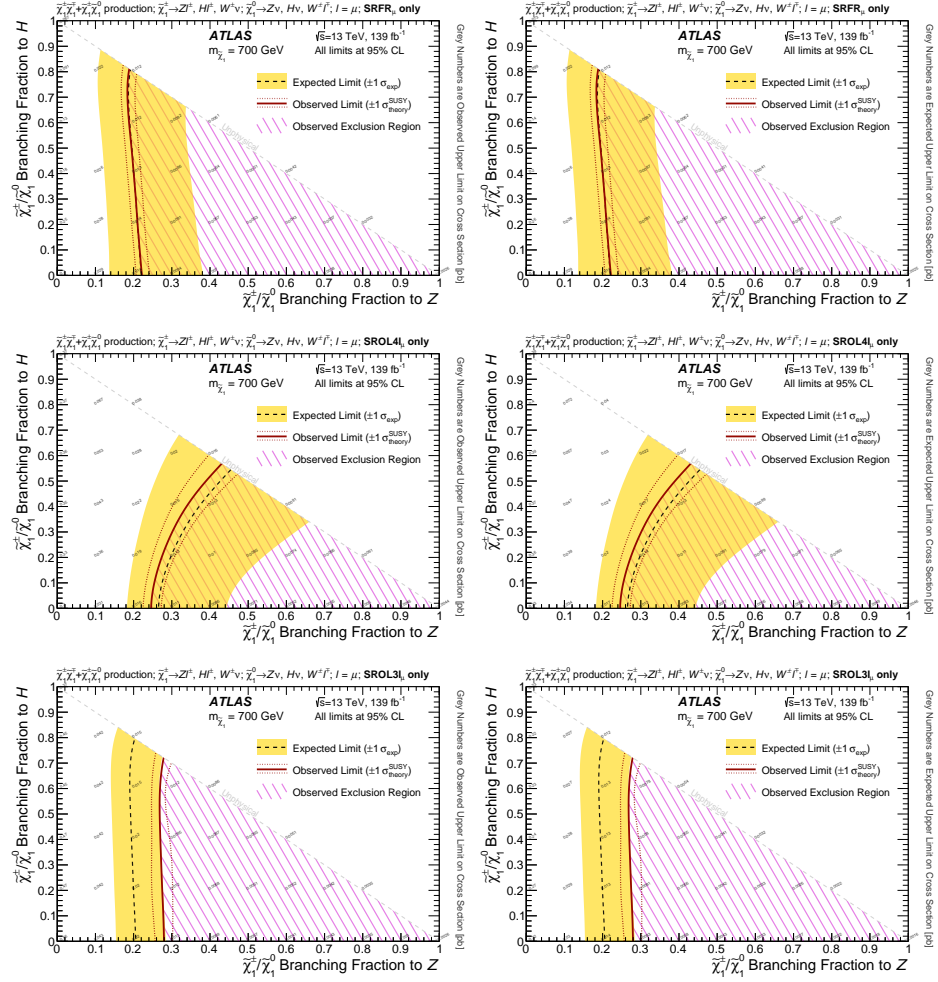
Figure D.11: Exclusion curves for the simplified model of $\tilde{\chi}_1^\pm \tilde{\chi}_1^\mp + \tilde{\chi}_1^\pm \tilde{\chi}_1^0$ production as a function of the branching fractions to Z and Higgs bosons. Results are shown for the (top) SRFR, (middle) SR4ℓ, and (bottom) SR3ℓ regions separately for $\tilde{\chi}_1^\pm / \tilde{\chi}_1^0$ masses of 700 GeV for the charged-lepton decays of $\tilde{\chi}_1^\pm / \tilde{\chi}_1^0$ into muons. The expected 95% CL exclusion (dashed black line) is shown with $\pm 1\,\sigma_{\mathrm{exp}}$ variations (shaded yellow band) from systematic and statistical uncertainties in the expected yields. The observed 95% CL exclusion (solid red line) is shown with $\pm 1\,\sigma_{\mathrm{theory}}^{\mathrm{SUSY}}$ variations (dotted red lines) from cross-section uncertainties for the signal models. The phase-space excluded by the search is shown in the hatched regions. Grey numbers represent the observed (left) and expected (right) upper cross-section limits.

D.4   Signal Region Cutflows

Table D.5:   Summary of event selections for $\tilde{\chi}_1^\pm/\tilde{\chi}_1^0$ masses of 200, 500, and 800 GeV, shown separately for the $\tilde{\chi}_1^\pm\tilde{\chi}_1^\mp$ and $\tilde{\chi}_1^\pm\tilde{\chi}_1^0$ processes. The yields are normalized to a luminosity of 139 fb^{-1}, and MC-to-data efficiency weights from triggering and from the reconstruction and identification of individual physics objects are applied to the final yields in each signal region. After the initial selections, the yields are assigned into inclusive SRFR, SR4ℓ, and SR3ℓ regions before further selections, and then separated into the e and μ channels after MC-to-data efficiency weights have been applied. Democratic branching fractions into bosons (W, Z, and Higgs) and leptons (e, μ, and τ) are used, with no branching fraction reweighting performed. The generator filters are discussed in detail in Section 5.2. The preliminary event reduction is a centralized stage that requires at least two electrons or muons of uncalibrated $p_\mathrm{T} > 9$ GeV and $|\eta| < 2.6$.

|	200 GeV		500 GeV		800 GeV	
Selection	$\tilde{\chi}_1^\pm\tilde{\chi}_1^0$	$\tilde{\chi}_1^\pm\tilde{\chi}_1^\mp$	$\tilde{\chi}_1^\pm\tilde{\chi}_1^0$	$\tilde{\chi}_1^\pm\tilde{\chi}_1^\mp$	$\tilde{\chi}_1^\pm\tilde{\chi}_1^0$	$\tilde{\chi}_1^\pm\tilde{\chi}_1^\mp$
Total production ($\mathcal{L} \times \sigma$)	251000	125000	6440	3070	661	307
Generator filters ($Z/3\ell$)	5800	8670	171	214	18.5	21.0
Preliminary event reduction	5640	6970	169	189	18.3	19.0
Triggering	5540	6790	168	187	18.1	18.9
≥ 3 signal leptons	2340	2200	82.1	74.4	8.89	7.66
Z candidate	1870	1600	63.0	52.0	6.79	5.41
SRFR assignment	107	236	4.58	11.1	0.475	1.05
$\quad$ $4\ell 2Z$ event veto	103	218	4.51	10.9	0.471	1.04
$\quad$ $m_{Z\ell}^\mathrm{asym} < 0.1$	75.6	163	2.82	7.35	0.293	0.692
$\quad$ $\Delta R(b_1, b_2) < 1.5$	74.3	131	2.80	6.74	0.287	0.661
$\quad$ MC-to-data eff. weights	68.2	121	2.59	6.33	0.271	0.627
$\quad\quad$ SRFR$_e$	15.1	22.5	0.589	1.53	0.069	0.154
$\quad\quad$ SRFR$_\mu$	17.4	32.0	0.665	1.61	0.063	0.166
SR4ℓ assignment	263	310	8.74	10.1	1.03	1.20
$\quad$ $4\ell 2Z$ event veto	240	272	8.29	9.81	0.992	1.18
$\quad$ $E_\mathrm{T}^\mathrm{miss,SF} > 80$ GeV	141	176	6.46	7.60	0.817	0.972
$\quad$ $\Delta R(b_1, b_2) < 1.5$	140	175	6.44	7.56	0.812	0.965
$\quad$ MC-to-data eff. weights	133	166	6.06	7.16	0.770	0.916
$\quad\quad$ SR4ℓ_e	63.7	83.7	2.95	3.62	0.383	0.462
$\quad\quad$ SR4ℓ_μ	69.3	82.3	3.11	3.54	0.386	0.454
SR3ℓ assignment	1500	1060	49.5	30.8	5.29	3.16
$\quad$ $E_\mathrm{T}^\mathrm{miss} > 150$ GeV	198	114	33.4	15.2	4.41	2.03
$\quad$ $m_\mathrm{T}^\mathrm{min} > 125$ GeV	139	80.5	25.8	11.2	3.65	1.59
$\quad$ $\Delta R(b_1, b_2) < 1.5$	132	78.9	24.8	10.7	3.54	1.49
$\quad$ MC-to-data eff. weights	125	73.4	23.5	10.0	3.34	1.41
$\quad\quad$ SR3ℓ_e	59.8	37.1	11.9	4.85	1.71	0.711
$\quad\quad$ SR3ℓ_μ	64.8	36.3	11.5	5.19	1.63	0.703

D.5   Signal Acceptances and Efficiencies
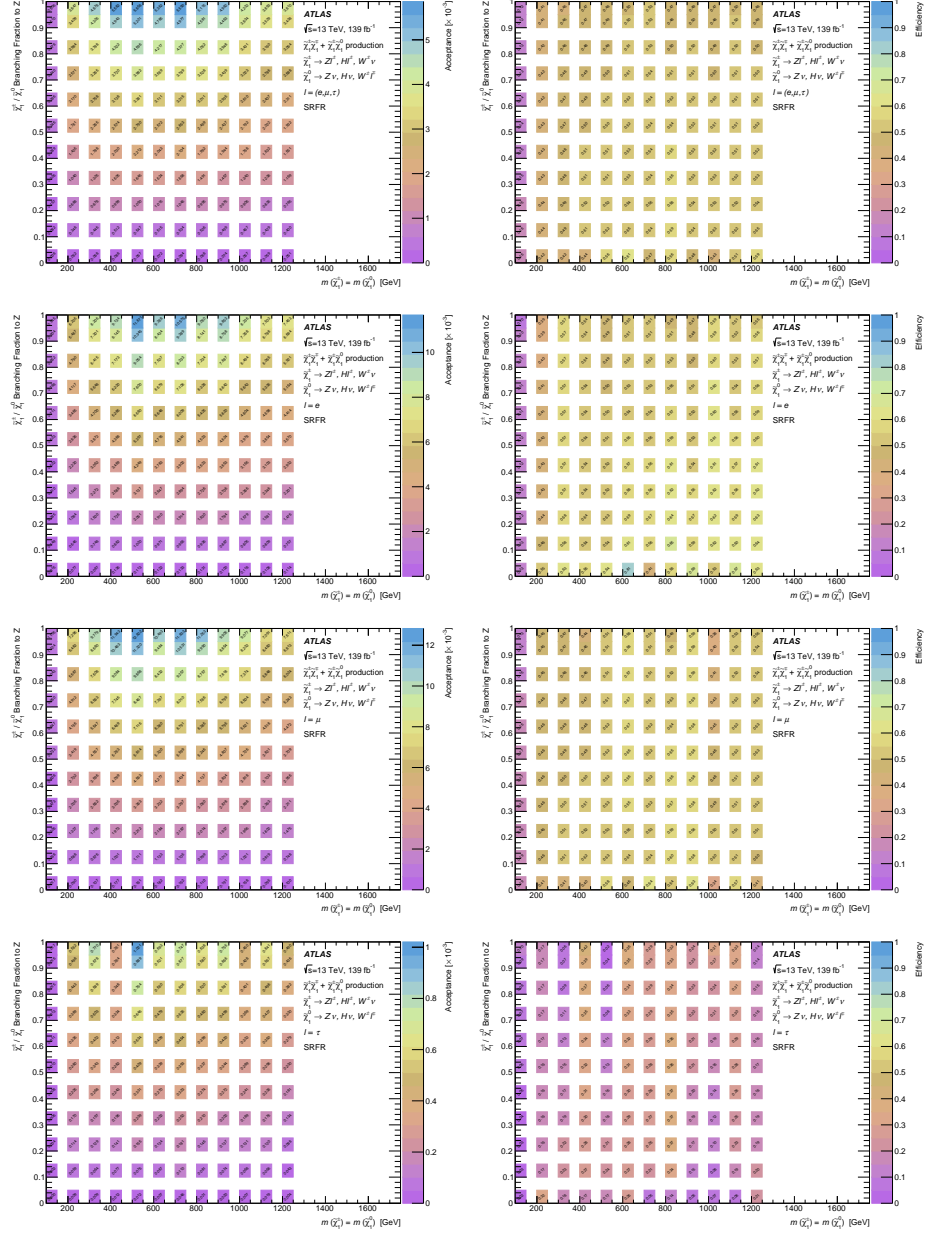
Figure D.12: The combined $\tilde{\chi}_1^\pm \tilde{\chi}_1^\mp + \tilde{\chi}_1^\pm \tilde{\chi}_1^0$ (left) truth-level acceptances and (right) reconstruction efficiencies in the inclusive SRFR region after MC-to-data efficiency weights are applied. Results are given as a function of $\tilde{\chi}_1^\pm / \tilde{\chi}_1^0$ mass and branching fraction to Z bosons, and are derived separately when requiring that the charged-lepton decays of $\tilde{\chi}_1^\pm / \tilde{\chi}_1^0$ are into (top) any leptons with equal probability, (second row) electrons only, (third row) muons only, or (bottom) τ-leptons only.
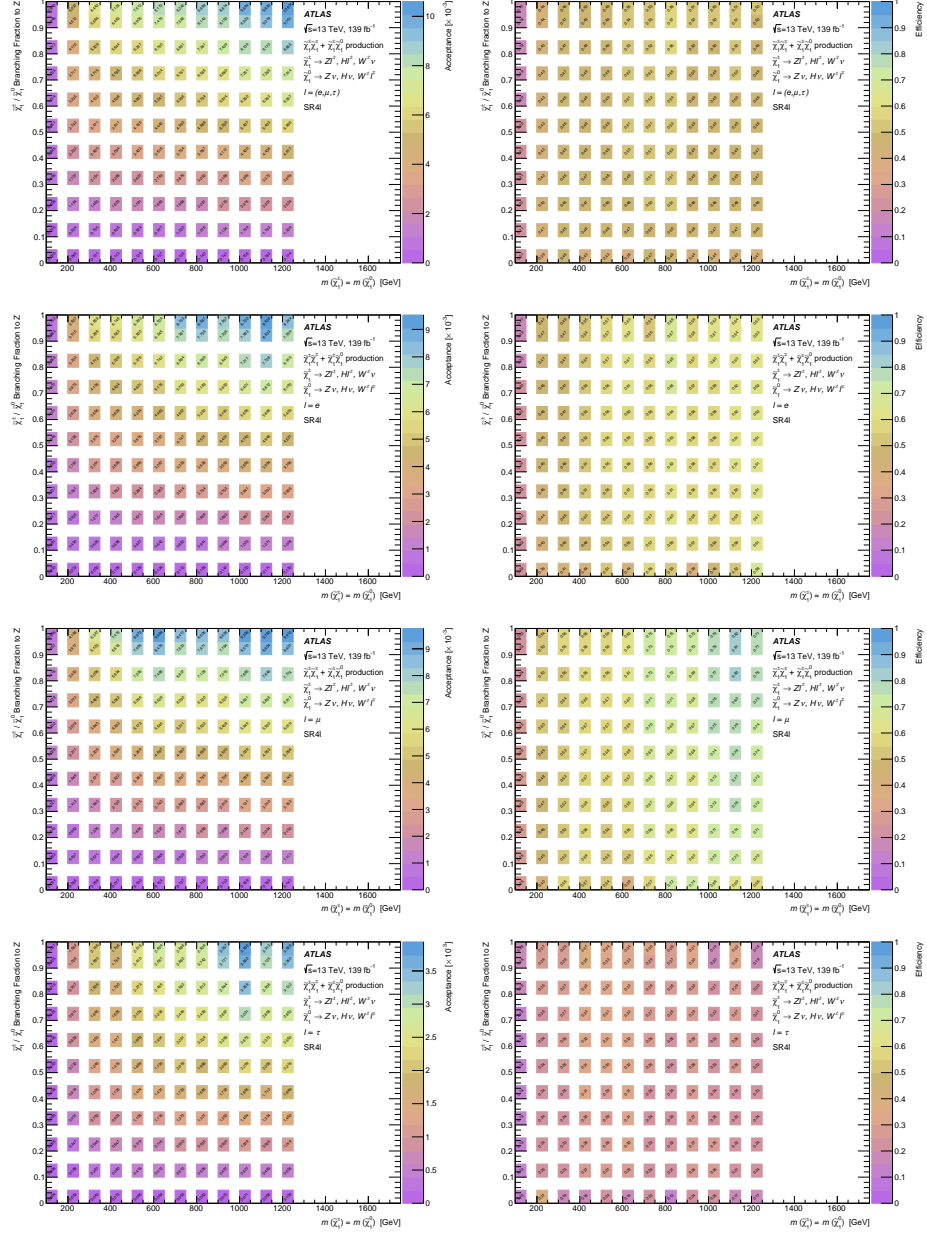
Figure D.13: The combined $\tilde{\chi}_1^\pm \tilde{\chi}_1^\mp + \tilde{\chi}_1^\pm \tilde{\chi}_1^0$ (left) truth-level acceptances and (right) reconstruction efficiencies in the inclusive SR4ℓ region after MC-to-data efficiency weights are applied. Results are given as a function of $\tilde{\chi}_1^\pm / \tilde{\chi}_1^0$ mass and branching fraction to Z bosons, and are derived separately when requiring that the charged-lepton decays of $\tilde{\chi}_1^\pm / \tilde{\chi}_1^0$ are into (top) any leptons with equal probability, (second row) electrons only, (third row) muons only, or (bottom) τ-leptons only.
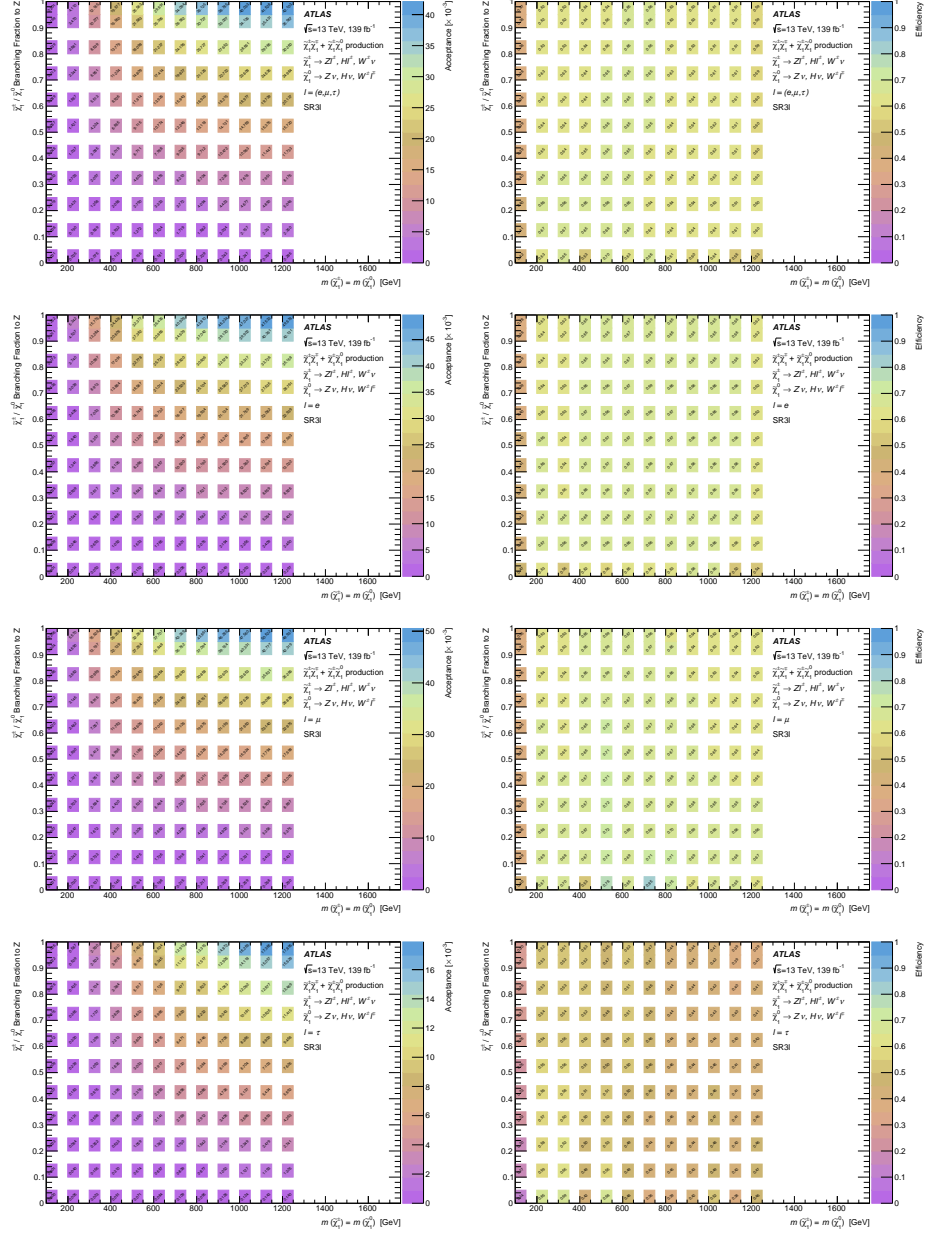
Figure D.14: The combined $\tilde{\chi}_1^\pm \tilde{\chi}_1^\mp + \tilde{\chi}_1^\pm \tilde{\chi}_1^0$ (left) truth-level acceptances and (right) reconstruction efficiencies in the inclusive SR3ℓ region after MC-to-data efficiency weights are applied. Results are given as a function of $\tilde{\chi}_1^\pm / \tilde{\chi}_1^0$ mass and branching fraction to Z bosons, and are derived separately when requiring that the charged-lepton decays of $\tilde{\chi}_1^\pm / \tilde{\chi}_1^0$ are into (top) any leptons with equal probability, (second row) electrons only, (third row) muons only, or (bottom) τ-leptons only.
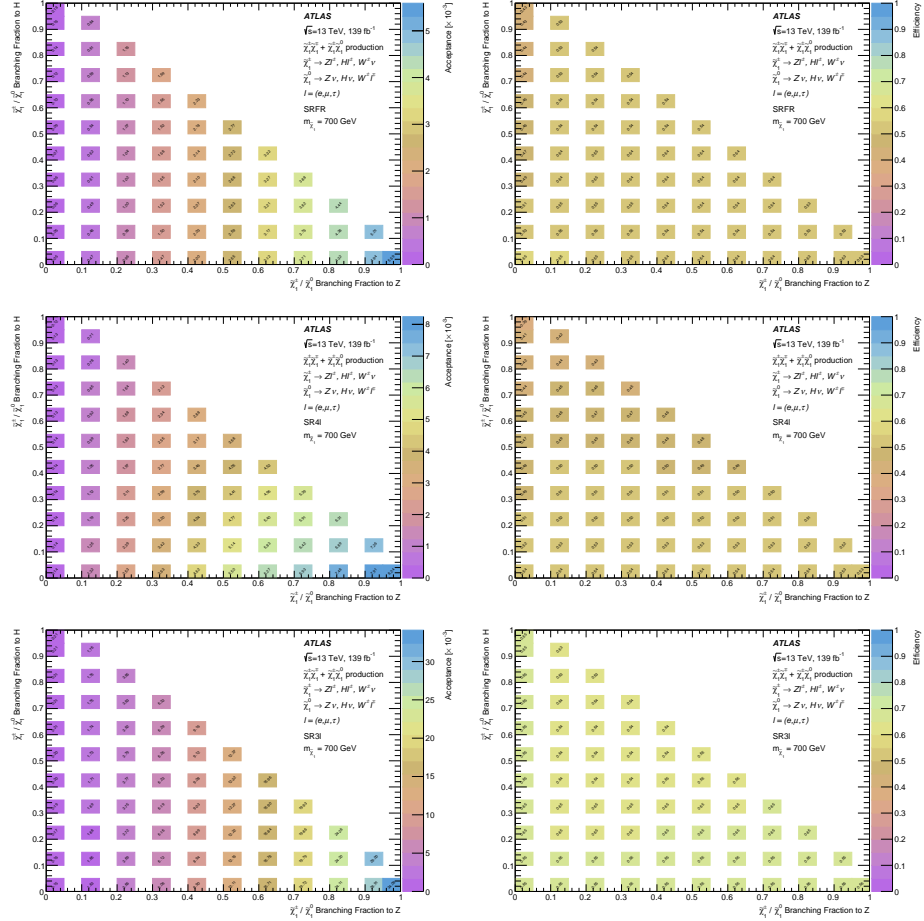
Figure D.15: The combined $\tilde{\chi}_1^\pm \tilde{\chi}_1^\mp + \tilde{\chi}_1^\pm \tilde{\chi}_1^0$ (left) truth-level acceptances and (right) reconstruction efficiencies in the inclusive (top) SRFR, (middle) SR4ℓ, and (bottom) SR3ℓ regions after MC-to-data efficiency weights are applied. Results are derived for $\tilde{\chi}_1^\pm / \tilde{\chi}_1^0$ masses of 700 GeV and given as a function of the branching fractions to Z and Higgs bosons.
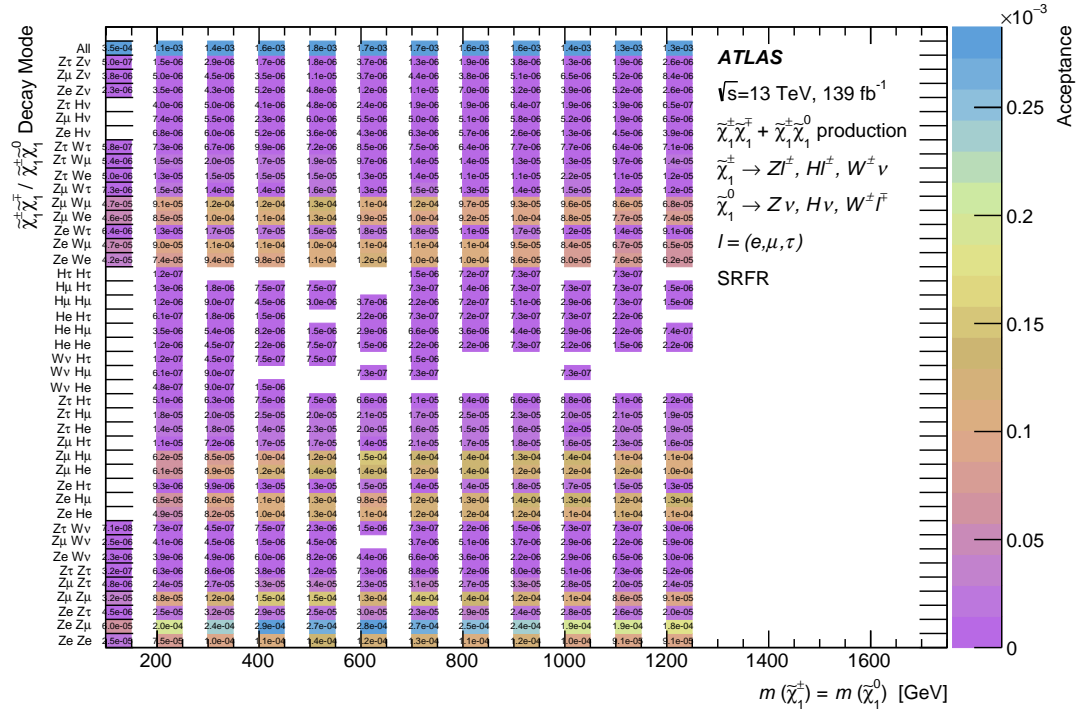
Figure D.16: The truth-level acceptances for each decay mode of the generated $\tilde{\chi}_1^{\pm}\tilde{\chi}_1^{\mp}$ + $\tilde{\chi}_1^{\pm}\tilde{\chi}_1^0$ signals in the inclusive SRFR region. Results are given as a function of $\tilde{\chi}_1^{\pm}/\tilde{\chi}_1^0$ mass and the final state boson and lepton combination.
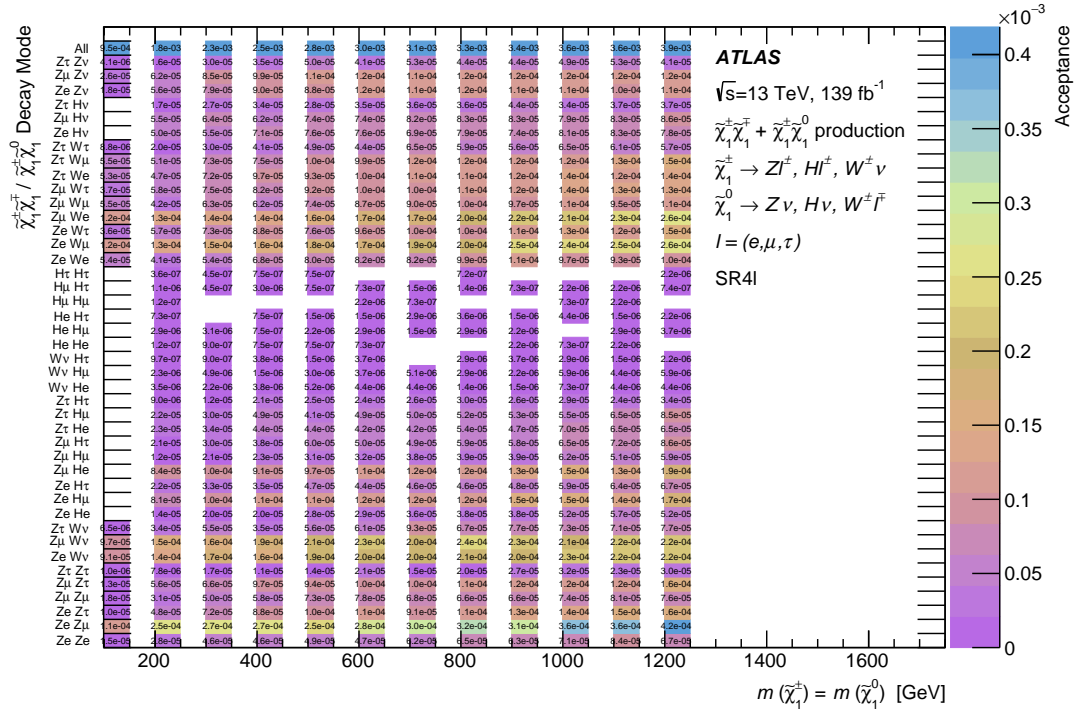
Figure D.17: The truth-level acceptances for each decay mode of the generated $\tilde{\chi}_1^\pm \tilde{\chi}_1^\mp + \tilde{\chi}_1^\pm \tilde{\chi}_1^0$ signals in the inclusive SR4ℓ region. Results are given as a function of $\tilde{\chi}_1^\pm / \tilde{\chi}_1^0$ mass and the final state boson and lepton combination.
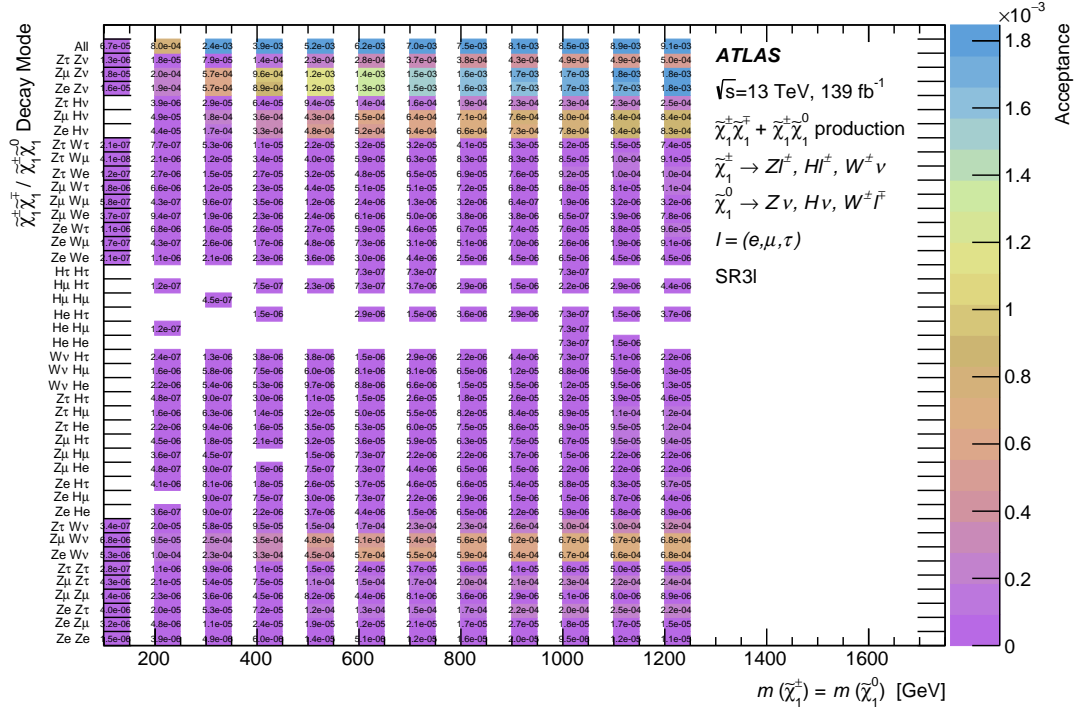
Figure D.18: The truth-level acceptances for each decay mode of the generated $\tilde{\chi}_1^\pm \tilde{\chi}_1^\mp + \tilde{\chi}_1^\pm \tilde{\chi}_1^0$ signals in the inclusive SR3ℓ region. Results are given as a function of $\tilde{\chi}_1^\pm / \tilde{\chi}_1^0$ mass and the final state boson and lepton combination.

Bibliography

[1] S. Weinberg, *A model of leptons*, Phys. Rev. Lett. **19** (1967) 1264–1266. 2.1

[2] S. Glashow, *Partial symmetries of weak interactions*, Nucl.Phys. **22** (1961) 579–588. 2.1

[3] A. Salam and J. C. Ward, *Weak and Electromagnetic Interactions*, Nuovo Cimento **11** (1959) 568–577. 2.1

[4] A. Salam and J. C. Ward, *Gauge theory of elementary interactions*, Phys. Rev. **136** (1964) B763–B768. 2.1

[5] J. Goldstone, A. Salam, and S. Weinberg, *Broken symmetries*, Physical Review **127** (1962) 965–970. 2.1

[6] C. N. Yang and R. L. Mills, *Conservation of isotopic spin and isotopic gauge invariance*, Phys. Rev. **96** (1954) 191–195. 2.1

[7] M. Gell-Mann, *A schematic model of baryons and mesons*, Physics Letters **8** (1964) 214–215. 2.1

[8] G. Zweig, *An SU(3) model for strong interaction symmetry and its breaking. Version 1*,. 2.1

[9] D. J. Gross and F. Wilczek, *Asymptotically free gauge theories. I*, Phys. Rev. D **8** (1973) 3633–3652. 2.1

[10] D. J. Gross and F. Wilczek, *Asymptotically free gauge theories. II*, Phys. Rev. D **9** (1974) 980–993. 2.1

[11] H. Yukawa, *On the Interaction of Elementary Particles I*, Proc. Phys. Math. Soc. Jap. **17** (1935) 48–57. 2.1

[12] P. W. Higgs, *Broken symmetries, massless particles and gauge fields*, Physics Letters **12** (1964) 132–133. 2.1

[13] P. W. Higgs, *Broken symmetries and the masses of gauge bosons*, Phys. Rev. Lett. **13** (1964) 508–509. 2.1

[14] F. Englert and R. Brout, *Broken symmetry and the mass of gauge vector mesons*, Phys. Rev. Lett. **13** (1964) 321–323. 2.1

[15] G. 't Hooft, *Renormalization of massless Yang-Mills fields*, Nuclear Physics B **33** (1971) 173–199. 2.1

[16] G. 't Hooft, *Renormalizable Lagrangians for massive Yang-Mills fields*, Nuclear Physics B **35** (1971) 167–188. 2.1

[17] G. 't Hooft and M. Veltman, *Regularization and renormalization of gauge fields*, Nuclear Physics B **44** (1972) 189 – 213. 2.1

[18] M. E. Peskin and D. V. Schroeder, *An Introduction to Quantum Field Theory*. Addison-Wesley, 1995. 2.1, 2.1.3, 2.3, 2.1.4

[19] S. Weinberg, *The Quantum Theory of Fields, Volume 1: Foundations*. Cambridge University Press, 1995. 2.1

[20] ATLAS Collaboration, *Observation of a new particle in the search for the Standard Model Higgs boson with the ATLAS detector at the LHC*, Phys. Lett. B **716** (2012) 1, `arXiv:1207.7214 [hep-ex]`. 2.1, 5

[21] CMS Collaboration, *Observation of a new boson at a mass of 125 GeV with the CMS experiment at the LHC*, Phys. Lett. B **716** (2012) 30, `arXiv:1207.7235 [hep-ex]`. 2.1, 5

[22] L. Boyle, *File:Standard Model Of Particle Physics, Most Complete Diagram.jpg*, 2020. `https://commons.wikimedia.org/w/index.php?title=File:Standard_Model_Of_Particle_Physics,_Most_Complete_Diagram.jpg&oldid=477459059`. [Online; accessed 7-January-2021]. 2.1

[23] R. Davis, D. S. Harmer, and K. C. Hoffman, *Search for Neutrinos from the Sun*, Phys. Rev. Lett. **20** (1968) 1205–1209, `https://link.aps.org/doi/10.1103/PhysRevLett.20.1205`. 1, 2.1.4

[24] Super-Kamiokande Collaboration, Y. Fukuda et al., *Evidence for oscillation of atmospheric neutrinos*, Phys. Rev. Lett. **81** (1998) 1562–1567, `arXiv:hep-ex/9807003`. 1, 2.1.4

[25] SNO Collaboration, Q. Ahmad et al., *Direct evidence for neutrino flavor transformation from neutral current interactions in the Sudbury Neutrino Observatory*, Phys. Rev. Lett. **89** (2002) 011301, `arXiv:nucl-ex/0204008`. 1, 2.1.4

[26] W. Commons, *File:Mexican hat potential polar with details.svg — Wikimedia Commons, the free media repository*, 2020. `https://commons.wikimedia.org/w/index.php?title=File:Mexican_hat_potential_polar_with_details.svg&oldid=507953715`. [Online; accessed 18-January-2021]. 2.2

[27] S. L. Adler, *Axial vector vertex in spinor electrodynamics*, Phys. Rev. **177** (1969) 2426–2438. 2.1.3, 2.1.4

[28] J. Bell and R. Jackiw, *A PCAC puzzle: $\pi^0 \rightarrow \gamma\gamma$ in the σ model*, Nuovo Cim. A **60** (1969) 47–61. 2.1.3, 2.1.4

[29] ATLAS Collaboration Collaboration,, *Standard Model Summary Plots Spring 2020*, Tech. Rep. ATL-PHYS-PUB-2020-010, CERN, Geneva, May, 2020. `https://cds.cern.ch/record/2718937`. 2.4

[30] S. Weinberg, *The cosmological constant problem*, Rev. Mod. Phys. **61** (1989) 1–23, `https://link.aps.org/doi/10.1103/RevModPhys.61.1`. 2.1.4

[31] A. de Gouvêa, D. Hernández, and T. M. Tait, *Criteria for natural hierarchies*, Physical Review D **89** (2014), `http://dx.doi.org/10.1103/PhysRevD.89.115005`. 2.1.4

[32] V. Rubin, N. Thonnard, and J. Ford, W.K., *Rotational properties of 21 SC galaxies with a large range of luminosities and radii, from NGC 4605 /R = 4kpc/ to UGC 2885 /R = 122 kpc/*, Astrophys. J. **238** (1980) 471. 2.1.4

[33] F. Zwicky, *Die Rotverschiebung von extragalaktischen Nebeln*, Helv. Phys. Acta **6** (1933) 110–127. 2.1.4

[34] R. Peccei and H. R. Quinn, *CP Conservation in the Presence of Instantons*, Phys. Rev. Lett. **38** (1977) 1440–1443. 2.1.4

[35] ALEPH, DELPHI, L3, OPAL, SLD, LEP Electroweak Working Group, SLD Electroweak Group, SLD Heavy Flavour Group Collaboration, S. Schael et al., *Precision electroweak measurements on the Z resonance*, Phys. Rept. **427** (2006) 257–454, `arXiv:hep-ex/0509008`. 2.1.4, 5.1

[36] R. Foot, H. Lew, and R. R. Volkas, *Electric-charge quantization*, Journal of Physics G: Nuclear and Particle Physics **19** (1993) 361–372, `http://dx.doi.org/10.1088/0954-3899/19/3/005`. 2.1.4

[37] G. Degrassi, S. Di Vita, J. Elias-Miro, J. R. Espinosa, G. F. Giudice, G. Isidori, and A. Strumia, *Higgs mass and vacuum stability in the Standard Model at NNLO*, JHEP **08** (2012) 098, `arXiv:1205.6497 [hep-ph]`. 2.1.4

[38] A. Sakharov, *Violation of CP Invariance, C asymmetry, and baryon asymmetry of the universe*, Sov. Phys. Usp. **34** (1991) 392–393. 2.1.4

[39] Y. Golfand and E. Likhtman, *Extension of the Algebra of Poincare Group Generators and Violation of P Invariance*, JETP Lett. **13** (1971) 323, [Pisma Zh. Eksp. Teor. Fiz. **13** (1971) 452]. 2.2

[40] D. Volkov and V. Akulov, *Is the neutrino a goldstone particle?*, Phys. Lett. B **46** (1973) 109. 2.2

[41] J. Wess and B. Zumino, *Supergauge transformations in four dimensions*, Nucl. Phys. B **70** (1974) 39. 2.2

[42] J. Wess and B. Zumino, *Supergauge invariant extension of quantum electrodynamics*, Nucl. Phys. B **78** (1974) 1. 2.2

[43] S. Ferrara and B. Zumino, *Supergauge invariant Yang-Mills theories*, Nucl. Phys. B **79** (1974) 413. 2.2

[44] A. Salam and J. Strathdee, *Super-symmetry and non-Abelian gauges*, Phys. Lett. B **51** (1974) 353. 2.2

[45] P. Horava and E. Witten, *Heterotic and type I string dynamics from eleven-dimensions*, Nucl. Phys. B **460** (1996) 506–524, `arXiv:hep-th/9510209`. 2.2

[46] P. Fayet, *Supersymmetry and weak, electromagnetic and strong interactions*, Phys. Lett. B **64** (1976) 159. 2.2.2

[47] P. Fayet, *Spontaneously broken supersymmetric theories of weak, electromagnetic and strong interactions*, Phys. Lett. B **69** (1977) 489. 2.2.2

[48] S. P. Martin, *A Supersymmetry Primer*, Adv. Ser. Direct. High Energy Phys. **18** (1998) 1, `arXiv:hep-ph/9709356`. 2.2.2, 2.2

[49] C. CSÁKI, *THE MINIMAL SUPERSYMMETRIC STANDARD MODEL*, Modern Physics Letters A **11** (1996) 599–613, `http://dx.doi.org/10.1142/S021773239600062X`. 2.2.2

[50] C. Csáki and P. Tanedo, *Beyond the Standard Model*, `arXiv:1602.04228 [hep-ph]`. 2.2.2

[51] H. E. Haber, *Introductory low-energy supersymmetry*, `arXiv:hep-ph/9306207`. 2.2.2

[52] Super-Kamiokande Collaboration, A. Takenaka et al., *Search for proton decay via $p \to e^+\pi^0$ and $p \to \mu^+\pi^0$ with an enlarged fiducial volume in Super-Kamiokande I-IV*, Phys. Rev. D **102** (2020) 112011, `arXiv:2010.16098 [hep-ex]`. 2.2.3

[53] J. Hajer, *Long-lived neutralinos as probes of gravitino dark matter.* PhD thesis, Hamburg U., 2013. 2.5

[54] G. R. Farrar and P. Fayet, *Phenomenology of the production, decay, and detection of new hadronic states associated with supersymmetry*, Phys. Lett. B **76** (1978) 575. 2.2.3

[55] L. M. Krauss and F. Wilczek, *Discrete gauge symmetry in continuum theories*, Phys. Rev. Lett. **62** (1989) 1221–1223, `https://link.aps.org/doi/10.1103/PhysRevLett.62.1221`. 2.2.3

[56] L. E. Ibanez and G. G. Ross, *Discrete gauge symmetry anomalies*, Phys. Lett. B **260** (1991) 291–295. 2.2.3

[57] H. K. Dreiner, M. Hanussek, and C. Luhn, *What is the discrete gauge symmetry of the R-parity violating MSSM?*, Phys. Rev. D **86** (2012) 055012, `arXiv:1206.6305 [hep-ph]`. 2.2.3, 2.3

[58] V. Barger, P. Fileviez Perez, and S. Spinner, *Minimal Gauged $U(1)_{B-L}$ Model with Spontaneous R-Parity Violation*, Phys. Rev. Lett. **102** (2009) 181802, `arXiv:0812.3661 [hep-ph]`. 2.3

[59] L. L. Everett, P. Fileviez Perez, and S. Spinner, *The right side of TeV scale spontaneous R-Parity violation*, Phys. Rev. D **80** (2009) 055007, `arXiv:0906.4095 [hep-ph]`. 2.3

[60] V. Braun, Y.-H. He, B. A. Ovrut, and T. Pantev, *A heterotic standard model*, Phys. Lett. B **618** (2005) 252–258, `arXiv:hep-th/0501070`. 2.3

[61] P. Fileviez Perez and S. Spinner, *Spontaneous R-Parity breaking and left-right symmetry*, Phys. Lett. B **673** (2009) 251–254, `arXiv:0811.3424 [hep-ph]`. 2.3

[62] P. Fileviez Perez and S. Spinner, *The Minimal Theory for R-parity Violation at the LHC*, JHEP **04** (2012) 118, `arXiv:1201.5923 [hep-ph]`. 2.3

[63] P. Fileviez Perez and S. Spinner, *Supersymmetry at the LHC and the Theory of R-parity*, Phys. Lett. B **728** (2014) 489–495, `arXiv:1308.0524 [hep-ph]`. 2.3

[64] R. Deen, B. A. Ovrut, and A. Purves, *The minimal SUSY B − L model: simultaneous Wilson lines and string thresholds*, JHEP **07** (2016) 043, `arXiv:1604.08588 [hep-ph]`. 2.3

[65] B. A. Ovrut, A. Purves, and S. Spinner, *The minimal SUSY B − L model: from the unification scale to the LHC*, JHEP **06** (2015) 182, `arXiv:1503.01473 [hep-ph]`. 2.3

[66] B. A. Ovrut, A. Purves, and S. Spinner, *Wilson lines and a canonical basis of SU(4) heterotic standard models*, Journal of High Energy Physics **2012** (2012), `http://dx.doi.org/10.1007/JHEP11(2012)026`. 2.3, 2.3

[67] S. P. Martin, *Some simple criteria for gaugedRparity*, Physical Review D **46** (1992) R2769–R2772, `http://dx.doi.org/10.1103/PhysRevD.46.R2769`. 2.3

[68] H. K. Dreiner, C. Luhn, H. Murayama, and M. Thormeier, *Baryon triality and neutrino masses from an anomalous flavor U(1)*, Nucl. Phys. B **774** (2007) 127–167, `arXiv:hep-ph/0610026`. 2.3

[69] D. J. Gross, J. A. Harvey, E. J. Martinec, and R. Rohm, *The Heterotic String*, Phys. Rev. Lett. **54** (1985) 502–505. 2.3

[70] P. Horava and E. Witten, *Eleven-dimensional supergravity on a manifold with boundary*, Nucl. Phys. B **475** (1996) 94–114, `arXiv:hep-th/9603142`. 2.3

[71] A. Lukas, B. A. Ovrut, and D. Waldram, *On the four-dimensional effective action of strongly coupled heterotic string theory*, Nucl. Phys. B **532** (1998) 43–82, `arXiv:hep-th/9710208`. 2.3

[72] A. Lukas, B. A. Ovrut, and D. Waldram, *The Ten-dimensional effective action of strongly coupled heterotic string theory*, Nucl. Phys. B **540** (1999) 230–246, `arXiv:hep-th/9801087`. 2.3

[73] A. Lukas, B. A. Ovrut, K. S. Stelle, and D. Waldram, *The Universe as a domain wall*, Phys. Rev. D **59** (1999) 086001, `arXiv:hep-th/9803235`. 2.3

[74] A. Lukas, B. A. Ovrut, K. S. Stelle, and D. Waldram, *Heterotic M theory in five-dimensions*, Nucl. Phys. B **552** (1999) 246–290, `arXiv:hep-th/9806051`. 2.3

[75] S. Dumitru, B. Ovrut, and A. Purves, *The R-parity violating decays of charginos and neutralinos in the B-L MSSM*, Journal of High Energy Physics **2019** (2019) . 2.3.1, 2.6, 2.3.1, 2.3.2

[76] ATLAS Collaboration, *Search for new high-mass phenomena in the dilepton final state using 36 fb^{-1} of proton–proton collision data at $\sqrt{s} = 13$ TeV with the ATLAS detector*, JHEP **10** (2017) 182, `arXiv:1707.02424 [hep-ex]`. 2.3.1

[77] ATLAS Collaboration, M. Aaboud et al., *Measurement of the Higgs boson mass in the $H \to ZZ^* \to 4\ell$ and $H \to \gamma\gamma$ channels with $\sqrt{s} = 13$ TeV pp collisions using the ATLAS detector*, Phys. Lett. B **784** (2018) 345–366, `arXiv:1806.00242 [hep-ex]`. 2.3.1

[78] S. Dumitru, B. A. Ovrut, and A. Purves, *The R-parity violating decays of charginos and neutralinos in the B-L MSSM*, JHEP **02** (2019) 124, `arXiv:1810.11035 [hep-ph]`. 2.3.1, 2.3.2, 2.8, 2.9, 2.10, 2.11, 2.12, 2.13, 2.14

[79] *LHC SUSY Cross Section Working Group*, `https://twiki.cern.ch/twiki/bin/view/LHCPhysics/SUSYCrossSections`. 2.7

[80] B. Fuks, M. Klasen, D. R. Lamprea, and M. Rothering, *Gaugino production in proton-proton collisions at a center-of-mass energy of 8 TeV*, JHEP **10** (2012) 081, `arXiv:1207.2159 [hep-ph]`. 2.7, 5.2

[81] B. Fuks, M. Klasen, D. R. Lamprea, and M. Rothering, *Precision predictions for electroweak superpartner production at hadron colliders with* RESUMMINO, Eur. Phys. J. C **73** (2013) 2480, `arXiv:1304.0790 [hep-ph]`. 2.7, 5.2

[82] Particle Data Group Collaboration, M. Tanabashi et al., *Review of Particle Physics*, Phys. Rev. D **98** (2018) 030001, `https://link.aps.org/doi/10.1103/PhysRevD.98.030001`. 2.3.2, 5.1

[83] L. R. Evans and P. Bryant, *LHC Machine*, JINST **3** (2008) S08001, `https://cds.cern.ch/record/1129806`, This report is an abridged version of the LHC Design Report (CERN-2004-003). 3.1

[84] ATLAS Collaboration, *The ATLAS Experiment at the CERN Large Hadron Collider*, JINST **3** (2008) S08003. 3.1, 3.4, 3.9, 3.2.4

[85] CMS Collaboration, *The CMS experiment at the CERN LHC*, JINST **3** (2008) S08004. 3.1

[86] LHCb Collaboration, J. Alves, A.Augusto et al., *The LHCb Detector at the LHC*, JINST **3** (2008) S08005. 3.1

[87] ALICE Collaboration, K. Aamodt et al., *The ALICE experiment at the CERN LHC*, JINST **3** (2008) S08002. 3.1

[88] J. Haffner, *The CERN accelerator complex. Complexe des accélérateurs du CERN*, `http://cds.cern.ch/record/1621894`, General Photo. 3.1

[89] R. Steerenberg and J. Wenninger, *Operational challenges and performance of the LHC during Run II. Operation Challenges and Performance of the LHC During Run II*, `https://cds.cern.ch/record/2640329`. 3.1, 3.1, 4.2.2

[90] J. Jimenez et al., *Observations, Analysis and Mitigation of Recurrent LHC Beam Dumps Caused by Fast Losses in Arc Half-Cell 16L2*, `https://cds.cern.ch/record/2646067`. 3.1, 3.1, 4.2.2

[91] B. Salvant et al., *Experimental Characterisation of a Fast Instability Linked to Losses in the 16L2 Cryogenic Half-Cell in the CERN LHC*, `https://cds.cern.ch/record/2646056`. 3.1, 3.1, 4.2.2

[92] W. Herr and B. Muratori, *Concept of luminosity*, `https://cds.cern.ch/record/941318`. 3.1

[93] ATLAS Collaboration, *ATLAS data quality operations and performance for 2015–2018 data-taking*, JINST **15** (2020) P04003, `arXiv:1911.04632 [physics.ins-det]`. 3.1, 3.2, 5.2, 5.3

[94] ATLAS Collaboration,, *LuminosityPublicResultsRun2*, `https://twiki.cern.ch/twiki/bin/view/AtlasPublic/LuminosityPublicResultsRun2`. Accessed: 2020-12-30. 3.2, 3.3

[95] ATLAS Collaboration,, *ATLAS inner detector: Technical Design Report, Vol. 1.* CERN, Geneva, 1997. `https://cds.cern.ch/record/331063`. 3.2.1

[96] ATLAS Collaboration,, *ATLAS inner detector: Technical Design Report, Vol. 2.* CERN, Geneva, 1997. `https://cds.cern.ch/record/331064`. 3.2.1

[97] ATLAS Collaboration, *The ATLAS Inner Detector commissioning and calibration*, Eur. Phys. J. C **70** (2010) 787, `arXiv:1004.5293 [hep-ex]`. 3.2.1

[98] ATLAS Collaboration, M. Alam et al., *ATLAS pixel detector: Technical design report,*. 3.2.1

[99] G. Aad et al., *ATLAS pixel detector electronics and sensors*, JINST **3** (2008) P07007. 3.2.1

[100] A. Ahmad et al., *The Silicon microstrip sensors of the ATLAS semiconductor tracker*, Nucl. Instrum. Meth. **A578** (2007) 98–118. 3.2.1

[101] A. Ahmad et al., *The Silicon microstrip sensors of the ATLAS semiconductor tracker*, Nucl. Instrum. Meth. A **578** (2007) 98–118. 3.2.1

[102] ATLAS Collaboration, *Operation and performance of the ATLAS semiconductor tracker*, JINST **9** (2014) P08009, `arXiv:1404.7473 [hep-ex]`. 3.2.1

[103] E. Abat et al., *The ATLAS Transition Radiation Tracker (TRT) proportional drift tube: Design and performance*, JINST **3** (2008) P02013. 3.2.1

[104] E. Abat et al., *The ATLAS TRT Barrel Detector*, JINST **3** (2008) P02014. 3.2.1

[105] E. Abat et al., *The ATLAS TRT end-cap detectors*, JINST **3** (2008) P10003. 3.2.1

[106] S. Fratina and E. Klinkby, *The Geometry of the ATLAS Transition Radiation Tracker*, ATL-COM-INDET-2010-002, 2010. 3.2.1

[107] ATLAS Collaboration, *Particle Identification Performance of the ATLAS Transition Radiation Tracker*, ATLAS-CONF-2011-128, 2011, `https://cds.cern.ch/record/1383793`. 3.2.1

[108] E. Abat et al., *The ATLAS TRT electronics*, JINST **3** (2008) P06007. 3.2.1, 4.1.1

[109] K. Yoshihara, B. Haney, C. Meyer, H. Williams, P. Keener, E. D. Resseguie, G. I. Dyckes, L. Schaefer, K. Mistry, V. W. S. Wong, D. Ponomarenko, and C. Gay, *TRT DAQ Performance for Run 2*, Tech. Rep. ATL-COM-INDET-2017-041, CERN, Geneva, Sep, 2017. `https://cds.cern.ch/record/2282001`. 3.2.1, 4.3.2, 4.4

[110] I. Dyckes, *TRT Compression and Readout Performance in Run 2*, Tech. Rep. ATL-COM-INDET-2018-057, CERN, Geneva, Oct, 2018. `https://cds.cern.ch/record/2640983`. 3.2.1, 4.3.2

[111] ATLAS Collaboration, *ATLAS Insertable B-Layer Technical Design Report*, Atlas-tdr-19, 2010, `https://cds.cern.ch/record/1291633`. 3.2.1

[112] B. Abbott et al., *Production and integration of the ATLAS Insertable B-Layer*, JINST **13** (2018) T05008, `arXiv:1803.00844 [physics.ins-det]`. 3.2.1

[113] ATLAS Collaboration, M. Aaboud et al., *Performance of the ATLAS Track Reconstruction Algorithms in Dense Environments in LHC Run 2*, Eur. Phys. J. C **77** (2017) 673, `arXiv:1704.07983 [hep-ex]`. 3.5

[114] ATLAS Collaboration, M. Aaboud et al., *Study of the material of the ATLAS inner detector for Run 2 of the LHC*, JINST **12** (2017) P12009, `arXiv:1707.02826 [hep-ex]`. 3.6

[115] ATLAS Collaboration,, *The ATLAS experiment at the CERN Large Hadron Collider*, JINST **3** (2008) S08003. 3.7

[116] ATLAS Collaboration,, *ATLAS liquid-argon calorimeter: Technical Design Report*. CERN, Geneva, 1996. `https://cds.cern.ch/record/331061`. 3.2.2.1

[117] I. Wingerter-Seez, *Particle Physics Instrumentation*, `https://cds.cern.ch/record/2315747`, * Brief entry *. 3.8

[118] ATLAS Collaboration,, *ATLAS tile calorimeter: Technical Design Report*. CERN, Geneva, 1996. `https://cds.cern.ch/record/331062`. 3.2.2.2

[119] ATLAS Collaboration,, *ATLAS muon spectrometer: Technical Design Report*. CERN, Geneva, 1997. `https://cds.cern.ch/record/331068`. 3.2.3

[120] ATLAS Collaboration, *Performance of the ATLAS muon trigger in pp collisions at $\sqrt{s} = 8$ TeV*, Eur. Phys. J. C **75** (2015) 120, `arXiv:1408.3179 [hep-ex]`. 3.9

[121] ATLAS Collaboration, *Performance of the ATLAS Trigger System in 2015*, Eur. Phys. J. C **77** (2017) 317, `arXiv:1611.09661 [hep-ex]`. 3.2.4, 24

[122] ATLAS Collaboration, *Quark versus Gluon Jet Tagging Using Charged-Particle Constituent Multiplicity with the ATLAS Detector*, ATL-PHYS-PUB-2017-009, 2017, `https://cds.cern.ch/record/2263679`. 3.3

[123] ATLAS Collaboration, *Quark versus Gluon Jet Tagging Using Jet Images with the ATLAS Detector*, ATL-PHYS-PUB-2017-017, 2017, `https://cds.cern.ch/record/2275641`. 3.3

[124] J. Pequenao and P. Schaffner, *How ATLAS detects particles: diagram of particle paths in the detector*, Jan, 2013. 3.11

[125] ATLAS Collaboration, E. Hines, *Performance of Particle Identification with the ATLAS Transition Radiation Tracker*, in *Meeting of the APS Division of Particles and Fields*. 9, 2011. `arXiv:1109.5925 [physics.ins-det]`. 4.5

[126] P. Moreira, G. Cervelli, J. Christiansen, F. Faccio, A. Kluge, A. Marchioro, T. H. Toifl, J. P. Cachemiche, and M. Menouni, *A radiation tolerant gigabit serializer for LHC data transmission*, `http://cds.cern.ch/record/588665`. 4.1.2

[127] H. C. van der Bij, R. A. McLaren, O. Boyle, and G. Rubin, *S-LINK, a data link interface specification for the LHC era*, IEEE Transactions on Nuclear Science **44** (1997) 398–402. 4.1.2

[128] A. R. Ruiz, J. Haee, E. van der Bij, and S. Haas, *High-Speed Optical Link for ATLAS*, `http://hsi.web.cern.ch/s-link/devices/hola/`. 4.1.2

[129] D. A. Huffman, *A Method for the Construction of Minimum-Redundancy Codes*, Proceedings of the IRE **40** (1952) 1098–1101. 4.2

[130] C. E. Shannon, *A mathematical theory of communication*, The Bell System Technical Journal **27** (1948) 379–423. 4.2

[131] *Huffman coding*, `https://en.wikipedia.org/wiki/Huffman_coding`, 2017. 4.8, 4.2

[132] F. Akesson, M. J. Costa, D. Dobos, M. Elsing, S. Fleischmann, A. Gaponenko, K. Gnanvo, P. T. Keener, W. Liebig, E. Moyse, A. Salzburger, M. Siebel, and A. Wildauer, *ATLAS Inner Detector Event Data Model*, Tech. Rep. ATL-SOFT-PUB-2007-006. ATL-COM-SOFT-2007-015, CERN, Geneva, Dec, 2007. `https://cds.cern.ch/record/1074712`. 4.4

[133] S. Smirnov, *TRTViewer: The ATLAS TRT detector monitoring and diagnosticstool*, Nuclear Instruments and Methods in Physics Research Section A: Accelerators, Spectrometers, Detectors and Associated Equipment **706** (2013) 90–92, `http://dx.doi.org/10.1016/j.nima.2012.05.018`. 4.4

[134] ATLAS Collaboration, G. Aad et al., *Search for trilepton resonances from chargino and neutralino pair production in $\sqrt{s} = 13$ TeV pp collisions with the ATLAS detector*, `arXiv:2011.10543 [hep-ex]`. 5

[135] ATLAS Collaboration, *Search for type-III seesaw heavy leptons in pp collisions at $\sqrt{s} = 8$ TeV with the ATLAS Detector*, Phys. Rev. D **92** (2015) 032001, `arXiv:1506.01839 [hep-ex]`. 5.1

[136] ATLAS Collaboration, *Search for heavy lepton resonances decaying to a Z boson and a lepton in pp collisions at $\sqrt{s} = 8$ TeV with the ATLAS detector*, JHEP **09** (2015) 108, `arXiv:1506.01291 [hep-ex]`. 5.1

[137] CMS Collaboration, *Search for Evidence of the Type-III Seesaw Mechanism in Multilepton Final States in Proton–Proton Collisions at $\sqrt{s} = 13$ TeV*, Phys. Rev. Lett. **119** (2017) 221802, `arXiv:1708.07962 [hep-ex]`. 5.1

[138] A. Lipniacka, *Understanding SUSY limits from LEP*, `https://cds.cern.ch/record/588813`. 5.1

[139] ATLAS Collaboration, *Search for electroweak production of supersymmetric particles in final states with two or three leptons at $\sqrt{s} = 13$ TeV with the ATLAS detector*, `arXiv:1803.02762 [hep-ex]`. 5.1

[140] ATLAS Collaboration, *Search for direct production of charginos and neutralinos in events with three leptons and missing transverse momentum in $\sqrt{s} = 8$ TeV pp collisions with the ATLAS detector*, JHEP **04** (2014) 169, `arXiv:1402.7029 [hep-ex]`. 5.1

[141] CMS Collaboration, *Search for electroweak production of charginos and neutralinos in multilepton final states in proton–proton collisions at $\sqrt{s} = 13$ TeV*, `arXiv:1709.05406 [hep-ex]`. 5.1

[142] CMS Collaboration, *Combined search for electroweak production of charginos and neutralinos in proton–proton collisions at $\sqrt{s} = 13$ TeV*, `arXiv:1801.03957 [hep-ex]`. 5.1

[143] ATLAS Collaboration, *Multi-Boson Simulation for 13 TeV ATLAS Analyses*, ATL-PHYS-PUB-2017-005, 2017, `https://cds.cern.ch/record/2261933`. 5.2

[144] ATLAS Collaboration, *ATLAS simulation of boson plus jets processes in Run 2*, ATL-PHYS-PUB-2017-006, 2017, `https://cds.cern.ch/record/2261937`. 5.2

[145] E. Bothmann et al., *Event Generation with Sherpa 2.2*, `arXiv:1905.09127 [hep-ph]`. 5.2

[146] T. Gleisberg and S. Höche, *Comix, a new matrix element generator*, JHEP **12** (2008) 039, `arXiv:0808.3674 [hep-ph]`. 5.2

[147] S. Schumann and F. Krauss, *A parton shower algorithm based on Catani–Seymour dipole factorisation*, JHEP **03** (2008) 038, `arXiv:0709.1027 [hep-ph]`. 5.2

[148] S. Catani, F. Krauss, R. Kuhn, and B. R. Webber, *QCD matrix elements + parton showers*, JHEP **11** (2001) 063, `arXiv:hep-ph/0109231`. 5.2

[149] S. Höche, F. Krauss, S. Schumann, and F. Siegert, *QCD matrix elements and truncated showers*, JHEP **05** (2009) 053, `arXiv:0903.1219 [hep-ph]`. 5.2

[150] S. Höche, F. Krauss, M. Schönherr, and F. Siegert, *A critical appraisal of NLO+PS matching methods*, JHEP **09** (2012) 049, `arXiv:1111.1220 [hep-ph]`. 5.2

[151] S. Höche, F. Krauss, M. Schönherr, and F. Siegert, *QCD matrix elements + parton showers: The NLO case*, JHEP **04** (2013) 027, `arXiv:1207.5030 [hep-ph]`. 5.2

[152] F. Cascioli, P. Maierhofer, and S. Pozzorini, *Scattering Amplitudes with Open Loops*, Phys. Rev. Lett. **108** (2012) 111601, `arXiv:1111.5206 [hep-ph]`. 5.2

[153] A. Denner, S. Dittmaier, and L. Hofer, *Collier: a fortran-based Complex One-Loop LIbrary in Extended Regularizations*, Comput. Phys. Commun. **212** (2017) 220–238, `arXiv:1604.06792 [hep-ph]`. 5.2

[154] NNPDF Collaboration, R. D. Ball et al., *Parton distributions for the LHC Run II*, JHEP **04** (2015) 040, `arXiv:1410.8849 [hep-ph]`. 5.2

[155] C. Anastasiou, L. J. Dixon, K. Melnikov, and F. Petriello, *High precision QCD at hadron colliders: Electroweak gauge boson rapidity distributions at NNLO*, Phys. Rev. D **69** (2004) 094008, `arXiv:hep-ph/0312266`. 5.2

[156] S. Frixione et al., *A positive-weight next-to-leading-order Monte Carlo for heavy flavour hadroproduction*, JHEP **09** (2007) 126, `arXiv:0707.3088 [hep-ph]`. 5.2

[157] H. B. Hartanto, B. Jager, L. Reina, and D. Wackeroth, *Higgs boson production in association with top quarks in the POWHEG BOX*, Phys. Rev. D **91** (2015) 094003, `arXiv:1501.04498 [hep-ph]`. 5.2

[158] E. Re, *Single-top Wt-channel production matched with parton showers using the POWHEG method*, Eur. Phys. J. C **71** (2011) 1547, `arXiv:1009.2450 [hep-ph]`. 5.2

[159] P. Nason, *A new method for combining NLO QCD with shower Monte Carlo algorithms*, JHEP **11** (2004) 040, `arXiv:hep-ph/0409146`. 5.2

[160] S. Frixione, P. Nason, and C. Oleari, *Matching NLO QCD computations with parton shower simulations: the POWHEG method*, JHEP **11** (2007) 070, `arXiv:0709.2092 [hep-ph]`. 5.2

[161] S. Alioli, P. Nason, C. Oleari, and E. Re, *A general framework for implementing NLO calculations in shower Monte Carlo programs: the POWHEG BOX*, JHEP **06** (2010) 043, `arXiv:1002.2581 [hep-ph]`. 5.2

[162] T. Sjöstrand, S. Ask, J. R. Christiansen, R. Corke, N. Desai, P. Ilten, S. Mrenna, S. Prestel, C. O. Rasmussen, and P. Z. Skands, *An introduction to PYTHIA 8.2*, Comput. Phys. Commun. **191** (2015) 159, `arXiv:1410.3012 [hep-ph]`. 5.2

[163] ATLAS Collaboration, *ATLAS Pythia 8 tunes to 7 TeV data*, ATL-PHYS-PUB-2014-021, 2014, `https://cds.cern.ch/record/1966419`. 5.2, 5.6

[164] R. D. Ball et al., *Parton distributions with LHC data*, Nucl. Phys. B **867** (2013) 244, `arXiv:1207.1303 [hep-ph]`. 5.2

[165] ATLAS Collaboration, *Studies on top-quark Monte Carlo modelling for Top2016*, ATL-PHYS-PUB-2016-020, 2016, `https://cds.cern.ch/record/2216168`. 5.2

[166] M. Czakon and A. Mitov, *Top++: A Program for the Calculation of the Top-Pair Cross-Section at Hadron Colliders*, Comput. Phys. Commun. **185** (2014) 2930, `arXiv:1112.5675 [hep-ph]`. 5.2

[167] M. Aliev, H. Lacker, U. Langenfeld, S. Moch, P. Uwer, and M. Wiedermann, *HATHOR: HAdronic Top and Heavy quarks crOss section calculatoR*, Comput. Phys. Commun. **182** (2011) 1034–1046, `arXiv:1007.1327 [hep-ph]`. 5.2

[168] P. Kant, O. M. Kind, T. Kintscher, T. Lohse, T. Martini, S. Mölbitz, P. Rieck, and P. Uwer, *HatHor for single top-quark production: Updated predictions and uncertainty estimates for single top-quark production in hadronic collisions*, Comput. Phys. Commun. **191** (2015) 74–89, `arXiv:1406.4403 [hep-ph]`. 5.2

[169] S. Frixione, E. Laenen, P. Motylinski, B. R. Webber, and C. D. White, *Single-top hadroproduction in association with a W boson*, JHEP **07** (2008) 029, `arXiv:0805.3067 [hep-ph]`. 5.2

[170] J. Alwall, R. Frederix, S. Frixione, V. Hirschi, F. Maltoni, O. Mattelaer, H. S. Shao, T. Stelzer, P. Torrielli, and M. Zaro, *The automated computation of tree-level and next-to-leading order differential cross sections, and their matching to parton shower simulations*, JHEP **07** (2014) 079, `arXiv:1405.0301 [hep-ph]`. 5.2

[171] K. Hamilton, P. Nason, E. Re, and G. Zanderighi, *NNLOPS simulation of Higgs boson production*, JHEP **10** (2013) 222, `arXiv:1309.0017 [hep-ph]`. 5.2

[172] ATLAS Collaboration, *Measurement of the Z/γ^* boson transverse momentum distribution in pp collisions at $\sqrt{s} = 7$ TeV with the ATLAS detector*, JHEP **09** (2014) 145, `arXiv:1406.3660 [hep-ex]`. 5.2

[173] J. Butterworth et al., *PDF4LHC recommendations for LHC Run II*, J. Phys. G **43** (2016) 023001, `arXiv:1510.03865 [hep-ph]`. 5.2, 5.6

[174] U. Aglietti, R. Bonciani, G. Degrassi, and A. Vicini, *Two-loop light fermion contribution to Higgs production and decays*, Phys. Lett. B **595** (2004) 432–441, `arXiv:hep-ph/0404071`. 5.2

[175] S. Actis, G. Passarino, C. Sturm, and S. Uccirati, *NLO electroweak corrections to Higgs boson production at hadron colliders*, Phys. Lett. B **670** (2008) 12–17, `arXiv:0809.1301 [hep-ph]`. 5.2

[176] J. Pumplin et al., *New generation of parton distributions with uncertainties from global QCD analysis*, JHEP **07** (2002) 012, `arXiv:hep-ph/0201195`. 5.2

[177] M. Ciccolini, A. Denner, and S. Dittmaier, *Strong and electroweak corrections to the production of Higgs + 2 jets via weak interactions at the Large Hadron Collider*, Phys. Rev. Lett. **99** (2007) 161803, `arXiv:0707.0381 [hep-ph]`. 5.2

[178] T. Han and S. Willenbrock, *QCD correction to the pp → WH and ZH total cross sections*, Phys. Lett. B **273** (1991) 167–172. 5.2

[179] O. Brein, A. Djouadi, and R. Harlander, *NNLO QCD corrections to the Higgs-strahlung processes at hadron colliders*, Phys. Lett. B **579** (2004) 149–156, `arXiv:hep-ph/0307206`. 5.2

[180] M. L. Ciccolini, S. Dittmaier, and M. Krämer, *Electroweak radiative corrections to associated WH and ZH production at hadron colliders*, Phys. Rev. D **68** (2003) 073003, `arXiv:hep-ph/0306234`. 5.2

[181] W. Beenakker et al., *The Production of Charginos/Neutralinos and Sleptons at Hadron Colliders*, Phys. Rev. Lett. **83** (1999) 3780, `arXiv:hep-ph/9906298`. 5.2

[182] J. Debove, B. Fuks, and M. Klasen, *Threshold resummation for gaugino pair production at hadron colliders*, Nucl. Phys. B **842** (2011) 51, `arXiv:1005.2909 [hep-ph]`. 5.2

[183] J. Fiaschi and M. Klasen, *Neutralino-chargino pair production at NLO+NLL with resummation-improved parton density functions for LHC Run II*, Phys. Rev. D **98** (2018) 055014, `arXiv:1805.11322 [hep-ph]`. 5.2

[184] C. Borschensky, M. Krämer, A. Kulesza, M. Mangano, S. Padhi, T. Plehn, and X. Portell, *Squark and gluino production cross sections in pp collisions at $\sqrt{s} = 13, 14, 33$ and 100 TeV*, Eur. Phys. J. C **74** (2014) 3174, `arXiv:1407.5066 [hep-ph]`. 5.2

[185] D. J. Lange, *The EvtGen particle decay simulation package*, Nucl. Instrum. Meth. A **462** (2001) 152. 5.2

[186] ATLAS Collaboration, *The ATLAS Simulation Infrastructure*, Eur. Phys. J. C **70** (2010) 823, `arXiv:1005.4568 [physics.ins-det]`. 5.2

[187] S. Agostinelli et al., GEANT4 – *a simulation toolkit*, Nucl. Instrum. Meth. A **506** (2003) 250. 5.2

[188] ATLAS Collaboration, *The Pythia 8 A3 tune description of ATLAS minimum bias and inelastic measurements incorporating the Donnachie-Landshoff diffractive model*, ATL-PHYS-PUB-2016-017, 2016, `https://cds.cern.ch/record/2206965`. 5.2

[189] ATLAS Collaboration, *Vertex Reconstruction Performance of the ATLAS Detector at $\sqrt{s} = 13$ TeV*, ATL-PHYS-PUB-2015-026, 2015, `https://cds.cern.ch/record/2037717`. 5.3

[190] ATLAS Collaboration, ATLAS Collaboration, *Electron reconstruction and identification in the ATLAS experiment using the 2015 and 2016 LHC proton-proton collision data at $\sqrt{s} = 13$ TeV*, Submitted to: Eur. Phys. J. (2019), `arXiv:1902.04655 [physics.ins-det]`. 5.3

[191] ATLAS Collaboration, *Muon reconstruction performance of the ATLAS detector in proton–proton collision data at $\sqrt{s} = 13$ TeV*, Eur. Phys. J. C **76** (2016) 292, `arXiv:1603.05598 [hep-ex]`. 5.3, 5.6

[192] ATLAS Collaboration, *Performance of pile-up mitigation techniques for jets in pp collisions at $\sqrt{s} = 8$ TeV using the ATLAS detector*, Eur. Phys. J. C **76** (2016) 581, `arXiv:1510.03823 [hep-ex]`. 5.3, 5.6

[193] ATLAS Collaboration, *Identification and rejection of pile-up jets at high pseudorapidity with the ATLAS detector*, Eur. Phys. J. C **77** (2017) 580, `arXiv:1705.02211 [hep-ex]`. 5.3

[194] ATLAS Collaboration, *Optimisation of the ATLAS b-tagging performance for the 2016 LHC Run*, ATL-PHYS-PUB-2016-012, 2016, `https://cds.cern.ch/record/2160731`. 5.3

[195] ATLAS Collaboration, *Photon identification in 2015 ATLAS data*, ATL-PHYS-PUB-2016-014, 2016, `https://cds.cern.ch/record/2203125`. 5.3

[196] ATLAS Collaboration, *Performance of missing transverse momentum reconstruction with the ATLAS detector using proton–proton collisions at $\sqrt{s} = 13$ TeV*, `arXiv:1802.08168 [hep-ex]`. 5.3, 5.6

[197] M. Baak, G. Besjes, D. Côté, A. Koutsman, J. Lorenz, and D. Short, *HistFitter software framework for statistical data analysis*, Eur. Phys. J. C **75** (2015) 153, `arXiv:1410.1280 [hep-ex]`. 5.4, 5.7, 5.8.4, A

[198] W. Buttinger and M. Lefebvre, *Formulae for Estimating Significance*, Tech. Rep. ATL-COM-GEN-2018-026, CERN, Geneva, Oct, 2018. `https://cds.cern.ch/record/2643488`. 5.6, 5.8.2

[199] ATLAS Collaboration, *Jet energy scale measurements and their systematic uncertainties in proton–proton collisions at $\sqrt{s} = 13$ TeV with the ATLAS detector*, Phys. Rev. D **96** (2017) 072002, `arXiv:1703.09665 [hep-ex]`. 5.6

[200] ATLAS Collaboration, *Jet energy resolution in proton–proton collisions at $\sqrt{s} = 7$ TeV recorded in 2010 with the ATLAS detector*, Eur. Phys. J. C **73** (2013) 2306, `arXiv:1210.6210 [hep-ex]`. 5.6

[201] ATLAS Collaboration, *Electron and photon performance measurements with the ATLAS detector using the 2015–2017 LHC proton–proton collision data*, JINST **14** (2019) P12006, `arXiv:1908.00005 [hep-ex]`. 5.6

[202] ATLAS Collaboration, *ATLAS b-jet identification performance and efficiency measurement with $t\bar{t}$ events in pp collisions at $\sqrt{s} = 13$ TeV*, Eur. Phys. J. C **79** (2019) 970, `arXiv:1907.05120 [hep-ex]`. 5.6

[203] G. Avoni et al., *The new LUCID-2 detector for luminosity measurement and monitoring in ATLAS*, JINST **13** (2018) P07017. 5.6

[204] S. Dulat, T.-J. Hou, J. Gao, M. Guzzi, J. Huston, P. Nadolsky, J. Pumplin, C. Schmidt, D. Stump, and C. P. Yuan, *New parton distribution functions from a global analysis of quantum chromodynamics*, Phys. Rev. D **93** (2016) 033006, `arXiv:1506.07443 [hep-ph]`. 5.6

[205] L. Harland-Lang, A. Martin, P. Motylinski, and R. Thorne, *Parton distributions in the LHC era: MMHT 2014 PDFs*, Eur. Phys. J. C **75** (2015) 204, `arXiv:1412.3989 [hep-ph]`. 5.6

[206] E. Bothmann, M. Schönherr, and S. Schumann, *Reweighting QCD matrix-element and parton-shower calculations*, Eur. Phys. J. C **76** (2016) 590, `arXiv:1606.08753 [hep-ph]`. 5.6

[207] ROOT Collaboration Collaboration, K. Cranmer, G. Lewis, L. Moneta, A. Shibata, and W. Verkerke, *HistFactory: A tool for creating statistical models for use with RooFit and RooStats*, Tech. Rep. CERN-OPEN-2012-016, New York U., New York, Jan, 2012. `https://cds.cern.ch/record/1456844`. 5.7, 5.8.4

[208] L. Moneta, K. Belasco, K. Cranmer, S. Kreiss, A. Lazzaro, D. Piparo, G. Schott, W. Verkerke, and M. Wolf, *The RooStats Project*, 2011. 5.7, 5.8.4

[209] R. D. Cousins, J. T. Linnemann, and J. Tucker, *Evaluation of three methods for calculating statistical significance when incorporating a systematic uncertainty into a test of the background-only hypothesis for a Poisson process*, Nuclear Instruments and Methods in Physics Research A **595** (2008) 480–501, `arXiv:physics/0702156 [physics.data-an]`. 5.7

[210] K. Cranmer, *Practical Statistics for the LHC*, `https://cds.cern.ch/record/2004587`, Comments: presented at the 2011 European School of High-Energy Physics, Cheile Gradistei, Romania, 7-20 September 2011 I expect to release updated versions of this document in the future. 5.7, 5.7

[211] S. S. Wilks, *The Large-Sample Distribution of the Likelihood Ratio for Testing Composite Hypotheses*, Ann. Math. Statist. **9** (1938) 60–62, `https://doi.org/10.1214/aoms/1177732360`. 30, 5.7

[212] A. Wald, *Tests of Statistical Hypotheses Concerning Several Parameters When the Number of Observations is Large*, Transactions of the American Mathematical Society **54** (1943) 426–482, `http://www.jstor.org/stable/1990256`. 30, 5.7

[213] A. L. Read, *Presentation of search results: the CL_s technique*, J. Phys. G **28** (2002) 2693–2704. 5.7

[214] G. Cowan, K. Cranmer, E. Gross, and O. Vitells, *Asymptotic formulae for likelihood-based tests of new physics*, Eur. Phys. J. C **71** (2011) 1554, `arXiv:1007.1727 [physics.data-an]`. 5.7

[215] ATLAS Collaboration,, *Search for trilepton resonances from chargino and neutralino pair production in $\sqrt{s}$ = 13 TeV pp collisions with the ATLAS detector*, 2020. `https://doi.org/10.17182/hepdata.99806`. 5.8.4, 5.8.4

[216] P. C. Bryan and M. Nottingham, *JavaScript Object Notation (JSON) Patch*, 2013. `https://www.rfc-editor.org/rfc/rfc6902.txt`. 5.8.4

[217] ATLAS Collaboration, M. Aaboud et al., *Performance of top-quark and W-boson tagging with ATLAS in Run 2 of the LHC*, Eur. Phys. J. C **79** (2019) 375, `arXiv:1808.07858 [hep-ex]`. 5.9

[218] ATLAS Collaboration, G. Aad et al., *Identification of boosted Higgs bosons decaying into b-quark pairs with the ATLAS detector at 13 TeV*, Eur. Phys. J. C **79** (2019) 836, `arXiv:1906.11005 [hep-ex]`. 5.9

[219] R. Franceschini, T. Hambye, and A. Strumia, *Type-III see-saw at LHC*, Phys. Rev. D **78** (2008) 033002, `arXiv:0805.1613 [hep-ph]`. 5.9

[220] A. Falkowski, D. M. Straub, and A. Vicente, *Vector-like leptons: Higgs decays and collider phenomenology*, JHEP **05** (2014) 092, `arXiv:1312.5329 [hep-ph]`. 5.9

[221] ATLAS Collaboration, M. Aaboud et al., *Measurement of $W^{\pm}Z$ production cross sections and gauge boson polarisation in pp collisions at $\sqrt{s} = 13$ TeV with the ATLAS detector*, Eur. Phys. J. C **79** (2019) 535, `arXiv:1902.05759 [hep-ex]`. C.2

[222] ATLAS Collaboration, M. Aaboud et al., *$ZZ \to \ell^+\ell^-\ell'^+\ell'^-$ cross-section measurements and search for anomalous triple gauge couplings in 13 TeV pp collisions with the ATLAS detector*, Phys. Rev. D **97** (2018) 032005, `arXiv:1709.07703 [hep-ex]`. C.2